Rock bed thermal storage for concentrating solar power plants

by
Kenneth Guy Allen

Dissertation presented for the degree of
Doctor of Philosophy in the
Faculty of Engineering at
Stellenbosch University

Promoter: Prof. Theodor W. von Backström
Co-Promoter: Prof Detlev G. Kröger

April 2014

The financial assistance of the National Research Foundation (NRF) towards this research is hereby acknowledged. Opinions expressed and conclusions arrived at are those of the author and are not necessarily to be attributed to the NRF.

Declaration

By submitting this dissertation electronically, I declare that the entirety of the work contained therein is my own, original work, that I am the sole author thereof (save to the extent explicitly otherwise stated), that reproduction and publication thereof by Stellenbosch University will not infringe any third party rights and that I have not previously in its entirety or in part submitted it for obtaining any qualification.

This dissertation includes one original paper published in peer-reviewed journals or books and one unpublished publication. The development and writing of the papers (published and unpublished) were the principal responsibility of myself and, for each of the cases where this is not the case, a declaration is included in the dissertation indicating the nature and extent of the contributions of co-authors.

Date: .....

Abstract

Concentrating solar power plants are a promising means of generating electricity. However, they are dependent on the sun as a source of energy, and require thermal storage to supply power on demand. At present thermal storage – usually molten salt – although functional, is expensive, and a cheaper solution is desired. It is proposed that sensible heat storage in a packed bed of rock, with air as heat transfer medium, is suitable at temperatures of 500 – 600 °C. To determine if this concept is technically feasible and economically competitive with existing storage, rock properties, packed bed pressure drop and thermal characteristics must be understood. This work addresses these topics.

No previously published data is available on thermal cycling resistance of South African rock, and there is limited data from other countries in the proposed temperature range for long-term thermal cycling, so samples were thermally cycled. There is rock which is suitable for thermal storage applications at temperatures of 500 – 600 °C. New maps of South Africa showing where potentially suitable rock is available were produced. Dolerite, found extensively in the Karoo, is particularly suitable.

Friction factors were measured for beds of different particles to determine the importance of roughness, shape, and packing arrangement. Five sets of rock were also tested, giving a combined dataset broader than published in any previous study. Limitations of existing correlations are shown. The friction factor is highly dependent on particle shape and, in the case of asymmetric particles, packing method. The friction factor varied by up to 70 % for crushed rock depending on the direction in which it was poured into the test section, probably caused by the orientation of the asymmetric rock relative to the air flow direction. This has not been reported before for rock beds. New isothermal correlations using the volume equivalent particle diameter are given: they are within 15 % of the measurements. This work will allow a techno-economic evaluation of crushed rock beds using more accurate predictions of pumping power than could previously be made.

Thermal tests below 80 °C show that bed heat transfer is insensitive to particle shape or type. A heat transfer correlation for air in terms of the volume equivalent diameter was formulated and combined with the E-NTU method. The predicted bed outlet temperatures are within 5 °C of the measurements for tests at 530 °C, showing that the influence of thermal conduction and radiation can be reasonably negligible for a single charge/discharge cycle at mass fluxes around 0.2 kg/m^{2}s.

A novel method for finding the optimum particle size and bed length is given: The Biot number is fixed, and the net income (income less bed cost) from a steam cycle supplied by heat from the bed is calculated. A simplified calculation using the method shows that the optimum particle size is approximately 20 mm for bed lengths of 6 – 7 m. Depending on the containment design and cost, the capital cost could be an order of magnitude lower than a nitrate salt system.

Opsomming

Gekonsentreerde son-energie kragstasies is ‘n belowende manier om elektrisiteit op te wek, maar hulle is afhanklik van die son as ‘n bron van energie. Om drywing op aanvraag te voorsien moet hulle energie stoor. Tans is termiese stoor – gewoonlik gesmelte sout – hoewel funksioneel, duur, en ‘n goedkoper oplossing word gesoek. Daar word voorgestel dat stoor van voelbare warmte-energie in ‘n gepakte rotsbed met lug as warmteoordrag medium geskik is by temperature van 500 – 600 °C. Om te bepaal of dié konsep tegnies gangbaar en ekonomies mededingend met bestaande stoorstelsels is, moet rotseienskappe, gepakte bed drukval en hitteoordrag verstaan word. Hierdie werk spreek hierdie aspekte aan.

Geen voorheen gepubliseerde data is beskikbaar oor die termiese siklus weerstand van Suid-Afrikaanse rots nie, en daar is beperkte data van ander lande in die voorgestelde temperatuurbereik, dus is monsters onderwerp aan termiese siklusse. Daar bestaan rots wat geskik is vir termiese stoor toepassings by temperature van 500 – 600 °C. Nuwe kaarte van Suid-Afrika is opgestel om te wys waar potensieel geskikte rots beskikbaar is. Doleriet, wat wyd in die Karoo voor kom, blyk om veral geskik te wees.

Wrywingsfaktore is gemeet vir beddens van verskillende partikels om die belangrikheid van grofheid, vorm en pak-rangskikking te bepaal. Vyf rotsstelle is ook getoets, wat ‘n saamgestelde datastel gee wyer as in enige gepubliseerde studie. Beperkings van bestaande korrelasies word aangetoon. Die wrywingsfaktor is hoogs sensitief vir partikelvorm en, in die geval van asimmetriese partikels, pakkings metode. Die wrywingsfaktor het met tot 70 % gevarieer vir gebreekte rots, afhanklik van die rigting waarin dit in die toetsseksie neergelê is. Dit is waarskynlik veroorsaak deur die oriëntasie van die asimmetriese rots relatief tot die lugvloei rigting, en is nie voorheen vir rotsbeddens gerapporteer nie. Nuwe isotermiese korrelasies wat gebruik maak van die volume-ekwivalente partikel deursnee word gegee: hulle voorspel binne 15 % van die gemete waardes. Hierdie werk sal ‘n tegno-ekonomiese studie van rotsbeddens toelaat wat meer akkurate voorspellings van pompdrywing gebruik as voorheen moontlik was.

Termiese toetse onder 80 °C wys dat die warmteoordrag nie baie sensitief is vir partikelvorm en -tipe nie. ‘n Warmte-oordragskorrelasie vir lug in terme van die volume-ekwivalente deursnee is ontwikkel en met die E-NTU-metode gekombineer. Die voorspelde lug uitlaat temperatuur is binne 5 °C van die meting vir toetse by 530 °C. Dit wys dat termiese geleiding en straling redelikerwys buite rekening gelaat kan word vir ‘n enkele laai/ontlaai siklus by massa vloeitempos van omtrent 0.2 kg/m^{2}s.

‘n Oorspronklike metode vir die bepaling van die optimum partikelgrootte en bedlengte word gegee: Die Biot-getal is vas, en die netto inkomste (die inkomste minus die bed omkoste) van ‘n stoomsiklus voorsien met warmte van die bed

word bereken. ‘n Vereenvoudigde berekening wat die metode gebruik wys dat die optimum grootte en lengte ongeveer 20 mm en 6-7 m is. Afhangende van die behoueringsontwerp en koste, kan die kapitale koste ‘n orde kleiner wees as dié van ‘n gesmelte nitraatsout stelsel.

Acknowledgments

Particular thanks to the following people for their part in this work:

My promoters, Prof Kröger and Prof von Backström, for their time, ideas, guidance, patience, vision, energy, and all that they have taught me;

My parents, who made it possible for me to pursue my studies, and who have supported me in every way imaginable;

Those in the Department of Mechanical Engineering who assisted with queries and experimental apparatus, especially Mr Zietsman, Julian, Kelvin, the workshop, and the Solar Thermal Energy Research Group staff;

Prof Kisters for his input and help with geological questions relating to chapter 2, including identification of rock samples;

Colleagues and friends who gave support, especially those in the postgraduate group who assisted error-checking equipment and discussed solutions to problems;

P. Gauché for helping collect rock samples from the Northern Cape;

L. Conradie and J. van der Merwe for their help with some of the experimental work and data logging;

The NRF/DST, CRSES and STERG for funding;

Portland Quarry for showing me the workings of a quarry and crushing plant.

" … For it became Him who created them to set them *in order*. …"
Sir Isaac Newton, *Opticks*

Table of contents

List of figures

List of tables

Nomenclature

A_c	Solar power plant collector area, m^2
A_{cs}	Cross-sectional area of packed bed, m^2
A_{flow}	Average duct flow area through packed bed, m^2
A_p	Particle/rock surface area in control volume/bed, m^2
A_s	Surface area of a sphere with the same volume as the particle, m^2
A_w	Wall correction term, Eisfeld and Schnitzlein friction factor
A_1	Ergun equation constant 1 (“laminar”)
A_2	Ergun equation constant 2
a	Packing ratio of total particle surface to total bed volume, m^2/m^3
a_f	Annuity factor
a_m	Montillet friction factor packing density constant
a_1	Curve fit constant (laminar), measured friction factors
a_2	Curve fit constant, measured friction factors
a_3	Curve fit, Reynolds number power, measured friction factors
a_4	Constant, pressure drop equation
a_5	Constant, pressure drop equation, mass flux power
a_6	Constant, pressure drop equation, particle size power
B	Deformation parameter in Zehner/Bauer/Schlünder model
Bi	Biot number, $hD/[2k_p]$
Bi_{seg}	Biot number for bed segment, 0.1 (Sragovich segment length)
Bi_v	Volume equivalent Biot number, $hD_v/[2k_p]$
B_w	Wall correction term, Eisfeld and Schnitzlein friction factor
b_1	General constant for pressure drop equation (laminar term)
b_2	General constant for pressure drop equation
C_a	Total annual power plant cost, R or $
C_b	Bed capital cost, R/s
C_e	Cost of energy (electricity), R/J
C_m	Material cost of bed, including interest $R/[m^3s]$
$C_{O\&M}$	Total annual power plant operating and maintenance costs, R or $
C_p	Pumping cost through bed, R/s
C_t	Total bed cost (combined capital and pumping), R/s
c	Specific heat capacity of fluid at constant pressure, J/[kgK]
c_p	Specific heat capacity of particle, J/[kgK]
c_v	Specific heat capacity of fluid at constant volume, J/[kgK]
c_w	Specific heat capacity of water, J/[kgK]
D	Particle diameter, $6\Sigma V_p/\Sigma A_p$ m
D_c	Container diameter, m
D_h	Hydraulic diameter, m
D_h/L_m	Geometric packing ratio used by Martin
D_v	Volume equivalent sphere diameter, $(6V_p/\pi)^{1/3}$
D_1	Sphere diameter (sphere 1)

D_2	Sphere diameter (sphere 2)
Fo	Fourier number
f_B	Brauer friction factor
f_C	Carman friction factor
f_{CPL}	Apparent friction factor, close packed layers
f_{da}	Duct apparent friction factor, $4\Delta pD\varepsilon^3/[3L\rho v_s^2(1-\varepsilon)]$
f_{Erg}	Ergun friction factor, $\Delta pD\varepsilon^3/[L\rho v_s^2(1-\varepsilon)]$
f_{ES}	Eisfeld and Schnitzlein friction factor
f_H	Hicks friction factor
f_I	Idelchik friction factor
f_{ins}	Insurance and administration cost for power plant
f_{JK}	Jones and Krier friction factor
f_M	Montillet friction factor
f_{Ma}	Mayerhofer *et al.* friction factor
f_{MS}	Apparent friction factor, mixed sizes of spheres
f_{NL}	Nemec and Levec friction factor
f_{OSC}	Apparent friction factor, offset simple cubic layers
f_S	Singh *et al.* friction factor
f_{SC}	Apparent friction factor, simple cubic packing
f_T	Tallmadge friction factor
f_v	Friction factor, vol. equivalent sphere $2\Delta pD_v\varepsilon^3/[L\rho v_s^2(1-\varepsilon)]$
g	Acceleration due to gravity, m/s^2
Hg	The Hagen number, as used by Martin
h	Convection heat transfer coefficient, W/[m^{2}K] (particle area)
h_{rp}	Particle radiative heat transfer, Yagi and Kunii correlation, W/m^{2}K
h_{rv}	Void radiative heat transfer, Yagi and Kunii correlation, W/m^{2}K
h_v	Volumetric heat transfer coefficient, W/[m^{3}K] (total bed volume)
I	Income from packed bed and steam cycle, R/s
I_c	Total initial investment for a solar power plant, R or $
I_{net}	Net income from packed bed and steam cycle, R/s
i_r	Interest rate
G	Mass flux, kg/[m^{2}s]
K_1	Eisfeld and Schnitzlein wall correction term – shape constant
k	Thermal conductivity of air, W/[mK]
k_e	Effective thermal conductivity of bed, W/mK
k_e^0	Effective thermal conductivity of bed (stagnation), W/mK
k_p	Thermal conductivity of particle, W/[mK]
k_1	Eisfeld and Schnitzlein wall correction shape constant 1
k_2	Eisfeld and Schnitzlein wall correction shape constant 2
L	Bed length in flow direction, m
L_m	Average distance between two particles in a packing, m
l_s	Thickness of slab with equivalent resistance to a sphere, m
m	Fluid/air mass flow rate, kg/s
m_{sc}	Counting variable, Shitzer and Levy solution to Schumann eqns

m_p	Particle mass in segment, kg
m_w	Water mass in heat capacity measurement, kg
NTU	Number of transfer units, $h_v L/[Gc]$
NTU_c	NTU corrected for internal particle thermal resistance
Nu	Nusselt number, hD/k
Nu_v	Volume equivalent diameter Nusselt number, hD_v/k
n	Counting variable, Shitzer and Levy solution to Schumann eqns
n_i	Number of contact points on a hemispherical particle in a packing
P_l	Longitudinal pitch, m
P_{t1}	Transverse pitch, m
P_{t2}	Transverse pitch, m
P_{wet}	Average wetted perimeter of a duct, m
Pe	Peclet number, $Re_p Pr$
Pr	Prandtl number of fluid, $\mu c/k$
Pr_L	Prandtl number of Summers, $\mu c/k_e$
p	Pressure, Pa
Q	Rate of heat transfer, W
Q_B	Rate of heat transfer into boiler (HRSG) to produce steam, W
R^2	Coefficient of determination
Re	Duct Reynolds number, $(2/3)\rho v_s D/[\mu(1-\varepsilon)]$
Re_{CPL}	Duct Reynolds number for close packed layers
Re_{Erg}	Ergun Reynolds number; $\rho v_s D/[\mu(1-\varepsilon)]$
Re_I	Idelchik Reynolds number; $0.45\ Re_{Erg}/\varepsilon^{0.5} = 0.45\rho v_s D/[\mu(1-\varepsilon)\varepsilon^{0.5}]$
Re_{MS}	Duct Reynolds number for mixed sizes of spheres
Re_p	Particle Reynolds number; $\rho v_s D/\mu$
Re_{pv}	Volume equivalent particle Reynolds number; $\rho v_s D_v/\mu$
Re_{OSC}	Duct Reynolds number for offset simple cubic packing
Re_{SC}	Duct Reynolds number for simple cubic packing
Re_v	Volume equivalent Ergun Reynolds number; $\rho v_s D_v/[\mu(1-\varepsilon)]$
T	Fluid/air temperature, °C
T_{amb}	Ambient temperature, °C
T_{avg}	Average temperature at which to evaluate material properties, °C
T_{ci}	Packed bed charge inlet temperature, °C
T_{co}	Packed bed charge outlet temperature, °C
T_{di}	Packed bed discharge inlet temperature, °C
T_{do}	Packed bed discharge outlet temperature, °C
T_{flue}	Flue gas (air) temperature at boiler outlet, °C
T_H	High temperature of steam cycle, Chambadal Novikov efficiency, K
T_i	Initial temperature of bed, °C
T_{in}	Fluid inlet temperature to bed (step change to this value), °C
T_L	Low temperature of steam cycle, Chambadal Novikov efficiency, K
T_o	Difference between air inlet and initial bed temp (step change), °C
T_{o*}	Centre temperature of particle with internal resistance, °C
T_p	Particle/rock temperature, °C

$T_{p,\,i\_avg}$	Particle/rock temperature average over a finite time step, °C
T_{r*}	Surface temperature of particle with internal resistance, °C
T_{sup}	Gas (air) supply temperature to boiler, °C
T_{∞}	Environmental temperature surrounding a single particle, °C
t	Time elapsed, s
t_c	Charging time, s
t_d	Discharging time, s
V	Volumetric (fluid) flow rate, m^3/s
V_p	Control volume/ particle volume, m^3
V_t	Control volume, m^3
V_v	Control volume/ void volume, m^3
v_d	Duct fluid flow speed (pore/interstitial flow speed), m/s
v_{th}	Idealised thermocline/temperature profile movement speed, m/s
v_s	Superficial fluid flow speed upstream of packed bed, m/s
W_e	Electrical power produced by steam cycle, W (J/s)
x	Position in bed from fluid inlet, m
x_f	Frictional fraction of total pressure drop, as used by Martin
y	Position variable: Shitzer and Levy solution to Schumann equations
z	Time variable: Shitzer and Levy solution to Schumann equation

Greek alphabet

α_p	Particle thermal diffusivity, $k_p/[\rho_p c_p]$
β	Packing geometric ratio, conduction correlation of Kunii and Smith
γ	Thermal geometric ratio, Kunii and Smith correlation
Δ	Change in/difference between
Δp	Pressure drop, Pa
Δp_B	Buoyancy related pressure difference, Pa
ΔT	Fluid (air) temperature change, °C
ΔT_{HRSG}	Design difference between HRSG air and steam superheat, °C
ΔT_p	Particle temperature change, °C
ΔT_{pa}	Temperature difference between fluid and particle, °C
ΔT_w	Change in water temperature, specific heat capacity test, °C
Δt	Discrete time step, s
Δt_1	Time for charging packed bed once, s
Δx	Segment length in bed, m
δ	Conductivity constant from Yagi *et al.;* 0.7 – 0.8
ε	Void fraction, V_v/V_t
ε_{CPL}	Void fraction, close packed layers
ε_{MS}	Void fraction, mixed sizes of spheres
ε_{OSC}	Void fraction, offset simple cubic packing
ε_{SC}	Void fraction, simple cubic packing
ε_1	Void fraction, 0.476
ε_2	Void fraction, 0.26
ϵ_p	Particle emissivity (thermal)

η	E-NTU dimensionless group
η_s	Steam cycle efficiency
θ	Dimensionless fluid temperature, $(T - T_i)/(T_{in} - T_i)$
θ_B	Dimensionless transient temperature of a single particle in a fluid
θ_p	Dimensionless particle temperature, $(T_p - T_i)/(T_{in} - T_i)$
κ	Thermal conductivity ratio, k_p/k
μ	Air viscosity, kg/ms
ξ	Dimensionless position, Riaz *et al.*; $\rho v_s c x/k_e$
ρ	Air density, kg/m^3
ρ_p	Particle density, kg/m^3
Σ	Sum of
ΣA_p	Total particle surface area, m^2
ΣV_p	Total particle volume, m^3
τ	Thermal time constant from Duffie and Beckman, $m_p c_p/mc$, s
τ_a	Dimensionless time, Riaz *et al.*; $(\rho v_s c)^2 t/[k_e(1-\varepsilon)\rho]$
ϕ	Fluid film thickness near particle contact; Kunii and Smith
ϕ_1	Fluid film thickness near particle contact; for ε_1
ϕ_2	Fluid film thickness near particle contact; for ε_2
ψ	Sphericity, $A_s/A_p = (36\pi V_p^2/A_p^3)^{1/3}$

Superscripts

+	Next time step, E-NTU model

Subscripts

(i)	Segment number *i*, E-NTU model
(t)	The current timestep
(t+1)	The next time step
e	Electrical (as in kWh_e)
th	Thermal (as in kWh_{th})

Abbreviations

CFD	Computational fluid dynamics
CGS	Council of Geosciences
CSP	Concentrating solar power
DNI	Direct normal irradiance
E-NTU	Effectiveness – Number of transfer units (method)
FCR	Fixed charge rate
GIS	Geographical information survey
HC	Hexagonal close packing of spheres
HRSG	Heat recovery steam generator (boiler)
KTA	Nuclear Safety Standards Commission
LCOE	Levelized cost of energy (electricity)
OSC	Offset simple cubic packing of spheres
SABS	South African Bureau of Standards

SC	Simple cubic packing of spheres
SUNSPOT	Stellenbosch University Solar Power Thermodynamic (cycle)

Other

$	United States $

1 Introduction

1.1 Background

The population of the world is dependent on the availability of energy, be it for warmth, light, communication, transport or manufacturing. A large part of this energy is used to generate electricity, for which there is a growing demand – it has been estimated that electricity generation will account for 40 % of the world's total energy use by 2040. At present, most of the electricity is generated from fossil fuel or nuclear energy sources (Imperial Oil, s.a.).

The cost of electricity produced by fossil fuel or nuclear power plants has been increasing, fuel reserves are diminishing, and there are also environmental concerns. For these reasons, renewable power generation in general has in recent years received greater attention, although the direct costs are higher than for fossil power plants (Australian Department of Resources, Energy and Tourism, 2011). Solar power generation is of particular interest, since the earth receives enough energy from the sun in half an hour to supply the world population's need for a whole year (Sandia, 2012).

However, power generation from the solar resource is relatively underdeveloped at present – In 2011, about 1 GW_e was in use worldwide, although more was under construction and development (Wang, 2011). The potential is vast: Fluri (2009) estimated a nominal plant generation capacity of over 500 GW for South Africa, and this was limited to favourable terrain with least-threatened vegetation and proximity to existing transmission lines.

South Africa relies heavily on coal for power generation and is currently suffering from a generating capacity shortage. One estimate suggests that half of Southern Africa's coal resource will be consumed by 2020 (Hartnady, 2010), which would counsel against over-reliance on coal in the future. It is possible that South Africa may have CO_2 emission targets imposed on it (Van der Merwe, 2009), which would also weigh against the extensive use of coal. Solar power plants have smaller generating capacities than conventional power stations, but they can be built in a shorter time frame (2 – 3 years), thereby relieving the immediate generation capacity shortage. Additionally, South Africa receives high solar irradiation levels (Fluri, 2009), which make solar power an attractive option. Construction is underway on a 100 MW parabolic trough plant and a 50 MW power tower (central receiver) plant in the Northern Cape (Gonzalez, 2012) – the first concentrating solar power (CSP) plants in the country.

One of the inherent difficulties of solar power is that solar radiation is not available at all times (because of cloud cover, and night), with the consequence that power supply and demand curves do not always match. There are two options

to circumvent this difficulty: either by constructing an excessive number of power plants throughout the world to ensure sufficient generation capacity at all times; or by storing the energy in order to supply it when there is a demand. In the case of photovoltaics, which convert the sun's energy directly to electricity, storage is currently costly, unless there is a pumped storage hydro-electric system available (for cost comparison of batteries and pumped hydro, see Sundararagavan and Baker, 2012).

In the case of concentrating solar thermal plants, it is feasible to store energy as heat before it is converted to electricity. As stated by Spiga and Spiga (1982), "In solar electrical conversion, the storage of large amounts of high-temperature energy is a key technology for the successful exploitation of this energy source on a significant scale."

In addition to the matching of supply and demand curves, storage can reduce the overall cost of electricity produced by a solar power plant (see Australian Department of Resources, Energy and Tourism, 2011). A power block of fixed cost and generation capability can produce power for a longer time period when there is stored energy available, and storage can allow more energy from the solar field to be used (Cabeza *et al.*, 2012), thereby making it more cost effective.

However, thermal storage is still relatively expensive (for example Kolb *et al.*, 2011) so there is scope to improve the existing concepts and motivation to explore and develop alternatives.

1.2 The state of thermal storage

Thermal storage concepts can mainly be divided into sensible heat and phase change systems, although there are also chemical thermal storage concepts which use exothermic and endothermic reactions (Cabeza *et al.* 2012).

Thus far, phase change materials have not been much used in CSP-related applications. Some of the sensible heat storage concepts already used or tested include molten salt; thermal oil (the SEGS parabolic trough plant); rock and sand immersed in thermal oil (the Solar 1 power tower); concrete with piped heat transfer fluid through it; and steam accumulators making use of pressurized water (Medrano *et al.*, 2010). Molten salt is the currently favoured system for CSP ("state of the art" for power towers – Kolb *et al.*, 2011) – for example, Solar Tres and Andasol I (Medrano *et al.*, 2010). The molten salt storage system at Andasol 1 (50 MW_e – Feldhoff *et al.*, 2012) uses two tanks, with a capacity of 28500 tons of salt, to provide 7.5 hours of storage (Adinberg, 2011), approximately 1010 MWh_{th} (Medrano *et al.*, 2010). Gemasolar, a 20 MW_e central receiver plant in Spain, incorporates 15 hours of molten salt storage in a two-tank system (NREL, 2011).

Several alternative thermal storage concepts have been proposed over the years: for example, a packed bed of iron spheres with liquid sodium as the heat transfer fluid for solar central receivers (Spiga and Spiga, 1981). Quartz sand is suited as a storage medium as it has good thermal stability, and an air-sand heat exchanger storage concept is given by Warerkar *et al.* (2008). A concrete mixture has been developed and tested at temperatures up to 600 °C, and is intended for a structured packed bed, which could be capable of storing energy at a cost of 0.78 US$/kWh (University of Arkansas, 2012).

1.3 Packed bed thermal storage

A packed bed of particles is one type of thermal storage system which may be suitable for concentrating solar power plants. Packed beds of ceramics or refractory materials have been used as regenerators or recuperators, at temperatures of several hundred degrees Celsius (Amelio and Morrone, 2007). The beds are filled with manufactured ceramic bricks or pebbles such as alumina, Al_2O_3. Examples are cowper stores in the iron industry (Glück *et al*., 1991; Zunft *et al.,* 2011), or regenerators in the glass industry, which may be used at temperatures as high as 1650 °C (Reboussin *et al.*, 2005). The capability to store heat at such high temperatures makes this type of storage suitable for use with central receiver CSP plants, which have been shown to be capable of producing pressurised air at temperatures up to 1000 °C (Heller *et al.,* 2006).

The PHOEBUS project (Fricker, 2004; Grasse, 1991) explored the use of air-ceramic beds at temperatures up to 700 °C. The use of refractory materials as a storage medium in high temperature solar applications should be a "straightforward solution," (Glück *et al.,* 1991) since they have been used in industrial storage systems, some of which may be charged and discharged as often as 12 – 24 times per day. Glück *et al.* constructed a structured bed of ceramics (checker bricks) for temperatures between 700 – 1300 °C. Research on packed beds of zirconium dioxide for use at temperatures above 400 °C may be found in Jalalzadeh-Azar *et al.* (1996) and Adebiyi *et al.* (1998).

Zunft *et al.* (2011) tested an alumina porcelain brick structured bed with a capacity of almost 9 MWh_{th} at temperatures up to 680 °C. They concluded that the technology "represents a promising basis for up-scaled implementations". However, although well suited to the application, with the potential for "substantial cost reduction," this type of storage "still lack[s] the required solar-specific adaptation" (Zunft *et al.*, 2009). While testing a packed bed (1 MWh_{th}) of Al_2O_3 spheres, they found that thermally induced mechanical loads during cyclic operation could cause stresses on the containment and particles. There are also questions with regard to the thermal cycling durability of the storage material.

Zunft *et al.* (2009) propose materials such as fireclay; silica, and some rock types, particularly those of magmatic origin. Since large quantities of the material are

required, it is desirable to seek low cost materials. Py *et al.* (2009) propose the use of vitrified asbestos waste. Sand and granite (rock) have also been proposed for storage up to 800 °C (Singh *et al.*, 2010).

Rock, which should be easily obtainable and cheap compared to ceramics, has been used extensively for thermal storage at low temperatures. Willits *et al.* (1985) tested an air-rock bed (38 tons of crushed granite) for heating and cooling greenhouses. A rock bed has air-conditioned a school (Marewo and Henwood, 2006), and boreholes into bedrock have been used for building heating/cooling – one such system has a rock volume greater than 1 million m^3 (Nordell and Hellström, 2000). Packed beds of rock are considered "the most suitable" storage units for air-based solar heating applications (Singh *et al.*, 2010). For other examples of applications at this temperature range, see King and Burns (1981), Beasley and Clark (1984), and Ramadan *et al.* (2007).

Solar One, a concentrating solar power plant at Daggett, California, used a packed bed of rock and sand with oil as the heat transfer fluid. The project met most of its technical objectives, generating 10 MW_e for several hours a day (Medrano *et al.*, 2010), and achieving a solar-to-electric efficiency of about 16 % (Cabeza *et al.*, 2012).

Air-rock (basalt) beds have been proposed for use in power plants (Williams and Stancich, 2010; Clarke, 2010). Zanganeh *et al.* (2012) have proposed a design for commercial power plants. However, most of the literature describing experimental work on rock beds is for temperatures below 100 – 150 °C. There is little information available on the performance of beds of rocks at temperatures in the region of 500 °C. Zanganeh *et al.* (2012), Fricker (1991) and Meier *et al.* (1991) are some of the few works that present research on the use of rock beds at temperatures in the region of 500 °C.

The advantages of air-rock beds (see Zanganeh *et al.*, 2012) are 1) abundant, cheap material; 2) suitability for a wide temperature range, limited by the melting point or fracture of the rock; 3) Direct heat transfer from the air; 4) No instability (unless the rock contains compounds which break down); 5) no safety concerns from corrosive or harmful materials, provided the rock does not release (for example) asbestos fibres or emit harmful levels of nuclear radiation.

1.4 Scope of enquiry

A combined cycle solar power plant with storage would improve the plant efficiency and reduce the cost of electricity from that of a single cycle power plant. The SUNSPOT (Stellenbosch UNiversity Solar Power Thermodynamic) cycle shown in Figure 1, proposed by Kröger (2008; see Allen *et al.*, 2009), is an example of a combined cycle solar power plant making use of storage. A similar

concept is presented by Curto and Stern (1980), who proposed the use of a packed bed of slag (iron orthosilicate) from a copper smelter.

The primary cycle is a Brayton cycle gas turbine. Ambient air is compressed and heated to 800 °C or more in a central receiver by means of solar heat before passing to a gas turbine. A combustion chamber could be used to reduce temperature fluctuations and to allow the turbine to run when the sun is not available; it would also allow higher turbine inlet temperatures. During periods of high demand, combustion of fuel could provide additional power.

The thermal energy in the exhaust from the turbine (≥ 500 °C) is retained in thermal storage and, when required, used to produce steam in a boiler (heat recovery steam generator – HRSG) for a Rankine steam cycle. Air-cooled condensers (dry-cooling) are desirable for the steam cycle, since solar power plants are likely to be situated in arid regions. The thermal storage allows the steam cycle to operate at night, when higher efficiencies are possible, since the ambient temperatures are lower than they are during the day and dry-cooling is more effective.

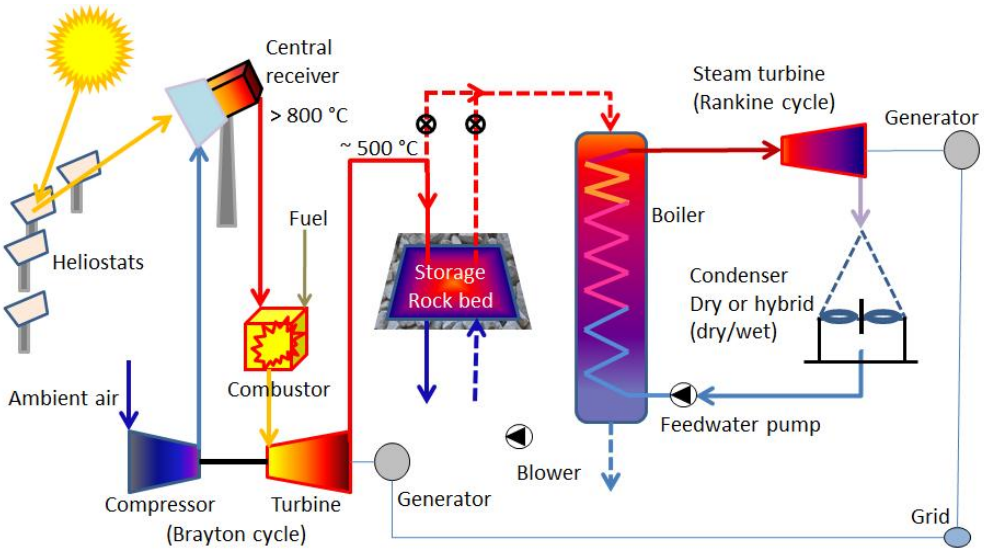

Figure 1: Simplified schematic of proposed SUNSPOT cycle (Kröger, 2008)

The packed bed, placed at the outlet of the gas turbine as shown in Figure 1, is charged by ducting the exhaust gas directly through the bed, which is a significant advantage, since no intermediate heat exchangers are required. At night time, or any period of demand when the gas turbine is not in use, the air flow through the packed bed is reversed and the thermal energy stored in the bed is carried to the HRSG.

An alternative concept which would be suitable to supply peak demand is shown in Figure 2. The thermal energy captured by the central receiver during the day is fed directly into thermal storage, and used to generate electricity for peak demand.

In South Africa, this time period typically occurs between 7 – 9 am and 5 – 8 pm, when a CSP plant could not generate electricity from the sun, so storage is necessary. During these time periods, open cycle gas turbines which cost at least 2.5 R/kWh$_e$ are used (SASTELA, 2012), so CSP plant costs of 2 – 2.5 R/kWh$_e$ with up to 9 hours of thermal storage (Rajpaul, 2012) are already competitive.

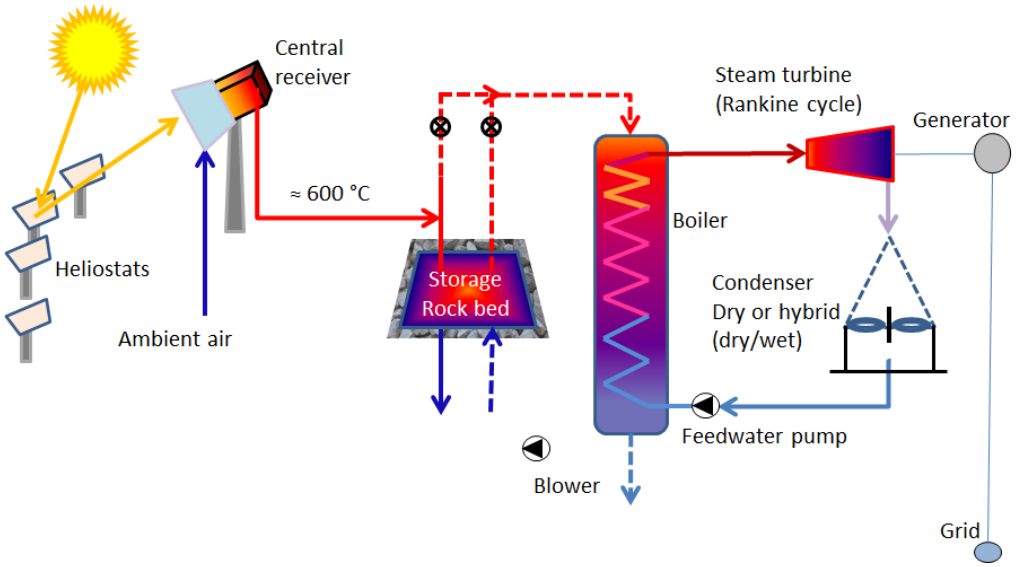

Figure 2: Concentrating solar power plant to supply power for peak demand (Kröger, 2013b)

CSP plants can also be used as baseload power plants, although some co-firing would probably be necessary. To act as a baseload power plant without co-firing, under solar conditions such as those at Las Vegas (USA), Granada (Spain) and Mitzpe Ramon (Israel) – annual direct normal irradiance (DNI) levels of 2–2.5 MWh/m^2/year – approximately 1000 hours (more than 40 days) of storage would be needed to ensure uninterrupted generation capability (Adinberg, 2011). Typical solar fractions for plants with 15 hours of storage are usually 0.5 – 0.6.

Packed beds of rock (or slag from smelters) may provide thermal storage that is favourable in terms of cost and environmental considerations when compared with other concepts currently in use. The goal of the present work is an improved understanding of rock properties, the pressure drop and heat transfer characteristics of rock beds, and a method for determining the optimum particle size and bed length based on these characteristics. The method should consider the use of the bed in the context of solar thermal plants such as those shown in Figure 1 or Figure 2.

1.5 Motivation

1.5.1 The need for thermal storage

If solar thermal plants are to be used extensively, they must supply economically viable power when there is insufficient insolation. Storage enables solar power plants to function more like a base load plant, and reduces the need for supplementary fuel. It can be possible to increase the solar share by almost 50 % as a consequence of using thermal storage (Powell and Edgar, 2012).

However, storage at present significantly increases the cost of solar power plants. The levelized cost of electricity (LCOE) of a 100 MW_e central receiver plant with 9 hours of two-tank molten salt storage is about 0.15 $/kWh (Kolb *et al*., 2011), to which storage contributes an estimated 0.011 $/kWh (13 %) at present. To help reduce the LCOE, a target has been set to reduce thermal storage system costs from 30 $/kWh$_{th}$ to 20 $/kWh$_{th}$. Rock beds have the potential for cost reduction because of low material costs, and should therefore be considered for this application.

1.5.2 Limitations of existing thermal storage solutions

Since thermal storage is relatively expensive, reduction of the storage cost will result in a significant decrease in electricity cost. This is the major reason to look for alternatives. Material costs from literature are summarised for a number of storage media in Table 1:

Table 1: Media cost (Cabeza *et al.*, 2012; Kotze *et al.*, 2011; Kearney *et al.*, *s.a.*)

Medium	Medium cost (US$/kg)	Medium cost (US$/kWh$_{th}$)
Sand – rock – mineral oil (200 – 300 °C)	0.15	4.2
Reinforced concrete (200 – 400 °C)	0.05	1.0
NaCl (solid) (200 – 500 °C)	0.15	1.5
Cast iron (200 – 400 °C)	1.00	32.0
Cast steel (200 – 700 °C)	5.00	60
Silica fire bricks (200 – 700 °C)	1.00	7.0
Magnesia fire bricks (200 – 1200 °C)	2.00	6.0
Mineral oil (200 – 300 °C)	0.30	4.2
Synthetic oil (250 – 350 °C)	3.00	43.0
Nitrite salts (250 – 450 °C)	1.00	12.0
Nitrate salts (265 – 565 °C)	0.50	3.7
Carbonate salts (450 – 850 °C)	2.40	11.0
Liquid sodium (270 – 530 °C)	2.00	21.0
Alsi12 (phase change, 577 °C; Kotze *et al.*)	2.30	15.0
Molten salt (Kearney et al.)	-	5 - 20

Depending on the particle size, the cost of crushed rock in South Africa is 0.1 – 0.20 R/kg (Afrisam, 2010; De Aar stonecrushers, 2012), approximately 0.01 – 0.02 US$/kg at 2013 exchange rates. This is a factor of 2- 5 lower than reinforced concrete. If 1 kg of rock undergoes a temperature change ΔT_p = 500 °C (c_p = 1000 J/kgK), it can store 5×10^5 J (0.14 kWh_{th}). For a rock cost of 0.2 R/kg – the upper end of the range (Afrisam, 2010) – this is a material cost of 1.4 R/kWh_{th} (0.14 \$/kWh_{th}). In practice, however, not all of the stored heat may be transferred to the power cycle, nor will all of the rock in the bed be heated and cooled over this temperature range, so the cost will be higher.

Oil has been used for thermal storage, but there is a relatively low temperature limit, and the high vapour pressure of the oil requires pressurised tanks, which implies a high cost (Medrano *et al.*, 2010). Thermal oil degrades at temperatures above approximately 400 °C (Mills, 2001). Although different types of oil may have slightly varying upper temperature limits, it is not currently possible to operate at 500 – 600 °C, where better cycle efficiencies are obtainable.

Molten salt, the current state of the art, typically potassium nitrate (40 %) and sodium nitrate (60%), freezes/melts at approximately 150 – 200 °C (Kearney *et al.*, 2003). Immersion heaters, which increase the parasitic energy cost, may be required to keep the salt from solidifying in piping. Some molten salt starts to break down at temperatures above about 500 – 600 °C (Kearney *et al.*, 2003), although the use of nitrate salts at temperatures up to 650 °C may be possible (Kolb *et al.*, 2011). Valve packing, flange gaskets, and instrumentation must use specialised materials that are capable of withstanding high-temperature molten salt (Kolb *et al*., 2011).

The sensible heat stored in material increases with increasing change in temperature of the material, which reduces the cost per unit energy stored. Because the molten salt temperature is typically only varied between limits of 270 – 300 °C and 565 °C (Medrano *et al.*, 2010; Cabeza *et al.*, 2012), it reduces the quantity of energy that can be stored and therefore more salt is required than would be the case if it could be cooled to a lower temperature, for example ambient conditions. The salt is the most significant cost in a molten salt storage system – 57 % – while the tank cost is 29 % (Kolb *et al*., 2011). Typical total capital costs for the storage system are stated to fall between 22 – 30 \$/kWh_{th}.

Concrete has been proposed as a storage medium (Dinter, 1992). Cast concrete or ceramic with embedded pipes for the heat transfer fluid (oil) was tested at the PSA and proven at temperatures up to 400 °C (Laing and Lehmann, 2008); efforts to increase this to 500 °C were intended. The low thermal conductivity of concrete makes heat transfer into the concrete difficult (Laing *et al.*, 2006). This low conductivity requires relatively closely-spaced pipes, which increases the cost. Laing *et al.* found that embedding fins did not help the cost-effectiveness of this type of system.

Phase change materials may have low thermal conductivities and form solid deposits on heat transfer surfaces (Cabeza *et al.*, 2012). However, metallic phase change materials do not suffer from low conductivity – for example the eutectic aluminium-silicon (AlSi12) phase change material storage concept of Kotze *et al.* (2013).

1.5.3 Need for further research on packed bed thermal storage

The ability of rock or slag to withstand high temperatures and thermal cycling without disintegrating has been neglected; there is very little published information. The number of cycles at a given heat transfer rate which rock can withstand before disintegrating significantly is important, since disintegration would clog the flow paths and increase the resistance and pumping power. There is a need to determine the availability of suitable rock in regions where solar power plants are likely to be built, since long-distance transport of rock is expensive.

Although packed beds have been "investigated both analytically and experimentally," the literature is considered to be lacking in information on the design optimization of rock beds based on *cost-effectiveness* (Singh *et al.*, 2010). Additionally, pressure drop tests show that the classical Ergun equation may be significantly in error in predicting the pressure drop of different particles; "… the details of heat, mass, and momentum transfers in these packed structures are not understood" (Hendricks *et al.*, 1998). Shitzer and Levy (1983) found that the equations of Ergun (1952) and Chandra and Willits (1981) under-predicted the measured pressure drop of a randomly packed rock bed by a factor between 1.5 – 5, which they attributed largely to the influence of rock shape. Further work is therefore needed to be able to estimate pressure drop and associated pumping costs.

Thermal tests on a test section filled with weathered, rounded rock (Allen, 2010) found that the Hughes Effectiveness-NTU one-dimensional temperature calculation method (Hughes, 1975; Duffie and Beckmann, 1991), combined with existing heat transfer coefficients from the literature, predicted temperatures within 2 – 4 °C of the measured values at low temperatures (60 – 70 °C). However, the influence of particle shape and thermal radiation at higher temperatures (≈ 500 – 600 °C) and the dispersion of heat due to conduction through particles needs to be better understood in order to predict the performance of a commercially sized bed.

The general consensus of literature is that radiation in packed beds is only significant at temperatures above about 250 °C – for example Schröder *et al.* (2006). The importance of radiation at higher temperatures is unclear: Jalalzadeh-Azar *et al.* (1996) tested up to 900 °C. For their operating conditions, thermal

radiation did not contribute significantly to the overall heat transfer. On the other hand, Balakrishnan and Pei (1979) state that radiation should be taken into account at temperatures above 250 – 300 °C.

Finally, there is not much information available on the design and construction of randomly packed rock beds for use in CSP plants, nor, as previously mentioned, on how to design for cost-effectiveness of the system as a whole.

1.6 Objectives and contributions

The objective of the present study is to determine the feasibility of using packed beds of rock or slag for thermal storage at temperatures of 500 – 600 °C, and provide recommendations for the design of this concept. This requires a means for estimating the performance characteristics (pressure drop, heat transfer) and pumping power requirements based on the rock properties, and a method for finding the optimum bed design parameters for cost-effectiveness.

The objectives are to:

- Determine, from existing literature and experimental work, which rock types are suitable for thermal storage at temperatures of 500 – 600 °C. Sample rocks should be tested for thermal cycling characteristics;
- Determine the availability of potentially suitable rock from regions suitable for constructing solar plants in South Africa;
- Develop, based on experimental work, adequate correlations for estimating pressure drop characteristics of rock beds;
- Find or develop heat transfer correlations for estimating the thermal characteristics of rock beds and compare measurements with predicted temperature profiles for tests up to at least 500 °C;
- Present a method to estimate the optimum bed length, particle size, and mass flux, based on cost effectiveness. The steam power generation cycle should be included;
- Provide design recommendations for the bed and estimate the size and cost of a rock bed to enable operation of steam power plants with an output between 1 – 100 MW_e.

2 Rock type, properties, suitability and availability[1]

This chapter gives a brief overview of the different types of rock found on earth. The method of formation of the rock is summarized, with a view as to how this may influence its characteristics for thermal storage. Desirable thermal storage material characteristics at temperatures up to 500 – 600 °C are presented, and the different rock types are discussed in the light of these requirements. Samples of rock were thermally cycled to determine their suitability for thermal storage applications in this temperature range. The availability and location of the rock types considered to be better suited for thermal storage in South Africa is shown from a 1 : 1 000 000 geological map.

2.1 Rock types: igneous, metamorphic and sedimentary

There are three types of rocks; they are classified as igneous, metamorphic and sedimentary (Foster, 1985). They are discussed in sections 2.1.1, 2.1.2 and 2.1.3, and brief descriptions of some common rocks and minerals are given in Table 2, section 2.1.4.

2.1.1 Igneous rock

Igneous rocks form as a result of the solidification (crystallization) of magma, which is molten rock that consists of a mixture of solid crystals and a silicate melt phase. The melting of rocks occurs at temperatures greater than 750 – 800 °C, with water acting as a fluxing agent, conditions that are reached at depths of 20-25 km or more in the continental crust. As the magma cools, the ions in the melt are arranged in orderly patterns, and crystals grow, until all the liquid has solidified into interlocking crystals (crystallization; Tarbuck and Lutgens, 2006). The molten material does not all crystallize at once – different minerals have different crystallization temperatures.

Two main types of igneous rocks can be distinguished: intrusive (or plutonic) rock, crystallized and solidified below the surface at higher ambient temperatures and pressures; and extrusive (or volcanic) rock, solidified on the surface (Foster, 1985). Plutonic and volcanic rocks may be compositionally similar, but are texturally different. The textural differences mainly relate to the rate of crystallization. Plutonic rock – such as granite – tends to have large, mm- to cm-size mineral grains (visible to the naked eye). These coarse textures are the result of the relatively slow cooling of the magmas. Volcanic rocks – such as basaltic lavas – have finer grain sizes that are the result of the rapid cooling of magmas

[1] A shortened version is under review for *Solar Energy Materials and Solar Cells* (Allen *et al.,* 2013b). Some work was presented in Allen *et al.* (2012). Section 2.1 was extensively revised with the input of A.F.M. Kisters, Dept. Earth Sciences, University of Stellenbosch.

under near-surface conditions. Porphyritic textures describe rock with larger minerals in a finer matrix in which the larger grains come from crystallization of a magma at depth, which has subsequently risen to shallower levels, where the remainder has cooled and crystallized more rapidly. Very rapid cooling may lead to amorphous, non-crystalline textures and volcanic glasses.

Granites are the most widespread plutonic rocks, forming a substantial component of the continental crust. On the surface, they are often exposed as extensive batholiths or in regions that have experienced deep erosion. Granites are commonly coarse- and even-grained rocks made up of quartz, feldspars and micas. Large plutonic bodies may be surrounded by metamorphic rock, thought to have formed from the heat released by the igneous rock during crystallization. Smaller bodies of igneous rock, for example dolerite, usually have a finer grain; they are found in bodies such as dikes, which are planar, sheet-like bodies (Encyclopaedia Britannica: Diabase, 2011).

Volcanic rocks result from magmas that have reached the Earth's surface to form lava flows, gas-rich eruptions (tuffs) or volcanoes. The most common volcanic rock is basalt (Tarbuck and Lutgens, 1984). Basaltic rocks form through partial melting of the mantle. Basaltic rocks in the continental crust have ascended through fracture (dike) systems from the mantle. These dike systems may feed extensive sheets of lava flows that erupt as so-called flood basalts covering extensive regions of several tens of thousands of square kilometres. The gases dissolved in the lavas may exsolve upon crystallization, leaving behind small voids (vesicles) filled with minerals that result in porous textures.

All igneous rocks have originated from the crystallization of molten rocks. The melting temperatures for different rocks vary considerably. Granites form through partial melting of crustal rocks at temperatures as low as 750 °C, whereas basaltic rocks require temperatures greater than 1000° C for melting to occur. Basaltic magma has a liquidus at about 1150 °C and a solidus at 800 °C, below which all minerals are crystallized (Encyclopaedia Britannica: Igneous rock, 2011). Murrell and Chakravarty (1973) give melting points for dolerite, microgranodiorite and peridotite (dunite) as 1240, 1220, and 1557 °C respectively, with partial melting at temperatures of about 1050 °C or more. All of these melting points are above the proposed storage temperatures of 500 – 600 °C.

2.1.2 Metamorphic rock

Metamorphic rocks originate from sedimentary or igneous rocks that have undergone mineralogical and textural changes as a consequence of increased pressure, temperature and deformation in the Earth's crust. Near-surface weathering and lithification of rocks are excluded from this definition. There are different grades of metamorphism, ranging from low-grade, with only slight

mineralogical and textural changes, to high-grade metamorphic rocks with substantial mineralogical and textural changes.

Heat is the main driver of metamorphic processes, as increases in temperature allow for the recrystallization and formation of new minerals through diffusive processes between mineral grains (Tarbuck and Lutgens, 2006). Maximum temperatures attained in the lower continental crust at depths of 20-30 km may lead to the melting of rocks and the formation of igneous rocks such as granites. For the most part, metamorphic reactions occur in the solid state.

There are two main groups of metamorphic rock (Foster, 1985) – thermal (contact-metamorphic) rock and regional metamorphic rock. Contact-metamorphic rock includes, for example, hornfels, which is found along the contacts and in the marginal zones of intrusive plutonic rocks. Hornfels is a very fine-grained, hard rock made up of closely interlocked mineral grains.

Regional metamorphic rocks are far more common. Deformation and the presence of directed stresses lead to the recrystallization of minerals with preferred orientations. The rocks acquire foliated (layered or platy) and/or lineated (stretched) textures, leading to the development of pronounced mechanical anisotropies in the rock. These textures greatly influence the mechanical behaviour of metamorphic rocks and the ability of the rock to split or break along certain preferred orientations. Examples of such regional metamorphic rocks that can cover large areas are gneiss and schist, commonly associated with igneous rock such as granite. Marble and quartzite are also products of regional metamorphism, but are typically non-foliated.

The mineralogical and textural changes of rocks during metamorphism depend on the composition of the original rock (the protolith) and the pressure and temperature to which the rock was subjected. For example, a clay mineral-rich shale will be metamorphosed to a slate under very low-grade metamorphic conditions. With increasing pressure and temperature, the slate will be transformed into a mica-rich schist and eventually, at a high metamorphic grade, into a feldspar-dominated gneiss. With the exception of the loss of water, the process of metamorphism is usually isochemical and is determined by the re-arrangement of minerals into different crystal structures.

Minerals formed during high-grade metamorphism typically have more closely packed crystal structures and higher densities. Rocks with a similar chemical composition produce similar metamorphic rocks, irrespective of the original rock type and mineral content. Since metamorphic reactions are largely driven by the exchange (by diffusion) of ions between minerals, coarser-grained rocks are susceptible to metamorphism only under medium- to high-grade conditions and temperatures above 500°C (Foster, 1985). Metamorphism of sedimentary rock typically improves the hardness, durability and toughness of the rock (Grieve,

2001), while igneous rock that undergoes metamorphism usually does not have these properties much improved. Hornfels and quartzite, which are formed under a combination of high temperature and high pressure, are tough and have good strength.

2.1.3 Sedimentary rock

Sedimentary rock occupies 5 % of the volume of the earth's crust, but covers about 66 % of the land surface area (Foster, 1985). This highlights the origin of sedimentary rock through weathering and deposition.

There are two major types of sedimentary rock: chemical and clastic (Tarbuck and Lutgens, 2006). Chemical rock includes limestone, chalk and gypsum. These rocks form due to the precipitation of soluble minerals from solution. The main mineral precipitates include calcium and magnesium carbonates to form limestone and dolomite, calcium sulphates such as gypsum, or sodium and potassium chloride. Silica and iron and manganese oxides may also be dissolved in appreciable quantities to form chert. Silica-rich cherts consist of cryptocrystalline quartz and are some of the hardest sedimentary rock types. Lignite and bituminous coal are biogenic sedimentary rocks, derived from the accumulation and compaction (lithification) of organic, mainly plant material (Tarbuck and Lutgens, 2006; but note that anthracite is metamorphic).

Clastic (or detrital) rocks form from the weathering and erosion of existing igneous, metamorphic or sedimentary rocks. Igneous and metamorphic rocks are more susceptible to weathering and erosion than older sedimentary rocks, since the stability of igneous and metamorphic minerals under near-surface conditions is limited (Grieve, 2001). Transport of the eroded material by water (or wind) followed by deposition and compaction or cementation lead to the formation of clastic sedimentary rocks, of which sandstone, shale and conglomerate are common examples. The distinction between chemical and detrital rock is somewhat arbitrary, as chemical rock normally contains some detrital component and most clastic rock is cemented by chemical precipitates (Tarbuck and Lutgens, 2006).

Sedimentary rock is typically layered (Grieve, 2001). The layering (bedding) may reflect the variability of the transport and deposition processes. Layering can be seen either in the variation of the grain-size or in the variation of the composition between different beds.

In addition to the bedding, sedimentary rocks can be very porous. The pores come from voids between grains that have not been filled during sedimentation. Porosities of sedimentary rocks may be as high as 30% (for example shale - Foster, 1985). During the process of cementation, the pores are filled by means of water-soluble minerals that precipitate between mineral grains. Cementation may

significantly reduce the porosity of sedimentary rocks. The weathering resistance of sedimentary rocks depends on the composition of the cementing mineral and the textural relationship between the detrital component and the cement, which determine how easily particles may be worn or broken off.

2.1.4 Summary of some common rock or mineral types

Some of the common rocks and minerals are listed with brief descriptions in Table 2.

Table 2: Rock and mineral description (Tarbuck and Lutgens, 2006; Foster, 1985; Encyclopaedia Britannica, 2011)

Rock/mineral	Basic type	Description (composition)
Amphibolite	Metamorphic	Coarse-grained. Medium – high grade; foliated.
Andesite	Igneous (extrusive)	Fine-grained
Anorthosite	Igneous (intrusive)	Calcium-rich plagioclase feldspar. Coarse crystals. Less abundant than basalt or granite.
Basalt	Igneous (extrusive)	Fine-grained; basaltic composition
Calcite	Mineral	$CaCO_3$, calcium carbonate.
Conglomerate	Sedimentary	Usually a sandy matrix with fragments of rock embedded
Diabase (dolerite)	Igneous (intrusive)	Fine-medium grained; dark grey to black. Hard and tough. Coarser than basalt, but mineralogically similar
Diorite	Igneous (intrusive)	Coarse-grained
Dolerite	Igneous (intrusive)	Same as diabase
Feldspars	Mineral	Most abundant minerals in crust. Na, Ca, K, with Si, Al, O.
Gabbro	Igneous (intrusive)	Coarse-grained; Basaltic composition
Gneiss	Metamorphic	Coarse-grained; foliated. From metamorphism of shale etc.
Granite	Igneous (intrusive)	Coarse-grained
Granodiorite	Igneous	Coarse-grained; composition between granite and gabbro
Greywacke	Sedimentary	Impure sandstone
Hornfels	Metamorphic	Medium to high grade. Non-foliated. From any rock
Limestone	Sedimentary	Composed of calcite. May contain fossils
Marble	Metamorphic	Low, medium or high grade. Non-foliated. From limestone or dolomite. Primarily calcite or dolomite

Rock/mineral	Basic type	Description (composition)
Mica	Mineral	Cleavage. Biotite – black mica; muscovite – white mica
Peridotite	Igneous (intrusive)	Coarse-grained. Source of Chrysotile asbestos.
Quartz	Mineral	SiO_2. Hardness high (7) and lack of cleavage
Quartzite	Metamorphic	Medium – high grade. Non-foliated. From quartzose sandstone; contains quartz and mica
Rhyolite	Igneous (extrusive)	Fine-grained; Felsic composition identical to granite
Sandstone	Sedimentary	Quartzose sandstone, mainly quartz; arkosic sandstone, over 20 % feldspar; greywacke, clay matrix
Schist	Metamorphic	Medium – high grade; from slate/granite/sandstone. Coarse-grained; foliated
Slate	Metamorphic	Low grade, from shale
Shale	Sedimentary	Formed from clay. Splits easily along bedding planes
Tuff	Pyroclastic/ igneous	Consolidated volcanic ash

Rock types with the same mineral constituents may have different names if they differ in texture – for example, granite (coarse-grained plutonic rock) and rhyolite (fine-grained volcanic rock) have the same mineral constituents and chemical composition (Tarbuck and Lutgens, 1984).

Granite contains up to 25 % quartz and more than 50 % potassium feldspar and sodium-rich feldspar (Tarbuck and Lutgens, 1984), although the term may describe any coarse-grained intrusive rock consisting mostly of light silicate minerals. Basalt is high in iron, magnesium and calcium but low in silica. The abundance of dark minerals such as biotite, amphibole or olivine gives basalt a black colour.

2.2 Required characteristics

If a packed bed undergoes one full charge-discharge cycle every day, 365 days a year, in ten years the storage will undergo 3650 full cycles. Any rock that weathers rapidly and forms dust or sand (disintegrates) is undesirable, as this will increase the pressure drop through the bed and possibly interfere with the flow distribution. Rock is required that withstands thermal cycling between temperatures of 20 °C and 500 – 600 °C without suffering from rapid weathering and fragmentation. A high heat capacity and density are desirable since this reduces the required storage volume, which should lead to a reduction in containment structure costs.

The thermal conductivity of rock needs to be sufficiently high to allow the heat to be conducted from the outer surface of the rock to the core with a small

temperature gradient through the particle. This requires that the ratio of the thermal resistance to the convection resistance, the Biot number, is less than approximately 0.1. A high particle thermal conductivity reduces the Biot number.

The rock needs to have sufficiently high compressive strength so that the bottom-most layer does not crush under the load of the rock above it. For a packed bed 25 m high, the average load at the bottom would be below 1 MPa for a rock density of 3000 kg/m^3. However, the point loads between particles could exceed the average load, and additional loads could arise from thermal expansion of the rock.

2.3 Rock property variation

2.3.1 Rock strength, thermal expansion and fracture

Rock strength usually increases with quartz content, and rocks containing quartz as a binding material are the strongest (Özkahraman *et al.*, 2004). Rock strength is generally greater for fine-grained rocks, while it decreases with increasing porosity. The unconfined compressive strength of South African rock typically crushed to produce aggregate ranges from 70 – 540 MPa (Grieve, 2001). Inada *et al.* (1997) give tensile strengths for dry tuff and granite at 15 °C as 2 MPa and 9 MPa respectively, and compressive strengths as 14 MPa and 190 MPa respectively. See GEOL 615 (2010) for additional values for a variety of rock. These values are at least an order of magnitude higher than the load of 1 MPa estimated above; however, as noted, stress concentration and thermal expansion effects may result in this value being exceeded.

Strength decreases with increasing temperature. Thermal cracking of rock occurs when it is heated at low confining pressures (atmospheric pressure), and the extent of thermal cracking increases with increasing temperature (Wong, 1982). The fracture strength of granite samples heated above 500 °C rapidly reduced (Wong, 1982). Homand-Etienne and Houpert (1989) found that the compressive strength of large and fine-grained granite samples reduced to approximately half of its initial value when heated to 600 °C. For the minimum compressive strength of 70 MPa given by Grieve, the high-temperature strength would be 35 MPa. Note that dunite samples underwent creep at temperatures above 595 °C (Murrell and Chakravarty, 1973).

The tensile strength of granite samples (40 mm in diameter, 60 mm long, 0.5 – 3 mm grain size) heated at 1 °C/min decreased by 30 % when heated at ambient pressure to 400 °C, and by 60 % when heated to 600 °C (Chaki *et al.*, 2008). The porosity and permeability of the samples increased at temperatures above 200 °C, and rose very rapidly as the temperature increased above 500 °C. Chaki *et al.* understand the reduction in strength of granite samples to be a consequence of crack formation or enlargement. They believe that the rapid formation of cracks

between 500 – 600 °C is a consequence of anisotropic expansion occurring because of quartz (which the granite contains) undergoing a phase transition, which takes place at about 573 °C. Murrell and Chakravarty (1973) agree that the degree of thermal cracking is related to the quantity of quartz in the rock.

The volumetric coefficient of expansion of the mineral quartz is significantly larger than the other minerals found in rock, particularly above 400 – 500 °C. The volume of quartz expands 4.6 % when heated from room temperature to 600 °C, while that of other minerals like olivine or pyroxene only increases by 1 – 2 % (Simmons and Cooper 1978). This differential expansion may lead to thermal stress between crystals, leading to cracking and disintegration.

The volumetric coefficient of expansion for the different rock types usually varies between about 10×10^{-6} – 25×10^{-6} $°C^{-1}$. Highly fractured samples give lower coefficients of expansion (Richter and Simmons, 1974). The coefficient of thermal expansion of South African aggregate is typically between 6×10^{-6} – 14.5×10^{-6} $°C^{-1}$ (Grieve, 2001). Samples of granodiorite and dolerite increased in volume by 0.3 – 0.4 % when heated to 500 – 600 °C, while dunite increased by 0.01 %, which shows the variation that may occur (Murrell and Chakravarty, 1973).

The thermal expansion and contraction of the rock can result in mechanical stress in the containment structure. When the container heats up during charging, the volume increases, and the particles settle under the action of gravity; during discharging, the container cools and contracts, and the particles are kept in place by gravity and friction, which results in mechanical stress on the container walls. This process is referred to as 'ratcheting' (Flueckiger *et al.*, 2011). The resulting stress may fracture the rock or container. The advantage of stackable particles is that they can be packed in a structure to avoid thermal ratcheting problems (see Zunft *et al.*, 2011).

Water appears to play a role in weakening quartz and other silicates (Murrell and Chakravarty, 1973). A correlation has been found between the presence of moisture and the extent of the disintegration of ancient monuments in Egypt (Moores *et al.*, 2008). Condensation of moisture in a packed bed (for example, from combustion gases) may therefore result in weakening of the rock.

2.3.2 Specific heat capacity, thermal conductivity and thermal diffusivity

Mineral composition, texture, structure, and saturation with water all influence the rock properties, and can result in significant variations in the measured rock properties between rock types or within the same type (Hanley *et al.*, 1978). The rock properties given in this section should, therefore, be considered as representative. On-site measurements should be made.

The specific heat capacity of rock increases with increasing temperature. Waples and Waples (2004) present data which shows this trend for a large number of rocks and minerals at temperatures from 0 °C to over 800 °C. The effect is significant: the specific heat capacity of quartzite increases from about 700 J/kgK at 0 °C to 1150 J/kgK at 500 °C – an increase of over 60 % of the heat capacity at 0 °C (see also Chou *et al.*, 2000). The rate of increase of the heat capacity is higher near 0 °C and decreases with increasing temperature. Heat capacities at 20 °C for a number of rocks are presented in Table 3 from Waples and Waples. The correlation of Waples and Waples was used to predict the specific heat capacities at 100 °C, 300 °C and 600 °C shown in Table 3.

Table 3: Specific heat capacity of rocks (Waples and Waples, 2004)

Rock type	ρ_p, kg/m^3	c_p, J/kgK (20 °C)	$\rho_p c_p$, MJ/m^{3}K	c_p, J/kgK (100 °C)	c_p, J/kgK (300 °C)	c_p, J/kgK (600 °C)
Amphibolite	3010	700	2.11	810	994	1097
Amphibolite	3010	1134	3.41	1313	1610	1777
Basalt	2870	898	2.58	1039	1275	1407
Clay	2680	860	2.30	995	1221	1348
Diabase	2790	731	2.04	846	1038	1145
Diabase	2790	860	2.40	995	1221	1348
Diorite	2870	1140	3.27	1320	1619	1786
Dolerite	2900	900	2.61	1042	1278	1410
Gabbro	3000	650	1.95	752	923	1019
Gneiss	2700	770	2.08	891	1093	1207
Gneiss	2700	979	2.64	1133	1390	1534
Granite	2650	600	1.59	694	852	940
Granite	2620	1172	3.07	1357	1664	1836
Granodiorite	2840	650	1.85	752	923	1019
Granodiorite	2730	1046	2.86	1211	1485	1639
Limestone	2770	680	1.88	787	966	1066
Limestone	2760	880	2.43	1019	1250	1379
Marble	2760	883	2.44	1022	1254	1384
Quartzite	2640	731	1.93	846	1038	1145
Quartzite	2640	1013	2.67	1173	1439	1587
Sandstone	2640	775	2.05	897	1101	1214
Schist	2770	790	2.19	914	1122	1238
Schist	2900	1096	3.18	1269	1556	1717
Slate	2780	740	2.06	857	1051	1160
Slate	2770	1113	3.08	1288	1581	1744
Tuff	2690	795	2.14	920	1129	1246
Tuff	2750	1090	3.00	1262	1548	1708

Waples and Waples warn that the specific heat capacity values for rock found in literature seem to be inflated by up to 15 %. The mean specific heat capacity of

the rock properties at 20 °C is 938 J/kgK, which is higher than the value for rocks and ceramics given by Dincer *et al.* (1997): 840 J/kgK (temperature unspecified).

A selection of measurements for South African rock found in the Witwatersrand Supergroup is shown in Table 4. The thermal conductivities given by Jones (2003) in the Witwatersrand mining area vary between 1.9 W/mK (shale, Ecca group) and 7.6 W/mK (quartzite, Venterspost formation). Values of thermal conductivity can be as low as 0.2 W/mK or higher than 10 W/mK (Hardy *et al.*, 1977). Rocks with a high quartz content tend to have conductivities of 3–5 W/mK (room temperature, Jõeleht and Kukkonen, 1998), and pure quartz can have conductivities of more than 7 W/mK (Özkahraman *et al.* 2004). The thermal conductivity of fine sand at 0 °C is about 0.55 W/mK (Riaz *et al.*, 1976).

Table 4: Selected South African rock properties (25 °C, Jones, 2003)

Rock type (avg of subgroups)	ρ_p, kg/m^3	k_p, W/mK	c_p, J/kgK	$\rho_p c_p$, MJ/m^{3}K
Pre-Karoo diabase	2900 (80)*	3.97 (0.78)	840 (30)	2.44
Lava (Ventersdorp Supergroup)	2850 (60)	3.46 (0.56)	880 (20)	2.51
Quartzite (Witwatersrand Supergroup)	2690 (40)	6.35 (0.78)	810 (40)	2.18
Conglomerate (Witwatersrand Supergroup)	2730 (60)	6.86 (0.75)	830 (50)	2.27
Shale (Witwatersrand Supergroup)	2790 (60)	4.77 (1.20)	880 (20)	2.46

*Figures in brackets are the standard deviation

The relation between thermal conductivity and temperature is not the same for all rock and minerals. The thermal conductivity of quartzitic sandstone reduces with increasing temperature by as much as 100 % from 0 – 300 °C. Slate, limestone, marble, calcite, gneiss and granite also follow this trend. A few rocks like Quebec or Transvaal anorthosite show the opposite trend – thermal conductivity increases with increasing temperature. Crack formation does not necessarily result in a decrease of thermal conductivity (see Birch and Clark, 1940).

The thermal conductivity of several rocks is given in Table 5 and Table 6

Table 5: Thermal conductivity of igneous rock (Birch and Clark, 1940)

Rock type	ρ_p, kg/m^3	k_p, W/mK (0 °C)	k_p, W/mK (100 °C)	k_p, W/mK (300 °C)
Granite (Rockport)	2610	3.5 – 3.8	3 – 3.2	2.5
Granite (Barre)	2648	2.8	2.5	
Diabase (Westfield)	2962	2.1	2.1	2.1
Gabbro (Mellen)	2870	2	2	2
Anorthosite (Doornspruit, Tvl)	2740	1.9	1.9	
Bronzitite (Pilansberg, Tvl)	3289	4.6	3.6	3.1

Where rocks had a distinct grain direction, measurements were made parallel (par.) and perpendicular (perp.) to the grain. More data may be found in Özkahraman *et al.*, 2004. Correlations for thermal conductivity and diffusivity as a function of temperature are given by Vosteen and Schellschmidt (2003). Conductivities of crystals and glasses are given in Table 7. The increase in thermal conductivity in the glasses may be caused by radiation effects (Birch and Clark, 1940).

Table 6: Thermal conductivity of sedimentary and metamorphic rock (Birch and Clark, 1940)

Rock type	ρ_p, kg/m^3	k_p, W/mK (0 °C)	k_p, W/mK (100 °C)	k_p, W/mK (200 °C)
Quartzitic sandstone (Allentown)	2640	5.7 (par.) 5.5 (perp.)	4.4 4.3	3.8 3.6
Limestone (Solenhofen)	2605	3	2.3	2
Dolomite (Bethlehem)	2826	5	3.9	3.3
Marble (Proctor)	2688	3.1 (par.) 3.0 (perp.)	2.5 2.4	2.2 2.1
Slate (Pa.)	2763	1.9 (perp.)	1.8	1.7
Gneiss (Pelham)	2643	3.1 (par.) 2.2 (perp.)	2.8 2.0	

Table 7: Thermal conductivity of crystals and glasses (Birch and Clark, 1940)

Rock type	ρ_p, kg/m^3	k_p, W/mK (0 °C)	k_p, W/mK (100 °C)	k_p, W/mK (400 °C)
Quartz	2652	11.4 (par.) 6.8 (perp.)	7.9 4.9	4.3 3.1
Calcite	2713	4.0 (par.) 3.5 (perp.)	3.0 2.7	2.1 2.0
Halite	2160	6.1	4.2	2.1
Silica (glass)	2199	1.4	1.5	1.8
Obsidian (glass)	2440	1.3	1.5	1.8
Diabase (glass)	2757	1.1	1.3	

Some alternative storage material properties from Sørensen (2011) and Dinter (1992) are given in Table 8 and Table 9 for purposes of comparison. Additional values may be obtained from Shitzer and Levy (1983).

Table 8: Material properties (Sørensen, 2011)

Material	k_p, W/mK	c_p, J/kgK	$\rho_p c_p$, MJ/m^{3}K
Dry earth	1	790	1
Cast iron	34 – 70 [700 – 1000 °C]	460	3.6
Granite	2.7 [1000 °C]	790	2.2
Bricks	0.6	840	1.4

Table 9: Material properties at 332.5 °C (Dinter, 1992)

Material	ρ_p, kg/m^3	k_p, W/mK	c_p, J/kgK	$\rho_p c_p$, MJ/m^{3}K
Concrete	2400	1.1	1000	2.4
Thermal oil (VP-1)	781.5	0.090	2404	1.9
Salt (NaCl)	2160	4	950	2.1
Steel plates	7850	35	550	4.3

At temperatures above 500 °C the thermal diffusivity of rock increases (Hanley *et al.*, 1978). This is attributed to increased heat transfer through the rock, caused by radiation effects at higher temperatures. Rock with a high silica (SiO_2) content, such as Berea sandstone or quartzite, tends to have a high thermal diffusivity. In igneous rocks, the thermal diffusivity depends on the quartz and feldspar content: a high feldspar content (poor conductor) reduces the diffusivity. Limestone and marble have low thermal diffusivities, caused by the absence of quartz (Hanley *et al.*, 1978). Rock texture also influences thermal diffusivity: rock with an interlocking crystalline structure should have thermal diffusivities that are higher than those of sedimentary rock, even if it is of a similar composition. The absorption of water alters the properties; for example, diffusivities up to 24 % more than the normal (dry) value have been obtained (Hanley *et al.*, 1978).

There is a critical temperature above which irreversible changes occur in rocks. Hanley *et al.* (1978) found that the thermal diffusivity in rocks was lower for rocks that were preheated to 727 °C and cooled to 27 °C. This is thought to be caused by differential thermal expansion of the minerals in the rock causing (irreversible) changes in the fit between the grains. The difference in thermal diffusivity between the preheated and non-preheated rock was 30 – 40 % of the non-preheated value. The change in diffusivity was smaller for rock with a large grain size than for rock with a fine grain.

For the purpose of this study, the effect of pressure on the thermal conductivity and heat capacity of rock is negligible. The thermal conductivity of igneous rocks increases by 0.05 – 0.15 % for every 10 MPa increase in pressure (Waples and Waples, 2004). Zhou *et al.* (2011) estimate the influence of Young's Modulus (E) of rock on the effective thermal conductivity of a packed bed. The higher the Young's Modulus, the weaker the increase, as the contact area between particles due to load becomes smaller. Since most rock Young's Moduli are between 1 – 70 GPa (granite 10 – 70 GPa, GEOL 615, 2010) this should mean that the rock loading has a small influence on the bed conductivity.

2.4 Suitability of rock types for thermal storage

The suitability of rock types is now discussed with respect to resistance to thermal fracture and thermal cycling.

2.4.1 Resistance to fracture, disintegration or thermal decomposition

Thermal expansion causes stresses which can fragment rocks. The composition of the rock and the orientation of the grains influences the magnitude of thermal stress. Fused quartz is thought to be negligibly affected by thermal stresses because it is homogeneous, isotropic and amorphous in structure (Thirumalai and Demou, 1970).

Sedimentary rock is unlikely to be suitable for storage, since it is not formed at elevated temperatures, which means it may undergo thermally induced reactions at elevated temperatures: for example, shale samples have undergone thermal reactions at temperatures in the region of 500 °C (Somerton and Boozer, 1960), and dolomite in sandstone samples dissociated at temperatures above 570 °C (Somerton *et al.*, 1965). Additionally, layers (strata) joined only by pressure may separate under thermal stress, and poorly bonded particles could loosen and block the air passages in the bed.

Igneous rock should be resistant to thermal decomposition, since it formed at high temperatures. Samples of granodioritic (igneous) rock from the Andes, containing quartz, were mechanically stable when heated to 500 °C. On further heating to 1000 °C, the quartz-containing samples fractured significantly (Arndt *et al.*, 1997). However, some volcanic rock contains the mineral nepheline, which, when exposed to the atmosphere and heated and cooled, can change into analcime, which has a larger volume. This process can make the rock disintegrate (Weinert, 1980). The gas in vesicles sometimes found in igneous rock might, when heated, expand, leading to high pressures that could fracture the rock.

Unweathered dolerite is a high-quality concrete aggregate, but there are often areas in large dolerite bodies which have undergone deuteric alteration, which is undesirable for use in concrete because of a high content of deleterious minerals including clays (Grieve, 2001). The clays are a problem when there is moisture in the environment (absorption/expansion). Hornblende, one of the main rock-forming minerals in dolerite, breaks down in the presence of moisture, to chlorite, a mica mineral (Grieve, 2001). Biotite, haughtonite and mica are examples of other minerals that break down rapidly when in the presence of water. Spalling of granite faces is commonly thought to be caused by the expansion of feldspars due to hydration. Basalt properties can vary widely in the same vicinity, and it can also contain clays. Greywacke varies in quality as the distance from granite increases – it becomes more shaly.

Cleavage planes in rock occur because of the preferred orientation of platy minerals, particularly mica, which causes the rock to break preferentially along these planes when stressed (Tarbuck and Lutgens, 2006). However, in the case of disintegration of rock – probably by thermal cycling – it does not necessarily crack along obvious lines of weakness (Hall, 1999). Rock with a tendency to split apart into sheets on cleavage planes is probably not suited to thermal cycling

stress. A foliated metamorphic rock such as gneiss or schist may split along planes of weakness, while a non-foliated metamorphic rock like hornfels should be less likely to suffer from this. Some gneisses can split along the foliations where there are minerals that form in 'plates' (for example mica), rather than granules. However, most fracture irregularly, in the same way as crystalline rock (Tarbuck and Lutgens, 1984).

Shale (sedimentary), slate and schist (metamorphic) have distinct cleavage planes (Grieve, 2001), which may lead to asymmetrically shaped particles from the crushing process. This has implications for the pressure drop characteristics (see Chapter 3 and 6), although crushing conditions can be adjusted to influence the shape to some extent.

2.4.2 Thermal cycling fatigue

The unequal thermally induced contraction and expansion of minerals may also cause rock to disintegrate (Hall, 1999). Moores *et al.* (2008) suggest that significant crack growth can occur at temperatures as low as 140 °C in some rocks. Rock temperature fluctuations of the order of 1 °C/min have been measured in regions where thermal stress is the only likely cause of rock weathering/disintegration (Hall and André, 2001); it is thought that granite is a rock that disintegrates as a consequence of this process.

The temperature difference required to cause cracking in rocks reduces as the rock volume increases – a larger rock will fracture more easily. Hall refers to 2 °C/min as the limit above which rock tends to suffer thermal shock or develop new cracks and permanent strain – apparently caused by crack formation along grain boundaries (so also Hall and André, 2001; Homand-Etienne and Troalen, 1984. Simmons and Cooper (1978) state 1 °C/min). For 'large' bodies the limiting temperature change rate may be lower than 2 °C/min. The crack density increases as the change in temperature increases, and fragmentation is dependent upon the thermal expansion and shear-strain characteristics of the rock.

Simmons and Cooper (1978) thermally cycled (approximately 20 - 900 °C, 4 cycles) samples of granite and diabase 3 cm long and 1.4 cm in diameter, at less than 1 °C/min under ambient pressure. They measured the increase of the crack porosity of the samples with each cycle, up to 4 cycles. They found that the crack porosity depends exponentially on the maximum temperature, and that the rate of increase of crack porosity is highest for the rock with the lowest initial crack porosity, whereas rock with a higher initial crack porosity has a slower rate of crack growth. The mineral composition of the rock is likely to influence the rate of increase of new cracks, since different minerals have different coefficients of expansion, thermal conductivity and heat capacity, and may cause local stresses.

Menendez *et al.* (1999) found (for granite samples with a 0.5 – 1.5 mm grain size) that thermally induced cracks mostly formed at the boundaries between different minerals – intergranular cracks. They too believe that the difference in thermal expansion between the minerals is the cause. Rock containing minerals of greatly differing sizes can potentially undergo magnified stresses near the surface due to thermal expansion differences. Granular disaggregation may not influence the "structural stability of masonry", but it does significantly affect the rock surface, which is eroded by this process. Studies on buildings have shown rock erosion rates up to 8 mm in 100 years from environmental processes. Granitic and coarse-textured rocks are prone to granular disaggregation "as a principal form of breakdown" (Gómez-Heras *et al.*, 2006).

Homand-Etienne and Troalen (1984) heated samples of different types of granite and limestone (50 mm diameter, 100 mm long) between 200 – 700 °C at 0.8 – 2 °C/min. Granite grain boundaries formed microcracks (intercrystalline) when heated above 150 – 200 °C. The larger grain size sample started to crack at the lower temperature. When heated to 500 – 700 °C, microcracks formed in the crystals (intracrystalline) and interconnected with the intercrystalline microcracks. Homogeneous limestone samples formed microcracks immediately when heated due to anisotropic expansion, while porous heterogeneous limestone cracked less easily. Heterogeneous rock textures are less responsive to change in temperature, and the length of time for which the rock is kept at the maximum temperature has an influence on the cracking.

Richter and Simmons (1974) thermally cycled (10 – 20 cycles) igneous rock samples (1 cm diameter, 4.5 – 5.0 cm length) at room pressure, at rates less than 2 °C/min and between temperatures of 25 °C and 550 °C. At temperatures below 250 °C, there was no permanent strain. At temperatures greater than about 300 °C, the samples underwent permanent strain, with the formation of more cracks continuing for up to 5 cycles, after which a steady state was seemingly reached. The degree of cracking appears to be a function of the maximum temperature to which the rock is heated, and the number of cycles to that temperature. Quartz-rich granite cracked at lower temperatures than the other igneous rocks, which was attributed to the difference between the expansion of quartz and the other minerals. A diabase sample was cycled to a maximum temperature of 500 °C before it permanently changed length; apparently smaller grain size allowed the sample to be heated to a higher temperature before it underwent permanent strain and fracture.

Inada *et al.* (1997) thermally cycled (5 cycles) granite and tuff samples at 1 °C/min between about 15 °C and 160 °C. They measured a drop in tensile and compressive strength, which occurred most rapidly within the first few cycles, and tended to reach a constant value by the fifth cycle. A similar trend was obtained for thermal expansion by Thirumalai and Demou (1974), who heated granitic rock at temperatures up to 400 °C at rates up to 50 °C/min. The most extensive damage

to the samples occurred during the initial cycle, and the damage reportedly reached a steady state within four thermal cycles.

Griggs (1936) thermally cycled the surface temperature of a coarse-grained (12 – 13 mm grain) granite sample (83 mm x 83 mm x 70 mm) from 32 – 142 °C (≈ 18 °C/min) for almost 90 000 cycles. No noticeable disintegration occurred. He also cycled 38 mm cubes of granite, syenite, felsite and sandstone for about 1400 cycles, and only a few flakes of the polished surface fell off. However, when the rock was cooled by a mist spray of water instead of air – at the same approximate rate of temperature change – it disintegrated rapidly.

Ramana and Sarma (1980) measured the thermal expansion coefficients of granitic rocks at temperatures between 30 – 800 °C and heating rates less than 2 °C/min. Rates higher than this gave rise to increased values of thermal expansion. After 3 cycles, the coefficient of expansion dropped significantly at temperatures less than 200 – 300 °C, which they attribute to crack growth. The coefficient of expansion increased slightly with thermal cycling at temperatures above 300 °C, which they attribute to broadening of fractures. The coefficient of expansion ranged from less than 1×10^{-6} to 30×10^{-6} $°C^{-1}$ depending on the temperature of the sample and the number of cycles it underwent. Samples suffered from permanent strain at temperatures above 450 – 500 °C, particularly above 600 °C for the heating rate of 2 °C/min. Higher heating rates reduced the temperature for onset of permanent strain.

Fricker (1991) found that limestone disintegrated during thermal cycling (unspecified number of cycles and heating rate) between 20 °C and 600 °C, while peridotite, basalt, granite, gneiss and diabase withstood the thermal cycling. Hall and André (2001) record that quartzite and taconite are more resistant to thermal shock than basalt. Zanganeh *et al.* (2012) tested a packed bed containing quartzite, calcareous sandstone, siliceous limestone, limestone and gabbro at temperatures over 500 °C. They record that no visible deterioration was detected in the rock after several tests.

2.4.3 Additional considerations, and conclusions

Hardy *et al.* (1977) are of the opinion that sedimentary rocks such as shale and limestone are generally unlikely to be suitable for thermal storage, whereas granites, gabbro, quartzites and possibly marble and some sandstones are likely to be suitable. This is consistent with the tests of Fricker (1991). Given the disintegration of limestone, and dolomite, as discussed above, marble, limestone, chalk, and any sedimentary rock that contains calcium carbonate is, for now, deemed unsuitable. Sedimentary rock also tends to have a lower density than igneous and metamorphic rock – for example, the density of Berea sandstone is 2150 kg/m^3, and Salem limestone has a density of 2320 kg/m^3 (Hanley *et al.*, 1978), which would require larger storage volumes.

In summary, most igneous rock (such as granite or dolerite) should be suitable, while sedimentary rock (such as shale) will probably not be, although the results of Griggs (1936) suggest that some sandstone might be. Metamorphic rock (such as gneiss or hornfels) that formed at high temperatures is also likely to be suitable, although cleavage planes or foliation may give rise to fracture during thermal cycling, which could be problematic with some gneisses, for example. The gas in vesicles that can be in some rapidly cooled igneous rocks might, when heated, expand, causing fracture of the rock.

The consensus from literature is that rock should not be heated at rates higher than 1 – 2 °C/min. The finding of Richter and Simmons that smaller grain size may allow the sample to be heated to a higher temperature before undergoing permanent strain and fracture may mean that smaller grain sizes are preferable, although this is not certain. Rock rich in quartz (for example, some granites) may be more susceptible to cracking as a consequence of different rates of thermal expansion between that and the other constituent minerals, even though quartz itself may resist cracking. It may be advisable for the first few thermal cycles of rock beds to be done more slowly and possibly to lower maximum temperatures in order to reduce the initial damage caused by heating. However, it may not necessarily reduce the overall damage, if it is only dependent on the temperature limits and rates.

An additional consideration that should be borne in mind is that some rock may have radioactive elements like uranium in it. If the level of radioactivity is sufficiently high, this might result in the radiation levels around the rock bed being above allowable limits. For example, some of the gold mines in South Africa have radioactive tailings and mine dumps (Macleod, 2011). Some of the rock in the Northern Cape region can have levels of radioactivity that might be above the exposure limit levels (Kisters, 2010). Finally, some rock has commercial value (for example, granite, as a decorative stone), and, if there is a limited source, it may be inadvisable to 'waste' it as crushed rock in a packed bed.

2.5 Available rock in South Africa and the Northern Cape region

A 1 : 1 000 000 scale geological map was obtained in GIS (Geographical Information Survey) compatible format from the Council of Geosciences (CGS). This shows the major types of surface/near surface rock throughout South Africa, with brief descriptions for each region. Portions of this work include intellectual property of the COUNCIL FOR GEOSCIENCE and are used herein by permission. Copyright and all rights reserved by the said COUNCIL.

In light of the rock storage requirements already discussed, it is likely that sedimentary rock is unsuitable for thermal storage, and it was therefore eliminated from the map. Only the igneous rock was kept, as were any metamorphic rocks

that do not contain large amounts of calcium carbonate. Any rock with the description such as 'heavily weathered' was eliminated. Rock containing minerals such as chrysotile was also excluded, since this is one of the asbestos minerals (Encyclopedia Britannica: *Chrysotile*, 2013), as was any rock containing commercially valuable deposits such as diamonds (kimberlite). The availability and location of the rock types considered to be better suited for thermal storage in South Africa is shown in Figure 3. The white areas are the rock types that are deemed unsuitable. The Northern Cape region is shown in greater detail in Figure 4.

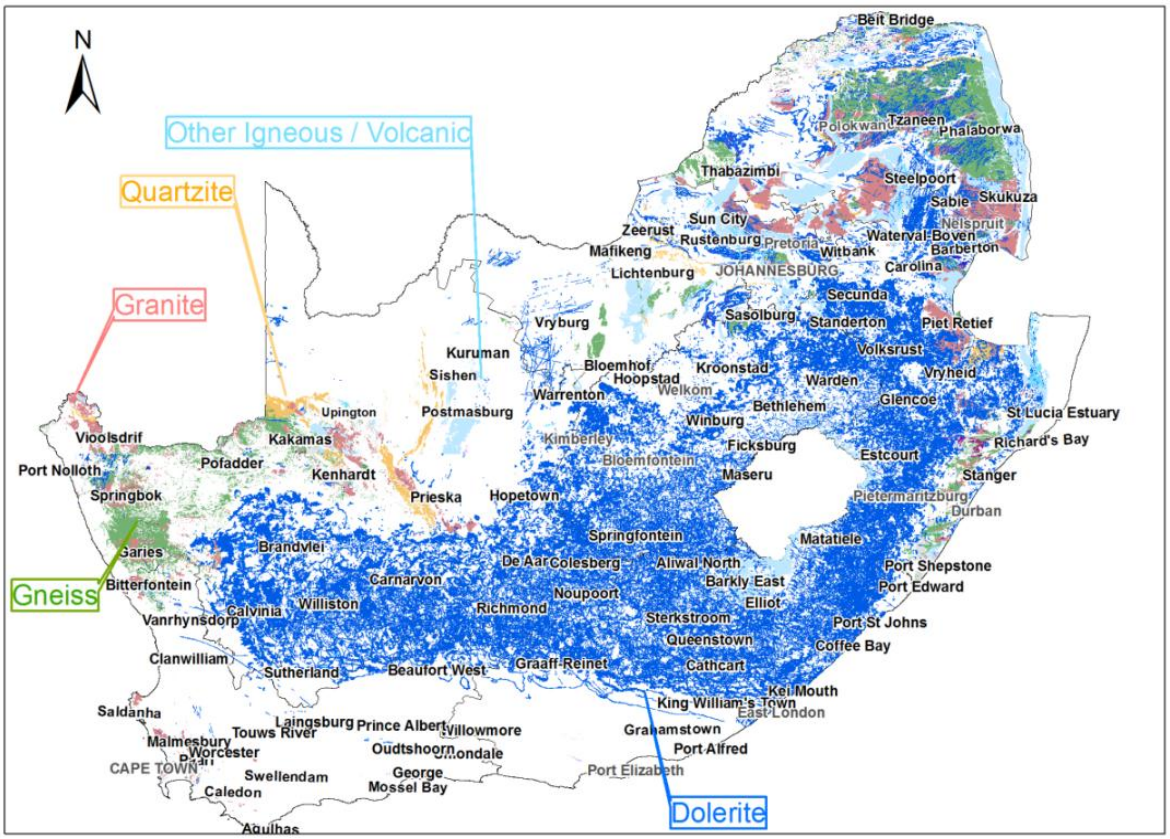

Figure 3: Overview of igneous and metamorphic rock types likely to be suitable for thermal storage in South Africa

The rock along the Orange River and the Namibian border, from Upington west to Springbok, is largely gneiss, with smaller deposits of granite, quartzite, schist and amphibolite amongst others. This is the region in which there is a particularly high solar resource and where solar power plants are currently being built. The N7 from the Namibian border south to Bitterfontein is largely surrounded by gneiss, although there are also small deposits of granite throughout this region.

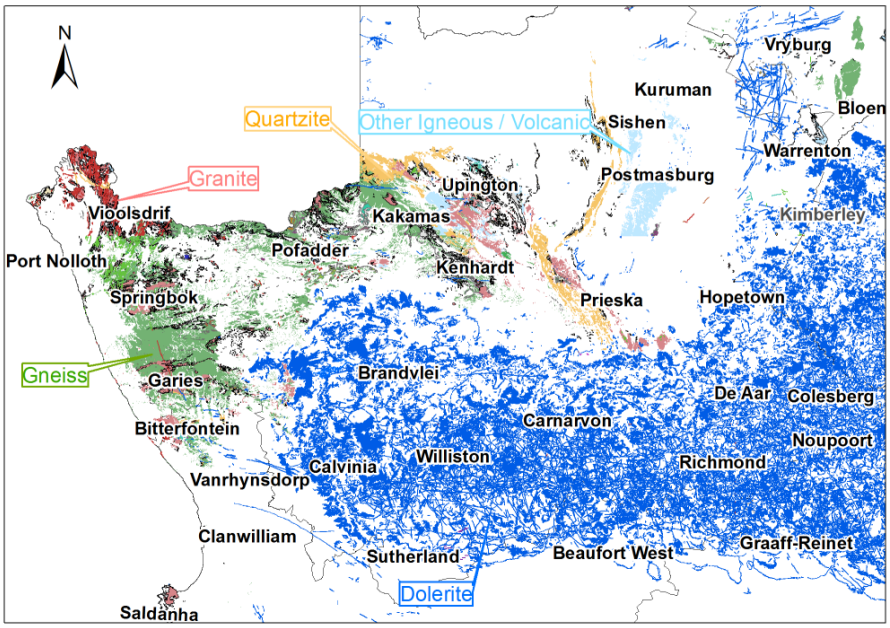

Figure 4: Rock in the Northern Cape region

Dolerite (igneous) is widespread in the central Karoo region - see Figure 5:

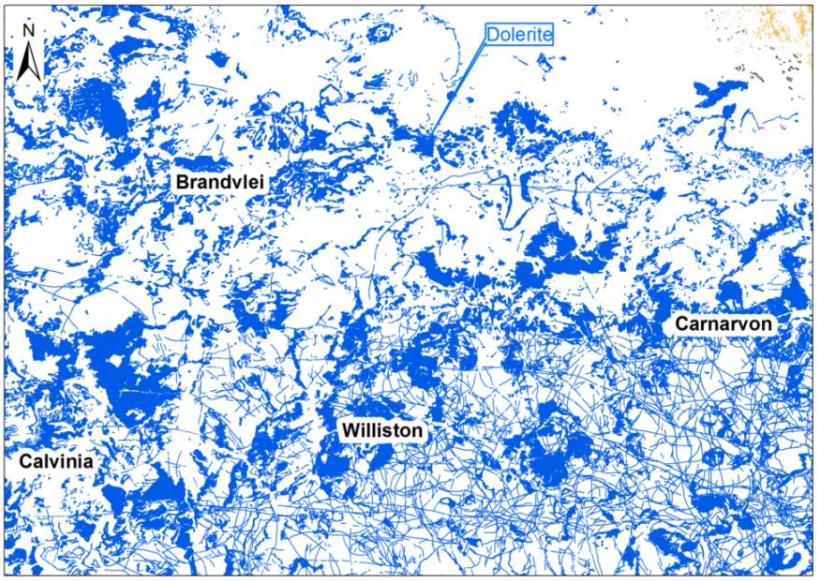

Figure 5: Dolerite deposits in the Calvinia - Carnarvon - Brandvlei region

2.6 Thermal cycling tests

A number of rock samples (mostly dolerite and gneiss) were collected from locations throughout the Northern Cape. They were placed in a kiln capable of repeatedly heating and cooling (with a forced draft) the samples at temperatures up to 1000 °C if desired. The samples were cycled approximately 950 times between average temperatures of 350 °C and 500 - 530 °C, at average rates of

2 °C/min (A number were also cycled 600 times at rates between 1 – 2 °C). The temperature of the air was measured around the samples, and the temperature at the centre of one sample was measured by drilling a hole into it. The average rate of temperature change in the rock centre was on average 1.8 °C/min compared to 2.1°C/min for the air. At the end of the cycling, the particles/fragments which had come loose were removed from the samples, and the mass was measured. The percentage of the rock mass that came loose during the thermal cycling is summarised for a number of rock samples in Table 10.

Table 10: Rock mass loosened by thermal cycling

Rock type	Comments	Sample	Mass, kg	% loosened
Gneiss; fine-grained, foliated, K feldspar	Friable/loose surface	11 12 a	3.5	1.3
Gneiss; biotite	Somewhat friable	11 12 b	2.2	1.3
Gneiss; no foliation, low mica	Slight friability	14 a	3.4	0.16
Granite; quartz, mica	Slight friability	14 b	0.57	2.3
Gneiss; coarse-grained K feldspar, biotite	Split in layers	14 c	0.54	4.7
Gneiss; coarse-grained K feldspar, biotite	No visible change	14 d	0.81	0
Gneiss; coarse-grained K feldspar, biotite	Many cracks; large pieces loose	14 e	2.4	2.6
Gneiss; fine/medium-grained, biotite	No visible change	7 a	0.43	0
Gneiss; fine/medium-grained, biotite	No visible change	7 b	0.91	0
Pegmatite; very coarse-grained, aligned biotite	Minor flaking/cracking	7 c	5.4	0.30
Granite; big feldspars (initially weathered)	Severe disintegration	7 d	0.49	21
Dolerite; coarse-grained (many samples)*	No visible change; no dust	De Aar	0.3 – 0.4	0
Sandstone*; hematitic, fine-grained	No visible change	0S	1.6	0
Hornfelsic shale/silt*; some thermal metamorphism	2 fine cracks appeared	D'ville	0.71	0
Greywacke*	No visible change	D'ville	2.5	0
Gneiss*; coarse-grained, feldspar-rich (augen gneiss)	Separation of layers	0G	4.5	1.1
Slag*	No visible change	Saldanha	0.41; 0.46	0

*Also cycled 600 times at rates between 1 – 2 °C/min before this test

The description "no visible change" means that there was no cracking or friability of the samples as a consequence of the thermal cycling; it does not mean that

there was no discoloration, which was observed in the dolerite and some other samples. A sample of the measured temperature profile is shown in Figure 6.

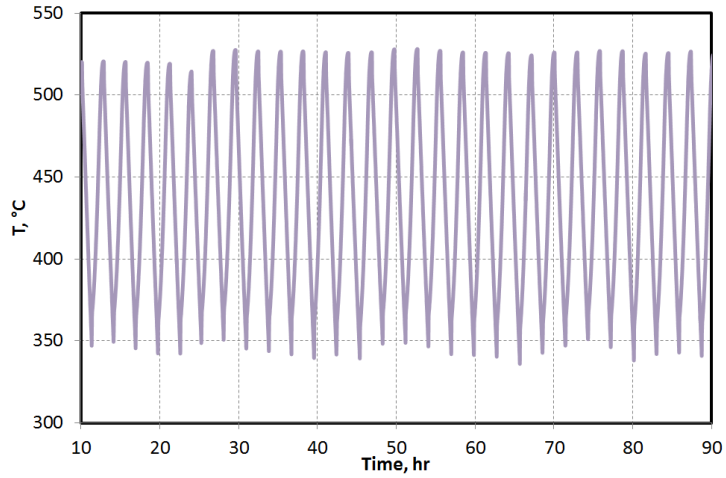

Figure 6: Sample thermal cycling air temperature profile

The fine-grained rock seems to have undergone less disintegration than the coarse-grained rock. The foliated rock (mostly gneiss) was more susceptible to cracking than the non-foliated rock. The cracking of the gneiss sample 'K' is shown in Figure 7. The disintegration of the weathered rock is shown in Figure 8. Other samples in shown in Figure 9 – Figure 12.

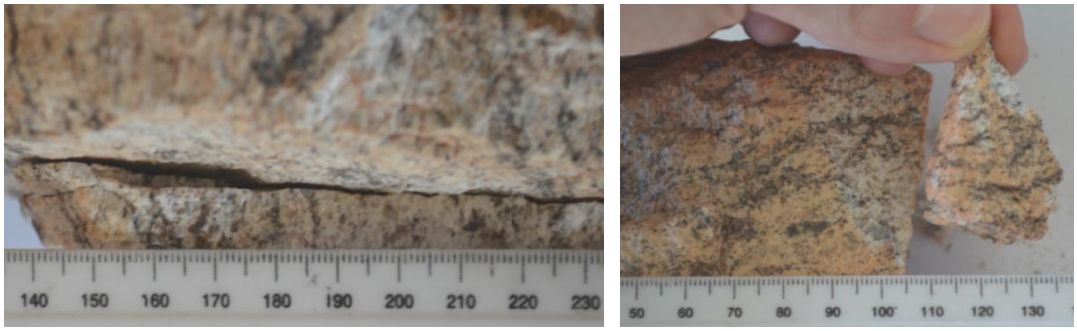

Figure 7: Degradation of gneiss sample 0G by separation of layers; mm scale

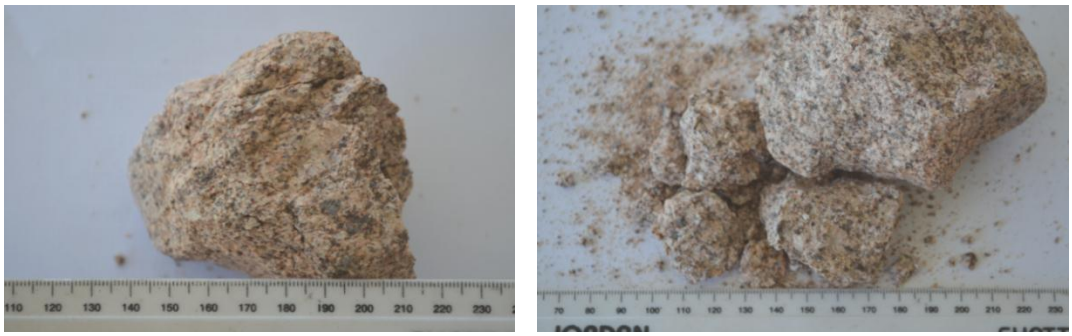

Figure 8: Disintegration of weathered granite (7 d) with handling (950 cycles)

Figure 9: Greywacke; no disintegration after 1500 cycles

Figure 10: Dolerite: a loose sample from the ground; crushed samples (1500 cycles)

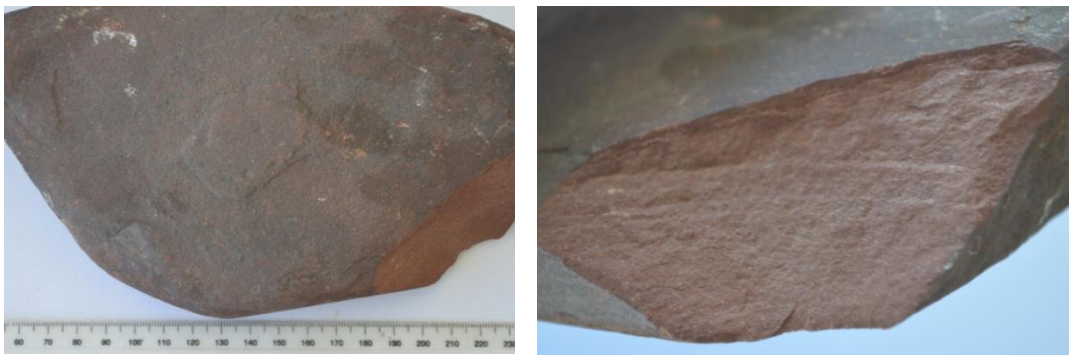

Figure 11: Sandstone unchanged after 1500 cycles (corner broken off before cycling)

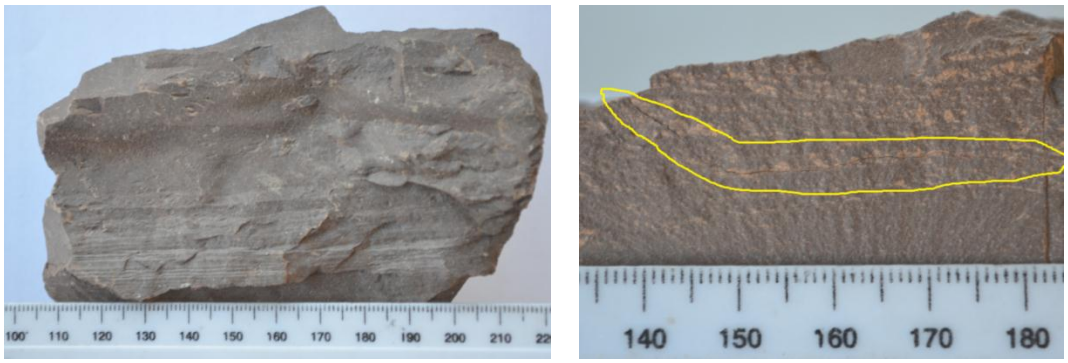

Figure 12: Hornfelsic shale, one of the cracks circled (1500 cycles)

2.7 Conclusion: rock types likely to be suited to thermal storage

The most suitable rock is likely to be igneous or metamorphic rock, without voids or minerals that will decompose when heated to temperatures of 500 – 600 °C. Non-foliated metamorphic rock like hornfels is preferable to foliated rock like gneiss. Although sedimentary rock was thought to be unsuitable, the samples of sandstone and greywacke that survived the thermal cycling process as well as the dolerite suggest that there may be sedimentary rocks in South Africa suited to this application.

Dolerite, which survived the thermal cycling extremely well, is the only igneous rock available in the central Karoo region. The most common rock along the Orange River is gneiss. The gneiss samples that were cycled show that there is variation from one to another, so it is difficult to know how well suited it is without site-specific testing. However, it has been shown in principle that some gneisses can withstand thermal cycling as well as the dolerite and hornfels.

This study only considered the influence of temperature fluctuation on the rock samples. Further work is needed to determine the influence of rock size. The rock in the bed will expand and contract with heating and cooling, rubbing and grinding, which will also tend to cause fracture and disintegration. This needs to be addressed in future work.

3 Packed bed pressure drop[2]

The pressure drop over a packed bed determines the pumping power requirement, and is therefore important in order to size the pumping equipment and to predict the pumping power costs. Fricker (1991) noted that, while rock beds offer "great potential" as a thermal storage solution, further work is needed on understanding pressure drop.

3.1 Previous work on packed bed pressure drop

3.1.1 The Ergun equation

The Ergun equation (Ergun, 1952) is based on the assumption of duct flow through a packed bed (see Blake, 1922; Carman, 1937), and is used for pressure drop prediction for flow through packed beds, columns and fluidized beds:

$$f_{Erg} = \frac{\Delta p}{L\,\rho\,v_s^2} D \frac{\varepsilon^3}{(1-\varepsilon)} = \frac{150}{Re_{Erg}} + 1.75 = \frac{A_1}{Re_{Erg}} + A_2 \quad \textbf{(1)}$$

where D is the particle size, defined by Ergun in terms of particle volume and surface area:

$$D = \frac{6\Sigma V_p}{\Sigma A_p} \quad \textbf{(2)}$$

where ΣV_p is the volume and ΣA_p the surface area of the particles in the bed. Ergun proposed estimating this ratio indirectly by means of pressure drop measurements over a packed bed of the material at low flow rates in the viscous regime. For a sphere, Eq. (2) reduces to the sphere diameter. Ergun does not explicitly state the range of validity of Eq. (1).

The Ergun Reynolds number Re_{Erg} is defined as

$$Re_{Erg} = \frac{\rho v_s D}{\mu(1-\varepsilon)} = \frac{Re_p}{1-\varepsilon} \quad \textbf{(3)}$$

where Re_p is the particle Reynolds number and μ and ρ are, respectively, the viscosity and density of the fluid. The superficial speed v_s is defined in terms of the fluid mass flow m through the total cross-sectional area of the packed bed A_{cs},

$$v_s = m/\rho A_{cs} \quad \textbf{(4)}$$

[2] Most of this chapter was published in Allen *et al.* (2013a)

The void fraction ε of the packing is defined in terms of the total bed volume V_t and the void volume in the bed V_v as

$$\varepsilon = V_v/V_t \quad \textbf{(5)}$$

Du Plessis and Woudberg (2008) state that the Ergun equation is only really applicable for void fractions from 0.38 – 0.47. The measurements with which the Ergun correlation is compared are in the range $1 < Re_{Erg} < 2400$. Ergun does not specifically state what particles he used, although tables and graph legends in Ergun (1952) and Ergun and Orning (1949) suggest spheres, pulverized coke/coal, sand, cylinders and tablets. The correlation is not based solely on measurements for spheres or smooth particles. The equation was examined "from the point of view of its dependence upon flow rate, properties of the fluids, and fractional void volume**, orientation, size, shape, and surface of the granular solids**" (Ergun, 1952, emphasis added).

However, "flow through porous media is far more complex than [ ] we might be led to believe by the simple Ergun equation…" (Nemec and Levec, 2005). According to Montillet (2004), equations of the form $\Delta p/L = b_1 v_s + b_2 v_s^2$ – such as the Ergun equation – should not be used for $Re_p > 500$ - 600, because, in the turbulent regime, the pressure drop in a finite packed bed is not proportional to the square of the flow speed. Niven (2002) argues that the v_s^2 pressure loss term is strongly dependent on local losses – expansion, contraction and change in flow direction, which occur even in laminar flow. In fully turbulent flow, the local losses should be dominant, rather than turbulent losses, which results in "a second transition" from laminar to turbulent flow, at Reynolds numbers higher than the transition within the Ergun equation.

While Middleman (1998) and De Nevers (1991) propose the Ergun equation for beds of spheres up to $Re_{Erg} \approx 1500 – 2000$, Tallmadge (1970) writes that the Ergun equation is only valid for the range $0.1 < Re_{Erg} < 1000$. Hicks (1970) warns that the constants in the Ergun equation may be dependent on the Reynolds number and notes that, although the Ergun equation is "advanced by several textbooks without restriction to flow range," it may not be applicable for spheres when $Re_{Erg} > 500$.

At $Re_{Erg} > 700$, the Ergun equation over-predicts the pressure drop for randomly packed beds of smooth spheres. The over-prediction can be seen in Ergun (1952) for some of the data. On the other hand, the measurements of Zavattoni *et al.* (2011) for rock beds were 10 – 30 % higher than the Ergun equation, and Shitzer and Levy (1983) measured rock bed pressure drops a factor of 1.5 – 5 times higher than the Ergun equation. Tobiś (2000) has shown, by inserting obstacles into the flow passages between spheres in a simple cubic packing arrangement, that the constant 1.75 in the Ergun equation can vary by a factor up to almost five, depending on the alignment and shape of the obstacle. He warns that many

researchers simply assume that the Ergun equation is experimentally established. The packing alignment of irregularly shaped wood chips has also been found to influence the pressure drop (Mayerhofer *et al.*, 2011).

Nemec and Levec (2005) found that the Ergun equation systematically under-predicts the pressure drop over non-spherical particles. Consequently, they recommend that the Ergun constants for each bed be determined empirically.

A range of correlations for spherical and non-spherical particles is given below. The selection includes recent correlations, two of which include parameters to estimate the influence of wall effects.

3.1.2 Other friction factor correlations - spheres

Carman (1937) gives the following correlation for spheres in a test section with negligible wall effects, for $0.1 < Re_{Erg} < 60\,000$:

$$f_C = \frac{\Delta p}{L\rho v_s^2} D \frac{\varepsilon^3}{(1-\varepsilon)} = \frac{180}{Re_{Erg}} + \frac{2.87}{Re_{Erg}^{0.1}} \quad \textbf{(6)}$$

Hicks (1970) proposes a relation for the range $300 < Re_{Erg} < 60\,000$ for spheres:

$$f_H = \frac{\Delta p}{L\rho v_s^2} D \frac{\varepsilon^3}{(1-\varepsilon)} = \frac{6.8}{Re_{Erg}^{0.2}} \quad \textbf{(7)}$$

Tallmadge (1970) gives an equation for spheres, valid for $0.1 < Re_{Erg} < 100\,000$ and $0.35 < \varepsilon < 0.88$. He made use of the measurements of Wentz and Thodos (1963a):

$$f_T = \frac{\Delta p}{L\rho v_s^2} D \frac{\varepsilon^3}{(1-\varepsilon)} = \frac{150}{Re_{Erg}} + \frac{4.2}{Re_{Erg}^{1/6}} \quad \textbf{(8)}$$

Brauer (1971) gives an equation for spheres, plotted against measured data for the range $0.01 < Re_{Erg} < 40\,000$,

$$f_B = \frac{\Delta p}{L\rho v_s^2} D \frac{\varepsilon^3}{(1-\varepsilon)} = \frac{160}{Re_{Erg}} + \frac{3.1}{Re_{Erg}^{0.1}} \quad \textbf{(9)}$$

This equation is almost identical to the equation used by the KTA 3102.3 standard for pebble bed nuclear reactors (Geschäftsstelle des Kerntechnischen Ausschusses, 1981); the only difference is that the constant 3.1 is changed to 3. The KTA correlation is valid for $1 < Re_{Erg} < 100\,000$, $0.36 < \varepsilon < 0.42$ and $L > 5D$, with an uncertainty of ± 15 % at a 95 % confidence interval. The fluid viscosity

must be calculated at the arithmetic mean temperature of the particle and fluid, and the fluid density at the fluid temperature. The ratio of container to particle diameter (D_c/D) for which the equation is valid is specified as a function of Re_{Erg}: the minimum required value reduces from 25 at Re_{Erg} = 10, to 16 at Re_{Erg} = 100, and 5 for Re_{Erg} > 10 000. Presumably, although not stated, this is to avoid edge effects caused by packing disruption near the walls.

Jones and Krier (1983) give a correlation for spherical glass beads in the range $1000 < Re_p < 100\,000$, $8 < D_c/D < 52$,

$$f_{JK} = \frac{\Delta p}{L\rho v_s^2} D \frac{\varepsilon^3}{(1-\varepsilon)} = \frac{150}{Re_{Erg}} + \frac{3.89}{Re_{Erg}^{0.13}} \quad \textbf{(10)}$$

Idelchik (1989) presents a correlation by Bernshtein for spheres of uniform diameter and void fractions between 0.3 – 0.8:

$$f_I = \frac{\Delta p}{L\rho v_s^2} D \frac{\varepsilon^3}{(1-\varepsilon)} = \frac{\varepsilon^3}{(1-\varepsilon)} \frac{0.765}{\varepsilon^{4.2}} \left(\frac{30}{Re_I} + \frac{3}{Re_I^{0.7}} + 0.3 \right) \quad \textbf{(11)}$$

where $Re_I = (0.45/\varepsilon^{0.5})\ Re_{Erg.}$ The range of applicability of the equation is not specifically stated; Idelchik uses it in graphs over the range $0.001 < Re_I < 1\,000$.

For spheres, Montillet *et al.* (2007) propose

$$f_M = \frac{\Delta p}{L\rho v_s^2} D \frac{\varepsilon^3}{(1-\varepsilon)} = a_m \left(\frac{D_c}{D} \right)^{0.20} \left(\frac{1000}{Re_p} + \frac{60}{Re_p^{0.5}} + 12 \right) \quad \textbf{(12)}$$

where a_m is 0.061 for dense packings ($\varepsilon < 0.4$) and 0.050 for loose packings ($\varepsilon > 0.4$). The equation is valid for $3.8 < D_c/D < 50$ and $10 < Re_p < 2500$. For $D_c/D > 50$, $(D_c/D)^{0.2}$ is set to 2.2. This equation was obtained from measurements with water or aqueous solutions of glycerol in a cylindrical column. Montillet *et al.* do not state how the bed diameter D_c should be calculated for test sections of a non-circular cross-section.

3.1.3 Friction factor correlations: non spherical particles

An equation for spherical or non-spherical particles with wall correction terms is found in Eisfeld and Schnitzlein (2001):

$$f_{ES} = \frac{\Delta p}{L\rho v_s^2} D \frac{\varepsilon^3}{(1-\varepsilon)} = \frac{K_1 A_w^2}{Re_{Erg}} + \frac{A_w}{B_w} \quad \textbf{(13)}$$

Here A_w and B_w are the wall correction terms, defined as

$$A_w = 1 + \frac{2}{3(D_c/D)(1-\varepsilon)} \quad (14)$$

$$B_w = [k_1(D/D_c)^2 + k_2]^2 \quad (15)$$

The values of K_1, k_1 and k_2 presented by Eisfeld and Schnitzlein are shown in Table 11. They are based on experimental data largely with spheres and cylinders for $0.33 < \varepsilon < 0.88$, $0.01 < Re_p < 17\,700$ and $2 < D_c/D < 250$. Eisfeld and Schnitzlein do not specify how D_c should be calculated for non-circular cross-sections.

Table 11: Constant values for use in Eq. (13) (Eisfeld and Schnitzlein, 2001)

Particle Shape	K_1	k_1	k_2
Spheres	154	1.15	0.87
Cylinders	190	2.00	0.77
All particles	155	1.42	0.83

Singh *et al.* (2006) present a correlation with the particle shape taken into account by means of a sphericity factor ψ. Apart from size distribution, Singh *et al.* (2010) believe that the particle shape is the most likely parameter to affect the packing pressure drop.

$$\psi = A_s/A_p = \left[36\pi V_p^2/A_p^3\right]^{1/3} \quad (16)$$

Here A_s is the surface area of a sphere that has the same volume as the particle. The correlation is based on data for pressure drop through spherical and other non-spherical objects from measurements in the range $1000 < Re_p < 2700$ (approx. $1500 < Re_{Erg} < 5000$), and the particle diameter D_v is defined as the diameter of a sphere that has the same volume as the particle volume V_p:

$$f_S = \frac{\Delta p}{L\rho v_s^2} D_v \frac{\varepsilon^3}{(1-\varepsilon)} = \frac{\varepsilon^3}{(1-\varepsilon)}\, 4.466 Re_p^{-0.2} \psi^{0.696} \varepsilon^{-2.945} e^{11.85(log\psi)^2} \quad (17)$$

where

$$D_v = \left(\frac{6}{\pi} V_p\right)^{1/3} \quad (18)$$

Nemec and Levec (2005) propose altering the constants in the Ergun equation by means of the particle sphericity ψ used in Eq. (16). For cylindrical particles, the friction factor is altered to

$$f_{NL} = \frac{\Delta p}{L\rho v_s^2} D \frac{\varepsilon^3}{(1-\varepsilon)} = \frac{150}{\psi^{3/2} Re_{Erg}} + \frac{1.75}{\psi^{4/3}} \quad (19)$$

This relation is based on experimental data for $Re_{Erg} < 400$.

Macdonald *et al.* (1979) give experimental data from several sources for measured pressure drops over packed beds of different particles. Sample values are given in Table 12 to show the extent to which the constants in the Ergun equation have been found to vary for different particle type, size or void fraction.

Table 12: Values of constants for the Ergun equation (Macdonald *et al.*, 1979)

Particle type	Equivalent size, mm	Void fraction ε	A_1	A_2
Glass spheres	0.68	0.64	124	1.09
Glass spheres	0.68	0.366	162	1.49
Smooth marbles	16	0.369	326	1.24
Smooth marbles	29	0.385	546	1.14
Cylindrical fibres	0.012	0.895	192	-1.524
Cylindrical fibres	0.042	0.682	236	14.1
Gravel	110	0.406	841	1.01
Sand	0.46	0.387	179	2.52
Ground blue metal	33	0.483	338	5.83

3.1.4 Comparison of correlations for beds of randomly packed spheres

The different predictions for randomly packed beds of spheres are compared in Figure 13.

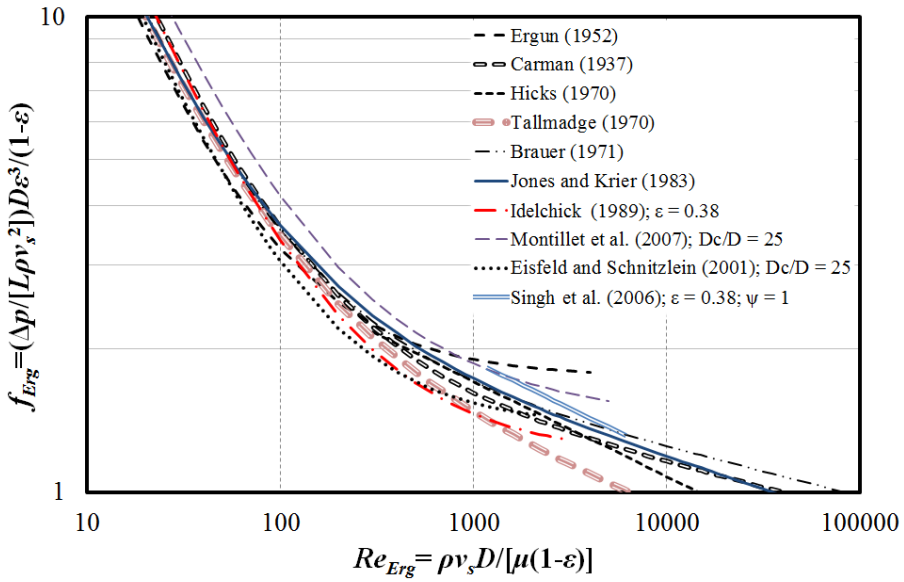

Figure 13: Comparison of existing friction factor correlations for a packed bed of smooth spheres

The equations of Eisfeld and Schnitzlein (2001) and Montillet *et al.* (2007) are plotted for a container to particle ratio of D_c/D = 25, where wall effects should be negligible. As the Reynolds number decreases below 500, the different correlations tend to converge; however, there is an increasing divergence for values of Re_{Erg} above 500. The Ergun equation approaches a constant value at Re_{Erg} > 1000 - 2000, as does that of Idelchik, while the Carman, Singh, Tallmadge, and Hicks equations tend towards lower friction factors.

3.1.5 Influence of packing arrangement of smooth spheres

Measurements from literature for different packing arrangements of spheres are plotted in Figure 14. Wentz and Thodos (1963a) tested five-layer thick structured close-packed packed and distended beds of 31 mm spheres (D_c/D = 11, 2500 < Re_{Erg} < 65 000 and 0.35 < ε < 0.88). They do not specify if they took measures to reduce edge effects. They concluded from their measurements that the friction factor through a bed of spheres is independent of the geometric orientation (see also Wentz and Thodos, 1963b) and the void fraction of the bed. However, their measurements were for packings only five layers in length, which Van der Merwe and Gauvin (1971) caution – based on their own tests – may not be representative of longer beds. Consequently, the equation of Tallmadge, which is based on the data of Wentz and Thodos, is in question.

The other data shown was read off the graph of Martin *et al.* (1951), who used fractional spheres at the walls to eliminate excess porosity. Their tests were for an estimated test section to particle size ratio $D_c/D \approx 8$ - 9, based on a picture of their test section. They found, in contrast to Wentz and Thodos, that rotating the packing arrangement so that the flow passed through it in a different direction altered the friction factor (see also Van der Merwe and Gauvin, 1971; Gauvin and Katta, 1973).

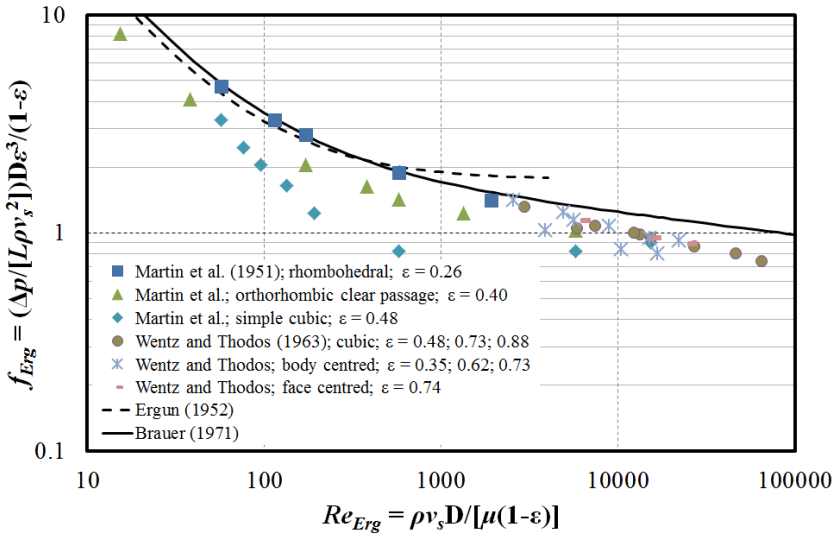

Figure 14: Influence of packing structure of spheres on friction factor

When spheres in a cubic arrangement were orientated so that the flow direction was at equal angles with the three principal axes of the packing (ε unchanged), a **lower** pressure drag on individual spheres and lower overall pressure drop over the packing was measured – even though the flow passages were more tortuous and blocked in this configuration (Gauvin and Katta, 1973; Van der Merwe and Gauvin, 1971). The authors suggest that this is because the tortuous nature of the flow reduces the wake region and delays separation.

Martin *et al.* state that the simple cubic packing was extremely unstable and shifted easily. This may be why the measured friction factors for the simple cubic packing reach a constant value and increase for $Re_{Erg} > 1000$. However, Yang *et al.* (2010) predict a similar trend with CFD, so this may be correct. The CFD simulations of Yang *et al.* show lower friction factors for body centred and face centred packing than for simple cubic packing.

3.1.6 Influence of particle roughness

According to Eisfeld and Schnitzlein (2001), "an observable influence of the particle surface roughness on the pressure drop is physically hardly plausible…". They state that those who do find an increase in pressure drop due to surface roughness probably misinterpret the data. According to Nemec and Levec (2005), pressure drop is increased by surface roughness in both the viscous and inertial flow regimes.

Crawford and Plumb (1986) present measurements showing a "substantially increased" pressure drop as a consequence of surface roughness on spheres for $10 < Re_{Erg} < 2000$ ($D_c/D \approx 30$; $L/D \approx 60$). They probably included the influence of the particle roughness on the total void fraction, but do not state this clearly. Jordi *et al.* (1990) measured friction factors 1.7 – 2.8 times higher than smooth packing through packed beds ($D_c/D = 42$; $L/D > 340$) of roughened spheres for $1 < Re_{Erg} < 62$. They did not take into account the additional area added by the roughness in the calculation of the particle volume-to-surface area ratio (V_p/A_p).

3.1.7 Influence of particle size distribution

Packed beds with mixed particle sizes usually have higher pressure drops than those that consist of a single particle size (Coulson, 1949). A wide particle size distribution generally results in the Ergun equation under-predicting pressure drop more than for a narrow particle size distribution (Keyser *et al.*, 2006). The use of a mean particle diameter in the Ergun equation is valid only if the particle size distribution is not broad or uneven (Gauvin and Katta, 1973; Nemec and Levec, 2005).

3.1.8 Void fraction

Wentz and Thodos (1963a) found, for differently arranged beds of five layers of spheres ($0.35 < \varepsilon < 0.88$), that the void fraction term in the friction factor resolved the measured pressure drop to one relationship, independent of the packing geometric orientation and void fraction. According to Nemec and Levec (2005), the duct pressure drop model – on which the Ergun equation is based – accurately reflects the void fraction dependence of the results in the region $0.35 < \varepsilon < 0.55$.

3.1.9 Edge effects

Edge effects are caused by the disturbance of the particle packing near the walls of the bed. It is thought that in the creeping flow regime the walls increase pressure drop, while for higher Reynolds number flow wall channeling reduces pressure drop (Reddy and Joshi, 2010).

According to Gauvin and Katta (1973) and Foumeny *et al.* (1993), edge effects on packed beds are negligible at $D_c/D > 50$ (> 40, Montillet *et al.*, 2007), and particularly significant below 12 (< 15, Reddy and Joshi, 2010). Dullien (1979) and Nemec and Levec (2005) state that wall effects are negligible if $D_c/D > 10$. Eisfeld and Schnitzlein (2001) show graphs which suggest that, for $Re_p > 100$, $D_c/D > 25$ should be sufficient to make edge effects negligible. $D_c/D = 20$ might cause a 10 % error or less, and a ratio of 10 an error of less than 18 %. From Di Felice and Gibilaro (2004), $D_c/D = 15$ in the viscous flow region will result in pressure drops 100 – 110 % of those over a bed with $D_c/D > 40$, while the pressure drop for the 'inertial' flow region might be between 85 – 100 %. They do not state the Reynolds number boundary between viscous and inertial flow.

As already stated, the KTA safety standard (Geschäftsstelle des Kerntechnischen Ausschusses, 1981) specifies the ratio of container to sphere diameter for which the equation is valid as a function of Re_{Erg}. The minimum required value reduces from 25 at $Re_{Erg} = 10$, to 16 at $Re_{Erg} = 100$, and 5 for $Re_{Erg} > 10\,000$, which is presumably to avoid edge effects.

Randomly packed beds of uniformly shaped particles have a void fraction which shows a damped oscillatory profile as a function of radius (Winterberg and Tsotsas, 2000). However, as the particle shape becomes more irregular, the oscillations reduce and eventually vanish. In other words, irregular, non-spherical particles are less likely to be influenced by wall effects (see also Roblee *et al.*, 1958). Montillet and Le Coq (2001) conclude that the influence of the wall on the variation of porosity in the radial direction is small for anisotropic particles; the velocity profile should be "little influenced". The wall effect is much reduced for irregular particles – constant void fractions in the radial direction have been obtained within a distance from the wall of one quarter of the particle size (Mayerhofer *et al.*, 2011).

Montillet and Le Coq (2001) constructed cylindrical packed beds ($D_c/D_v \approx 16$ - 18) of plates and cylinders. They found that the top and bottom of the bed showed void fraction variation within 2 – 4 particle diameters. The KTA correlation (Geschäftsstelle des Kerntechnischen Ausschusses, 1981) is valid for a bed length greater than 5 particle diameters ($L > 5D$), which implies entrance and exit effects must be relatively negligible above this limit. The CFD of Calis *et al.* (2001) leads to the conclusion that a bed length of 6 particle diameters is representative of longer beds. Crawford and Plumb (1986) show that the flow in the packed bed is fully developed almost immediately (within 4 – 5 particle diameters, for smooth spheres) upon entering the bed.

These values suggest that a minimum D_c/D of 15-20 is needed for spheres, if no other means of reducing edge effects is used. A length greater than 5-10 particle diameters should be sufficient. However, Dullien (1979) observes that, for random packing of spheres, the base layer was almost perfectly rhombohedral; completely random packing was only reached by the 8th layer of spheres.

3.1.10 Non-spherical particles and packing orientation

Gauvin and Katta (1973) lamented that packed bed pressure drop "can be predicted with so little reliability" for particles that are not reasonably spherical. Previous researchers (for example, Zavattoni *et al.*, 2011; Nemec and Levec, 2005; Ammar *et al.*, 1992) have found that, for non-spherical particles such as hollow cylinders, rock, Raschig rings, trilobes, or quadrolobes, the Ergun equation under-predicts the pressure drop. Shitzer and Levy (1983) found that the Ergun equation under-predicted their measurements for rock beds by a factor of 1.5 – 5, and attribute this mainly to the difference in shape of the rock used, warning that "… engineering judgment should be exercised when calculating the pressure drop of a rock-bed storage facility on the basis of published correlations."

Cylinders and other particles can orientate themselves differently, giving rise to scatter in measurements (Nemec and Levec, 2005; Coulson, 1949). Experimental results presented by Coulson for oil flow through beds of spheres, cylinders, cubes, prisms and plates, show that particle shape does influence the pressure drop. A further variable such as tortuosity is required to take this difference in into account. However, Gauvin and Katta (1973) and Nemec and Levec complain of the vagueness and lack of physical meaning in the definitions proposed thus far.

Further confirmation of the influence of bed geometry and particle shape is given by Tobiś (2000; 2001), who constructed a bed of smooth spheres in simple cubic packing, and inserted bands in different positions and orientations to block the flow paths between the spheres. Changing the position and orientation of the bands significantly altered the friction factor. For the same number of bands (and therefore void fraction) in a variety of different orientations and positions, he measured differences in the friction factor. He showed (at a fixed Reynolds

number) that the constant 1.75 in the Ergun equation can vary depending on the obstacle shape and orientation – for example a flat plate parallel to the flow direction and a flat plate perpendicular to the flow direction, which resulted in a value of 8.6, almost 5 times greater than the Ergun value of 1.75.

In fluidized beds, the particles tend to align so the orientation causes the least resistance, while particles in fixed beds tend to lower their centre of gravity (Barnea and Mednick, 1978). Photographs of packed beds of flat plates and cylinders (Montillet and Le Coq, 2001) show alignment of the plates and cylinders with the major axis tending to be parallel to the horizontal base of the container.

Mayerhofer *et al.* (2011) tested crushed, irregularly shaped particles of wood in a packed bed with vertical air flow. When the particles were poured into the test section, they tended to align with their largest cross-sectional area parallel to the base, and therefore perpendicular to the air flow direction. When Mayerhofer *et al.* packed the test section with the particles aligned parallel to the flow direction, they measured smaller pressure drops. This equation for particles mostly perpendicularly to the air flow direction was obtained for $Re_{Erg} < 1000$:

$$f_{Ma} = \frac{\Delta p}{L\rho v_s^2} D \frac{\varepsilon^3}{(1-\varepsilon)} = \frac{554}{Re_{Erg}} + 4.2 \qquad \textbf{(20)}$$

D was defined as in Eq. (2), although they approximated the value by assuming the wood chips to be cubic in shape.

Gauvin and Katta (1973) suggest that particle wakes and stagnant void fraction could reduce the effective void fraction and available flow area in a packed bed. Nemec and Levec (2005) found that packings of rings require Ergun equation constants that are 2.5 times higher – they mention Carman's suggestion that this type of effect is due to eddies and stagnant spaces. This may explain why the orientation of a packing can influence the friction factor (see Martin *et al.*, 1951).

3.1.11 Flow regime

The Reynolds number at which fully turbulent flow occurs is unclear. Morcom (1946) states that for $Re_p > 400$, the laws of turbulent flow apply, with pressure loss proportional to a power of 1.85 – 2 of the fluid flow speed. Van der Merwe and Gauvin (1971) state that flow through randomly packed spheres of a single size undergoes a transition to turbulence at $Re_p = 115$ ($Re \approx 128$ at $\varepsilon \approx 0.4$). Eisfeld and Schnitzlein (2001, 2005) consider turbulent flow to be at $Re_p > 300$ ($Re \approx 330$ at $\varepsilon \approx 0.4$), while Montillet (2004) declares fully turbulent flow to be at $Re_p > 530$ ($Re \approx 590$ at $\varepsilon \approx 0.4$), similar to the range given by Nemec and Levec (2005). Carpinlioğlu *et al.* (2009) list values for transition from laminar to

turbulent at $Re \approx 130 - 200$, and for turbulent flow for $Re > 3000$ ($Re_p > 2700$ at $\varepsilon \approx 0.4$).

3.1.12 Conclusion

In the light of the difficulties of predicting pressure drop over randomly packed beds of rough or irregular particles, and the divergence between existing correlations, even for smooth spheres, further measurements are needed to explore the influence of particle packing arrangement, shape, alignment, and size distribution, and to characterise rock beds, which consist of asymmetric, irregular, rough particles.

3.2 Presentation of pressure drop measurements

A summary of packed bed pressure drop analysis based on the assumption of duct flow – the assumption underlying the Ergun equation (Du Plessis and Woudberg, 2008) – is presented and applied to different packing arrangements in Appendix A.

The pressure drop measurements in this work are presented as apparent friction factors, based on the assumption of duct flow, as derived in the appendix:

$$f_{da} = \frac{\Delta p}{L(\rho v_s^2/2)} \frac{\varepsilon^3}{(1-\varepsilon)} \frac{4\Sigma V_p}{\Sigma A_p} = f(Re) \quad \textbf{(21)}$$

where

$$Re = 4 \frac{\rho v_s}{\mu(1-\varepsilon)} \frac{\Sigma V_p}{\Sigma A_p} \quad \textbf{(22)}$$

This applies to spherical or non-spherical particles. All friction factor measurements are presented in terms of these groups. Eq. (21) is Eq. (A-37). The Reynolds number is derived from Eq. (A-11) by introducing the hydraulic diameter of the ducts between the rocks, the interstitial (pore) flow speed, and the relationship between the void and particle volume. Eq. (22) is Eq. (A-38).

The packing dimension $\Sigma V_p/\Sigma A_p$, the ratio of the total particle volume to surface area – used as early as Blake (1922) and Carman (1937) – should be understood to refer to the duct size rather than an equivalent particle size $6\Sigma V_p/\Sigma A_p$, as used by Ergun. f_{da} may depend on the particle shape, surface roughness, packing arrangement and void fraction; consequently, every packing arrangement should have a particular apparent friction factor associated with it.

4 Packed bed heat transfer and storage

4.1 Governing equations

The Schumann (1929) model is commonly used to predict the temperature profile through a packed bed. The equations are obtained as follows: Consider a control volume of length Δx in a packed bed of cross-sectional area A_{cs} and length L with a fluid mass flux G flowing through it as shown in Figure 15.

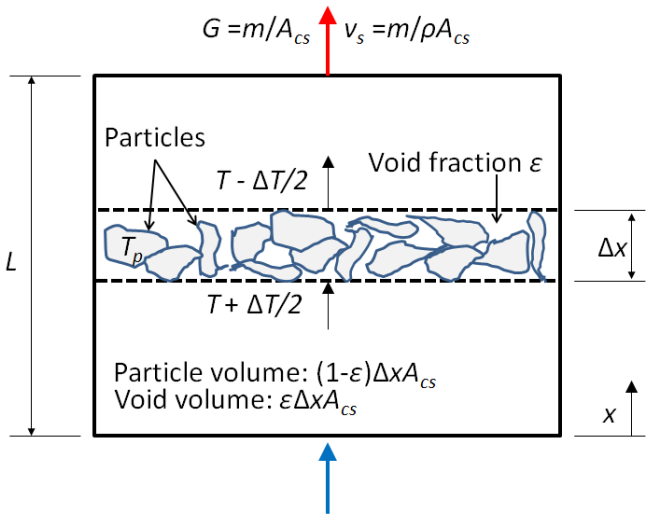

Figure 15: Control volume of packed bed for thermal analysis

Assume that there is no thermal loss from the packed bed walls and that the fluid flow is one-dimensional and has a uniform axial flow speed (plug flow). Then the fluid and particle temperatures $T(x,t)$ and $T_p(x,t)$ are functions of time t and position x in the packed bed. At a given point in time, T_p is assumed to be constant throughout the control volume (that is, the particles have no internal thermal resistance), in the small time interval during which the fluid temperature varies by ΔT. If there is no radiant or conductive heat transfer in the air stream, an energy balance on the fluid in the control volume over time Δt gives

$$\varepsilon A_{cs}\,\Delta x \rho c\left(T_{(t+1)} - T_{(t)}\right) = \Delta t\, h_v A_{cs}\,\Delta x\left(T_p - T\right) - \Delta t\, mc\,\Delta T \qquad \textbf{(23)}$$

where h_v is the volumetric heat transfer coefficient between the particles and fluid, based on the total control volume; ρ is the fluid density and c the fluid specific heat capacity. The subscripts (t) and (t+1) refer to time. Eq. (23) can be rearranged as

$$\varepsilon A_{cs}\rho c\left(T_{(t+1)} - T_{(t)}\right)/\Delta t = h_v A_{cs}(T_p - T) - mc\,\Delta \mathrm{T}/\Delta x \qquad \textbf{(24)}$$

Eq. (24) can be rewritten as

$$\varepsilon A_{cs}\rho c\frac{\partial T}{\partial t} = h_v A_{cs}(T_p - T) - mc\frac{\partial \mathrm{T}}{\partial \mathrm{x}} \quad \textbf{(25)}$$

or

$$\varepsilon\rho c\frac{\partial T}{\partial t} = h_v(T_p - T) - \rho v_s c\frac{\partial \mathrm{T}}{\partial \mathrm{x}} \quad \textbf{(26)}$$

Note that neither c nor ρ need to be constant (see Rohsenow *et al.*, 1998; Klein *et al.*, 2013).

If the fluid thermal capacitance term is negligible, which should be the case for an air–rock bed (Duffie and Beckmann, 1991; Adebiyi and Chenevert, 1996) this can be simplified to

$$\frac{\partial \mathrm{T}}{\partial \mathrm{x}} = \frac{h_v A_{cs}}{mc}(T_p - T) = \frac{NTU}{L}(T_p - T) \quad \textbf{(27)}$$

as in Duffie and Beckman. The Number of Transfer Units (NTU) is defined as

$$NTU = h_v A_{cs} L/(mc) = h_v L/(Gc) \quad \textbf{(28)}$$

Adebiyi and Chenevert (1996) give the following condition in order to neglect the fluid thermal capacitance:

$$\frac{\varepsilon}{(1-\varepsilon)}\frac{c_v\rho}{c_p\rho_p} \ll 1 \quad \textbf{(29)}$$

where c_v is the fluid specific heat capacity at constant volume. For an air-rock bed, ε = 0.4, at room temperature, c_p = 820 J/kgK, ρ_p = 2700 kg/m^3, c_v = 718 J/kgK (Moran and Shapiro, 1998), and ρ = 1.1 kg/m^3, the value of the left-hand side of Eq. (29) is 2 x 10^{-4}, well below the required limit.

An energy balance on the stationary particles gives:

$$h_v A_{cs}\,\Delta x(T - T_p)\,\Delta t = m_p c_p (T_{p\,(t+1)} - T_{p\,(t)}) \quad \textbf{(30)}$$

where c_p and ρ_p are the particle specific heat capacity and density, respectively, and it is assumed that there is no heat conduction or radiation between neighbouring particles. The particle mass in a segment is

$$m_p = (1 - \varepsilon) A_{cs} \Delta x \rho_p \quad \textbf{(31)}$$

Eq. (30) may be rewritten as

$$(1-\varepsilon)\rho_p c_p \frac{\partial T_p}{\partial t} = h_v (T - T_p) \quad \textbf{(32)}$$

This may be arranged in the form used by Duffie and Beckmann (1991):

$$\frac{\partial T_p}{\partial t} = \frac{h_v}{(1-\varepsilon)\rho_p c_p}(T - T_p) = \frac{NTU}{\tau}(T - T_p) \quad \textbf{(33)}$$

where the thermal time constant τ is defined as

$$\tau = \rho_p (1-\varepsilon) A_{cs} L c_p / (mc) = m_p c_p / (mc) \quad \textbf{(34)}$$

Eq. (25) and (32) are often referred to as the Schumann equations, although they were published a few years earlier by Anzelius (Vortmeyer and Schaefer, 1974). Governing equations which include greater detail, such as the influence of thermal conduction through the fluid or between particles, internal particle resistance, or heat transfer to the containment wall, may be found in Wakao *et al.* (1979), Adebiyi *et al.* (1998), or Ismail and Stuginsky (1999).

The importance of neglecting internal particle resistance may be estimated from the Biot number (Bejan, 1993; Incropera *et al.*, 2007; see Appendix B), defined as

$$Bi = \frac{hD}{2k_p} \quad \textbf{(35)}$$

Bi < 0.1 implies that there are relatively negligible thermal gradients within a particle (see also Waked, 1986). Eq. (35) is a factor of three greater than Eq. (B-2), and Incropera *et al.* (2007) consider it to be more appropriate.

There are analytical solutions to Eq. (25) and (32) for the case of a bed, initially at a uniform temperature, which is subjected to a step change in inlet temperature. Shitzer and Levy (1983) give the following solution:

$$\frac{T_p}{T_o} = e^{-y-z} \sum_{n=1}^{\infty} \sum_{m_{sc}=0}^{\infty} \frac{y^{m_{sc}} z^{m_{sc}+n}}{m_{sc}!\,(m_{sc}+n)!} \quad \textbf{(36)}$$

$$\frac{T}{T_o} = e^{-y-z} \sum_{n=0}^{\infty} \sum_{m_{sc}=0}^{\infty} \frac{y^{m_{sc}} z^{m_{sc}+n}}{m_{sc}!\,(m_{sc}+n)!} \tag{37}$$

where T_o is the difference between the fluid temperature at the inlet of the bed and the initial bed temperature before charging begins. y and z are defined as

$$y = h_v x/[\rho c v_s] \tag{38}$$

$$z = \frac{h_v}{\rho_p c_p (1-\varepsilon)} (t - x\varepsilon/v_s) \tag{39}$$

Riaz *et al.* (1976) took into account thermal conduction through the bed, but simplified the solution by assuming that particle and fluid temperatures are approximately equal, which should be valid for long-term prediction of thermal storage performance, provided that the flow speed through the bed is "low". Their calculations are for particle Reynolds numbers less than 100. For a step change in fluid temperature at the inlet, from T_i to T_{in}, where the bed is initially at a constant temperature T_i throughout, Riaz *et al.* (1976; see Riaz, 1977, 1978; Spiga and Spiga, 1981) give an analytical solution, including the effect of one-dimensional axial conduction through the rock, for $\rho c << \rho_p c$ (as is the case for air-rock beds):

$$\theta = \frac{T - T_i}{T_{in} - T_i} = \frac{1}{2} erfc\left[\frac{\xi - \tau_a}{2\sqrt{\tau_a}}\right] + \sqrt{\frac{\tau_a}{\pi}}\; e^{-\frac{[\xi-\tau_a]^2}{4\tau_a}} - \frac{1}{2}[1 + \xi + \tau_a]\, e^{\xi} \times erfc\left[\frac{\xi + \tau_a}{2\sqrt{\tau_a}}\right] \tag{40}$$

where (as also defined by Adebiyi and Chenevert, 1996),

$$\xi = \frac{Re_p Pr}{k_e/k} \frac{x}{D} = \frac{\rho v_s c}{k_e} x \tag{41}$$

and

$$\tau_a = \frac{(Re_p Pr)^2 (\alpha_p t/D^2)}{(k_e/k)(k_p/k)(1-\varepsilon)} = \frac{(\rho v_s c)^2}{k_e (1-\varepsilon)\rho_p c_p} t \tag{42}$$

For values of τ_a and ξ that exceed 10, the first term of Eq. (40) is dominant and the other terms can be neglected. The effective conductivity of the bed is represented by k_e, and α_p is the thermal diffusivity of the particle, $k_p/\rho_p c_p$. Spiga and Spiga (1981) found that the one-phase model of Riaz approached their two-phase model (separate fluid and particle temperatures) for $\rho c\varepsilon/[(1-\varepsilon)\rho_p c_p] < 0.001$.

Adebiyi and Chenevert (1996) give a solution for the fluid and particle temperatures in the case of a step change of the inlet temperature. The volumetric heat transfer coefficient is estimated as (Adebiyi and Chenevert, 1996; from Vortmeyer and Schaefer, 1974)

$$h_v = G^2c^2 / \left[\delta Re_p Pr\ k\right] = Gc/[\delta D] \quad \textbf{(43)}$$

The fluid and particle temperatures are given by

$$\theta = \frac{T - T_i}{T_{in} - T_i} = \frac{1}{2} erfc\left[\frac{\xi - \tau_a}{2\sqrt{\tau_a}}\right] + \frac{1}{2} e^{\xi} erfc\left[\frac{\xi + \tau_a}{2\sqrt{\tau_a}}\right] \quad \textbf{(44)}$$

$$\theta_p = \frac{T_p - T_i}{T_{in} - T_i} = \theta - \frac{\delta Re_p Pr}{k_e/k}\left[\frac{1}{\sqrt{\pi\tau_a}} e^{\frac{-(\xi-\tau_a)^2}{4\tau_a}} - \frac{1}{2} e^{\xi} erfc\left[\frac{\xi + \tau_a}{2\sqrt{\tau_a}}\right]\right] \quad \textbf{(45)}$$

D is defined only as the "storage particle diameter". This solution is based on the approximation that

$$\frac{\partial\theta_p}{\partial\tau_a} \approx \frac{\partial\theta}{\partial\tau_a} \quad \textbf{(46)}$$

$$\frac{\partial^2\theta_p}{\partial\xi^2} \approx \frac{\partial^2\theta}{\partial\xi^2} \quad \textbf{(47)}$$

Adebiyi and Chenevert (1996) and Vortmeyer and Schaefer (1974) use the following relation to calculate the effective axial thermal conductivity in the bed, from experimental work by Yagi *et al.* (1960):

$$\frac{k_e}{k} = \frac{k_e^0}{k} + \delta Re_p Pr \quad \textbf{(48)}$$

where δ has a value of 0.7 for steel balls and porcelain rings and 0.8 for broken limestone and glass beads and k_e^0 is the stagnation axial conductivity of the bed, which may be estimated from the correlation of Krupiczka (1967):

$$\frac{k_e^0}{k} = \left(\frac{k_p}{k}\right)^{0.280 - 0.757\log(\varepsilon) - 0.057\log(k_p/k)} \quad \textbf{(49)}$$

The speed with which the temperature profile (thermocline) moves through the bed may be estimated from (Vortmeyer and Schaefer, 1974)

$$v_{th} = \frac{\rho v_s c}{\varepsilon \rho c + (1-\varepsilon)\rho_p c_p} \quad \textbf{(50)}$$

This approximates the temperature profile as a step change.

Lateral fluid mixing appears to be better in packed beds of cylinders than spheres (Freiwald and Paterson, 1992). If this is the case for non-spherical particles in general, the assumption of a uniform temperature profile transverse to the flow direction is reasonable for rock beds.

4.2 Heat transfer coefficient

Handley and Heggs (1968) give a correlation for metallic spheres, from experiments in the range $100 < Re_p < 4000$ and $8 < D_c/D < 22$:

$$h = Nu\, k/D = (k/D)(0.255/\varepsilon) Re_p^{0.665} Pr^{1/3} \quad \textbf{(51)}$$

where *Nu* is the Nusselt number, *Pr* the Prandtl number, and *k* the fluid thermal conductivity.

Gunn (1978) proposed the correlation

$$h = Nu\, k/D = (k/D)[(7 - 10\varepsilon + 5\varepsilon^2)\left(1 + 0.7 Re_p^{0.2} Pr^{1/3}\right) + (1.33 - 2.4\varepsilon + 1.2\varepsilon^2) Re_p^{0.7} Pr^{1/3}] \quad \textbf{(52)}$$

Gunn defines *D* as the particle diameter but does not specify this further. The correlation is intended for use where $0.35 < \varepsilon < 1.0$ and $Re_p < 10^5$.

Wakao *et al.* (1979) present a correlation that is corrected for axial thermal dispersion through the fluid:

$$h = Nu\, k/D = (k/D)(2 + 1.1 Re_p^{0.6} Pr^{1/3}) \quad \textbf{(53)}$$

This is valid for $15 < Re_p < 8500$. The correlation was based on measurements with spheres, cylinders and cubes. Wakao *et al.* do not state what range of void fractions it is applicable to, or how the particle diameter was defined. The '2' represents heat transfer by conduction for a single sphere in a stationary infinite fluid (see Incropera *et al.*, 2007; Wakao and Funazkri, 1978). Guardo *et al.* (2006) compared the Wakao correlation with CFD predictions for packed beds of spheres in air. There was agreement at particle Reynolds numbers above 10, but below this the CFD predictions, though scattered, were higher than the correlation.

The KTA 3102.2 nuclear safety standard (Geschäftsstelle des Kerntechnischen Ausschusses, 1983) gives an equation for spheres, valid for $10^2 < Re_p < 10^5$, $D_c/D > 20$ and $0.36 < \varepsilon < 0.42$:

$$h = Nu\, k/D = (k/D)[1.27Re_p^{0.36}Pr^{1/3}/\varepsilon^{1.18} + 0.033Re_p^{0.86}Pr^{1/2}/\varepsilon^{1.07}] \quad \textbf{(54)}$$

Kays and London (1984) give a correlation for smooth spheres, from data in the range $3 < Re_{Erg} < 75\,000$, at void fractions between 0.37 – 0.39:

$$h = Nu\, k/D = (k/D)(0.345(2/3)^{0.7}/\varepsilon)Re_p^{0.7}Pr^{1/3} \quad \textbf{(55)}$$

Martin (2005) gives a correlation that links heat transfer to frictional pressure drop through a packed bed of spherical or non-spherical particles:

$$h = Nu\, k/D = (k/D)0.4038(2x_f\, Hg\, D_h/L_m)^{1/3}Pr^{1/3} \quad \textbf{(56)}$$

The packing geometric ratio D_h/L_m is a function of the void fraction,

$$D_h/L_m = (2/3)\varepsilon/(1-\varepsilon)^{2/3} \quad \textbf{(57)}$$

where L_m represents the average distance between two particles.

The Hagen number Hg is calculated from the Ergun equation,

$$Hg = Re_p[150(1-\varepsilon) + 1.75Re_p](1-\varepsilon)/\varepsilon^3 = f_{Erg}(1-\varepsilon)Re_p^2/\varepsilon^3 \quad \textbf{(58)}$$

The frictional fraction of the total pressure drop, x_f, ranges between 0.197 for cubes and 0.447 for spheres. Martin uses the equivalent diameter $6V_p/A_p$ for non-spherical particles.

The correlations are compared in Figure 16. Martin's correlation for cubes is lower than the others, which are mostly for spheres.

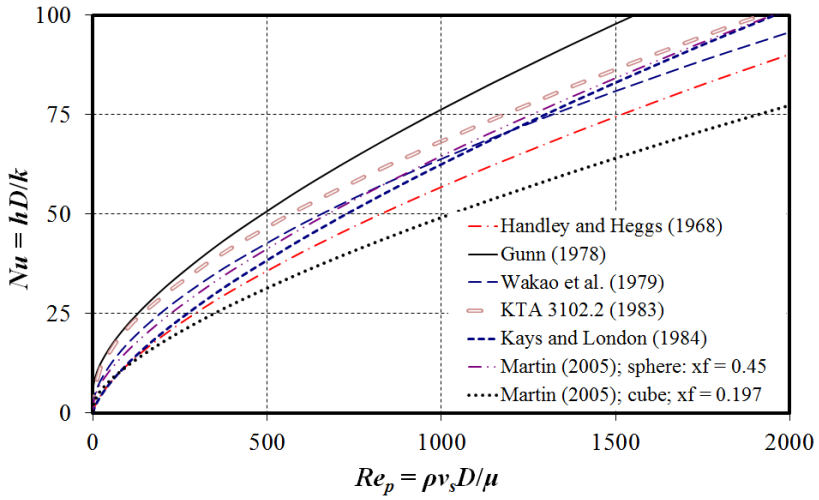

Figure 16: Comparison of Nusselt number correlations from literature; ε = 0.4

The volumetric heat transfer coefficient for a packed bed, h_v, is related to the surface area heat transfer coefficient h by:

$$h_v = ha = h\Sigma A_p/V_t = h\Sigma A_p/[\Sigma V_p/(1-\varepsilon)] = h(1-\varepsilon)\Sigma A_p/\Sigma V_p \quad \textbf{(59)}$$

Where a is the particle surface area per unit volume of the bed. In the case of spheres or cubes,

$$\Sigma V_p/\Sigma A_p = D/6 \quad \textbf{(60)}$$

CFD calculations predict lower Nusselt numbers for structured packing than those for random packing (Yang *et al.* 2010).

Heggs and Burns (1988) give details of the methods to calculate heat transfer coefficients from measurements. They recommend the least squares method. Additional information on heat transfer and thermal conductivity in packed beds may be found in Dixon and Cresswell (1979) and Achenbach (1995).

4.3 Effective thermal conductivity of packed beds

4.3.1 Pure conduction

Hänchen et al (2011) compared predicted temperature profiles for packed beds of aluminium and rock. Despite the significant difference in thermal conductivity between aluminium and rock, there was little difference in the predicted temperature profile, leading to the conclusion that the particle thermal conductivity is not important. They do not specify at what flow rate this calculation was made. The predictions of Zanganeh *et al.* (2012) also suggest that pure conduction has a negligible influence on the temperature profile in a conical container, for mass fluxes between 0.03-0.15 kg/m^{2}s.

Summers *et al.* (1989) state that axial thermal conduction through a packed bed may be neglected when $Pr_L Re_p(L/D) >> 1$, where $Pr_L = \mu c/k_e = Pr\ k/k_e$. Adebiyi and Chenevert (1996) specify that the Peclet number, $Re_p\,Pr$, should exceed 50 for axial conductivity to be negligible. For air with a Prandtl number of 0.7, this requires particle Reynolds numbers in excess of 70.

Previous work (see Sagara *et al.*, 1970) suggests that particle-to-particle thermal conduction increases as the particle size decreases, as a consequence of stagnant fluid surrounding point contacts. However, at high ratios of k_p/k, the effective conductivity has been found to increase with increasing particle size above about 10 mm, because of larger interparticle contact areas (Zhou *et al.*, 2011).

To estimate the bulk conductivity of a bed of *spheres*, Kaviany (1995) recommends the correlation of Krupiczka (Eq. (49)) or the Zehner/Bauer/Schlünder model which takes into consideration fluid conduction and point contact (see Van Antwerpen *et al.*, 2010; Tsotsas and Martin, 1987):

$$\frac{k_e}{k} = 1-(1-\varepsilon)^{\frac{1}{2}} + \frac{2(1-\varepsilon)^{1/2}}{1-Bk/k_p}\left[\frac{B(1-k/k_p)}{(1-Bk/k_p)^2}\ln[1/(Bk/k_p)] - \frac{B+1}{2} - \frac{B-1}{1-Bk/k_p}\right] \quad (61)$$

where the deformation parameter $B = 1.25[(1-\varepsilon)/\varepsilon]^{10/9}$. See Hsu *et al.* (1994) for a modified version which relaxes the assumption of point-contact between spheres.

4.3.2 Conduction and radiation

Morrone *et al.* (2006) and Amelio and Morrone (2007) assumed that conduction or radiation through the bed is negligible compared to convection. They also neglected internal particle thermal resistance, for Biot numbers below 0.1 (definition: $hD_v/[6\psi k_p]$), but permitted the fluid speed to vary as a consequence of large temperature (and density) change. They obtained good agreement with existing experimental measurements (Chou *et al.*, 2000) for a granite-filled regenerator at temperatures up to 400 °C (D_v = 12.5 mm, ε = 0.41; G = 0.25 kg/m^{2}s).

Kunii and Smith (1960) state that for packed beds with gases as the heat transfer fluid, the radiation contributions to effective conduction through the bed are negligible except for 'large' particles and temperatures around 500 °C or more. Van Antwerpen *et al.* (2010) predict the components of effective thermal conductivity in a bed (ε = 0.385) of 60 mm spheres (emissivity ϵ_p = 0.8) surrounded by helium. Only at temperatures of 400 – 500 °C does radiation become more significant than pure conduction. Beveridge and Haughey (1971) show similar results for alumina-silicate spheres in air, and according to Sagara *et al.* (1970) radiation is "probably" only important at temperatures above 400 – 500 °C. Balakrishnan and Pei (1979) give a temperature between 650 – 700 °C at which radiation becomes more significant than conduction; however, they recommend that it be taken into account at temperatures above 250 °C.

Schröder *et al.* (2006) found that radiation may be ignored for beds of slate (in nitrogen) at temperatures below 300 °C and mass fluxes of about 0.1 kg/m^{2}s. At higher temperatures, the temperature difference between the particle and fluid at a given position was reduced by about 10 % of the value calculated without taking radiation into account. Jalalzadeh-Azar *et al.* tested a packed bed of 18 mm diameter zirconium dioxide (ZrO_2) cylinders (k_p = 2 W/mK) at mass fluxes of 0.26 – 0.43 kg/m^{2}s and temperatures up to 900 °C. For the conditions under which they tested, the neglection of axial thermal dispersion seemed to be valid.

Provided there are small temperature differences between adjacent particles, radiation transfer between them should be negligible.

Zanganeh *et al.* (2012) compare predicted temperatures for rock (D_v = 0.03 m) with and without radiation taken into consideration. With radiation, the predicted temperature at the high-temperature (top) end of the bed is a maximum of 15 – 25 °C lower at 600 °C, after 8 hours of charging at an average mass flux of 0.03-0.04 kg/m^{2}s at the top. This is a difference of 3 – 4 % of the total change in temperature of the bed. Their calculations suggest that radiation transfer is similar in magnitude to pure conduction transfer at temperatures around 200 °C. At 700 °C, the predicted effective bed conductivity k_e = 2.5 W/mK. At room temperature, where radiation is negligible, k_e = 0.5 W/mK.

Zanganeh *et al.* (2012) use an equation for estimating the effective conductivity – including radiation – from Kunii and Smith (1960), which excludes heat transfer through the contact surfaces of the particles, a component Kunii and Smith declare to be unimportant except at 'very low' gas pressures. The equations are based on data from spherical and non-spherical metallic and non-metallic objects, including firebrick, limestone and pumice.

$$\frac{k_e}{k} = \varepsilon\left(1 + \beta\frac{h_{rv}D_v}{k}\right) + \frac{\beta(1-\varepsilon)}{\dfrac{1}{1/\phi + h_{rp}D_v/k} + \gamma k/k_p} \qquad \textbf{(62)}$$

where the void radiative heat transfer coefficient (from Yagi and Kunii, 1957)

$$h_{rv} = \left[0.1952/(1 + \frac{\varepsilon}{2(1-\varepsilon)}\frac{1-\epsilon_p}{\epsilon_p})\right](T/100)^3 \qquad \textbf{(63)}$$

and the particle to particle radiative heat transfer coefficient

$$h_{rp} = 0.1952(\frac{\epsilon_p}{2-\epsilon_p})(T_p/100)^3 \qquad \textbf{(64)}$$

Temperatures T and T_p must be in kelvin. Zanganeh *et al.* used a rock emissivity ϵ_p = 0.85, and an equivalent sphere volume diameter D_v. Values in the literature for the thermal infrared emissivity of basalt and dolomite are 0.96 and 0.97 respectively, while soils range from 0.93 – 0.98 (Rubio *et al.*, 2003).

β is defined as the ratio between the average length separating two neighbouring particles, and the particle diameter. It can range from 0.82 for close packing of spheres to 1 for loose packing. The value of β should be between 0.9 – 1 for most packed beds (Kunii and Smith, 1960) - Zanganeh used a value of 0.9. The thermal resistance parameter γ is the ratio l_s/D_v, where l_s is the thickness of the solid slab required to offer the same resistance to heat transfer as a spherical particle; γ was

approximated as 2/3. The thickness of the fluid film ϕ in the vicinity of the contact between two particles is:

$$\phi = \phi_2 + (\phi_1 - \phi_2)\frac{\varepsilon - \varepsilon_2}{\varepsilon_1 - \varepsilon_2} \quad \textbf{(65)}$$

where ϕ_1 and ϕ_2 correspond to maximum and minimum void fractions ε_1 = 0.476 and ε_2 = 0.26. They are calculated from

$$\phi_i = \frac{1}{2}\frac{[(\kappa-1)/\kappa]^2 sin^2(\theta_i)}{\ln(\kappa-(\kappa-1)cos\theta_i) - [(\kappa-1)/\kappa](1-cos\theta_i)} - \frac{2}{3\kappa} \quad \textbf{(66)}$$

where $\kappa = k_p/k$ and $sin^2\theta_i = 1/n_i$, where n_1 = 1.5 and $n_2 = 4\sqrt{3}$, the number of contact points on a hemispherical surface of one particle. They correspond to loose and close packing respectively.

The Kunii and Smith model fails for $k_p/k > 10^3$ because the contact area between particles, which is neglected in Eq. (62), becomes important (Van Antwerpen *et al.*, 2010). For rock and air, however, k_p/k should be of the order of 10 – 100, which is sufficiently small to avoid this limit. The more detailed Zehner, Bauer and Schlünder model (for spheres, specifically) including thermal radiation and conduction through contact areas between particles may be found in Van Antwerpen *et al.* (2010).

The contribution of radiation to effective thermal conductivity is dependent upon the particle conductivity (Bauer and Schlünder, 1978b). Poor conductors result in beds with lower radiation heat transfer than good conductors. The bed conductivity can also vary significantly with particle size distribution, and particle size – for irregularly shaped particles (cement clinker), increasing values of bed conductivity were measured with increasing particle size (from 0.2 – 5 mm).

Radiation heat transfer between air and particles should be negligible unless there are combustion gases present (Reboussin *et al.*, 2005).

4.4 Numerical solution

The temperature profile through the bed is obtained by means of the Hughes effectiveness – NTU (E-NTU) method (Hughes, 1975; Hughes *et al.*, 1976; Duffie and Beckmann, 1991). It is a numerical solution of the Schumann equations.

The bed is divided into segments of length Δx along the direction of flow, as shown in Figure 17. The temperature of the rock is assumed to be uniform throughout each segment.

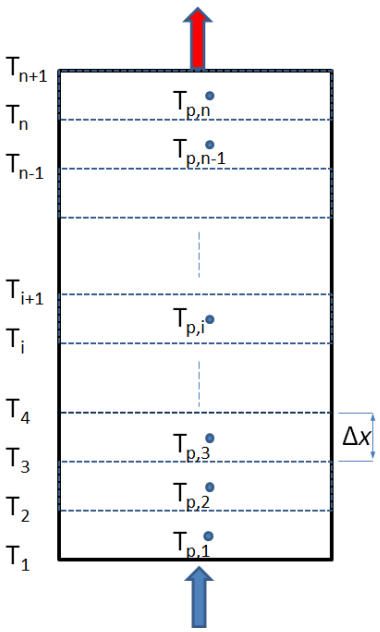

Figure 17: Application of the Hughes E-NTU method to a packed bed of *n* segments

The air temperature profile is exponential. The equation is the same as that for a heat exchanger where evaporation or condensation occurs, since the particle temperature within a segment is assumed to be uniform (Hughes, 1975; Duffie and Beckmann, 1991; Incropera *et al.*, 2007):

$$T_{(i+1)} = T_{(i)} - (T_{(i)} - T_{p,i})(1 - e^{-NTU(\Delta x/L)}) \quad \textbf{(67)}$$

i represents the segment number. NTU (see Eq. (28)) is scaled by the number of segments in the bed ($\Delta x/L$) to give a value for a single segment.

An energy balance on the rock contained in segment length Δx, number *i*, gives

$$\rho_p(1-\varepsilon)A_{cs}\Delta x c_p \frac{dT_p}{dt} = mc(T_{(i)} - T_{p,i})(1 - e^{-NTU(\Delta x/L)}) \quad \textbf{(68)}$$

This may be rewritten as

$$\frac{dT_p}{dt} = \frac{L}{\Delta x}\frac{mc}{\rho_p(1-\varepsilon)A_{cs}Lc_p}(T_{(i)} - T_{p,i})(1 - e^{-NTU(\Delta x/L)}) \quad \textbf{(69)}$$

$$\frac{dT_p}{dt} = \frac{L}{\Delta x}\frac{1}{\tau}(T_{(i)} - T_{p,i})(1 - e^{-NTU(\Delta x/L)}) \quad \textbf{(70)}$$

The finite difference solution to solve Eq. (70) is described by Duffie and Beckmann (1991) and is as follows: Euler-stepping is used as an approximation

for the derivative. The notation uses a superscript '+' to indicate the next time step. The time derivative is approximated as

$$\frac{dT_p}{dt} \approx \frac{T_{p,i}^{+} - T_{p,i}}{\Delta t} \tag{71}$$

The temperature $T_{p,i}$ in Eq. (70) is replaced with an average over the time interval,

$$T_{p,i\_avg} \approx (T_{p,i}^{+} + T_{p,i})/2 \tag{72}$$

Equations (71) and (72) are substituted into Eq. (70) to get

$$\frac{T_{p,i}^{+} - T_{p,i}}{\Delta t} = \frac{L}{\Delta x}\frac{1}{\tau}(T_{(i)} - T_{p,i}^{+}/2 - T_{p,i}/2)(1 - e^{-NTU(\Delta x/L)}) \tag{73}$$

This may be solved for $T_{p,i}^{+}$, giving

$$T_{p,i}^{+} = \frac{T_{p,i}\left(1 - \frac{\Delta t}{2\tau}\frac{L}{\Delta x}\eta\right) + T_{(i)}\left(\frac{\Delta t}{\tau}\frac{L}{\Delta x}\eta\right)}{1 + \frac{\Delta t}{2\tau}\frac{L}{\Delta x}\eta} \tag{74}$$

where

$$\eta = 1 - e^{-NTU(\Delta x/L)} \tag{75}$$

For alternative solutions or comparisons of solutions, see, for example, Willmott (1964) or Sragovich (1989). Sragovich (1989) proposes that the suitable segment size be estimated from

$$\Delta x \leq Bi_{seg}\, k_p/h \tag{76}$$

where Bi_{seg} is chosen to be 0.1.

Duffie and Beckmann (1991) make use of a correlation from Jeffreson (1972) to take into account the particle thermal conductivity (internal resistance) and its influence on heat transfer. They calculate a corrected value of *NTU*, NTU_c, and use it in place of *NTU*:

$$NTU_c = NTU/[1 + Bi/5] \tag{77}$$

For charge-discharge simulations, the final temperatures at the end of the charge time period are used as the initial bed temperatures for the discharge process. When the flow direction is changed, the bed inlet position and temperature during charging become the bed outlet position and temperature during discharging.

For repeated charge-discharge simulations, if the fluid energy density ρc is much lower than the storage material density $\rho_p c_p$, as is the case for an air-rock bed, the charge-discharge process must be iterated "many times" to reach a steady state condition of bed operation, when the temperature profiles obtained during successive charge/discharge cycles are repeatable (Li *et al.*, 2012). Hänchen *et al.* (2011) and Zanganeh *et al.* (2012) show that this can require 10 – 20 or even 20 – 30 cycles, although the first ten are the most significant.

5 Experimental apparatus and method[3]

This chapter gives details about the experimental apparatus, testing method and particles tested. Isothermal pressure drop tests, low temperature (< 80 °C) and high temperature (150 – 530 °C) thermal tests were conducted with a range of particle types to better understand packed bed pressure drop and heat transfer characteristics.

5.1 Wind tunnel for pressure drop and low temperature thermal tests

The isothermal pressure drop over a packed bed test section was measured by means of the wooden wind tunnel shown in Figure 18. Air is drawn through a bell mouth at the tunnel inlet, where the temperature is measured, and then through the test section, where the pressure drop is measured. Subsequently, the air passes into a settling chamber upstream of a 50 mm elliptical nozzle. At flow rates above 0.02 kg/s, the mass flow rate is calculated from the pressure drop over this nozzle as described in Kröger (2004). The air then passes into a fan controlled by a variable speed drive, and out of the fan exhaust. At flow rates below 0.02 kg/s, a DISA 55D41 calibration unit with venturi nozzle was attached to the wind tunnel exit to measure the flow rate.

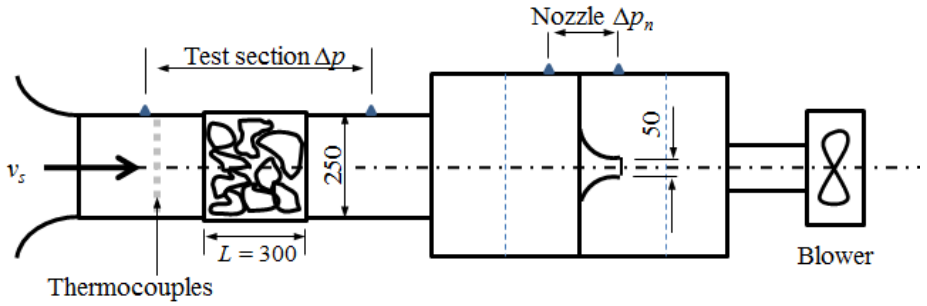

Figure 18: Wind tunnel layout

The pressure drop was measured by means of two Endress + Hauser 0 – 2500 Pa pressure transducers and one Foxboro 0 – 25 000 Pa transducer, which were calibrated using two independent Betz 5000 manometers. The readings were logged by with an Agilent 34970 logger and 34901A 20 channel multiplexer modules.

The particles were contained in a wooden box with the ends covered by expanded steel (diamond-shaped) grating, with the maximum inner dimensions as shown in Figure 19.

[3] Sections relating to isothermal pressure drop were published in Allen *et al.* (2013a)

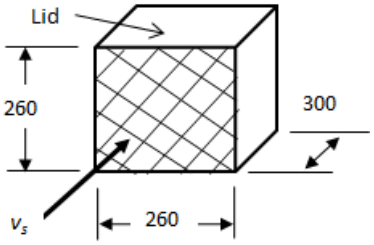

Figure 19: Test section showing lid and grating to allow air flow

Based on the literature survey (see section 3.1.9), the dimensions of the test section are sufficiently large to test beds of spheres with an average diameter of 16 mm (D_c/D > 16). It should be possible to test larger non-spherical, irregularly shaped objects.

A heat exchanger was attached to the wind tunnel inlet (Figure 20) to heat the incoming air upstream of the test section for the thermal tests. This allowed the bed to be fully charged to temperatures up to a maximum of ≈ 75 °C. The heat exchanger was removable, which allowed the bed to be discharged after charging. Seven thermocouples were spread out over the cross-section at the inlet of the test section to measure the air temperature. The air temperature at the outlet was measured with fourteen thermocouples spread over the cross-section; nine additional ones were positioned near the walls. Up to three were placed in the bed approximately halfway along the length to indicate the internal temperature of the bed prior to charging or discharging. The particle temperature was not measured.

In order to obtain a uniform temperature profile over the cross-section at the test section inlet, aluminium honeycomb was placed between the heat exchanger and test section. This was to counteract losses into the wind tunnel wall or non-uniform temperature profiles from the heat exchanger. It was necessary to insulate the test section on the inside with polystyrene and foam-plastic up to 20 mm thick to reduce the energy absorbed by the wooden walls, which proved to be significant without this precaution (10 – 15 % of the energy stored in the test section).

There was substantial thermal stratification in the horizontal wind tunnel layout: the thermocouples measured a temperature profile that increased from the bottom of the duct to the top. To prevent this, the entire wind tunnel was rotated to a vertical orientation, as shown in Figure 20. This did not affect the repeatability of pressure drop tests. An unexpected consequence of the vertical orientation was that, at the relatively low flow speeds in the duct during the thermal tests, the cooler air in the upper wind tunnel seemed to sink down the duct and ‘pool’ at the outlet of the test section (see Figure 21). This manifested itself as temperature fluctuations at some of the thermocouples. This was rectified by placing aluminium honeycomb and a choke downstream from the test section (as shown in Figure 20).

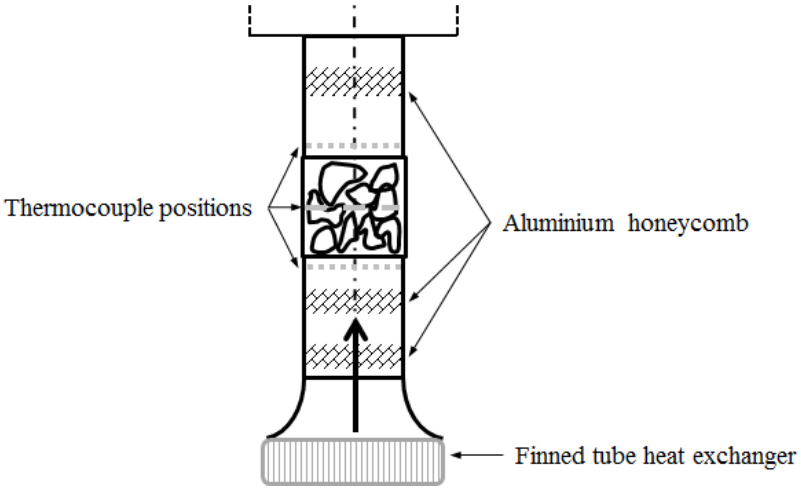

Figure 20: Vertical wind tunnel for thermal tests

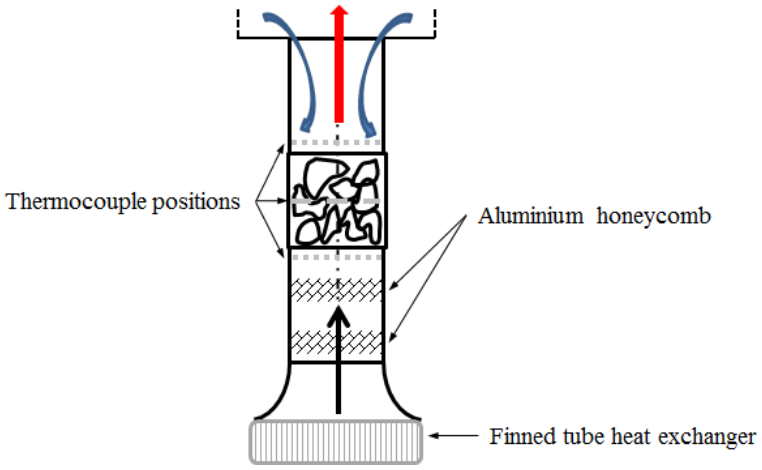

Figure 21: Cold air sinking and causing false temperature readings at the bed outlet

5.2 Method of testing

For the isothermal pressure drop tests, the fan was set to a number of different speeds and the flow rate and pressure drop were logged at each speed. A minimum of 10 readings were logged over one minute and averaged. Sufficient time was left between each fan speed change to allow the system to reach steady state.

For the thermal tests, the bed was at room temperature initially. It was heated to the maximum temperature of which the heat exchanger was capable (70 – 75 °C). The bed was charged until steady state was reached and the outlet air temperature was constant with time. At this point the heat exchanger was rapidly removed, allowing room-temperature air to flow through the bed and discharge it. The fan speed was kept constant, but the mass flow rate did vary as a consequence of the air density variation with temperature change. This test method is essentially that

described by Kays and London (1984) for matrix packings, which include packed beds. See also Jones and Hill (1979) on the testing of thermal storage.

5.3 Particle and packing characteristics and measurement

The test section was packed randomly by pouring the particles into it from one of two different directions: either through the lid in a **cross-current** direction relative to the air flow; or through the flow inlet in a **co-current** or **counter-current** direction relative to the air flow by temporarily removing the grating and standing the test section on the flow outlet or inlet. This is illustrated in Figure 22:

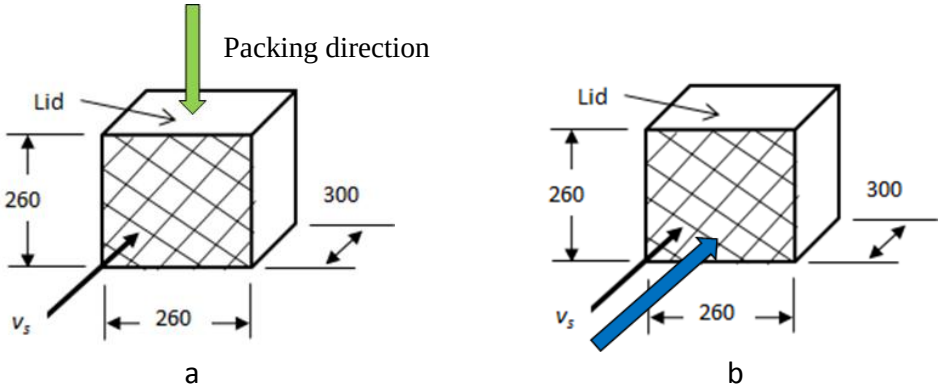

Figure 22: Test section packing in a (a) cross-current or (b) co-current direction

The particles were not vibrated while they were poured in, although they were tamped by hand at intervals to try to avoid voids forming near the wall. The repeatability of the packing was tested by emptying the test section, re-filling it with the same particles, and taking a second set of pressure drop measurements.

The pressure drop was measured for randomly packed beds of smooth and rough glass spheres (marbles), steel spheres (ball bearings), wooden cubes, aluminium cubes, wooden cylinders, ellipsoids (acorns), mixed smooth spheres of different sizes, weathered (rounded) rock and crushed rock. Measurements were also obtained for smooth spheres and ellipsoids in structured packing arrangements.

The wooden cylinders and cubes were cut from lengths of the required cross-section, and the splinters removed. The aluminium cubes were cut in a similar manner, and burrs removed from the ends. Two sets of mixed size spheres were used – a mixture of 8 mm plastic beads and 16 mm glass marbles, and a mixture of marbles sized between 16 – 44 mm. The acorns were approximated as ellipsoids and the length of the major and minor axes was measured. The rough spheres were obtained by coating them with sand from a vibrating sieve, sized between 0.18 – 0.25 mm and 0.425 – 1 mm.

All regularly shaped particles were measured by means of a vernier calliper (0.1 mm divisions). A tape measure with 1 mm divisions was used for the test

section dimensions, and mass was measured on a scale with increments of 0.005 kg. The number of particles in the test section was calculated from the average mass per particle and the total mass of particles in the test section. The number of spheres was counted for one test to confirm this.

To stop channelling of the flow near the wall for structured packing, the particles at the wall were embedded in a dough mixture. For random packing the wall was lined with a sponge layer ≈ 0.01 m thick (acorns only) or cloth ≈ 0.003 m thick (see also Adebiyi *et al.*, 1998). However, the cloth was found to have little or no influence and was removed due to the increase in void fraction uncertainty which it caused. The mesh holding the particles at the inlet and outlet was moved to fit each packing arrangement, so the length of the packed section varied between 0.27 – 0.30 m.

Spheres were packed in the test section in 3 structured arrangements: Hexagonal close (HC) packing, a layered packing with offset simple cubic (OSC) layers so that the layers packed closer together than they would for normal simple cubic packing (a rhombohedral arrangement – Martin *et al.*, 1951), and simple cubic (SC) packing. A plan view of the SC packing layers in the horizontal test section is shown in Figure 23a. These layers were repetitively packed directly on top of each other until the test section was filled. The OSC layers are shown in Figure 23b. The HC packing was orientated to the flow direction as shown in c). The measured void fractions of b) and c) (0.28 – 0.29) in Table 13 were higher than the theoretical value of 0.26. This is a consequence of small gaps between some of the marbles during packing (2-3 mm per row).

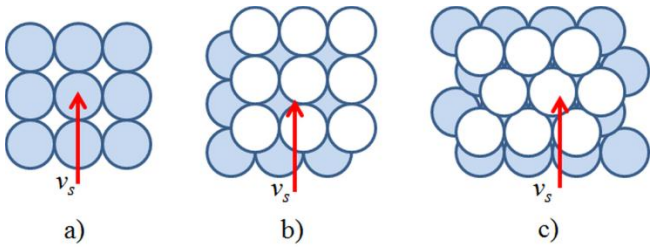

Figure 23: Structured packing arrangements of spheres

The acorns were packed randomly, and also orientated parallel and perpendicular to the flow as shown in Figure 24.

Rock samples were scanned with a *NextEngine 3D* scanner in order to calculate the average volume and surface area of the rock. These scans are time-consuming, so only 25 – 50 were done for each rock type. The average volume per rock from the scans was checked against that measured by a volume displacement test on a larger number of samples (≈ 2 % of the test section mass) to confirm that it was a representative average volume.

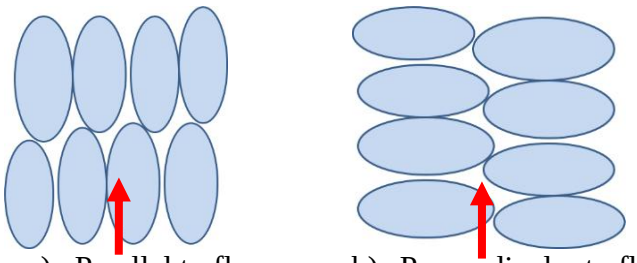

a) Parallel to flow b) Perpendicular to flow

Figure 24: Plan view of different acorn packing relative to flow direction

The rounded rock (marble) had no specified size range. The sizes of the crushed rock (predominantly hornfels and greywacke) were 13.2 mm and 26.5 mm, defined by South African Bureau of Standards (SABS) specification 1083 for aggregates. For example, 26.5 mm aggregate is specified to be in a size range such that 100 % of the rock mass falls through a grid with square holes of side length 37.5 mm; 85 – 100 % through 26.5 mm, 0 – 50 % through 19 mm, 0 – 25 % through 13.2 mm, and 0 – 5 % through 9.5 mm (see Grieve, 2001). One of the 26 mm rock sets was hand-collected, which may have reduced the percentage of the smallest particle sizes and dust.

The tested particle dimensions and packing void fractions are summarized in Table 13.

Table 13: Particle types & packing characteristics for isothermal pressure drop tests

Particle type	D_v, mm	$6\Sigma V_p/\Sigma A_p$, mm	$\Sigma V_p/\Sigma A_p$, mm	ε	ψ
Random packing, single size spheres (smooth glass)	15.8	15.8	2.6	0.36; 0.38; 0.39; 0.40	1
Structured single size spheres (smooth glass)	15.8	15.8	2.6	0.28 – 0.48	1
Random packing, single size rough spheres (0.18 – 0.25 mm sand)	16.2 – 16.3	16.2 – 16.3	2.7	0.43 – 0.44	1
Random packing, single size rough spheres (0.43 – 1 mm sand)	16.3 – 16.4	16.3 – 16.4	2.7	0.44 – 0.45	1
Random packing, mixed spheres (8 mm & 16 mm)	10.4	10.5	1.7	0.37	1
Random packing, mixed spheres (16 – 44 mm)	16.2	16.3	2.7	0.37	1
Random packing, cubes (wood)	20.1	16.2	2.7	0.37; 0.43	0.81
Random packing, cylinders (wood)	18.4	16.1	2.7	0.40; 0.42	0.87
Random packing, Al cubes	19.8	16.0	2.7	0.36; 0.38; 0.40	0.81

Particle type	D_v, mm	$6\Sigma V_p/\Sigma A_p$, mm	$\Sigma V_p/\Sigma A_p$, mm	ε	ψ
Random packing, steel spheres	15.7	15.7	2.6	0.38 (thermal)	1
Random packing, acorns (approx. ellipsoids)	22.4; 19.5	20.6; 17.9	3.4; 3	0.34 – 0.35	0.95
Aligned acorns (approx. ellipsoids)	22.4	20.6	3.4	0.33; 0.34; 0.35	0.95
Random packing, rounded rock (marble)	19.2	17.3	2.9	0.34; 0.38; 0.41	0.86
Random packing, crushed "13.2 mm" rock (Durbanville)	9.7	7.5	1.3	0.44; 0.45; 0.46; 0.47	0.77
Random packing, crushed "26.5 mm" rock (greywacke)	29.5	24.3	4.1	0.42; 0.43	0.80
Random packing, crushed "26.5 mm" rock (Durbanville)	27.7	21.8	3.6	0.46; 0.47	0.79
Random packing, crushed "53 – 73 mm" ballast (dolerite)	49.1	39.0	6.5	0.45	0.79

The increased wetted surface area from the sand roughness was not taken into account. If it were taken into account it would reduce the hydraulic diameter and lower f_{da} and Re (see Eq. (21) and (22)). Any reduction in wetted surface area that occurs for the non-spherical particles as a consequence of overlapping particles will increase the hydraulic diameter and therefore increase Re and f_{da}. No attempt was made to quantify these effects.

The different void fractions for the randomly packed smooth marbles and 13 mm rock were obtained by varying the height from which the particles were poured into the test section, from the level of the test section opening up to 1 m above the opening. The lower void fraction (0.37) of the wooden cubes was obtained by tamping during the packing process.

The diameter of the sand-roughened spheres was measured with vernier callipers and by volume displacement in water. The reason that there is not much difference in the diameter of the spheres covered in two different grain sizes of sand is that the larger grains did not bond as well and only about 30 % of the marble surface was covered. The reduction of the void volume by the sand particle volume is taken into account in the void fraction, which was measured with methods I and III discussed below.

Representative samples of some of the particles tested are shown in Figure 25.

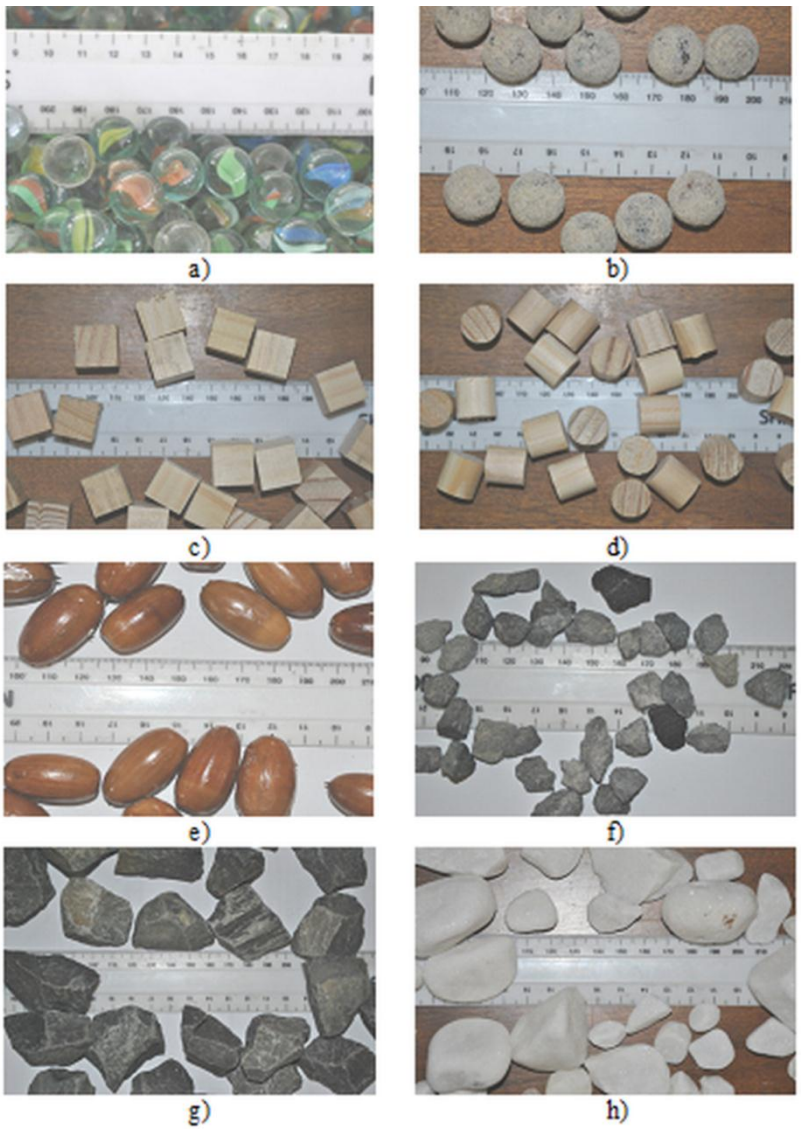

Figure 25: Samples of some of the particles listed in Table 13. a) glass spheres; b) sand-coated glass spheres; c) wooden cubes; d) wooden cylinders; e) acorns (ellipsoids); f) "13 mm" crushed rock; g) "26 mm" crushed rock; h) rounded rock

The density of irregular particles was measured by volume displacement of liquid (water or cooking oil) for particles of known mass. The void fraction of the packing was obtained by one or more of three methods. (I) The total mass of particles in the test section was measured or (II) the total number of regular particles of known dimension in the test section was counted. The total particle volume was obtained from I or II, and subtracted from the total volume occupied by the packing to give the void volume. Alternatively, (III) the void volume was measured by pouring the particles into a waterproof container of similar volume and shape to the test section, and measuring the quantity of liquid required to fill the void volume.

The disadvantage of (I) and (II) is that, if a wall lining is used, the uncertainty of the volume in which the particles are packed increases. The disadvantages of method (III) are twofold: the particles are poured into a different container, so it is not a direct measurement of the void fraction in the test section; and, if the particles absorb the liquid, it causes an erroneous measurement. To reduce the error, the particles were packed according to the same method in a container of similar shape and size. The particles were pre-soaked in the liquid to avoid absorption during void measurement, and excess liquid was drained off before the measurement.

5.4 Thermal properties

The specific heat capacity of the materials was measured by means of a custom-built calorimeter (see Appendix C). The measured heat capacity of the different materials is summarized in Table 14. Values from literature are given in Table 15, together with thermal conductivity for Biot number estimates.

Table 14: Measured particle heat capacity

Particle type	c, J/kgK, 50 – 60 °C
Glass (marbles)	840 (19)*
Al cubes (6082 alloy)	932 (32)
Steel spheres	460 (30)
Rounded rock (marble)	890 (9)
Crushed "13 mm" rock (hornfels)	822 (24)
Crushed "26 mm" rock (hornfels)	820 (30)
Crushed "53 – 73 mm" rock (dolerite)	815 (19)

*Standard deviation

Table 15: Literature values of heat capacity and thermal conductivity at 20 – 25 °C

Particle type	c, J/kgK	k_p, W/mK	Reference
Glass (soda lime)	840	1.7	Brown University, s.a.
Al cubes (6082 alloy)	900	170	Ahamat & Tierney, 2011
Steel spheres (carbon/silicon)	430-450	50-60	Incropera *et al.*, 2007
Rounded rock (marble)	880	2.5 - 3	Waples & Waples, 2004; Birch and Clark, 1940
Crushed "13.2 mm" & "26.5 mm" rock (hornfels)			Not available
Crushed "53 – 73 mm" rock	840 (30)	4.0	Jones, 2003

The specific heat capacity of the dolerite was estimated at higher temperatures from the measured value in Table 14 and the correlation of Waples and Waples (2004). A curve was fitted for the range from 50 – 550 °C:

$$c_p = -0.00129T_p^2 + 1.518T_p + 748 \quad \textbf{(78)}$$

where T_p is in degrees Celcius and the units of c_p are J/kgK.

5.5 High temperature thermal tests

A high temperature facility with a stainless steel vertical packed bed test section of 1 × 1 × 1.5 m^3 (nominal internal dimensions) was constructed for tests up to 600 °C. This allows tests to be conducted at realistic rock bed temperatures, where radiation may be more significant. The layout allows the bed to be heated from the top down, and the control valves permit discharge with a reverse flow direction as shown in Figure 26. A photograph of the facility with the test section upper plenum removed is shown in Appendix D. The plenum chambers at the top and bottom are 0.5 m deep, and have a perforated grid to distribute the air flow evenly over the cross-section. The particles are supported at the bottom on a stainless steel grid (20 – 30 mm) of the type used for heavy duty walkways.

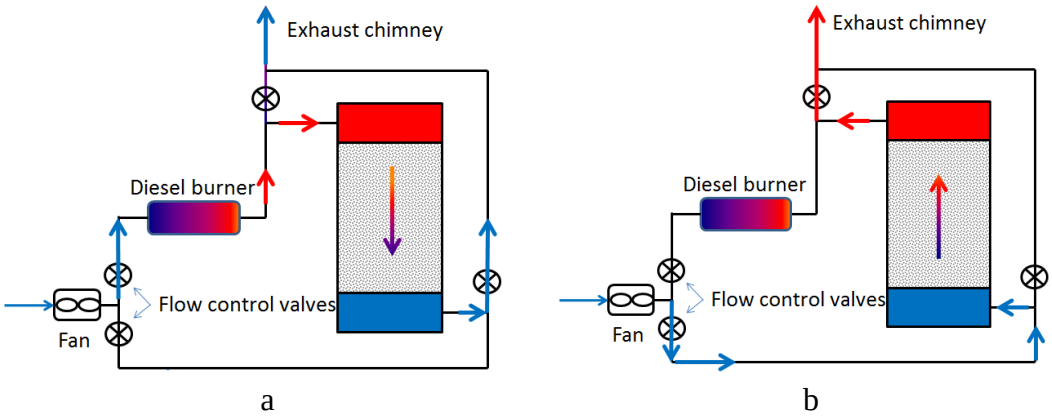

Figure 26: Charge (a) and discharge (b) flow paths of high temperature facility

Air passes through a bellmouth into the fan, which forces the air through the system. During charging, the air passes from the fan to a mixer tube surrounding a diesel burner (140 kW maximum), and then through the bed, after which it passes to the chimney, where there is an orifice flow meter. During discharging, the air from the fan bypasses the burner and is fed into the bottom of the test section, from where it flows through the packing and out to the chimney. The pressure drop over the bellmouth and orifice plate (British Standard 1042) is measured by means of Endress + Hauser PMD75 0 – 3 kPa transducers, calibrated in the same way as those in the low temperature wind tunnel.

The bellmouth and the orifice plate allow flow rate measurement at the inlet and the outlet, which can be used to check for leaks in the system. The consumption of diesel fuel is also measured, so the additional mass flow rate from the burner can be taken into account. For these tests, it was typically of the order of 0.5 – 1 % of the air flow.

The air temperature is measured with K-type sets of six thermocouples in perforated metal tubes (see also Adebiyi *et al.*, 1998). Two sets are at the top and bottom plenums, immediately adjacent to the rock. Three sets are placed inside the bed at varying heights. The measurements from a set of six thermocouples are combined and presented as an average temperature. The tubes allow the thermocouples to be withdrawn radially to measure the radial temperature profile, but they are sealed with a flexible sealant to prevent air escaping from the test section. This is particularly useful at steady state to estimate the thermal loss through the test section wall. Tests at higher temperatures would require more shielding for radiation, for example the double-shield gas-suction system used by Reboussin *et al.* (2005). The positioning of the layers is shown in Figure 27.

For the highest temperature test conducted (530 °C - Figure 81), during charging, the combined average of the time-averaged difference in temperature between each individual thermocouple and the associated layer temperature was 5 °C.

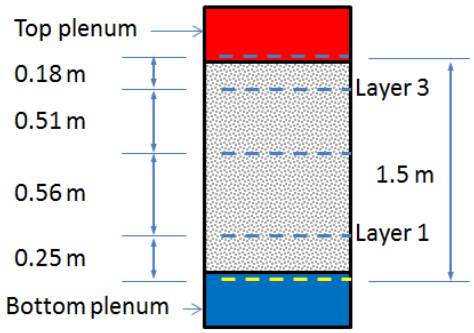

Figure 27: Thermocouple positions

The inlet temperature to the bed is controlled by turning the diesel burner on and off. This leads to an oscillating temperature profile, despite the fact that there is a thermal damping mass between the burner and test section inlet. It is necessary to calculate a moving average temperature for plotting and as input to the E-NTU method.

The stainless steel test section is internally lined with ≈ 10 mm thick insulation to allow the particles to bed into the walls, and to reduce thermal losses. The outside of the test section is insulated on all sides with 50 mm rock wool and stainless steel reflective panels. An additional 100 mm layer is added to two sides to reduce thermal losses at low flow rates.

During initial charging tests, the moisture in the combustion gases condensed in the bed at temperatures of 30 – 40 °C (see also Willits *et al.*, 1985). This caused noticeable deviations in the air temperatures, particularly at the outlet, as shown in Figure 28. In order to avoid this, the bed was pre-heated to a uniform temperature of 50 °C before the tests were commenced.

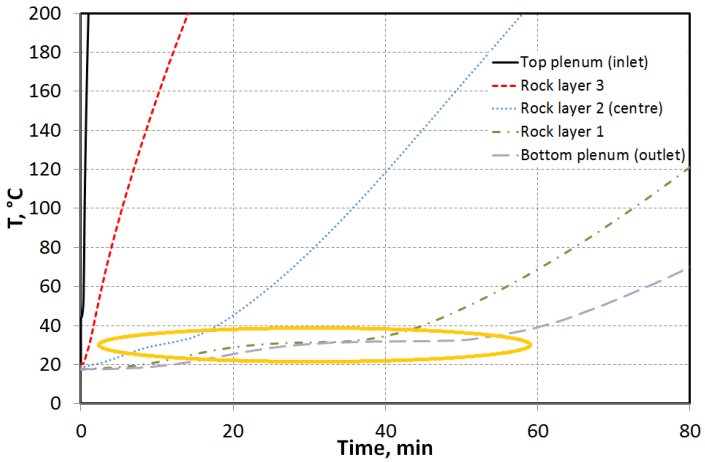

Figure 28: Condensation of moisture from combustion gases during charging

5.6 Error and uncertainty

5.6.1 Pressure drop

The Betz manometer minor divisions are 2 Pa, which allows readings to an accuracy of ± 0.5 Pa. For some measurements, a Betz with divisions of 1 Pa was available. Comparison between all of the calibration curves (a time-span of more than a year) for the 0 – 2500 Pa Endress + Hauser pressure transducers, which give a voltage output sensitive to ambient temperature, shows a standard deviation of approximately 0.5 Pa at a pressure of 10 Pa increasing linearly to 6 Pa at the upper limit, 2500 Pa. The Foxboro transducer was more inaccurate, with a standard deviation of 4 Pa at 10 Pa, increasing roughly linearly to 21 Pa at 5000 Pa, the maximum pressure at which measurements were taken.

New calibration curves were obtained at regular intervals throughout the testing program, so the maximum error should be less than 1 Pa.

5.6.2 Particle and packing characteristics

The standard deviation of the test section dimension measurements varies between 0 – 3 mm for transverse dimensions, depending on whether or not a wall lining was used, and 0 – 1 mm for the flow length. The standard deviation of the cylinder and cube dimensions is less than 0.2 mm. That of the spheres is less than 0.3 mm. The value of $\Sigma V_p/\Sigma A_p$ calculated from the ellipsoid approximation of the acorns is about 3 % lower than that obtained from a sample three dimensional (3D) scan. The total rock volume from the 3D scans is on average within 3 % of that measured by volume displacement in water. The scanner is specified to measure to within 0.2 – 0.3 mm for the range in which the particles were measured. However, the post-scan processing is probably only accurate to the order of 1 mm as a consequence of trimming edges and aligning multiple scans.

The influence of the grate at the entrance and exit of the low temperature test section was estimated by measuring the pressure drop over the empty test section. The pressure drop over the empty test section was negligible (< 0.1 – 1 %) in comparison to that measured with packing at any given mass flow.

5.6.3 Test facility measurement: overall uncertainty

The low temperature wind tunnel measurement system is capable of measuring the flow rate to within 2 % in the range for which the equations of Kröger (2004) are valid. The tunnel was checked for leaks by blocking the inlet and turning the fan on while measuring the flow rate. Leakage was negligible relative to the pressure drop and mass flow characteristics at which the tests were performed. Sample plots showing the overall uncertainty of f_{da} (due to error propagation) are given in Appendix E. The shown uncertainties without the use of a wall liner are ± 10 – 15 % for most of the measurements. At low flow rates and pressure drops near the limitations of the measurement capabilities, the uncertainty exceeds 20 % and in extreme cases 30 %. The calculated uncertainty for the acorns was an exception, ranging from 20 – 30 % in the high flow region and exceeding 40 % in the low flow region. This was predominantly caused by the large uncertainty of the void fraction.

The near-wall temperature at the outlet was consistently lower than the temperature nearer the centre of the duct, which indicated the presence of thermal losses. Thermocouples near the walls which were more than 2 °C lower than the average of the other thermocouples at steady state were excluded from the average outlet temperature. A minimum of fourteen thermocouples were used in calculating the average to ensure that the temperature was representative of the cross-section. Bare thermocouple junctions were used at the inlet to the bed, as the thermal inertia of 3 mm diameter probes caused them to lag the temperature by 1 – 3 minutes at the low mass flow rates at which the tests were conducted.

The high temperature facility was checked for leaks by blocking the outlet pipe and pressurizing it from the fan to the outlet valve. There was a leak through the fan axle (1 – 2 % of the total mass flow), which was measured as a function of fan outlet pressure and used to correct the flow rate. The remainder of the system had a loss of less than one percent. With the fan loss and diesel fuel combustion addition to the mass flow taken into account, the bellmouth and orifice plate mass flow rates differed during charging and discharging on average by 1 %, provided that the valve stems were sealed each time the valve settings were changed.

The difference in mass flow rate between the orifice plate and bellmouth was 2.8 % during charging for the first thermal test of those presented (250 °C – Figure 73). This difference was thought to be caused by leakage along the valve stems. For subsequent tests, the valve stems were resealed with tape each time they were used.

5.6.4 E-NTU numerical method

Timesteps of less than 1 s and segment lengths (Δx) of less than 20 mm were found sufficient for the convergence of the predicted temperature profiles for the charge-discharge tests.

To ensure that energy was conserved by the E-NTU method, the incremental energy transferred from/to the air stream and the particles was summed and compared with analytical values calculated by integrating the specific heat capacity curve for the rock (Eq. (78)) and air (from Incropera *et al.*, 2007) as a function of temperature. For the highest temperature test (530 °C) the difference between the maximum and minimum of these values was less than 0.05 % (5×10^{-4}) of the total energy transferred (timesteps of 1 s and Δx = 10 mm).

6 Experimental results: pressure drop and heat transfer

This chapter presents the isothermal friction factors calculated from pressure drop measurements over packed beds of spheres, cubes, cylinders, ellipsoids and rocks (see Allen *et al.*, 2013a). Temperatures measured during low and high temperature thermal tests are compared with predictions using the E-NTU method and existing heat transfer correlations. Correlations to predict the friction factors and heat transfer coefficients in packed beds of crushed rock are formulated.

6.1 Friction factor measurements[4]

6.1.1 Spheres

Present measurements for randomly packed smooth spheres (marbles) are compared with the data of Kays and London (1984) in Figure 29. Friction factors are shown for seven tests, some of which were conducted with the wall liner discussed in section 5.3.

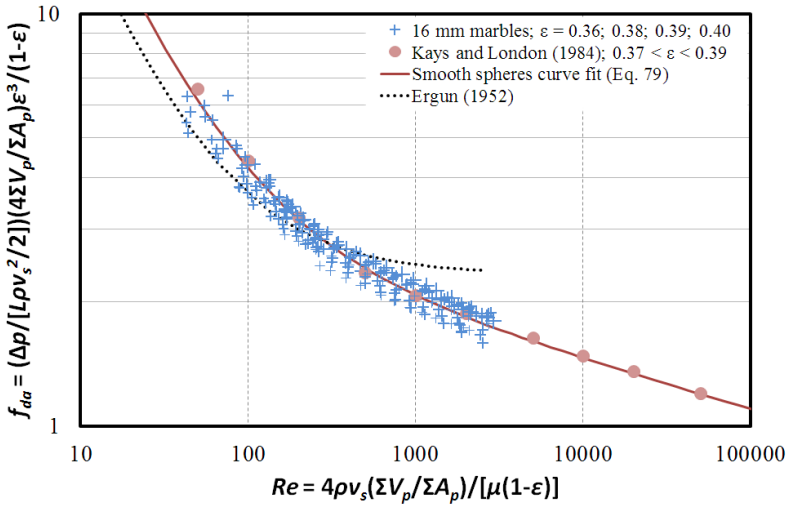

Figure 29: Friction factor for randomly packed smooth glass spheres

The smooth spheres curve in Figure 29 is

$$f_{da} = \frac{\Delta p}{L(\rho v_s^2/2)} \frac{\varepsilon^3}{(1-\varepsilon)} \frac{4\Sigma V_p}{\Sigma A_p} = \frac{172}{Re} + \frac{4.36}{Re^{0.12}} \qquad \textbf{(79)}$$

The coefficient of determination (R^2) is 0.95, including the data of Kays and London (1984). Eq. (79) for smooth spheres is compared with some of the other

[4] Most of the work in this section was published in Allen *et al.* (2013a)

correlations from the literature in Figure 30. For Re < 500, it is almost indistinguishable from the equation of Montillet *et al.* – Eq. (12) – for D_c/D = 16, the value if D_c is taken as the hydraulic diameter of the test section. For Re > 300, Eq. (79) is similar to the equations of Carman (Eq. (6)) and Jones and Krier (Eq. (10)). It is plotted in all further graphs to provide a common basis of comparison for the other measurements presented.

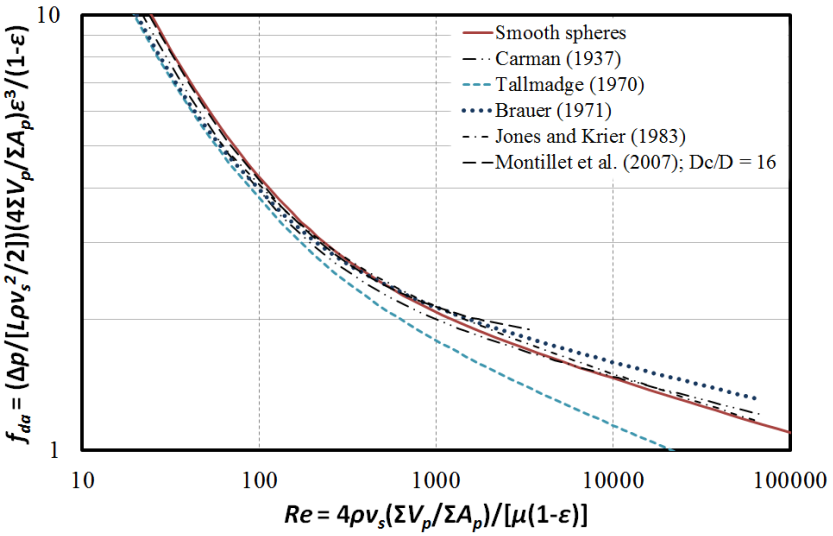

Figure 30: Comparison of Eq. (79) with other correlations for randomly packed beds of smooth spheres

Measured values of f_{da} for structured arrangements of smooth spheres (see Figure 23 for the arrangement) are compared with those for random packing in Figure 31. The simple cubic packing differs less (up to 30 %) from the randomly packed data than the data of Martin *et al.* (1951) shown in Figure 14, section 3.1.5.

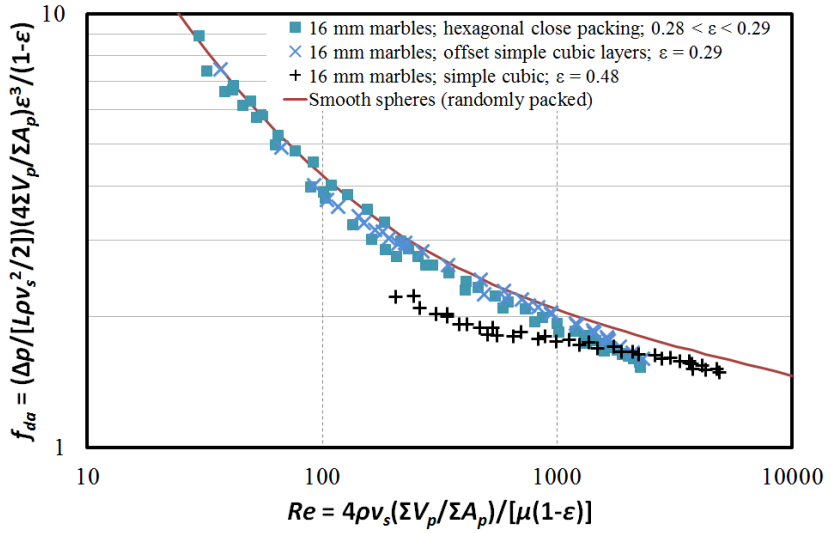

Figure 31: Influence of structured packing on friction factor (smooth spheres)

For Re > 600, the slope of f_{da} steepens as the void fraction decreases from 0.48 to 0.28. It is possible that the steeper slope of f_{da} for the lowest void fractions may be linked to the structure of the packing: for low void fraction, the flow is forced to follow the surfaces of the particles more than for high void fraction. If so, in dense packings, form drag is reduced and surface friction losses are higher, whereas, in low density packings, the reverse is true.

The influence of mixed particle sizes and roughness is shown in Figure 32 for random packing. Neither size mixture significantly altered f_{da} from that of single-sized spheres (< 9 %). However, the surface roughness, for both sand grain sizes, increased f_{da} by up to 20 – 45 % of the value for smooth spheres. At low Re (< 100), the friction factors appear to tend towards those obtained for smooth spheres. This trend is consistent with pipe flow under low Reynolds number laminar flow conditions, where surface roughness has no effect on the apparent friction factor.

If the additional surface area due to particle roughness were included in the calculation of f_{da} and Re, the values of both would reduce and the data would move towards the origin on both axes. This would reduce the apparent increase in friction factor relative to smooth spheres.

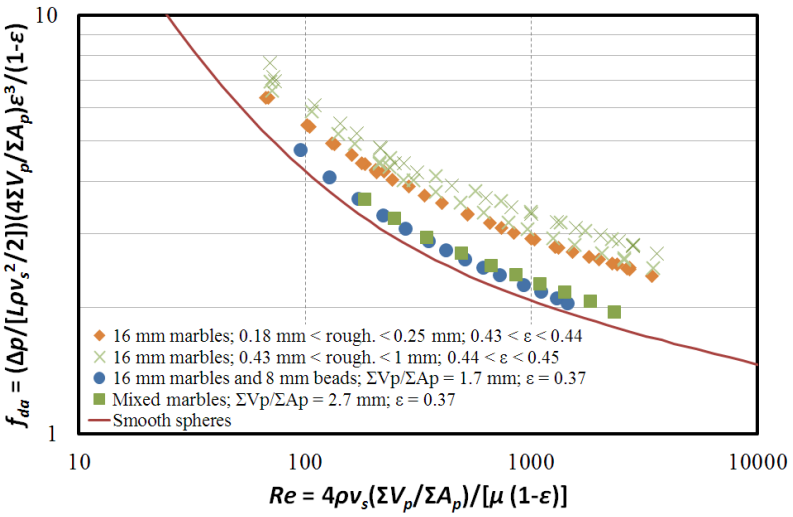

Figure 32: Influence of particle roughness and size distribution (spheres)

Jordi and Young (1990) are of the opinion that including the additional area from particle roughness is not sufficient to explain the friction factor increase in packed beds. This is based on the work of Crawford and Plumb (1986), who showed that including the additional area allowed for reasonable agreement of the friction factor at low Reynolds numbers, but did not eliminate deviations at higher Reynolds numbers. Jordi and Young propose that this is due to finer surface detail becoming relevant at higher Reynolds numbers, which would not be important at low Reynolds numbers because of the boundary layer thickness.

Small spheres only pack into the voids between large spheres if the diameter ratio is greater than about 3:1 (Dullien, 1979). The beads were only half the diameter of the marbles, so these results do not reflect the friction factor characteristic which could be obtained in such a case.

6.1.2 Non-spherical, symmetric particles

The influence of particle shape and alignment for smooth ellipsoids (acorns) is shown in Figure 33.

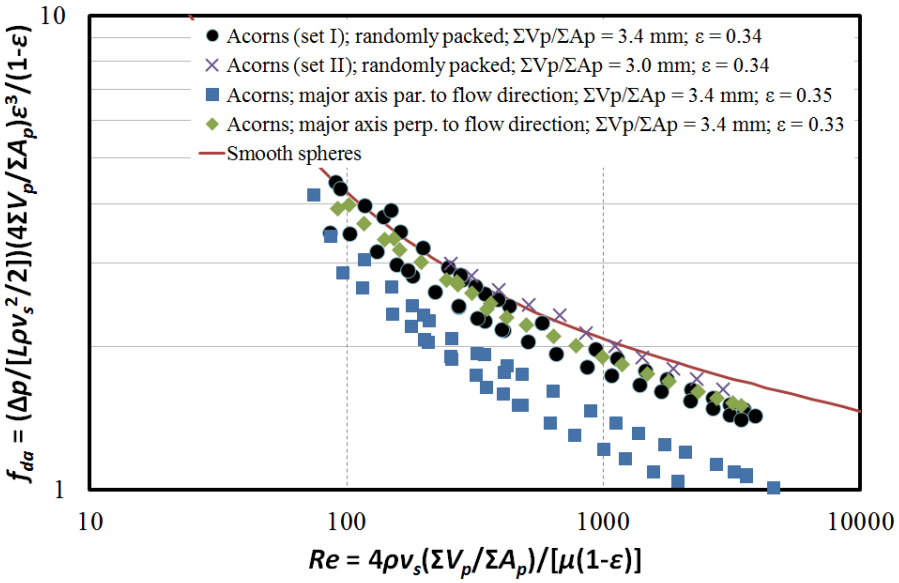

Figure 33: Influence of shape and packing arrangement (acorns – ellipsoids)

The alignment of the acorns with the major axis approximately parallel to the flow direction resulted in values of f_{da} as much as 30 – 40 % lower than the other arrangements. They are also lower than those for spheres, which is consistent with the CFD predictions of Yang *et al.* (2010). The relatively poor repeatability for the aligned acorns is probably because of different acorn sizes disturbing the packing arrangement and alignment. The acorns in random packing give f_{da} values similar to those for randomly packed smooth spheres. These results show that void fraction and particle size alone are not sufficient to describe a packed bed accurately if the particles are non-spherical and aligned in a particular direction.

The influence of particle shape is seen in Figure 34 for randomly packed beds of cubes and cylinders. The f_{da} values for the cubes and cylinders are respectively up to almost 200 % and 100 % higher than those for smooth spheres. To ensure that there were no entrance or exit effects influencing the measurements, an additional test was conducted with the wooden cubes in a longer test section with $L/D \approx 31$, the measurements of which are also shown. If the reduction in particle surface area (caused by particle overlap) exposed to the flow were included in the

calculation of f_{da} and Re, the values of both would increase and the data points would move further away from the origin and the smooth sphere data.

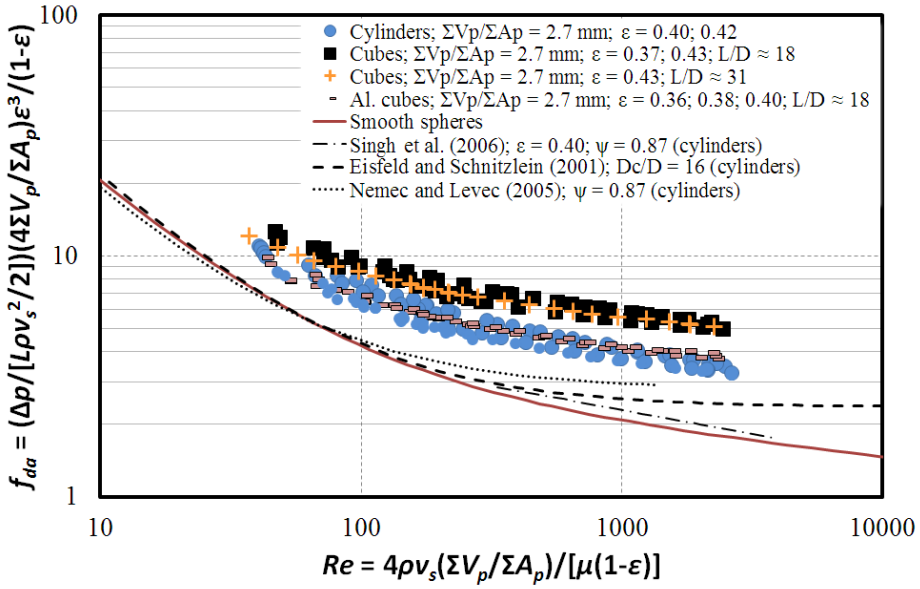

Figure 34: Friction factor for wooden cubes and cylinders, and aluminium cubes

The friction factors for the wooden cubes are 10 – 30 % larger than those for the aluminium cubes. This may be caused by surface roughness: the average roughness of a wooden cube was measured as 7 μm (ranging from 4.4 – 9.5), and an aluminium cube as 3 μm (0.75 – 1.4 on the supplied surface).

If the duct flow analogy is used, D = 16 mm and ε = 0.4, the duct diameter $D_h = 4V_v/A_p$ = 7.1 mm. This gives e/D_h values of 0.001 and 0.0004 respectively for the wood and aluminium. For turbulent flow, Darcy pipe friction factors from the Moody chart are 0.0195 and 0.016 – the wooden 'pipe' friction factor is 22 % larger than the aluminium. So it is possible that the difference may be caused by particle roughness. However, the marble roughness with sand particles was higher (e/D_h = 0.01 – 0.04) relative to smooth marbles (e/D_h = 0) and the measured friction factors were 15 – 40 % higher than those for smooth glass. Following the Moody chart analogy, higher friction factors would be expected for the higher roughness ratio of the rough marbles compared to the aluminium/wood.

6.1.3 Crushed and rounded rock

The friction factors for three sets of crushed rock and the rounded marble are shown in Figure 35. They were packed through the test section lid in a cross-current direction relative to the air flow. The values of f_{da} are up to 40 % more than the smooth sphere curve. Even though the rounded rock did not have sharp edges, its measurements lie between those of the crushed rock.

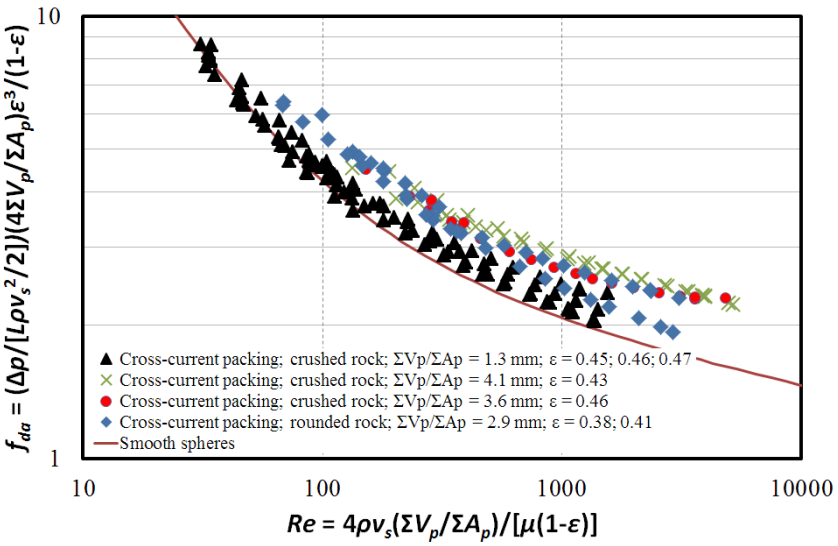

Figure 35: Cross-current packing friction factors for crushed and rounded rock

The friction factors for the crushed rock packed in co/counter-current and cross-current directions relative to the air flow are compared in Figure 36. Friction factors for the co-current packing are up to 35 – 70 % more than those for cross-current packing for the same rock, and as much as 120 % more than those for smooth spheres.

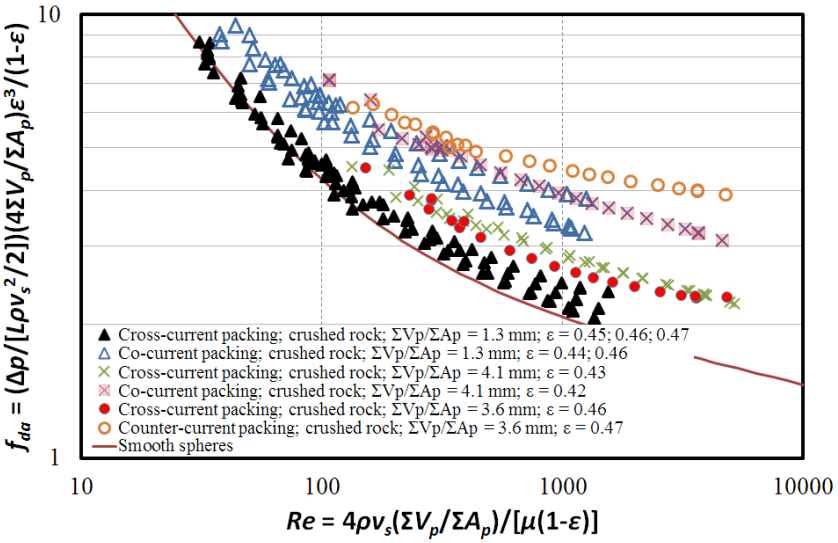

Figure 36: Comparison of friction factors for the two different packing directions

It is suggested that, because the crushed rock is asymmetric, it tends to align during packing so that the larger areas are parallel to the bottom of the test section; that is, irregularly shaped particles poured in the presence of gravity will not form an isotropic packing arrangement. This would result in the larger cross-sectional area of the rock particles obstructing flow when packed in a co-current direction relative to the air flow, which could cause a higher form drag and f_{da}. At

low *Re* in the viscous flow region, particle form drag is negligible relative to surface friction, so the difference in f_{da} would reduce with reducing *Re*, until the measurements converge, provided the duct shape is not particularly different. This appears to be the case for the smallest ($\Sigma V_p/\Sigma A_p$ = 1.3 mm) crushed rock, which could be tested to lower values of *Re* than the larger rock.

The packing alignment effect is visibly discernible for a single layer of rock on a surface (Figure 25f), but not for further layers. Discrete element modelling (DEM) by Nel (2013) indicated that the rock particles tended to align with the major axis at an average of about 25° to the container floor.

This explanation is consistent with the measurements for acorns (Figure 33) and previous work by Coulson (1949), Tobiś (2000) and Mayerhofer *et al.* (2011) which has shown that particle alignment influences friction factor. It may be that this effect explains (to some extent, at least) the variability in rock bed pressure drop tests recorded in the existing literature.

6.1.4 Conclusion

The Ergun equation should not be used for pressure drop prediction in packed beds of smooth spheres where $Re_{Erg} > 700$, as it over-predicts the pressure drop. It is not suitable for predicting pressure drop over packed beds of rock or other non-spherical particles like cylinders or cubes, as the measured values can differ from the Ergun equation by as much as 100 % or more.

The friction factor of a packed bed has been shown to change significantly (of the order of 10 – 100 %) from that of randomly packed smooth spheres, depending on particle shape, roughness and packing arrangement. A variation in the particle size ratio of spheres of almost 40 % by the addition of spheres of half the diameter did not result in much deviation of f_{da} from that of spheres of a single size. The change in f_{da} relative to the value for smooth spheres is summarized in Table 16.

Table 16: Varying f_{da} caused by shape, roughness, arrangement and size distribution

Particle type	% Increase in f_{da} relative to smooth spheres	
	$50 < Re < 100$	1900 < Re < 2300
Cubes (wooden)	85 – 90	180 – 185
Cylinders	50 – 55	95 – 100
Acorns, parallel	-25 to -30	-35 to -45
Acorns, perpendicular/random	-10 to -15	-10 to -15
Mixed spheres	5 - 10	5 - 10
Rough spheres	25	40 - 45
Cross-current rock	0 - 15	0 – 40
Co/counter-current rock	15 – 50	40 – 120

In the case of irregularly shaped particles, the friction factor is dependent on the packing method, which presumably alters the packing arrangement. Random packing of irregularly shaped particles is not necessarily isotropic, as shown by the crushed rock packed in a co-current direction relative to the air flow, which gave rise to apparent friction factors up to 80 % higher than those obtained from the same rock packed in a cross-current direction. The direction in which the particles are packed into the test section relative to the flow must be stated for all experimental work. This should be taken into consideration in the design and construction of commercial systems.

Curve fits for some of the data are given in Table 17. They are only valid for the range of *Re* in which measurements were made.

Table 17: Friction factor curve fit constants for $f_{da} = (a_1/Re) + (a_2/Re^{a_3})$

Particle type and packing description	a_1	a_2	a_3	R^2
Wooden cubes (random)	200	10.8	0.1	0.94
Wooden cylinders (random)	192	8.8	0.12	0.94
Rough spheres (random)	185	6.5	0.12	0.97
Acorns (parallel to flow)	150	3.25	0.15	0.96
"13 mm" crushed rock, $\Sigma V_p/\Sigma A_p$ = 1.3 mm (co-current, random)	180	7.5	0.12	0.97
"13 mm" crushed rock, $\Sigma V_p/\Sigma A_p$ = 1.3 mm (cross-current, random)	180	4.8	0.12	0.97
"26.5 mm" crushed rock, $\Sigma V_p/\Sigma A_p$ = 4.1 mm (co-current, random)	200	8.4	0.12	0.97
"26.5 mm" crushed rock, $\Sigma V_p/\Sigma A_p$ = 4.1 mm (cross-current, random)	200	6.0	0.12	0.97
"26.5 mm" crushed rock, $\Sigma V_p/\Sigma A_p$ = 3.6 mm (co-current, random)	240	6.3	0.06	0.98
"26.5 mm" crushed rock, $\Sigma V_p/\Sigma A_p$ = 3.6 mm (cross-current, random)	240	3.7	0.06	0.95
Rounded rock, $\Sigma V_p/\Sigma A_p$ = 2.9 mm (cross-current, random)	210	6.5	0.15	0.97

For crushed rock, which may vary from quarry to quarry, or even within a quarry where the rock is not homogeneous, it is not possible to take the various factors such as roughness and shape into account. In order to predict the pressure drop over a large packed bed with reasonable certainty, a correlation should be obtained from a sample test with the particular material and packing method.

As shown by the duct analysis (Appendix A), the appropriate dimension for the flow channel is obtained from the ratio of the total particle volume to surface area in the packed bed, not the diameter of a volume-equivalent sphere. For rough particles, this raises the question as to which scale and degree of accuracy the

surface area should be based on. The results in this work are based on surface dimensions to the order of 0.1 – 1 mm, as limited by the measurement equipment .

6.2 Prediction of rock bed friction factor

Since the proposed operating range of the packed bed will be for Reynolds numbers of the order of 100 - 500, calculated from Biot number constraints (see section 7.4.3), the range in which the friction factor must be known can be narrowed. The measurements for crushed and rounded rock are plotted for co/counter-current flow in Figure 37 (see Appendix F for a plot of all data over the full range of flow rates), and for cross-current flow in Figure 38. The smooth sphere correlation (Eq. (79)) is included for comparison purposes. A data set obtained for the "53 – 73 mm" ballast (crushed dolerite), obtained under isothermal conditions from the high temperature test facility, is shown in addition to the data from the low temperature test facility.

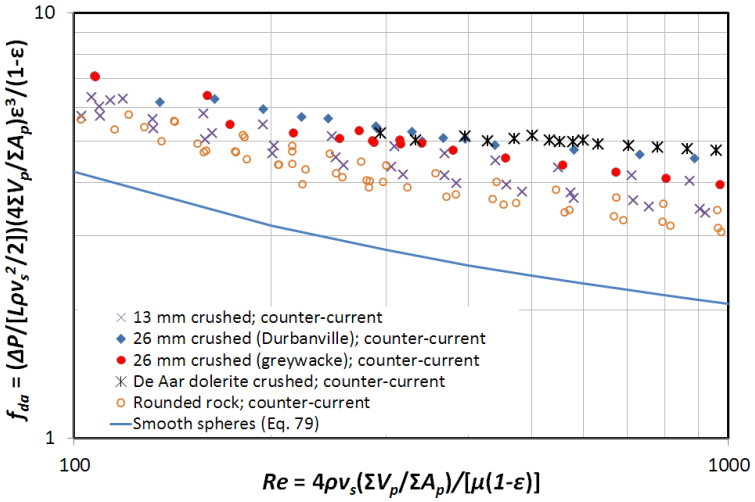

Figure 37: Limited Reynolds number plot, all rock (co/counter-current)

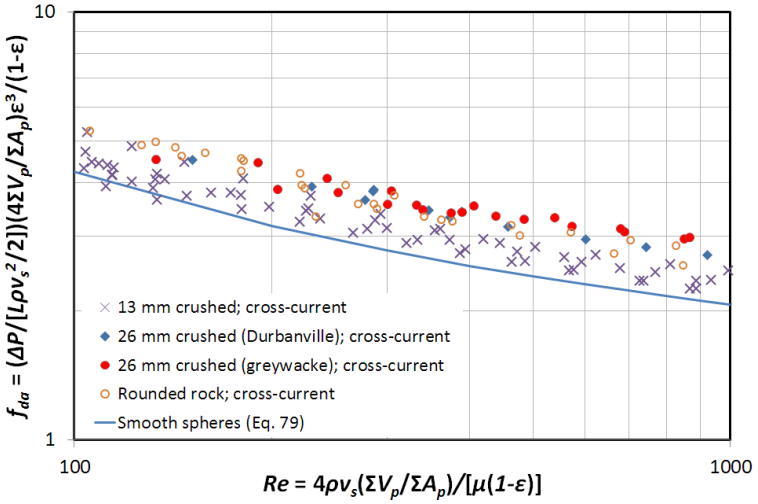

Figure 38: Limited Reynolds number plot, all rock (cross-current)

For use in the field, where the rock surface area cannot be easily or quickly measured, it is preferable to use the average volume equivalent sphere diameter of a sample of rocks, which is defined for a sample of *n* particles as

$$D_v = \left(\frac{6}{\pi} \left[\frac{1}{n} \sum_{i=1}^{n} V_{pi} \right] \right)^{1/3} \quad \textbf{(80)}$$

Co/counter current measurements are plotted in Figure 39 in terms of D_v.

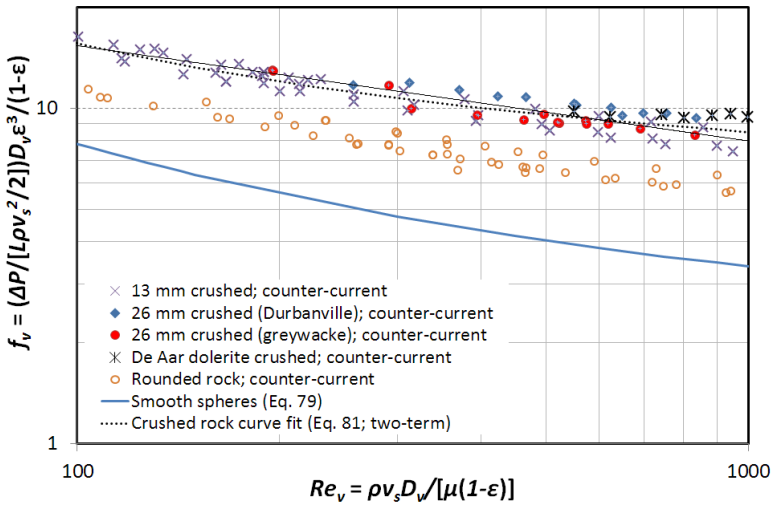

Figure 39: Limited Reynolds number plot for crushed and rounded rock (co/counter-current; D_v)

The curve fitted through the 13 mm and 26 mm crushed rock measurements in Figure 39 is

$$f_v = \frac{\Delta p}{L(\rho v_s^2/2)} \frac{\varepsilon^3}{(1-\varepsilon)} D_v = \frac{620}{Re_v} + \frac{13.7}{Re_v^{0.08}} \approx \frac{56.6}{Re_v^{0.284}} \quad \textbf{(81)}$$

For the shown range in Figure 39, all the crushed rock measurements (including the dolerite) are within 15 % of the two-term correlation (R^2 = 0.93). The correlation may be expressed in terms of a volume-equivalent particle Reynolds number:

$$f_v = \frac{\Delta p}{L(\rho v_s^2/2)} \frac{\varepsilon^3}{(1-\varepsilon)} D_v \approx 56.6 \left(\frac{1-\varepsilon}{Re_{pv}} \right)^{0.284} \quad \textbf{(82)}$$

where R^2 = 0.88 and

$$Re_{pv} = Re_v(1-\varepsilon) = \frac{\rho v_s D_v}{\mu} \quad \textbf{(83)}$$

Eq. (82) should only be used for co/counter-current packing of crushed rock where $0.38 < \varepsilon < 0.45$, $0.009\text{ m} < D_v < 0.045\text{ m}$; $50 < Re_{pv} < 500$; $\psi \approx 0.8$.

The cross-current measurements are plotted in Figure 40 in terms of D_v:

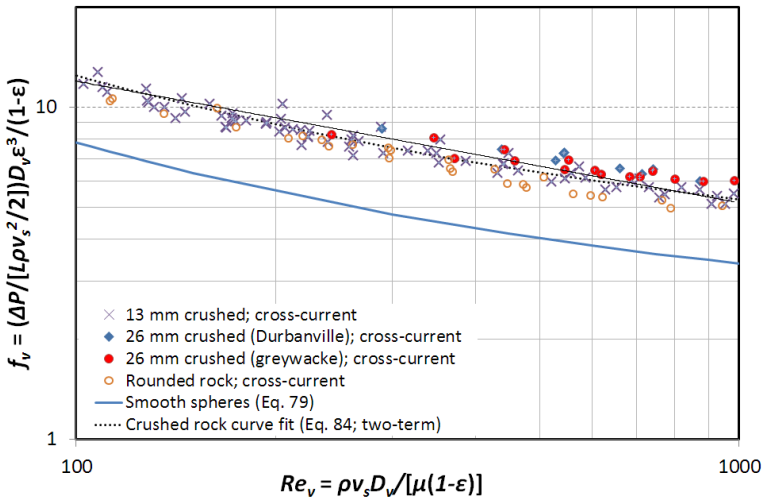

Figure 40: Limited Reynolds number plot for crushed and rounded rock (cross-current; D_v)

The curve fitted through the 13 mm and 26 mm crushed rock measurements is

$$f_v = \frac{\Delta p}{L(\rho v_s^2/2)}\frac{\varepsilon^3}{(1-\varepsilon)}D_v = \frac{600}{Re_v} + \frac{12.3}{Re_v^{0.14}} \approx \frac{64.4}{Re_v^{0.366}} = 64.4\left(\frac{1-\varepsilon}{Re_{pv}}\right)^{0.366} \quad \textbf{(84)}$$

which is valid for $0.38 < \varepsilon < 0.45$, $0.009\text{ m} < D_v < 0.030\text{ m}$; $50 < Re_{pv} < 500$. For the two-term correlation, $R^2 = 0.96$; for the single term approximation, $R^2 = 0.92$.

Equations (81) and (84) were obtained under isothermal conditions. In non-isothermal conditions in a vertical flow bed with a significant temperature difference over it, there will be a buoyancy-related pressure term. Zanganeh *et al.* (2012) made use of a buoyancy term from Andersen (2003):

$$\Delta p_B = \rho g L \frac{\Delta T}{T} \quad \textbf{(85)}$$

ΔT is the temperature difference over length L. During charging, if the hot air enters the bed from the top, it tends to increase the pressure drop; during discharging, to decrease it.

6.3 Packed bed thermal characteristics

The low temperature test facility was used to measure temperature profiles over packed beds of differently shaped particles of different materials. The high temperature facility was used to obtain temperature profiles for the crushed "53-73 mm" dolerite at temperatures ranging between 150 °C to 530 °C.

6.3.1 Low temperature profiles

Measured air temperature profiles at the outlet of a packed bed are compared with predictions made by means of the Hughes Effectiveness-NTU method (refer to section 4.2) and the heat transfer correlations of Wakao *et al.* (1979) and Martin (2005). The inlet temperature and the mass flow rate inputs were obtained for every time-step from a curve fit to the measured values. The heat capacity of the steel grate which held the particles in the test section was included. For most particle types, this effectively increased the specific heat capacity by 10 – 15 J/kgK, 1 – 1.5 % of the particle value.

Only the discharge measurements are presented, since thermal losses into the wind tunnel should influence the discharge measurements less – the wind tunnel is at an intermediate temperature during the discharge, whereas it has to heat up from ambient temperature during charging. The initial temperature of the test section before discharging was calculated as an average of the inlet, central and outlet temperatures. For the first measurements shown (Figure 41) the combined time-averaged difference between each individual thermocouple temperature and the average inlet and outlet temperature was 0.7 °C and 0.9 °C respectively. At a higher flow rate (Figure 42) the outlet difference reduced to 0.8 °C.

The tests were conducted at Reynolds numbers ranging from $Re \approx 150 - 600$, limited by the flow measurement accuracy, and the approximate range in which rock beds are likely to be used (see Chapter 7). Tests were conducted on glass marbles (spheres), steel bearing balls, aluminium cubes, and crushed and rounded rock in both counter-current and cross-current packing. The temperature measured and predicted at the outlet is compared for each case in Figure 41 - Figure 59, at two different Reynolds numbers per packing. The measured temperature presented is the combined average of the thermocouples, as stated in section 5.6.3.

The conclusions that may be drawn from Figure 41 - Figure 59 are as follows:

- Comparison with uniform shapes (spheres, Figure 41 – Figure 44; cubes, Figure 45 – Figure 47) confirms that the temperature measurements from the test section match existing heat transfer correlations (Wakao *et al.*, 1979, and Martin, 2005).
- There is relatively little difference between the temperature profile through a packed bed of spheres and cubes, as illustrated by the measurements from

the aluminium cubes (Figure 45 – Figure 47). The correlation of Martin (2005) has a shape factor which accounts for the shape of the particles, whereas the correlation of Wakao *et al*. (1979) does not – yet the predictions made with each correlation are similar.

- The correlations of Martin and Wakao *et al.* give predicted temperatures that closely match the measured temperatures for all the rock tested, in both co- and cross-current packing orientations: the 13 mm (Figure 48 - Figure 51) and 26 mm (Figure 52 - Figure 55) crushed rock, and the rounded rock (Figure 56 - Figure 59). Particle shape and packing direction have relatively little influence on the temperature profile – unlike the case for the friction factor.
- The Jeffreson particle conductivity correction factor (Eq. (77)) was found to make a maximum difference in the predicted air temperature of 1 °C at a Biot number of 0.27, the highest value at which tests were conducted on the 26 mm crushed rock. This is 2 % of the total change in temperature of the bed, and 10 % of the temperature change which the bed had undergone at the time this difference occurs. Provided the Biot number is below 0.2, the Jeffreson correction factor is not necessary.
- The tests are for a range of Biot numbers, from less than 0.01 to more than 0.2. The variation of Biot number has no apparent influence on the temperature profile at this range of values, so it is reasonable to use rock beds at Biot numbers up to 0.2 without taking k_p into account.
- Thermal conductivity of the particles appears to have little influence on the axial thermal conductivity and heat transfer for these particular test sections. The thermal conductivity of the glass marbles is in the range of 1 – 2 W/mK, while that of the steel spheres is 60 W/mK, yet there is no obvious difference between these tests.
- The existing heat transfer correlations and Hughes E-NTU method at this temperature range adequately predict the temperature profile at the outlet of the test section for spheres, cubes, and crushed and rounded rock.

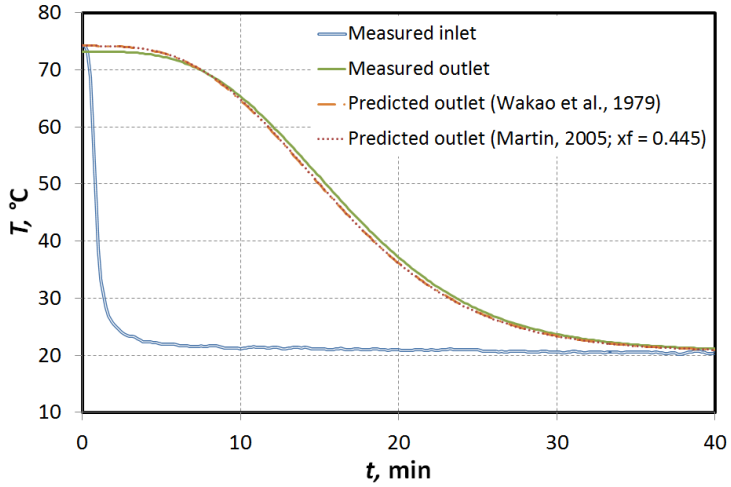

Figure 41: Marbles; avg. $Re_p \approx 350$; $Re \approx 360$; $Bi \approx 0.15$; $\varepsilon = 0.36$; $D = 0.016$ m

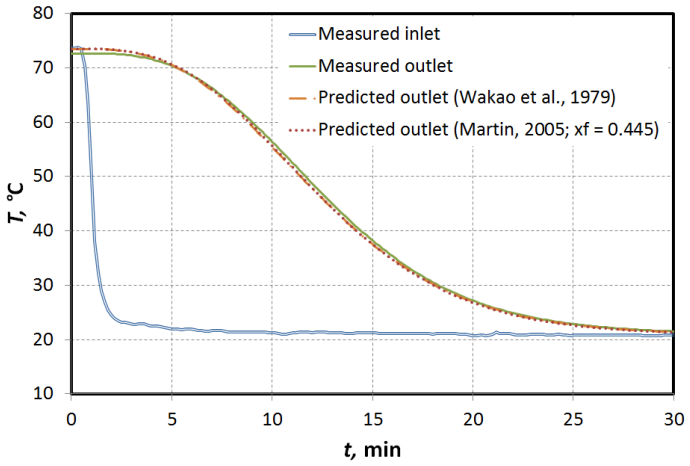

Figure 42: Marbles; avg. $Re_p \approx 470$; $Re \approx 490$; $Bi \approx 0.18$; $\varepsilon = 0.36$; $D = 0.016$ m

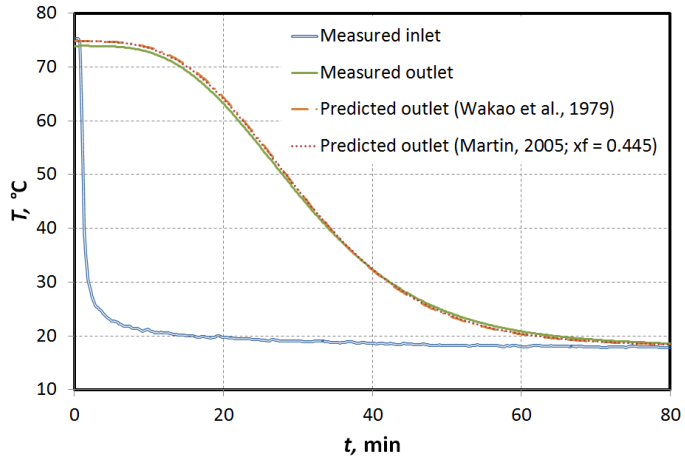

Figure 43: Steel spheres; avg. $Re_p \approx 290$; $Re \approx 320$; $Bi \approx 0.007$; $\varepsilon = 0.38$; $D = 0.016$ m

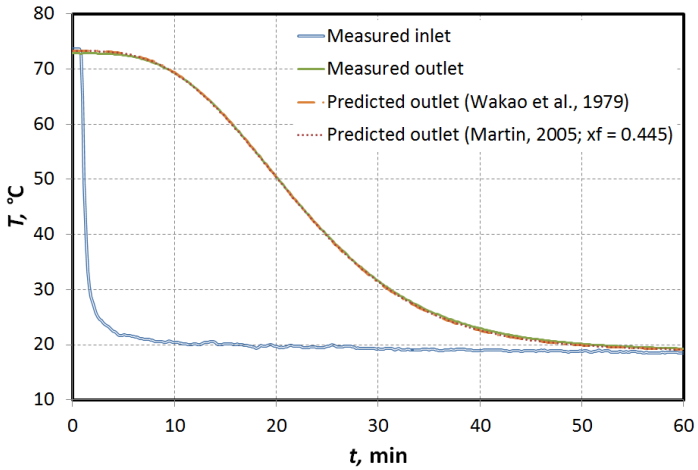

Figure 44: Steel spheres; avg. $Re_p \approx 410$; $Re \approx 440$; $Bi \approx 0.009$; $\varepsilon = 0.38$; $D = 0.016$ m

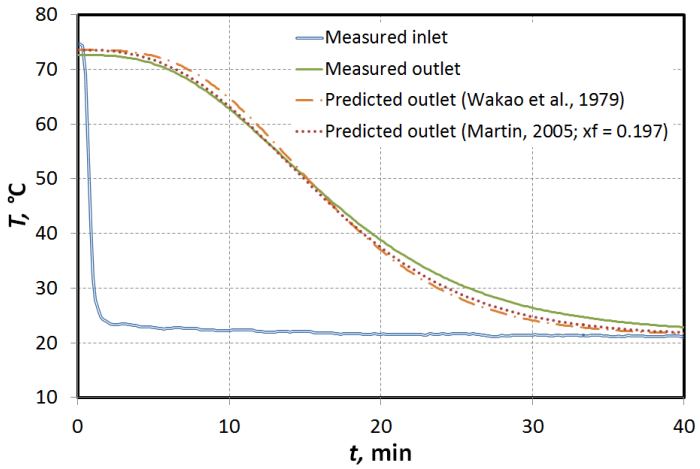

Figure 45: Aluminium cubes; avg. $Re_p \approx 440$; $Re \approx 440$; $Bi \approx 0.003$; $\varepsilon = 0.34$; $D = 0.016$ m

The difference between the measured and predicted outlet temperature in Figure 45 at $t = 0$ (see also Figure 47, Figure 52 or Figure 54) is a consequence of using the average temperature of the bed (instead of the actual temperature profile) as the initial bed temperature for the E-NTU method. The average outlet temperature was below the average inlet temperature at steady state, presumably because of thermal losses in the test section and wind tunnel. In Figure 45, the difference was 2 °C.

The correlations of Martin for cubes and spheres (x_f = 0.197 and 0.445 respectively) are compared in Figure 46. There is very little difference between the predicted temperatures, despite the difference in particle shape and friction factor. The Martin correlation is calculated with x_f = 0.197 for the rock for Figure 48 – Figure 59, as the sphericity is approximately 0.8 for the crushed rock, which is similar to the sphericity of a cube.

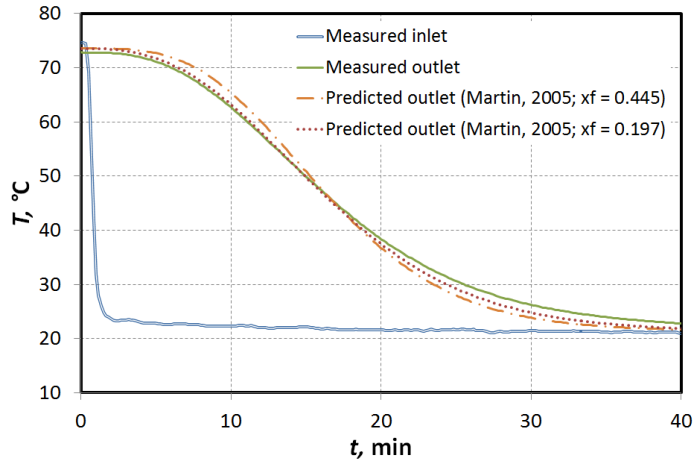

Figure 46: Aluminium cubes; avg. $Re_p \approx 440$; $Re \approx 440$; $Bi \approx 0.003$; $\varepsilon = 0.34$; $D = 0.016$ m

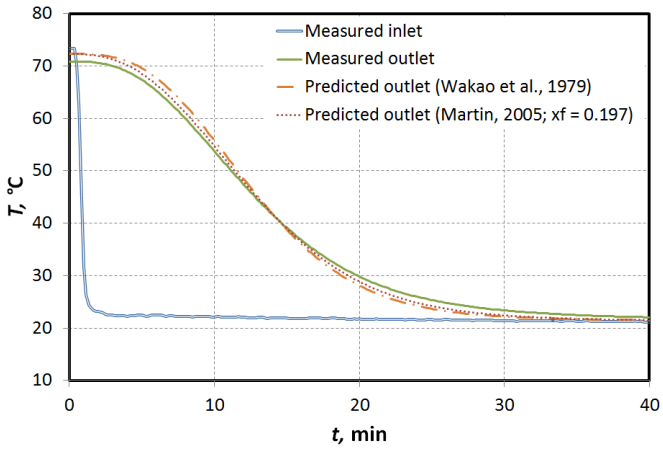

Figure 47: Aluminium cubes; avg. $Re_p \approx 580$; $Re \approx 580$; $Bi \approx 0.004$; $\varepsilon = 0.34$; $D = 0.016$ m

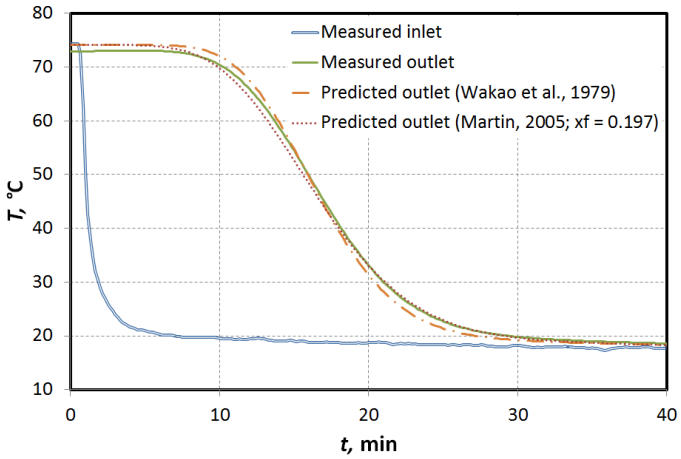

Figure 48: 13 mm rock; counter-current; avg. $Re_p \approx 160$; $Re \approx 180$; $Bi \approx 0.1$; $\varepsilon = 0.43$; $D = 0.007$ m

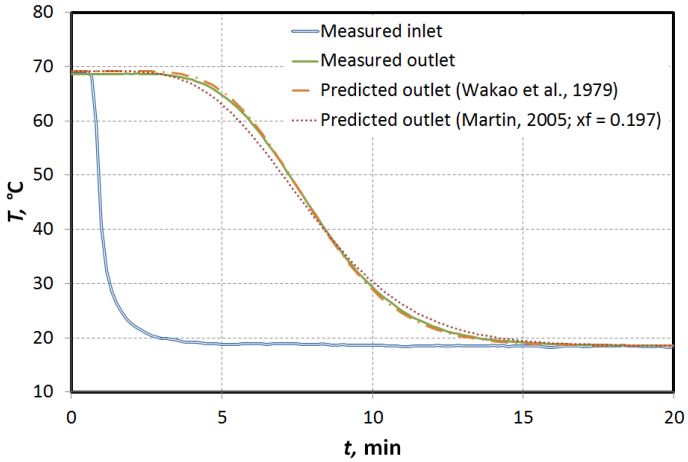

Figure 49: 13 mm rock; counter-current; avg. $Re_p \approx 350$; $Re \approx 410$; $Bi \approx 0.15$; $\varepsilon = 0.43$; $D = 0.007$ m

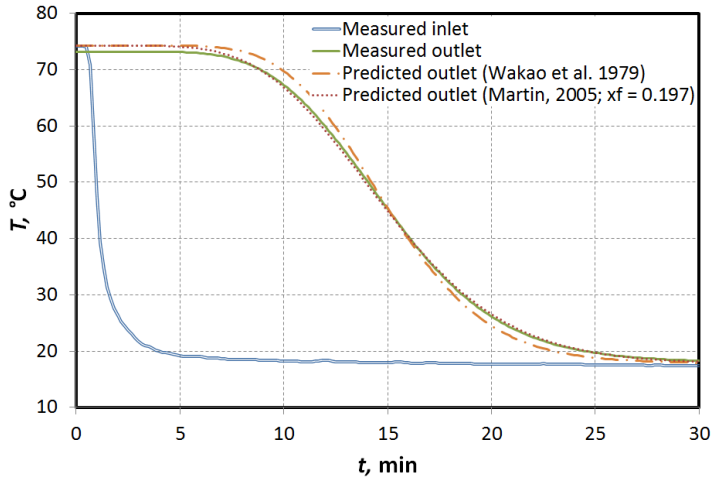

Figure 50: 13 mm rock; cross-current; avg. $Re_p \approx 180$; $Re \approx 200$; $Bi \approx 0.1$; $\varepsilon = 0.43$; $D = 0.007$ m

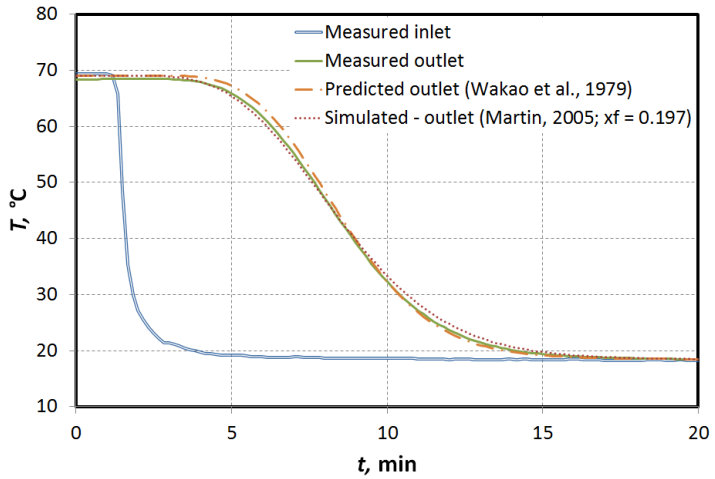

Figure 51: 13 mm rock; cross-current; avg. $Re_p \approx 350$; $Re \approx 410$; $Bi \approx 0.15$; $\varepsilon = 0.43$; $D = 0.007$ m

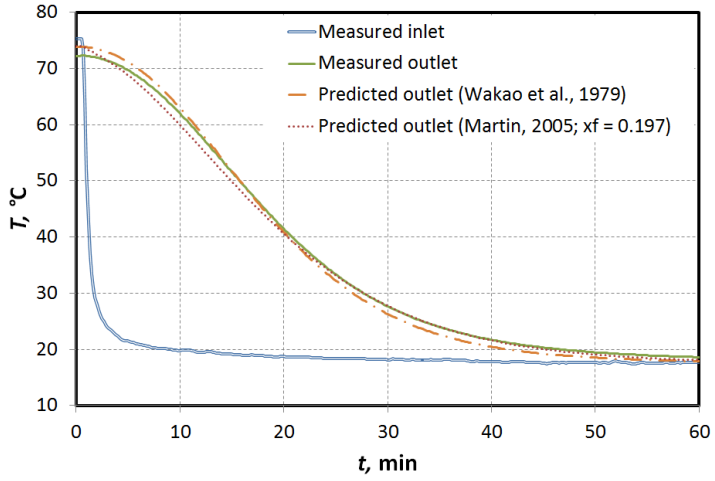

Figure 52: 26 mm rock; counter-current; avg. $Re_p \approx 440$; $Re \approx 500$; $Bi \approx 0.17$; $\varepsilon = 0.41$; $D = 0.023$ m

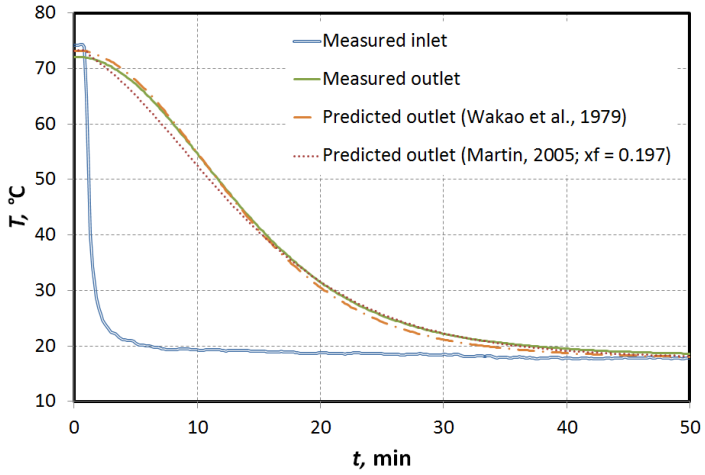

Figure 53: 26 mm rock; counter-current; avg. $Re_p \approx 600$; $Re \approx 690$; $Bi \approx 0.21$; $\varepsilon = 0.41$; $D = 0.023$ m

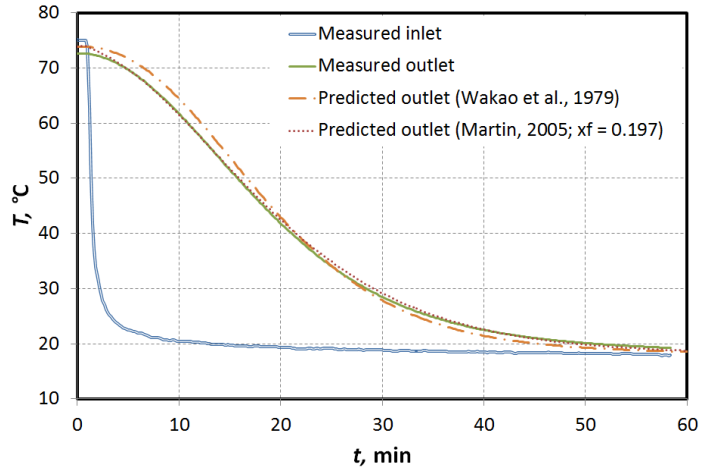

Figure 54: 26 mm rock; cross-current; avg. $Re_p \approx 430$; $Re \approx 480$; $Bi \approx 0.17$; $\varepsilon = 0.40$; $D = 0.023$ m

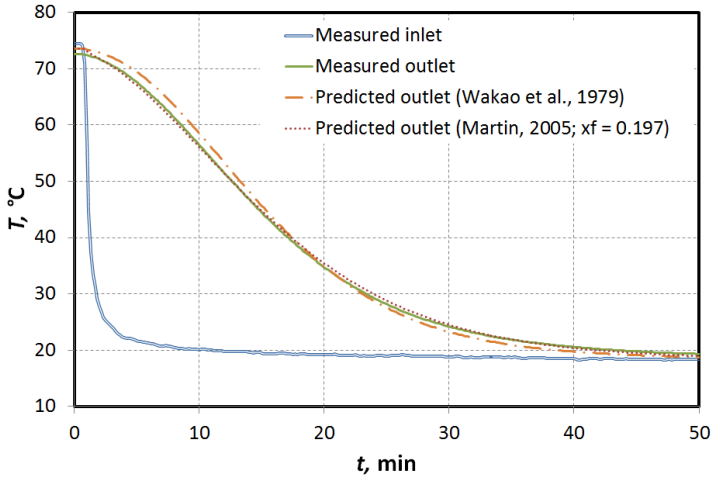

Figure 55: 26 mm rock; cross-current; avg. $Re_p \approx 540$; $Re \approx 600$; $Bi \approx 0.2$; $\varepsilon = 0.40$; $D = 0.023$ m

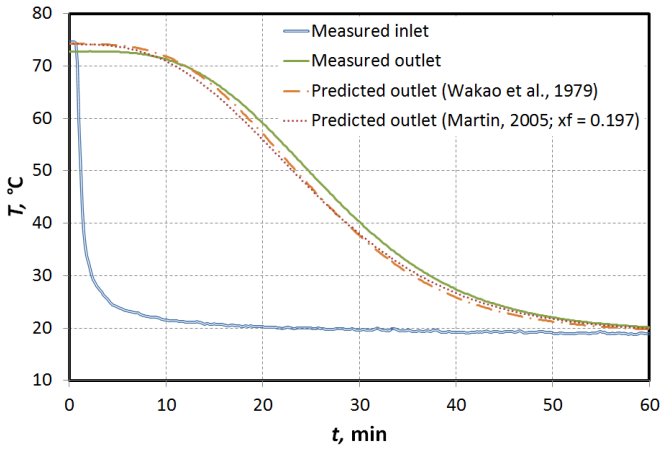

Figure 56: Rounded rock; counter-current; avg. $Re_p \approx 320$; $Re \approx 320$; $Bi \approx 0.15$; $\varepsilon = 0.33$; $D = 0.018$ m

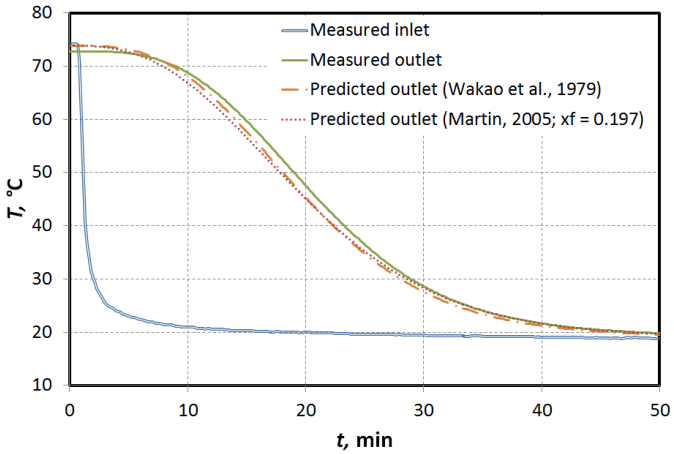

Figure 57: Rounded rock; counter-current; avg. $Re_p \approx 420$; $Re \approx 420$; $Bi \approx 0.17$; $\varepsilon = 0.33$; $D = 0.018$ m

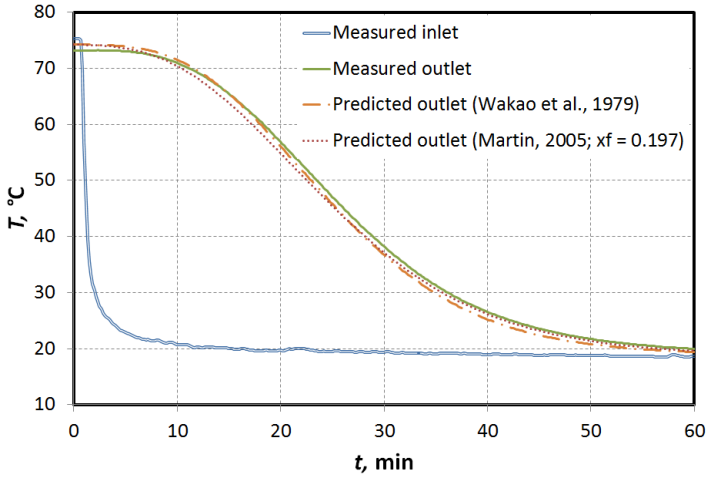

Figure 58: Rounded rock; cross-current; avg. $Re_p \approx 320$; $Re \approx 320$; $Bi \approx 0.15$; $\varepsilon = 0.34$; $D = 0.018$ m

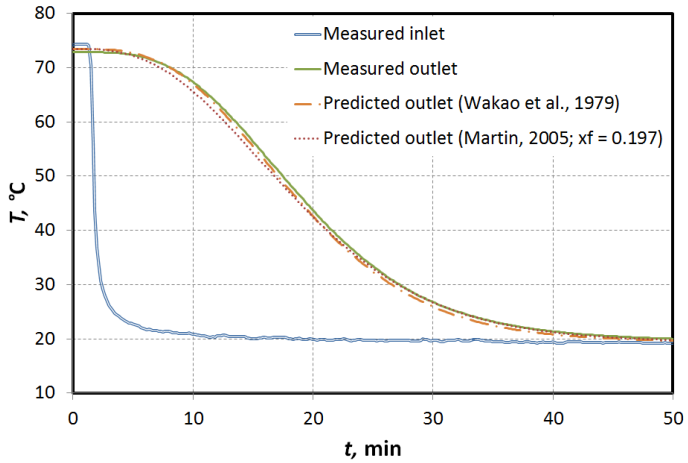

Figure 59: Rounded rock; cross-current; avg. $Re_p \approx 450$; $Re \approx 450$; $Bi \approx 0.18$; $\varepsilon = 0.34$; $D = 0.018$ m

6.3.2 Comparison with analytical solutions

The temperature profiles are plotted in dimensionless form with the step-change analytical solutions of Riaz *et al.* (1976) and Adebiyi and Chenevert (1996) in Figure 60 and Figure 61 for 13 mm and 26 mm crushed rock, respectively. The Riaz equation assumes an infinite heat transfer coefficient, which is more incorrect for the larger rock with a smaller surface area-to-volume ratio. The equation of Adebiyi and Chenevert, which does calculate a heat transfer coefficient (Eq. (43)), overestimates the heat transfer.

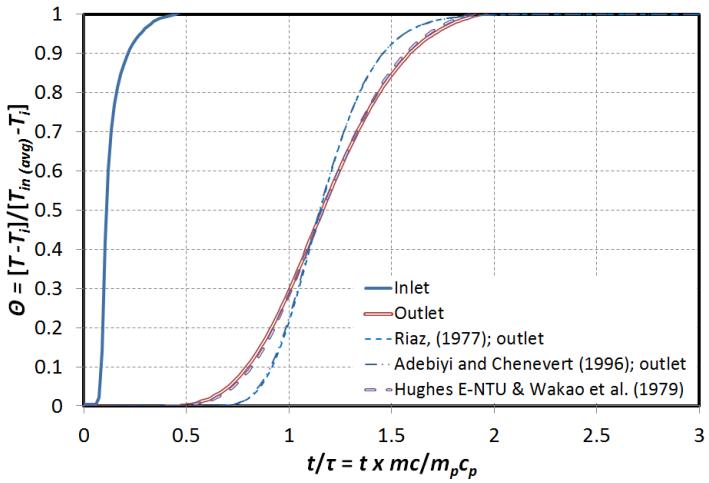

Figure 60: Dimensionless temperature-time curve for "13 mm" discharging; avg. $Re_p \approx 205$; $Re \approx 240$ (counter-current); $Bi = 0.1$

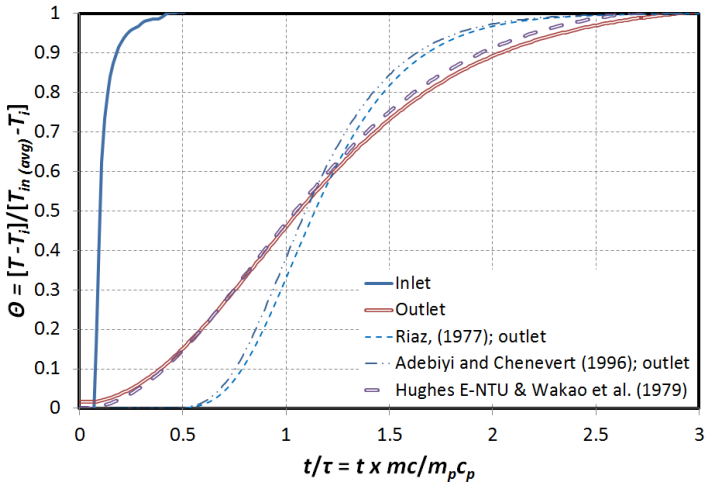

Figure 61: Dimensionless temperature-time curve for "26 mm" discharging; avg Rep ≈ 605; Re ≈ 690 (counter-current); Bi = 0.2

The analytical solutions assume a step change in inlet temperature – the starting time of the step change was taken as being the halfway point for the inlet value to change from 0 to 0.95.

6.3.3 Heat transfer prediction from measured friction factors

The measured friction factors presented in section 6.1 may be substituted into Eq. (56)– Martin's GLE – in place of the Ergun equation to estimate Nusselt numbers. The Hagen number may be rewritten in terms of f_{da} as:

$$Hg = (3/4)f_{da}(1-\varepsilon)Re_p^2/\varepsilon^3 = (27/16)f_{da}(1-\varepsilon)^3Re^2/\varepsilon^3 \quad \textbf{(86)}$$

The predicted Nusselt numbers from Eq. (86) and the friction factor correlation for smooth spheres (Eq. (79)) are shown as a function of *Re* in Figure 62.

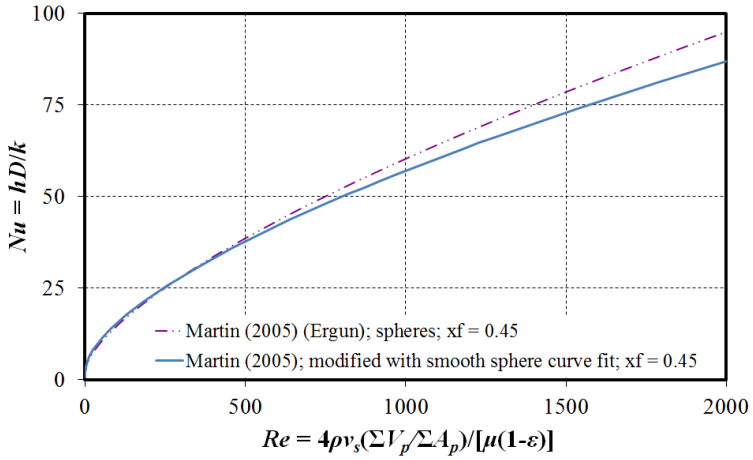

Figure 62: Comparison of the Martin Nusselt number correlation calculated from the Ergun equation and from the smooth sphere equation (Eq. (79))

There is little difference between the values obtained Re < 500, since the Ergun equation is relatively similar to the smooth spheres correlation in this range. The friction factor only appears in Eq. (56) to a power of one third, which reduces its influence on the Nusselt number.

The predicted Nusselt numbers for crushed and rounded rock (from f_{da} equations in Table 17) are shown in Figure 63. The variation of the predicted Nusselt numbers falls within the range of values predicted by the other correlations presented in section 4.2.

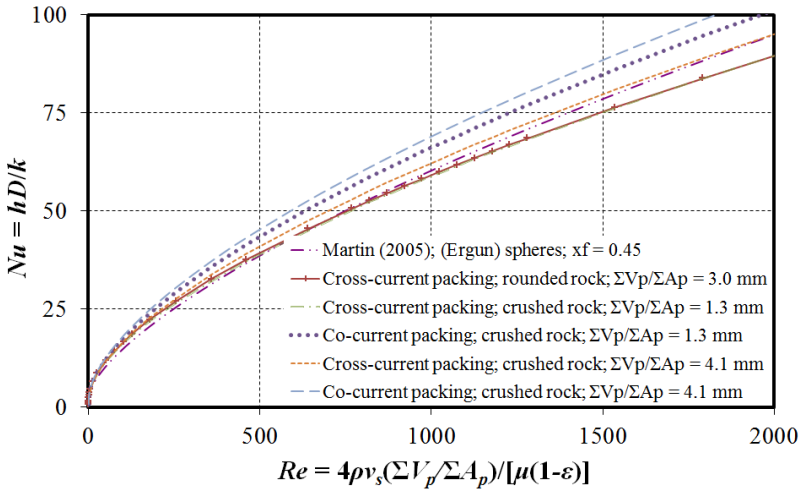

Figure 63: Nusselt number correlations based on measured friction factor correlations for different rock samples (x_f = 0.45)

6.3.4 Practical application for field use

As previously noted, the measurement of the rock surface area is time-consuming and requires relatively sophisticated equipment, so, if possible, a purely volume-based particle size would be more practical. For this reason, temperatures are predicted for some of the above cases based on the measured volume-equivalent sphere diameter for the crushed and rounded rocks. This adequately predicts the measured temperature profiles, as shown in Figure 64, Figure 65, and Figure 66 for crushed and rounded rock. The diameter and Reynolds number are defined as they were in Eq. (80) and (83), section 6.2, repeated here for convenience:

$$D_v = \left(\frac{6}{\pi} \left[\frac{1}{n} \sum_{i=1}^{n} V_{pi} \right] \right)^{1/3} \quad \textbf{(87)}$$

$$Re_{pv} = Re_v(1-\varepsilon) = \frac{\rho v_s D_v}{\mu} \quad \textbf{(88)}$$

The Biot number Bi_v is defined in terms of D_v as

$$Bi_v = \frac{hD_v}{2k_p} \tag{89}$$

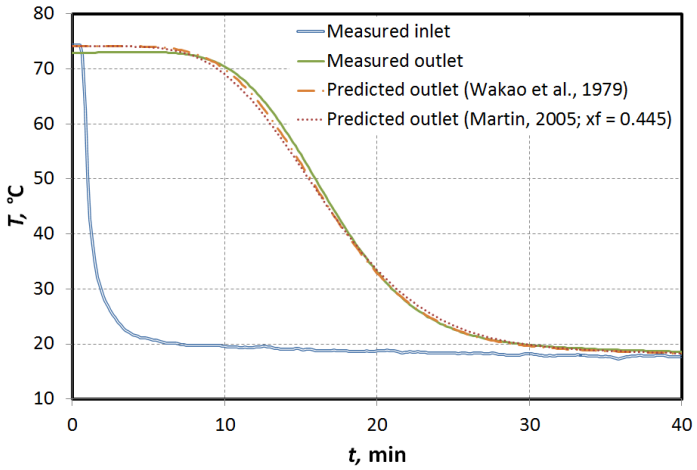

Figure 64: 13 mm rock; counter-current; avg. $Re_p \approx 160$; $\varepsilon = 0.43$; $D_v = 0.0097$ m ($Re_{pv} \approx 200$; $Bi_v \approx 0.11$)

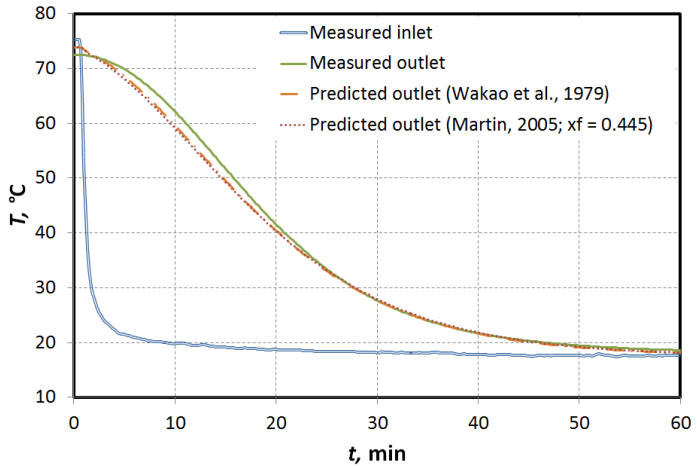

Figure 65: 26 mm rock; counter-current; avg. $Re_p \approx 440$; $\varepsilon = 0.41$; $D_v = 0.029$ m ($Re_{pv} \approx 560$; $Bi_v \approx 0.2$)

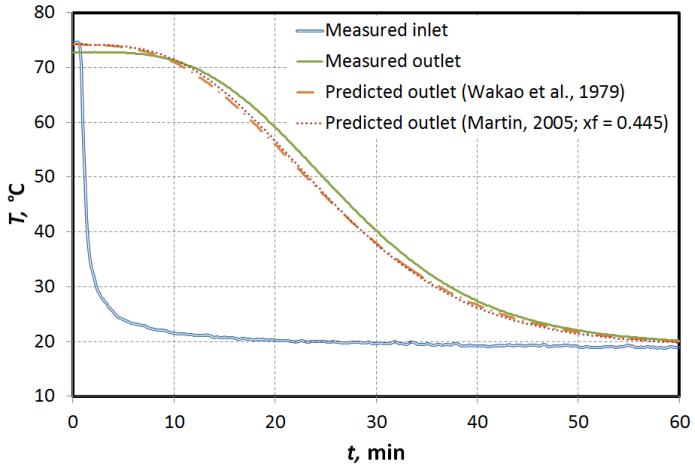

Figure 66: Rounded rock; counter-current; avg. $Re_p \approx 320$; $\varepsilon = 0.33$; $D_v = 0.019$ m ($Re_{pv} \approx 355$; $Bi_v \approx 0.16$)

The Nusselt number was simplified to Eq (90), which was obtained by fitting it to the correlations of Wakao *et al.* (1979) and Martin (2005), shown in Figure 67. The correlation should only be used for $0.35 < \varepsilon < 0.45$ and $80 < Re_{pv} < 600$.

$$Nu_v = hD_v/k = 1.15Re_{pv}^{0.6}Pr^{1/3} \quad \textbf{(90)}$$

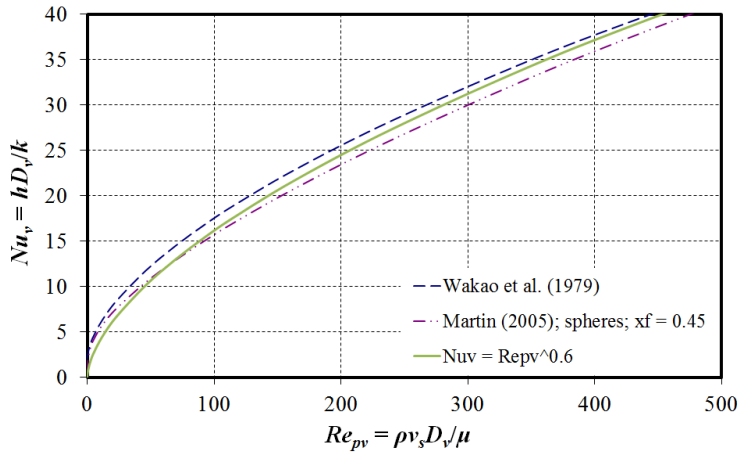

Figure 67: Simplified Nusselt number curve fit to existing correlations; $\varepsilon = 0.4$ used for Martin (2005)

For air, the Prandtl number decreases from 0.707 at 30 °C to 0.683 at 280 °C and then increases to 0.716 at 580 °C (Incropera *et al.*, 2007). If an average value of 0.70 is substituted into Eq. (90), it reduces in rounded form to

$$Nu_v = hD_v/k = Re_{pv}^{0.6} \quad \textbf{(91)}$$

valid for $0.35 < \varepsilon < 0.45$ and $0.009 \text{ m} < D_v < 0.045$ m; $80 < Re_{pv} < 600$.

The predictions from Eq. (91) are compared with the measurements and existing predictions in Figure 68 - Figure 70.

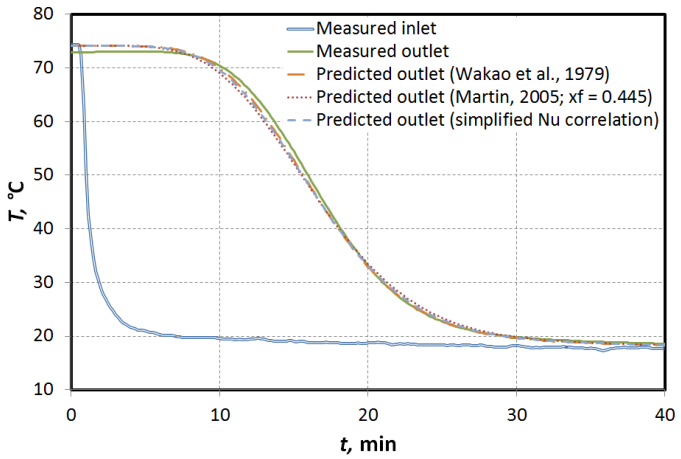

Figure 68: 13 mm rock; counter-current; avg. $Re_{pv} \approx 200$; $Bi_v \approx 0.11$

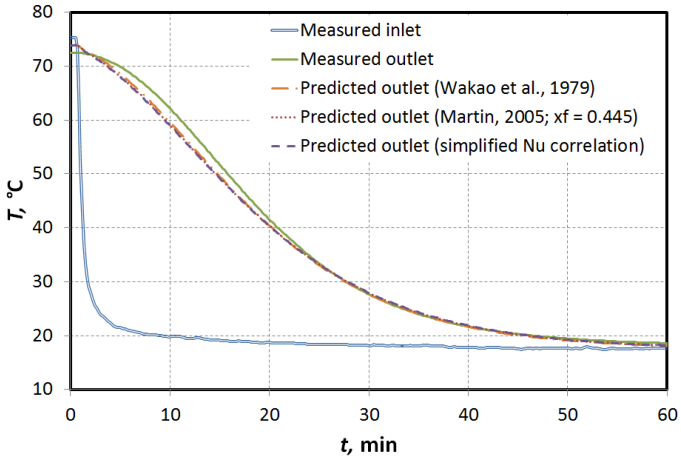

Figure 69: 26 mm rock; counter-current; avg. $Re_{pv} \approx 560$; $Bi_v \approx 0.2$

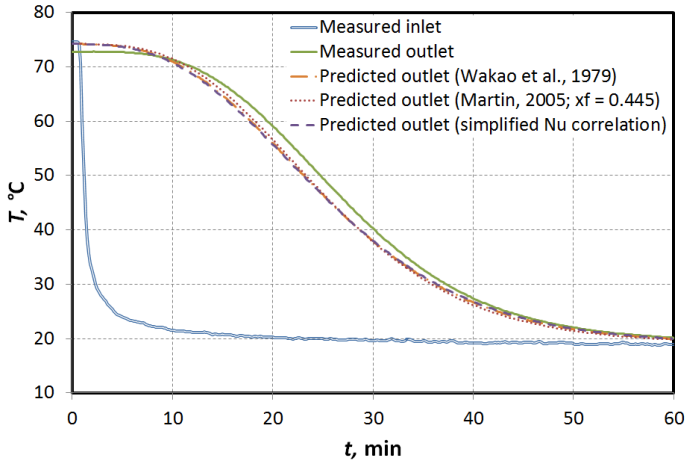

Figure 70: Rounded rock; counter-current; avg. $Re_{pv} \approx 355$; $Bi_v \approx 0.16$

It is of interest to compare Eq. (91) with the equation obtained by using the Martin correlation and the friction factor correlation from Eq. (82). From Eq. (58),

$$Hg = Re_p[150(1-\varepsilon) + 1.75Re_p](1-\varepsilon)/\varepsilon^3 = f_{Erg}(1-\varepsilon)Re_p^2/\varepsilon^3 \quad \textbf{(92)}$$

If $D \approx 0.8D_v$, as is the case for all of the crushed rock tested in this work, then

$$Re_p = \rho v_s D/\mu = 0.8\rho v_s D_v/\mu = 0.8Re_{pv} \quad \textbf{(93)}$$

The dimensionless group of Ergun can be expressed as

$$f_{Erg} = \frac{\Delta p}{L\rho v_s^2}\frac{\varepsilon^3}{1-\varepsilon}\,0.8D_v = \frac{0.8}{2}f_v \quad \textbf{(94)}$$

$$f_v = \frac{\Delta p}{L(\rho v_s^2/2)}\,\frac{\varepsilon^3}{(1-\varepsilon)}\,D_v \approx 56.6\left(\frac{1-\varepsilon}{Re_{pv}}\right)^{0.284} \quad \textbf{(95)}$$

where Eq. (95) is a repeat of Eq. (82). The Hagen number

$$Hg = f_{Erg}(1-\varepsilon)Re_p^2/\varepsilon^3 \approx \frac{0.8}{2}f_v(1-\varepsilon)(0.8Re_{pv})^2/\varepsilon^3 \quad \textbf{(96)}$$

Thus for counter-current packing,

$$\begin{aligned} Hg &\approx \frac{\frac{0.8}{2}f_v(1-\varepsilon)(0.8Re_{pv})^2}{\varepsilon^3} \\ &= 0.4(0.64)(1-\varepsilon)(Re_{pv})^2 56.6\left(\frac{1-\varepsilon}{Re_{pv}}\right)^{0.284}/\varepsilon^3 \end{aligned} \quad \textbf{(97)}$$

$$Hg = 14.49(1-\varepsilon)^{1.284}(Re_{pv})^{1.716}/\varepsilon^3 \quad \textbf{(98)}$$

For $\varepsilon = 0.4$ this reduces to

$$Hg = 117.5(Re_{pv})^{1.716} \quad \textbf{(99)}$$

$$Nu_v = 0.4038(2x_f\, Hg\, D_h/L_m)^{1/3}Pr^{1/3} \quad \textbf{(100)}$$

The value of $Pr = 0.7$ as before, and

$$D_h/L_m = (2/3)\varepsilon/(1-\varepsilon)^{\frac{2}{3}} = 0.3749 \quad \textbf{(101)}$$

Since D_v is being used, $x_f = 0.445$, so

$$Nu_v = 0.4038(2 \times 0.445 \times 117.5(Re_{pv})^{1.716} \times 0.3749)^{1/3} 0.7^{1/3} \quad \textbf{(102)}$$

$$Nu_v = 1.22(Re_{pv})^{0.572} \quad \textbf{(103)}$$

This is compared with the other correlations in Figure 71. It is consistent with the simplified Nusselt correlation presented in Eq. (91), and those of Wakao *et al.* and Martin, in the shown range.

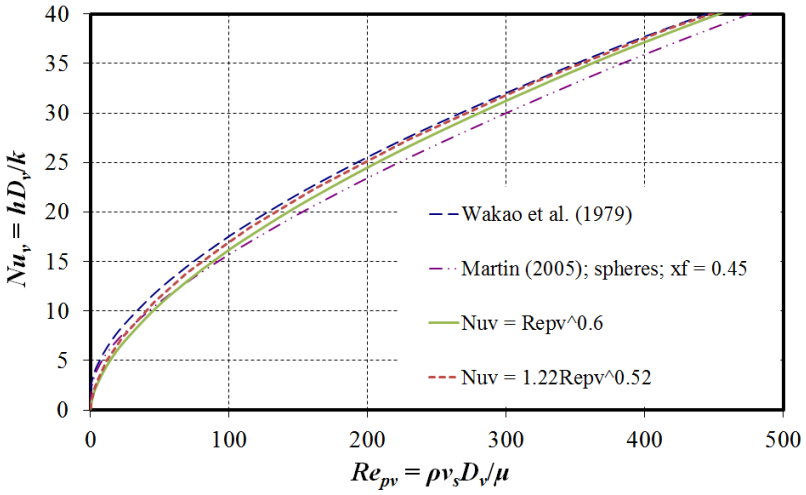

Figure 71: Comparison of Nusselt number correlations

6.3.5 High temperature tests

The 1.5 m^3 rock bed was heated at a number of inlet temperatures ranging from 150 °C up to 530 °C. The outlet temperature is limited to ≈ 250 °C because of material constraints, so the bed could only be charged to steady state at inlet temperatures below this. Since it was not possible to charge the bed to a uniform temperature above 250 °C, all measurements are compared for the charging cycle. The shown measurements for each layer are an average of the six thermocouples.

The air temperature was predicted by means of the Hughes E-NTU method (section 4.4) combined with the simplified heat transfer correlation in Eq. (91). The fluid properties were initially calculated as those of ideal air; however, at the higher temperature tests where the burner was used more extensively and the combustion gases accounted for a higher percentage of the total flow through the bed, the influence of the combustion gases on the air specific heat capacity and density was calculated based on the assumption of ideal gas properties and complete combustion (Moran and Shapiro, 1998; see Appendix G).

It was assumed that radiation heat transfer between the air – combustion gas mixture and the rock was negligible. This is reasonable, based on findings referred

to by Adebiyi *et al.* (1998) for tests (0.27 – 0.44 kg/m^{2}s) at temperatures up to 900 °C.

The heat capacity of the stainless steel container walls between the upper and lower thermocouples was included in the E-NTU calculation – it increases the effective specific heat capacity of the rock by 3 – 4 %. The rock heat capacity was calculated from Eq. (78), section 5.4.

The average temperatures for each thermocouple layer in the bed are shown in Figure 72 and Figure 73 for inlet temperatures of 150 °C and 250 °C. The rock specific heat capacity was calculated at the average between the initial and final bed temperature. The stated values of *Bi*, Re_{pv} and *G* are time-averaged for the duration of the test. The variation in the inlet temperature in Figure 73 was caused by fan speed and burner inlet temperature alterations during the test.

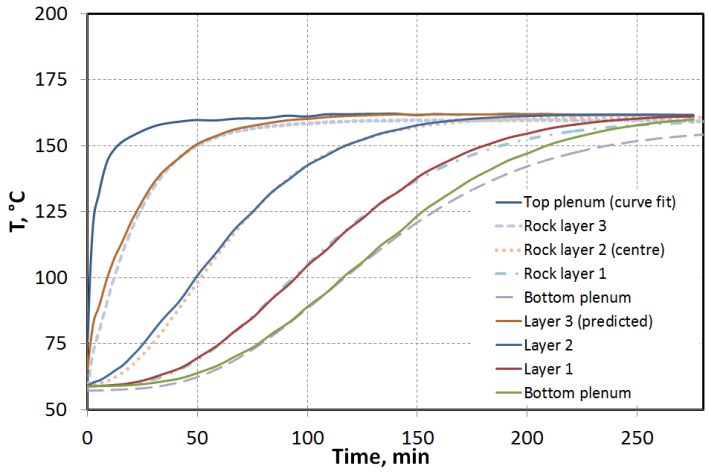

Figure 72: Comparison of measured and predicted temperature for an average rock specific heat capacity at 100 °C ($G \approx 0.28$ kg/m^{2}s; $Re_{pv} \approx 605$; $Bi_v \approx 0.31$)

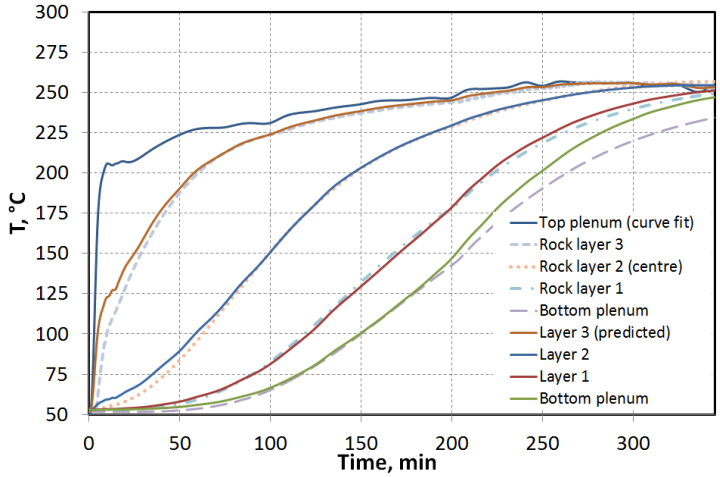

Figure 73: Comparison of measured and predicted temperature for an average rock specific heat capacity at 150 °C ($G \approx 0.24$ kg/m^{2}s; $Re_{pv} \approx 470$; $Bi_v \approx 0.29$)

Figure 73 was the first of the shown tests to be conducted.

Measurements for an inlet temperature of 330 °C are shown in Figure 74. The predicted temperatures nearer the exit of the bed initially diverge from the measurements. The use of an average specific heat capacity means that at low temperatures the rock heat capacity in that region is over-estimated, which results in more energy being stored in the prediction than is actually the case. An additional calculation was performed with variable rock specific heat capacity (Figure 75) which confirms that this is the case, since the divergence is diminished. Zanganeh *et al.* (2012) have shown numerically that the varying specific heat capacity can significantly affect the temperature profile.

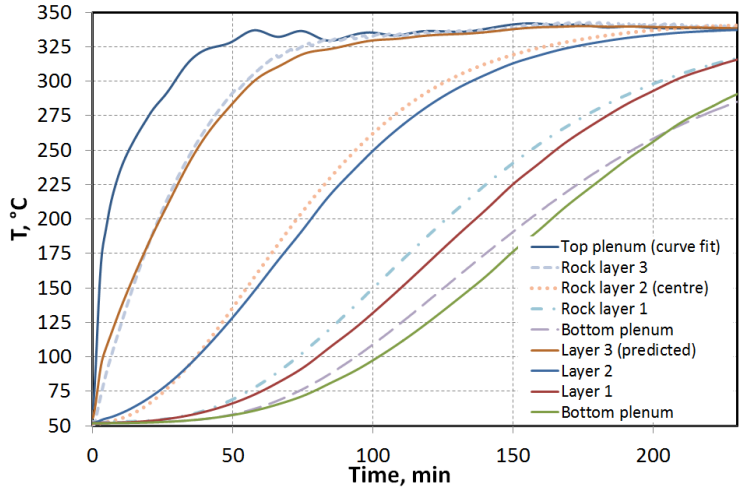

Figure 74: Comparison of measured and predicted temperature for an average rock specific heat capacity at 200 °C ($G \approx 0.26$ kg/m^{2}s; $Re_{pv} \approx 470$; $Bi_v \approx 0.32$)

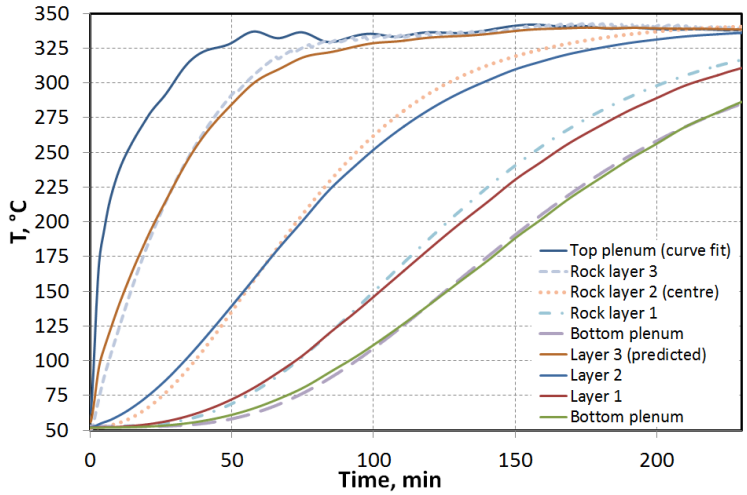

Figure 75: Comparison of measured and predicted temperature for varying rock specific heat capacity

A similar comparison is made for an inlet temperature of 450 °C in Figure 76 and Figure 77, and 530 °C in Figure 79 and Figure 80. The divergence nearer the outlet measurements is larger for constant specific heat than was the case for the 330 °C test, which is consistent with the explanation that the divergence is caused by the use of an average specific heat capacity.

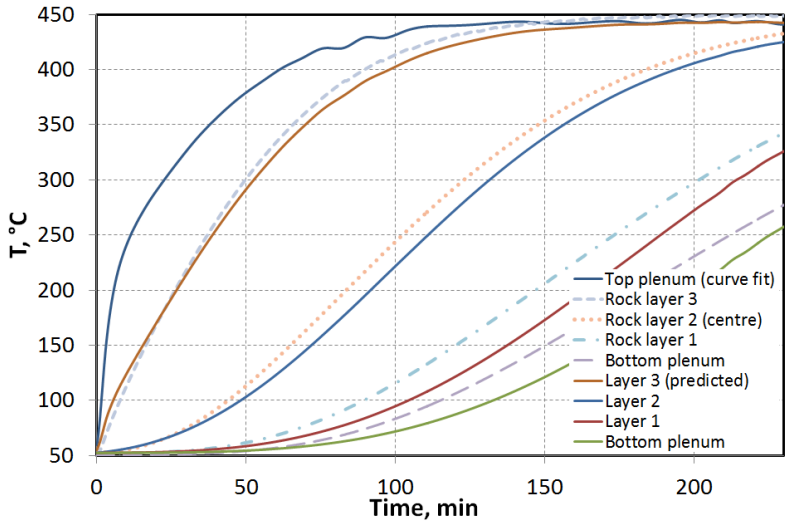

Figure 76: Comparison of measured and predicted temperature for an average rock specific heat capacity at 250 °C ($G \approx 0.20$ kg/m^{2}s; $Re_{pv} \approx 360$; $Bi_v \approx 0.28$)

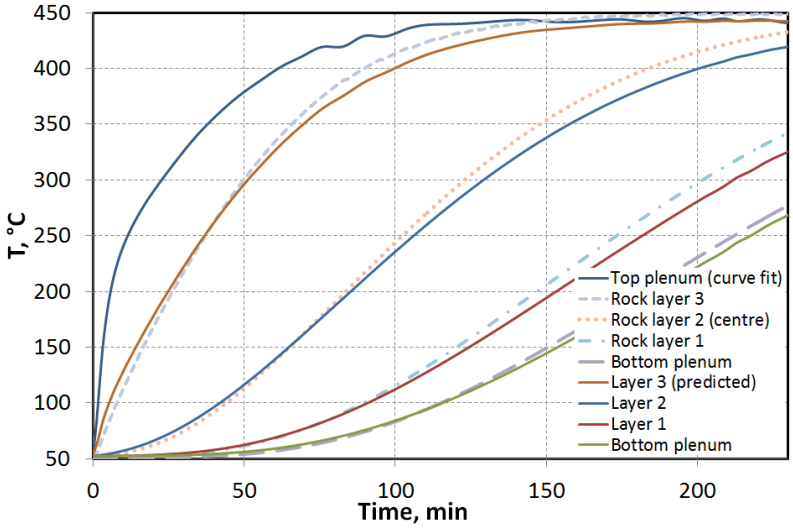

Figure 77: Comparison of measured and predicted temperature for varying rock specific heat capacity

The influence of the combustion gases from the diesel burner on the air specific heat capacity (increase of ≈ 2.5 %) is taken into consideration in Figure 78. It is relatively small, but slightly improves the agreement between the prediction and measurement at the bed outlet.

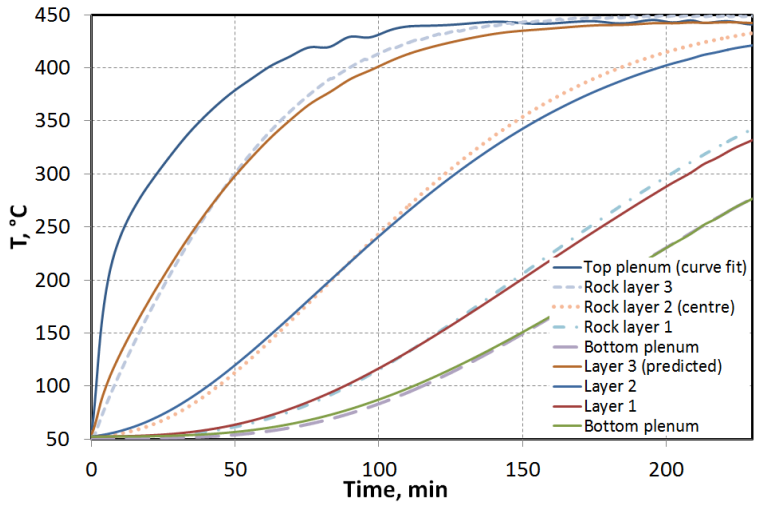

Figure 78: Comparison of measured and predicted temperature for varying rock specific heat capacity and influence of combustion gas on air specific heat capacity

The measured and predicted temperatures are compared for an inlet temperature up to 530 °C in Figure 79 - Figure 81 for constant heat capacity, varying heat capacity, and the influence of combustion gases, respectively.

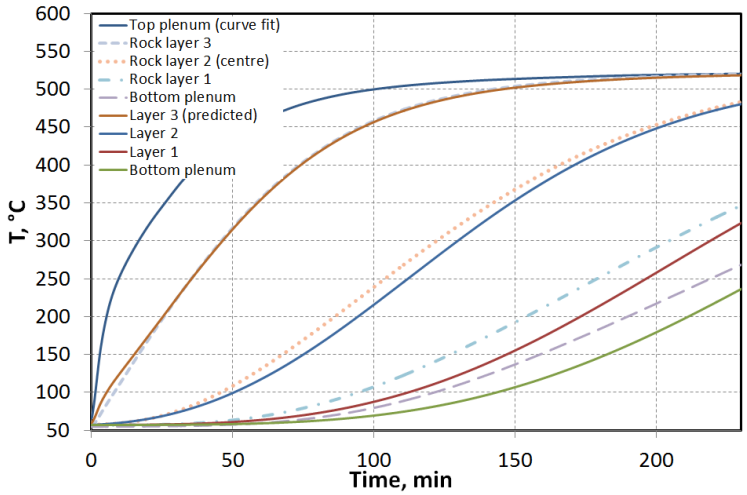

Figure 79: Comparison of measured and predicted temperature for an average rock specific heat capacity at 290 °C ($G \approx 0.18$ kg/m^{2}s; $Re_{pv} \approx 315$; $Bi_v \approx 0.26$)

The influence of the combustion gases from the diesel burner on the air specific heat capacity (increase of ≈ 3 %) is shown in Figure 81. Again the effect is relatively small, but it does improve the agreement between the prediction and the measurement. Although no attempt was made to account for the influence of thermal radiation or conduction through the bed, the outlet temperature prediction is within 5 °C of the measured value.

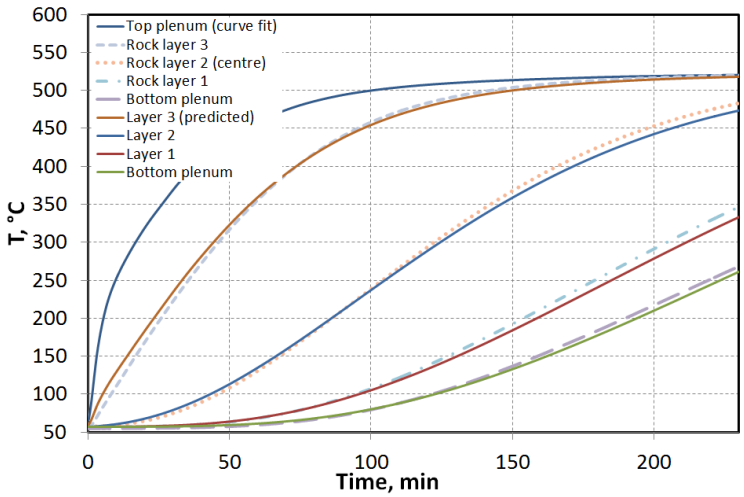

Figure 80: Comparison of measured and predicted temperature for varying rock specific heat capacity

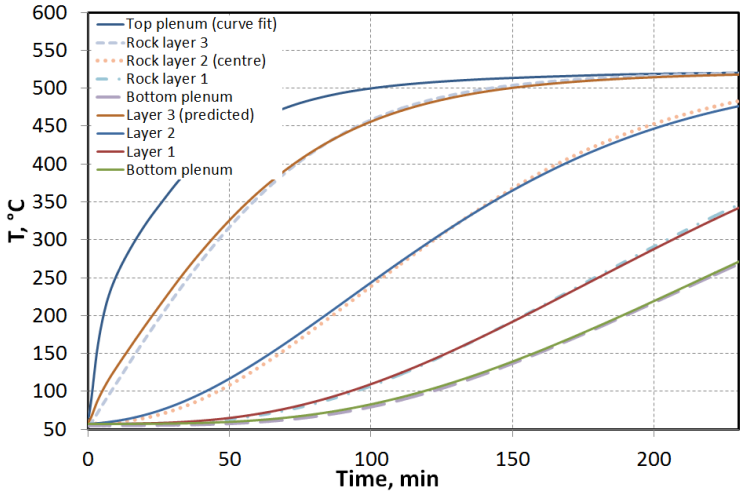

Figure 81: Comparison of measured and predicted temperature for varying rock specific heat capacity and influence of combustion gas on air specific heat capacity

To check that the combustion gases were not influencing the results, the measured temperatures from the discharge cycle of the 250 °C test are compared with the predicted temperatures in Figure 82. This was the highest temperature test where the bed could be heated to a uniform temperature prior to discharging. The agreement is similar to that obtained during charging (see Figure 73), with the exception of the top plenum.

During discharging, the cold air from the walls of the top plenum appeared to sink and form a ‘pool’ of cooler air above the rock. This caused false low temperature readings in the top plenum in a way similar to the recirculation in the low temperature wind tunnel (section 5.1).

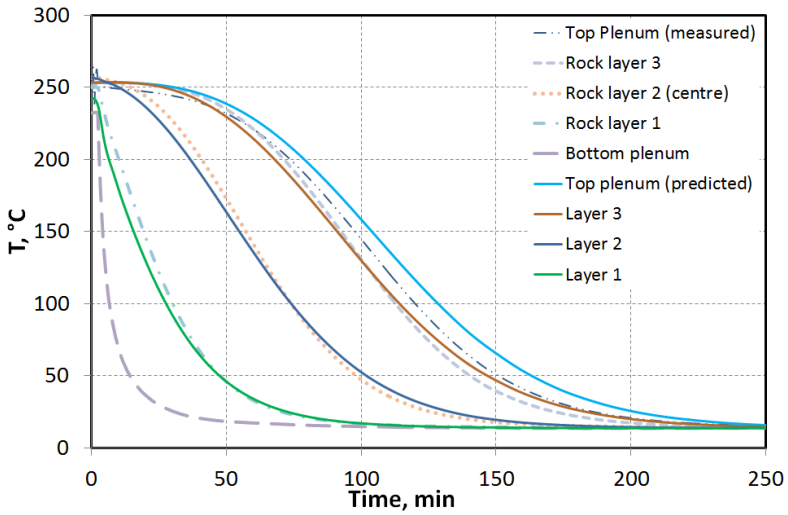

Figure 82: Comparison of measured and predicted temperature for varying rock specific heat capacity (discharging; $G \approx 0.34$ kg/m^{2}s; $Re_{pv} \approx 820$; $Bi_v \approx 0.33$)

The findings of Zunft *et al.* (2011) bear on this problem: they constructed an 8.6 MWh_{th} packed bed (7 x 7 x 6 m^3) of alumina bricks in an internally insulated steel container. A thermal loss test was conducted on the bed by fully charging it (680 °C) and allowing it to stand stagnant for 24 hrs. The inlet pipe at the top of the bed allowed natural convection effects that resulted in the top layer of the storage suffering a temperature drop of 80 °C in 24 hours. The recommendation to avoid this is the use of valves to close the pipe.

To conclude, the Hughes E-NTU method, with the rock specific heat capacity varying as a function of temperature, predicts the air temperature at the bed outlet to within 5 °C for the charging tests at 400 – 530 °C (≈ 0.2 kg/m^{2}s and 300 <Re_{pv} < 400). This is despite the fact that no attempt was made to include the influence of radiation or axial conduction through the bed. The estimated conductivity of the bed from Eq. (61), section 4.3, is 0.3 W/mK. Including radiation, the estimated conductivity from Eq. (62) is a maximum of 1.8 W/mK at 530 °C. Based on the maximum temperature gradient between the top plenum and the next thermocouple layer in the rock (0.18 m below), this would have resulted in a maximum heat flow in that region of less than 1.5 kW. Over the same distance, at the same time, the air flow transferred heat at a rate of 28 kW. The conduction transfer amounts to 5 % or less of the heat transferred by the air flow.

It is an advantage if the Schumann equations and Hughes E-NTU method can be used at high temperatures, as this requires less computational time than more physically detailed models. This is of particular value where charge-discharge cycles must be repeated 10 – 20 times to estimate the steady state operation of the bed.

The time-averaged measured pressure drops for the high temperature tests are displayed in Table 18 and compared with predictions calculated in a similar

manner to Zanganeh *et al.* (2012), using the buoyancy correction Eq.(85), and the isothermal curve fit for crushed rock in co/counter-current packing, Eq. (81) from section 6.2. Pressure drop tests under isothermal conditions showed that the two-term correlation in Eq.(81) under-predicted the measured pressure drop by 12 % or less.

The friction factors were calculated for air properties evaluated at the mean of the bed inlet and outlet temperatures, averaged between the start and completion of charging or discharging. The discharging pressure drop for the tests above 250 °C was estimated by using the final predicted charging temperature of the rock as the initial temperature for discharging.

The predicted pressure drop for these thermal tests, corrected for buoyancy, is 30 – 35 % lower than the measured pressure drop. The exception is the 250 °C test, which was the first of the listed tests to be conducted, which suggests that the packing friction factor characteristic may have altered during the thermal tests. The discrepancy does not appear to be related to the non-isothermal nature of the test, because even at a steady state temperature of 150 °C, the error is -27 %. Likewise, at the end of the charging cycle, the 250 °C prediction is 18 % lower than the measured pressure drop.

Table 18: Comparison of time-average measured and predicted pressure drop

Test	Δp meas., Pa	f_v	Δp pred., Pa	Δp incl. buoyancy, Pa	f_v	Error, %
150 °C ch	107	13.4	69	70	8.8	- 34
150 °C disch	95	9.7	69	67	6.9	- 29
250 °C ch	76	12.3	60	61	10.0	- 18
250 °C disch	93	7.6	84	81	6.7	- 13
340 °C ch	117	14.5	75	78	9.7	- 33
340 °C disch	104	9.7	75	72	6.7	- 32
450 °C ch	90	17.4	49	53	10.2	- 41
450 °C disch	77	9.0	54	50	5.9	- 35
530 °C ch	74	17.2	42	46	10.8	- 37
530 °C disch	59	8.8	46	42	6.3	- 29

An isothermal test after completion of the thermal tests confirmed that the pressure drop characteristics of the bed did change permanently during the thermal tests: Eq.(81) under-predicted the measured pressures under isothermal conditions by approximately 30 % in the same range of Reynolds numbers in which the thermal tests were conducted. This may be a consequence of rock breaking down with thermal expansion and contraction of the bed.

With buoyancy taken into account, the Ergun equation under-predicts the measured pressure drop by 50-60 % (with the exception of the 250 °C test). The isothermal correlation developed in section 6.2 is still a significant improvement.

7 Packed bed design and cost effectiveness

Before considering the design of a packed bed, it is appropriate to consider the context in which it will be used. A brief overview of gas turbines and steam cycles is therefore given to provide an idea of the flow rates and temperatures supplied to the packed bed and demanded from it. Basic design considerations are given, after which a method for determining the mass flux and optimum particle size and bed length is presented.

7.1 Gas turbine operating parameters

In the SUNSPOT cycle, the mass flow and temperature of the flow through the bed during charging are fixed by the gas turbine exhaust flow rate and exhaust temperature. The exhaust gas is likely to be at temperatures between 500 – 600 °C, although it can range from 450 – 650 °C (Kehlhofer *et al.*, 1999; Siemens A.G., 2008, 2009, 2010), and there are turbines operating at higher outlet temperatures – for example 743 °C for a combined cycle (Ordys *et al.*, 1994).

In CSP plants, it may be necessary to use fuel to reach the required turbine inlet temperature, due to current central receiver limitations – turbine inlet temperatures typically range between 1050 – 1450 °C (Miyashita, 1997; Kehlhofer *et al.*, 1999), while most of the volumetric receivers discussed by Ávila-Marín produced gas temperatures of 1000 °C or less, although there are some high temperature receivers. Heller *et al.* (2006) operated a 230 kW_e gas turbine on a pressurized air receiver that almost reached 1000 °C, and a volumetric receiver (DIAPR) has been demonstrated up to 1200 °C and 2 MPa (Ávila-Marín, 2011). A receiver using argon as the heat transfer fluid has reached temperatures of up to 1600 °C (Verlotski *et al.*, 1997).

7.2 Steam cycle characteristics

Typical steam superheat temperatures are around 500 – 550 °C (for example, Miyashita, 1997, Kehlhofer *et al.*, 1999), and steam turbine pressures can range from 1 MPa (Ordys *et al.*, 1994) to 10 MPa or more (Zunft *et al.*, 2011). Steam temperatures of 540 °C can give a thermal-to-electric steam turbine efficiency of about 42 % with a wet-cooled condenser (Kolb *et al.*, 2011). Supercritical steam power plants are moving towards operating conditions of 33 MPa and 610 – 630 °C or more, which can result in steam cycle efficiencies greater than 50 % (Blum and Hald, 1997). Efficiencies are generally in the range 40 – 50 % for newer plants (Blum and Hald, 1997; Miyashita, 1997). By way of comparison, the annual solar-to-electric efficiencies of a central receiver steam power cycle are about 15 % (Kolb *et al.*, 2011).

In a combined cycle, the boiler or heat recovery steam generator (HRSG) may be fired or unfired. If it is unfired, then the air temperature at the HRSG exhaust is a function of the incoming air temperature and mass flow through the HRSG, and the operating steam pressure and temperature, and the HRSG design (see Hicks, 2006). In this case it is not possible to choose a desired flue gas outlet temperature – it is fixed by the operating parameters. If additional fuel is used in the boiler (firing) then this limitation no longer applies – flue gas temperatures well below 100 °C are obtainable, limited only by corrosion at the water dew point (40 – 45 °C) or sulphuric acid dew point (60 – 160 °C depending on the fuel; Woudstra *et al.*, 2010, Kehlhofer *et al.*, 1999).

Unfired HRSG's are likely to have flue gas temperatures of 100 – 150 °C or more, depending on the steam superheat temperature and pressure, and the HRSG design. The higher the flue gas temperature, the more the energy wasted: in unfired power plants, more than 10 % of the energy entering the gas turbine can be lost in the flue gas (Kehlhofer *et al.*, 1999, Hicks, 2006). The steam superheat temperature is typically 30 – 80 °C below the HRSG inlet air/gas temperature (for example Woudstra *et al.*, 2010; Kehlhofer *et al.*, 1999), although greater differences do occur. See Appendix H for further information on HRSG's and sample flue temperatures calculated from the method of Hicks (2006).

7.3 Packed bed design

7.3.1 General design considerations

Hollands *et al.* (1984, and King and Burns, 1981) warn that low pressure drops over packed beds can result in variations of the flow with position in the bed, which may reduce the thermal storage capacity, since this will result in parts of the bed discharging more rapidly than others. This is consistent with Becker et al (2006), who found that flow through porous material in a central (volumetric) receiver tends to be unstable (unequally distributed) for low flow speeds.

The causes of the non-uniform flow are variations in the bed flow resistance, or in the pressure within the plenums upstream and downstream of the bed (Hollands *et al.*, 1984). Variations in the bed resistance may be caused by the walls if L/D is not sufficiently high, or from not packing the rock uniformly – for example regions of high or low void fraction, or regions where the rock size is larger or smaller than average. Pressure variations in the plenums are a consequence of the deceleration of incoming air, and resistance from the walls or rock surface around the plenum. The higher the pressure drop over the bed, the less the influence of variation in the plenum pressure.

Hollands *et al.* (1984) measured air flow speeds near packed bed walls up to a factor of two higher than the flow in the centre of the cross-section ($D_c/D_v > 60$, $D_v \approx 29$ mm, $G = 0.124$ kg/m^{2}s). The loss in performance of a solar heating

system making use of such a rock bed would be about 2 %. They recommend that the dynamic pressure of the air at the inlet to the plenum should be less than 0.3 of the total pressure drop over the test section, to avoid non-uniform flow caused by plenum pressure variation.

To make allowance for poor flow distribution, a greater bed length than that based on the assumption of equally distributed flow should be specified.

The thermocline in a packed bed tends to degrade over time (reduction of stratification) due to losses from the container or natural convection in the bed. This is undesirable, since the high temperature region degrades (by mixing) to a less useful low temperature, and lower power generation efficiencies are possible.

Margolis (1979) shows analytically how the thermocline degrades with time in a stagnant bed as a consequence of wall losses and conduction through the bed (excluding radiation heat transfer). When the wall losses were assumed to be zero, it took a factor of several times longer for the thermocline to degrade than was the case with wall losses. Margolis concludes that it is heat loss from the bed due to poor wall insulation which causes the thermocline to break down, rather than internal diffusion alone.

Sullivan *et al.* (1984;) heated, from the top down, a 1.8 m sided cube of 18 mm and 29 mm rocks (D_v) to about 60 °C, and measured the destratification over time. Destratification due to bed conductivity can be ignored if a bed stands idle at this temperature for a few hours. Natural convection was not a major contributor even for the relatively low hydraulic resistance of the 29 mm rock (see also Jones and Golshekan, 1989).

A number of other considerations from literature and the present work are listed below:

- Rock should be washed to remove dust and prevent clogging of the flow passages (King and Burns, 1981). However, this may not be practical in most regions where solar power plants are built and water is scarce.
- Particles will disintegrate over time and increase the pressure drop; to allow for this, it is probably best slightly to oversize the rock. To estimate the influence of particle disintegration, Wu *et al.* (2003) mechanically compressed packed beds of particles to induce fracture. They found that provided the mass of fines (< 1.3 mm) did not account for more than 1 % of the bed mass, the influence on the pressure drop was relatively small for $Re_p \leq 150$. It is not clear if they took into account the void fraction change of the bed from compression, and the consequent effect on the pressure drop.
- The bed should be constructed in such a way as to be protected from groundwater, which could cause accelerated weathering of the rock, higher thermal loss to the surrounding ground, and environmental complications if the groundwater temperature rises significantly (Hardy *et al.*, 1977).

- The expense of transporting and handling the rock is significant relative to the raw material cost, which makes it advisable to mine the rock at the site of use (see Hardy *et al.*, 1977).
- If supplementary firing is used in the gas turbine or HRSG, there will be water vapour in the exhaust gases passing through the packed bed. Condensation in the bed is undesirable as it may cause the rock to disintegrate more rapidly, so the minimum temperature should be kept above the dew point (35 – 45 °C).
- Zanganeh *et al.* (2012) measured significant variation in the void fraction of a rock-packed test section with a depth change of 1.5 m: from 0.366 at the top to 0.325 at the bottom. The assumption of constant void fraction may be questionable.
- As previously mentioned, Zunft *et al.* (2011) found that the inlet pipe at the top of the bed allowed convection effects that resulted in the top layer of the storage suffering a temperature drop of 80 °C in 24 hours. They recommend the use of valves to close the pipe to reduce or prevent the problem.
- Zunft *et al.*, 2009 give a cost-breakdown estimate for constructing and commissioning a packed bed (honeycomb regenerator with ceramics). The most significant costs are for the ceramic material, followed by assembly, containment, insulation and air distribution.
- The finding that the packing direction of crushed rock influences the pressure drop (see section 6.1.3) is an important design consideration. If the pressure drop is to be kept to a minimum, then rock should be packed in a cross-current direction relative to the air flow. However, in practice this may not be possible; for example if rock is dumped by truck or conveyor on a bed with vertical air flow.

7.3.2 Existing rock bed design concepts

Riaz *et al.* (1976) discuss a rock bed for storage up to 500 °C, formed from a 170 m diameter sphere of rock broken up in-situ by drilling and blasting, covered with a 22 m layer of sand for insulation and containment. This would facilitate the generation of 100 MW_e for about one week. Alternatively, they propose parallel trenches in the ground, covered with 1 m of soil for insulation. Air is fed into the trenches from above or below by means of an air distribution manifold (no details are given). The trenches would be charged and discharged over a period of six months each.

Riaz *et al.* (1976) proposed that the rocks be heated from below in order to prevent losses from the top surface to the environment. Generally speaking, thermal destratification is likely to be a consequence of this method of operation. However, work by Elder (1967) suggests that when porous systems are heated *from beneath*, the stratification can be maintained provided the Rayleigh number is less than 40. In order to meet this stipulation,

$$L < 8.6 \times 10^{-0}/D^2 \quad \textbf{(104)}$$

A value of D = 0.05 m gives L < 0.34 m; D = 0.01 m gives L < 8.6 m.

In later work, Blackshear *et al.* (1977) and Hardy *et al.* (1977) designed the bed so that the hot air is ducted into in the middle of the trenches (that is, at $L/2$) during charging, with cold manifolds at the top and bottom. This layout was proposed to reduce thermal losses (see also Abdel—Wahed *et al.*, 1979).

Hardy *et al.* (1977) discuss a number of design concepts, such as narrow trenches in the ground (as per Riaz *et al.*, 1976), subterranean rock-filled caverns, and rock piles above or partially below ground level. Design air flow speeds of 0.01 m/s or less, bed heights less than 40 m, and particle sizes as low as 0.003 m are specified to meet their requirements of low pumping power and thermal stability.

Zanganeh *et al.* (2012) constructed and tested a rock bed (L = 2.9 m, D_v = 25 mm) in a cone-shaped concrete container at temperatures in the region of 500 – 600 °C. The container had a dodecagonal cross-sectional area, and the walls were inclined at 12 °, which increased the radius from 1.25 m at the bottom to 2 m at the top. This design is intended to avoid the problem of ratcheting and allow the rock to expand without damaging the container. The top of the test section was closed with a concrete lid, which formed a plenum above the rock. Air exited at the bottom through a pipe covered with a perforated metal grid. The lid was lined on the inside with a 0.4 m thick layer of insulation. The side walls and base were concrete. There were losses through the walls and lid of about 14 % of the total energy fed into the storage.

They propose a scaled-up industrial storage system with a 20 m diameter lid ($G \approx$ 0.11 kg/m^{2}s at the inlet during charging) and a height of 25 m. Predicted losses are 0.5 % of the input energy. Pumping energy amounts to 2 % of the energy entering the storage. The overall thermal efficiency at steady state is 95 %. By way of comparison, the measured molten salt efficiency for Solar Two was 97 % (Medrano *et al.*, 2010).

7.3.3 Method of design and parameter selection

Numerous ‘rules of thumb’ for bed parameter selection may be found in the literature. For example, it is fairly frequently assumed that the pumping energy should not exceed 1 - 2 % of the total energy stored in the bed (Abdel-Wahed *et al.*, 1979; Zanganeh *et al.*, 2012), or that optimum particles are a few centimetres in size (Sørensen, 2011).

Coutier and Farber (1982), whose work is primarily directed at low temperature beds, propose that the bed be sized by estimating the desired storage capacity and then choosing values of G and D to keep the pressure drop as low as possible.

King and Burns (1981) advise that rock beds for thermal storage in houses should be short with a large cross-sectional area, to give low air velocities and pressure drops. On the other hand, if the available space is limited, Sanderson and Cunningham (1995) advise that packed beds should use the smallest particles, the longest bed lengths, and the smallest cross-sectional areas practical.

Li et al. (2012) provide generalised curves for energy storage effectiveness of thermocline systems as a basis for design. A number of works favour the use of an exergy analysis on storage systems to determine their performance, since this should give a more reasonable reflection on the loss of availability in the storage, with the associated economic effect (for example, Rosen *et al.,* 1988). Torab and Beasley (1987) sought to optimise the design parameters by maximising the ratio of total availability in the storage to the pumping energy. The total availability increases with decreasing particle size (and increasing bed length); however, their calculated *ratio* of total availability to pumping energy increases with increasing particle size and decreasing bed length.

Domanski and Fellah (1998) consider a thermo-economic approach to be preferable to an exergy analysis alone, since it is desirable to find the minimum total cost of constructing, operating and maintaining the storage system as a whole.

7.4 Bed parameter selection by cost optimum: One-step estimate

A one-step method for estimating the cost-optimum bed parameters is presented in this section. The approximations used for this calculation do not include thermal losses through the bed containment. It is assumed that the bed is supplied with air at a constant temperature and mass flow for the duration of charging, and that fuel is used to balance insolation fluctuations and provide a constant heat input.

7.4.1 Analytical method

The pumping cost C_p through the packed bed in R/s is

$$C_p = C_e \Delta p V \tag{105}$$

where C_e is the cost or value of the energy (electricity) used for pumping, in R/J, and V is the volumetric flow rate at the blower.

The capital cost of the bed in R/s is

$$C_b = C_m A_{cs} L \tag{106}$$

where C_m is the storage capital cost in R/[m^{3}s], which includes the cost of the storage medium, construction, containment, and interest repayment. The total cost of the storage in R/s is

$$C_t = C_p + C_b \quad \textbf{(107)}$$

The rate at which the heat is transferred through the surface area ΣA_p from the air to the particles is

$$Q = h\Sigma A_p \Delta T_{pa} \quad \textbf{(108)}$$

where ΔT_{pa} is the average temperature difference between the air and the particles. The surface area of the particles, if they are cubic or spherical, is

$$\Sigma A_p = 6A_{cs}L(1-\varepsilon)/D \quad \textbf{(109)}$$

In the range 15 < *Re* < 700, the heat transfer coefficient can be approximated for spheres as

$$h = Nu\, k/D = (2k/D)Pr^{1/3}Re^{0.5} \quad \textbf{(110)}$$

This equation is based on correlations from literature, shown in Figure 83, and was chosen specifically to simplify the following analysis.

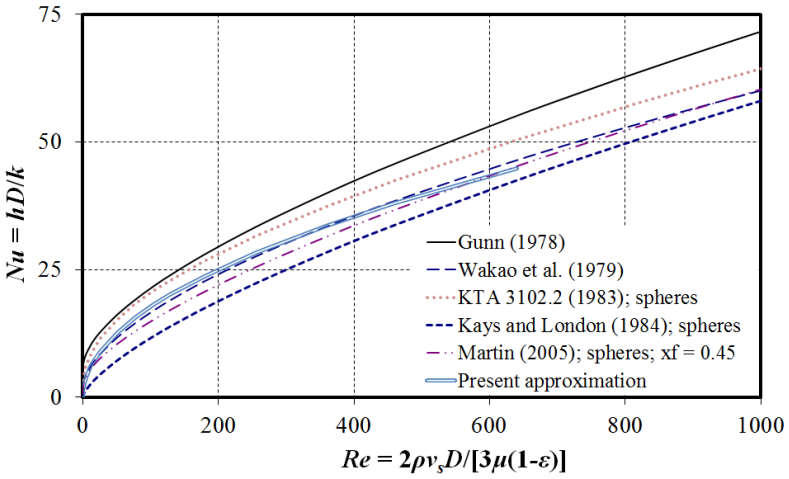

Figure 83: Heat transfer correlations for packed beds; ε = 0.40

The rate at which heat is transferred by the air flowing through the bed is

$$Q = \rho A_{cs} v_s c\Delta T \quad \textbf{(111)}$$

where ΔT is the change in air temperature.

The rate of change of the energy stored in the particles is

$$Q = A_{cs}L(1-\varepsilon)\rho_p c_p \Delta T_p/\Delta t_1 \quad \textbf{(112)}$$

where $\Delta T_p/\Delta t_1$ is the average change in temperature of the particles over the time period Δt_1 in which it is charged.

v_s is expressed in terms of the bed parameters from Eq. (111), (110) and (108):

$$v_s = \left[\frac{9.79\ Pr^{1/3}k(1-\varepsilon)^{0.5}\Delta T_{pa}}{\mu^{0.5}\rho^{0.5}c\Delta T}\right]^2 L^2 D^{-3} \quad \textbf{(113)}$$

And, from Eq. (111) and (112):

$$v_s = \frac{\rho_p c_p (1-\varepsilon)\left(\Delta T_p/\Delta t_1\right)L}{\rho c \Delta T} \quad \textbf{(114)}$$

Eq. (113) and (114) are equated to give

$$L = \frac{\rho_p c_p c\mu\Delta T\left(\Delta T_p/\Delta t_1\right)}{95.8Pr^{2/3}k^2\ \Delta T_{pa}^2} D^3 \quad \textbf{(115)}$$

If it is assumed that the packing friction characteristics are similar to those for smooth spheres, the friction factor may be approximated in the range 40 < *Re* < 900 to within 10 % of the equation for smooth spheres (Eq. (79)) by

$$f_{da} = \frac{\Delta p}{L(\rho v_s^2/2)}\ \frac{\varepsilon^3}{(1-\varepsilon)}\ \frac{4\Sigma V_p}{\Sigma A_p} = \frac{29.6}{Re^{0.4}} \quad \textbf{(116)}$$

The total cost of the bed from Eq. (107), (113), (105) and (116) is

$$\frac{C_t}{Q} = \frac{38764\ Pr^{3.2/3}\mu^{-1.2}(1-\varepsilon)^3 k^{3.2}\Delta T_{pa}^{3.2}}{c^{4.2}\Delta T^{4.2}\rho^2\ \varepsilon^3} C_e L^{4.2} D^{-6.2} + \frac{c\Delta T\mu}{95.8Pr^{2/3}(1-\varepsilon)k^2\ \Delta T_{pa}^2} C_m L^{-1} D^3 \quad \textbf{(117)}$$

Eq. (115) is substituted into Eq. (117), giving

$$\frac{C_t}{Q} = \frac{C_e\rho_p^{4.2}c_p^{4.2}\mu^3(1-\varepsilon)^3(\Delta T_p/\Delta t_1)^{4.2}}{5459\ Pr^{1.73}\rho^2\ \varepsilon^3 k^{5.2}\Delta T_{pa}^{5.2}} D^{6.4} + \frac{C_m}{\rho_p c_p(1-\varepsilon)(\Delta T_p/\Delta t_1)} \quad \textbf{(118)}$$

It is assumed that the pumping cost is continuous over the entire duration for which C_t is calculated.

Eq. (118) can be written in terms of the Biot number, repeated here for convenience:

$$Bi = \frac{hD}{2k_p} \tag{119}$$

Substitution of Eq. (110), (113) and (115) into Eq. (119) gives

$$\frac{\Delta T_p}{\Delta t_1} = \frac{12Bi\ k_p \Delta T_{pa}}{\rho_p c_p} D^{-2} \tag{120}$$

This allows $\Delta T_p/\Delta t_1$ to be calculated from *Bi* and *D*. Eq. (120) is substituted in to Eq. (118) to give

$$\frac{C_t}{Q} = \frac{C_e 6.24\mu^3(1-\varepsilon)^3(Bi\ k_p)^{4.2}}{Pr^{1.73}\rho^2\ \varepsilon^3 k^{5.2}\Delta T_{pa}} D^{-2} + \frac{C_m}{12(1-\varepsilon)Bi\ k_p \Delta T_{pa}} D^2 \tag{121}$$

The partial derivative of Eq. (121) with respect to *D* gives a minimum at

$$D = \left[\frac{C_e 74.93(1-\varepsilon)^4\mu^3(Bi\ k_p)^{5.2}}{C_m \varepsilon^3 \rho^2 Pr^{1.73} k^{5.2}}\right]^{1/4} \tag{122}$$

This assumes that C_m and ΔT_{pa} are constant with respect to *D*, which is not necessarily the case: see Appendix I for samples of crushed rock costs as a function of size. The cost increases as the size is reduced.

Eq. (122) is solved with the fluid properties evaluated for air at an average temperature of 250 °C; ΔT = 500 °C; k_p = 3 W/mK, ε = 0.4, C_e = 2.8 x 10^{-7} R/J, and C_m = 7.7 x 10^{-7} R/m^{3}s (C_e/C_m = 0.36 m^{3}s/J). The solution is plotted as a function of *Bi* in Figure 84. Variation of the optimum value of *D* is shown for differing particle thermal conductivity values within the range of those generally found in rock. At a Biot number of 0.1, the optimum *D* = 0.02 m.

The ratio C_t/Q is plotted as a function of *D* for *Bi* values of 0.05, 0.1 and 0.3 in Figure 85. where ρ_p = 2700 kg/m^3 and c_p = 820 J/kgK and it was assumed that the average ΔT_{pa} = 5 °C.

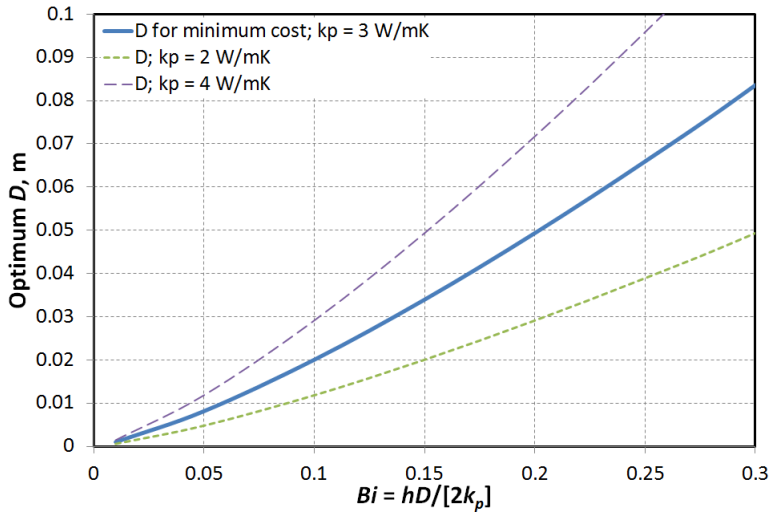

Figure 84: Optimum particle size for minimum cost

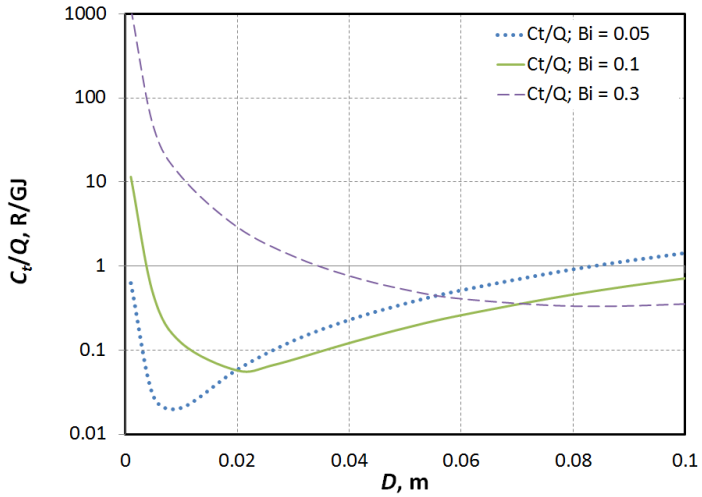

Figure 85: Total cost Ct/Q as a function of particle size for different values of Bi

To illustrate the variation in the value of ΔT_{pa}, sample predictions from the E-NTU method are plotted in Figure 86 at different positions for charging a bed initially at 20 °C. Different positions in the bed experience significantly different and varying values of ΔT_{pa} – from 0 °C to almost 50 °C for these conditions. The overall time averaged value of ΔT_{pa} at x = 1 m, 2 m and 3 m is 5 °C. However, as the length of the bed is altered, the average ΔT_{pa} will alter. Different particle sizes will also influence it. This makes this method of analysis highly problematic.

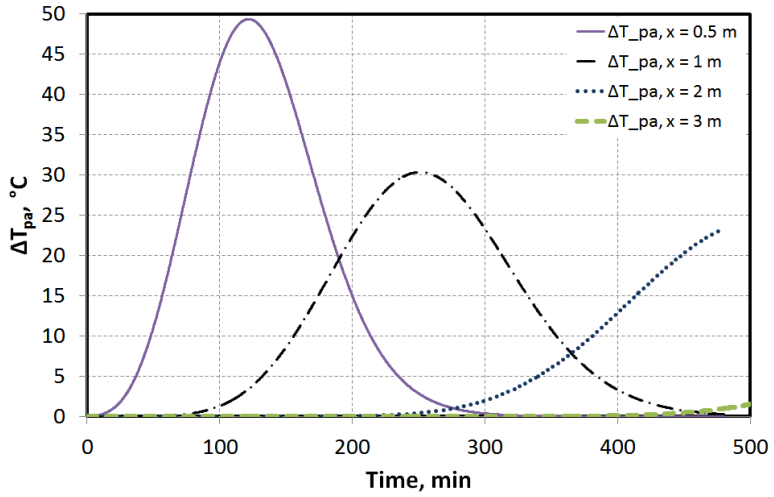

Figure 86: Values of ΔT_{pa} at different positions (G = 0.1 kg/m^{2}s, D = 0.03 m, ΔT = 500 °C)

Seemingly, from Figure 84 and Figure 85, the optimum particle size for Bi = 0.1 is D = 0.02 m. However, because $\Delta T_p/\Delta t_1$ is calculated from Bi and D (Eq. (120)), no limit is placed on its value. But it is not possible for the particles to undergo a temperature change larger than that undergone by the fluid. This is illustrated in Figure 87 for a fluid temperature change over the storage ΔT = 500 °C. The optimum value of D = 0.02 m requires a physically impossible value of ΔT_p > 500 °C for a charging time t_1 = 12 hours. There is insufficient thermal capacity – the mass of particles is too small. The achievable minimum cost occurs at ΔT_p = 500 °C, where D = 0.0265 m. In practice, due to diffusion through the bed and spreading of the thermocline, it will be impossible to achieve $\Delta T_p = \Delta T$ while capturing all the energy from the air stream.

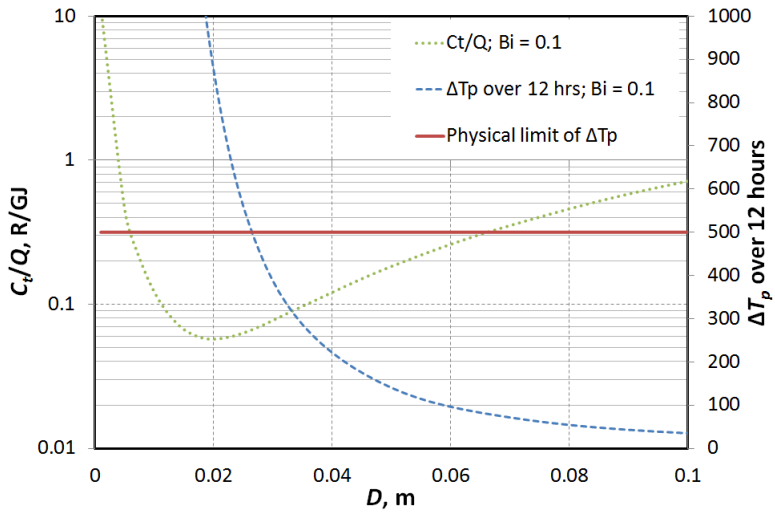

Figure 87: Limited change of particle temperature

7.4.2 Income from power produced in the steam cycle

The heat removed from the storage is used to produce electrical power in a Rankine (steam) power cycle. The income from the power produced (R/s) is

$$I = C_e W_e = C_e \eta_s Q_B \quad \textbf{(123)}$$

where W_e is the electrical power (J/s) produced by the steam cycle. The power produced in the steam cycle is dependent on the efficiency η_s and the heat rate Q_B transferred into the working fluid at the boiler (HRSG):

$$W_e = \eta_s Q_B \quad \textbf{(124)}$$

The efficiency may be estimated from the Chambadal Novikov equation (Bejan, 1996):

$$\eta_s = 1 - (T_L/T_H)^{1/2} \quad \textbf{(125)}$$

where T_H and T_L are the maximum and minimum temperatures of the working fluid, which must be in units of K for Eq. (125). The maximum temperature T_H is the steam superheat temperature leaving the boiler, and T_L the temperature of the condensed steam.

The heat transferred at the boiler is

$$Q_B = \rho A_{cs} v_s c (T_{sup} - T_{flue}) \quad \textbf{(126)}$$

T_{sup} is the air temperature at the boiler inlet, which will equal the air temperature at the exit of the rock bed if there are no losses, and T_{flue} the temperature at the boiler flue outlet.

The steam superheat temperature will not be the same as the air supply temperature from the storage – as mentioned in section 7.2, it is usually 30 – 80 °C lower than the inlet air/gas temperature in an unfired boiler, depending on the system design (Woudstra *et al.*, 2010; Kehlhofer *et al.*, 1999). The flue gas temperature is typically 100 – 150 °C, and is a function of the boiler design and operating conditions. The steam condensate temperature is usually 30 – 40 °C (see Kehlhofer *et al.*, 1999), although in dry cooling applications it would be 40 – 60 °C.

Eq. (123) may be expressed in terms of Eq. (124) - (126) as

$$I = C_e \eta_s Q_B = C_e \rho A_{cs} v_s c \, [1 - (T_L/T_H)^{1/2}](T_{sup} - T_{flue}) \quad \textbf{(127)}$$

If the boiler operating conditions are known, T_H may be expressed in terms of T_{sup}.

Eq. (127) should be combined with Eq. (107). The pumping cost is continuous during charging and discharging, while power is only generated from the storage during discharge. If it is assumed that the charge and discharge of the bed each take 12 hours per day, this will mean that generation of power only occurs for half as long as consumption of power in pumping. The net income

$$I_{net} = 0.5I - (C_p + C_b) \tag{128}$$

Eq. (128) is rewritten in normalised form,

$$\frac{I_{net}}{Q} = \frac{0.5I}{Q} - \frac{C_p + C_b}{Q} \tag{129}$$

where Q is the rate of heat transfer out of the storage. Eq. (127) becomes

$$\frac{I}{Q} = \frac{C_e \rho A_{cs} v_s c \, [1 - (T_L/T_H)^{1/2}](T_{sup} - T_{flue})}{\rho A_{cs} v_s c \Delta T} \tag{130}$$

Eq. (130) and (121) are substituted into Eq. (129):

$$\frac{I_{net}}{Q} = \frac{0.5 C_e \, [1 - (T_L/T_H)^{\frac{1}{2}}](T_{sup} - T_{flue})}{\Delta T} - \frac{C_e 6.24 \mu^3 (1-\varepsilon)^3 (Bi \, k_p)^{4.2}}{Pr^{1.73} \rho^2 \, \varepsilon^3 k^{5.2} \Delta T_{pa}} D^{-2} - \frac{C_m}{12(1-\varepsilon) Bi \, k_p \Delta T_{pa}} D^2 \tag{131}$$

If ΔT is the same for charging and discharging, then $T_H = \Delta T + T_{amb} - \Delta T_{HRSG}$ and $T_{sup} = \Delta T + T_{amb}$. T_{amb} is the ambient temperature and ΔT_{HRSG} is the temperature difference between the steam superheat temperature and the air entering the boiler from the storage. Eq. (131) becomes

$$\frac{I_{net}}{Q} = \frac{0.5 C_e \, [1 - (T_L/[\Delta T + T_{amb} - \Delta T_{HRSG}])^{\frac{1}{2}}](\Delta T + T_{amb} - T_{flue})}{\Delta T} - \frac{C_e 6.24 \mu^3 (1-\varepsilon)^3 (Bi \, k_p)^{4.2}}{Pr^{1.73} \rho^2 \, \varepsilon^3 k^{5.2} \Delta T_{pa}} D^{-2} - \frac{C_m}{12(1-\varepsilon) Bi \, k_p \Delta T_{pa}} D^2 \tag{132}$$

Eq. (130) and (132) are plotted as a function of D in Figure 88, for ΔT = 500 °C, ΔT_{pa} = 5 °C. T_{amb} = 25 °C and ΔT_{HRSG} = 60 °C. The cost C_t is small compared to I. The maximum net income is produced at $\Delta T_p = \Delta T$, the maximum theoretically possible, which in practice is not possible, due to thermal diffusion and thermocline spreading.

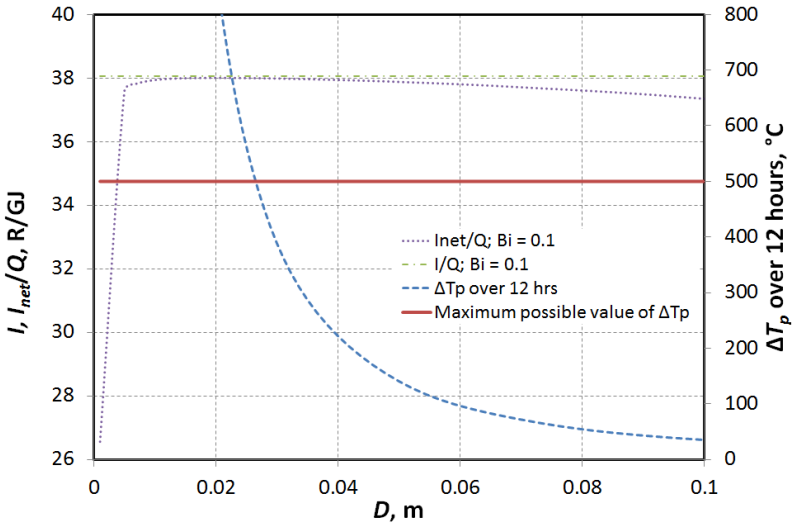

Figure 88: Total value V_t/Q as a function of particle size for Bi = 0.1

7.4.3 Calculation assuming an idealised step-change thermocline

Consider the packed bed temperature profile shown in Figure 89:

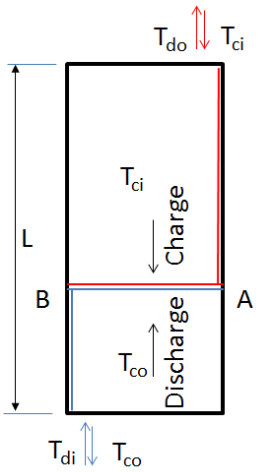

Figure 89: Idealised packed bed temperature profile showing thermocline

To avoid the uncertainty associated with using ΔT_{pa}, the thermocline (A-B) is assumed to be narrow – the bed is either at the maximum temperature T_{ci} (T_{do}) or at the minimum temperature T_{co} (T_{di}). The whole bed is heated between the maximum and minimum temperatures. The charging and discharging time $t_c = t_d$. During discharging, the thermal capacity of the bed is related to the energy in the air stream by

$$\rho A_{cs} v_s c(T_{do} - T_{di}) t_d = \rho_p A_{cs} L(1-\varepsilon) c_p (T_{do} - T_{di}) \quad \textbf{(133)}$$

This is rewritten as

$$\rho v_s = \rho_p L(1-\varepsilon)c_p/(ct_d) \quad \textbf{(134)}$$

The Biot number (Eq. (119)) is fixed at a known value. The Nusselt number is calculated from the Biot number as shown in Eq.(135), and substituted into the correlation of Wakao *et al.* (1979) to calculate the Reynolds number (Eq. (136)):

$$Nu = hD/k \quad = 2Bi\, k_p/k = \ 2 + 1.1Re_p^{0.6}Pr^{1/3} \quad \textbf{(135)}$$

$$Re_p = \ \rho v_s D/\mu = \left[(2Bi\, k_p/k - 2)/(1.1Pr^{1/3})\right]^{1/0.6} \quad \textbf{(136)}$$

For k_p = 2 W/mK, a value at the lower end of the range for rock (see section 2.3.2), Bi = 0.1 gives $Re_p \approx 80$ at room temperature. Eq. (136) is rewritten as

$$\rho v_s = (\mu/D)\left[(2Bi\, k_p/k - 2)/(1.1Pr^{1/3})\right]^{1/0.6} \quad \textbf{(137)}$$

Eq. (134) is substituted into Eq. (137),

$$\rho v_s = \ \rho_p L(1-\varepsilon)c_p/(ct_d) = (\mu/D)\left[(2Bi\, k_p/k - 2)/(1.1Pr^{1/3})\right]^{1/0.6} \quad \textbf{(138)}$$

The required bed length is then determined from

$$L = (\mu/D)ct_d/[\rho_p(1-\varepsilon)c_p]\left[(2Bi\, k_p/k - 2)/(1.1Pr^{1/3})\right]^{1/0.6} \quad \textbf{(139)}$$

For t_d = 12 × 3600 s, D = 0.01 m, Pr = 0.695, k_p = 3 W/mK, Bi = 0.1, ε = 0.40, ρ_p = 2650 kg/m^3, c_p = 820 J/kgK, c = 1035 J/kgK, k = 0.0423 W/mK and μ = 2.79 × 10^{-5} kg/ms, the bed length L = 6.45 m. For D = 0.03 m, L = 2.15 m. These values underestimate the bed length, because they do not take into consideration the thermocline spreading. They can be compared with the predictions obtained by means of realistic bed temperature profiles in section 7.5.2, shown in Figure 96. The optimum bed length calculated in section 7.5.2 for D = 0.01 m is about 8-9 m, and for D = 0.03 m, 5 m.

The income generated by the steam cycle during discharging is defined by Eq. (123). Ignoring HRSG limitations, the boiler flue gas outlet temperature is estimated as the ambient temperature – and therefore T_{co} and T_{di} – and the heat transferred into the boiler is

$$Q_B = \rho_p A_{cs} L(1-\varepsilon)c_p(T_{do} - T_{di}) \quad \textbf{(140)}$$

Therefore,

$$I = \ C_e \eta_s \rho_p A_{cs} L(1-\varepsilon)c_p(T_{do} - T_{di}) \quad \textbf{(141)}$$

For C_e = 1 R/kWh, T_{do} = 500 °C and T_{di} = 20 °C, A_{cs} = 1 m^2 and the other properties listed above, this gives

$$I = (1/3600\,000)(0.3)(2650)(0.6)(820)(500-20)\,L = 52.2\,L \quad \textbf{(142)}$$

By comparison, the slope of the straight line segment for L < 6 m shown in Figure 91 for realistic temperature profiles is I = 52.9 L. However, the optimum is found after the straight line segment ends, so this method is of limited value. As particle sizes increase, the thermocline spreads out further and further, and the assumption of uniform temperature throughout the bed leads to an increasingly significant error. This method also fails to lead to an optimum. It is necessary to take into account thermocline spreading in the bed, which may be achieved by making use of the bed temperature profile.

7.5 Bed parameter selection using the temperature profile[5]

7.5.1 Solution in principle

The particle size D is chosen for a unit cross-sectional area bed. The Biot number (Eq. (35)) is fixed at a chosen value. The Nusselt number is calculated from the Biot number in Eq. (143), and the correlation of Wakao *et al.* (1979) is used to calculate the Reynolds number (Eq. (144)), as in Eq. (135) and Eq. (136):

$$Nu = hD/k \quad = 2Bi\,k_p/k = 2 + 1.1Re_p^{0.6}Pr^{1/3} \quad \textbf{(143)}$$

$$Re_p = \rho v_s D/\mu = \left[(2Bi\,k_p/k - 2)/(1.1Pr^{1/3})\right]^{1/0.6} \quad \textbf{(144)}$$

If D is chosen, the mass flow rate is calculated from

$$m = \rho A_{cs} v_s \quad \textbf{(145)}$$

where A_{cs} is fixed at 1 m^2.

The Hughes effectiveness-NTU method (section 4.2) is implemented to solve the temperature profile through the bed for consecutive charge-discharge cycles, and a range of values for D and L. Charging and discharging takes place for time periods t_c and t_d respectively. At the end of the charging cycle, the flow direction is reversed for discharging. The final temperature profile of the bed at the end of charging is used as the initial profile for discharging. This process is repeated n times to reach 'steady-state' operation, where the temperature profiles are repeatable with successive charge/discharge cycles.

[5] This section was presented at SolarPACES 2013 and (as part of the proceedings) is due to be published in Elsevier Energy Procedia, probably in 2014. See Allen *et al.* (2013c)

The thermal energy in the storage is supplied to a steam cycle to generate power. The flue outlet temperature from the boiler is T_{flue}. The minimum working fluid temperature in the steam cycle is T_L, based on typical air-cooled condenser temperatures. The rate of heat transfer into the steam at the boiler is

$$Q_B = \rho A_{cs} v_s c(T_{do} - T_{flue}) \quad \textbf{(146)}$$

The electrical power generated by the steam cycle is

$$W_e = \eta_s Q_B \quad \textbf{(147)}$$

where the steam cycle efficiency was estimated from the Chambadal Novikov equation (Bejan, 1996):

$$\eta_s = 1 - (T_L/T_H)^{1/2} \quad \textbf{(148)}$$

The income from the electrical power produced (R/s) is

$$I = C_e W_e \quad \textbf{(149)}$$

The pumping cost C_p through the packed bed in R/s is

$$C_p = C_e \Delta p V \quad \textbf{(150)}$$

where C_e is the cost of energy in R/J. The pressure drop is obtained from friction factors for the appropriate particle type. In this case, the smooth sphere friction factor curve (Eq. (79)), which is similar to the lowest measured friction factors for the crushed rock in cross-current packing, is used:

$$f_{da} = \frac{\Delta p}{L(\rho v_s^2/2)} \frac{\varepsilon^3}{(1-\varepsilon)} \frac{4\Sigma V_p}{\Sigma A_p} = \frac{172}{Re} + \frac{4.36}{Re^{0.12}} \quad \textbf{(151)}$$

This was used because it represents the minimum likely pressure drop. Since the buoyancy effect increases the pressure drop over the bed during charging, and decreases it during discharging, it should make relatively little difference to the overall pumping energy requirement, and is neglected in this analysis.

The air volumetric flow rate V at the blower is calculated from

$$V = m/\rho \quad \textbf{(152)}$$

where ρ is evaluated at T_{flue} , or another temperature appropriate to the operating conditions of the blower.

The capital cost of the bed in R/s is

$$C_b = C_m A_{cs} L \quad \textbf{(153)}$$

where C_m is the material capital cost in R/[m^{3}s], which includes construction and interest repayment.

Since v_s and therefore m are expressed as a function of D, they will decrease as D increases. Consequently, the quantity of thermal energy stored will differ, and the net income for the different particle sizes must be normalised by the total heat stored.

The net income over a full charge-discharge cycle, in R, for constant properties, is

$$I_{net} = \int_0^{t_d} I\, dt - C_p(t_c + t_d) - C_b(t_c + t_d) \quad \textbf{(154)}$$

This is normalized by the quantity of heat recovered from the bed, I_{net}/Q, where

$$Q = \int_0^{t_d} m \int_{T_{di}}^{T_{do}} c(T) dT\, dt \quad \textbf{(155)}$$

I_{net}/Q is calculated for a range of particle sizes and bed lengths, and the maximum value allows the optimum value of L and D to be chosen.

7.5.2 Sample solution

The values used for the sample solution are summarised in Table 19. The air inlet temperature during charging (T_{ci}) and discharging (T_{di}) was fixed. The steam cycle efficiency was estimated by setting T_H equal to the time-varying bed outlet temperature T_{do}. The bed was assumed to be at an initial temperature T_{di} before charging began.

Table 19: Values used for calculating the optimum *D* and *L*

Variable	Value	Variable	Value
T_{di} °C	20	t_c s	12 x 3600
T_{ci} °C	500	t_d s	12 x 3600
T_{flue} °C	100	*n (cycles)*	15
T_L °C	50	*Bi (flow calc)*	0.1
T_{avg} °C	250	*Years of use*	20
C_e R/J	1/3 600 000	*Rock density*	2650 kg/m^3
C_m R/m^{3}s	8.403 x 10^{-7} (0.2 R/kg/20 yrs)	*Rock heat capacity*	820 J/kgK
ε	0.4	*Rock conductivity*	3 W/mK

The cost C_e (1 R/kWh$_e$) is based on the South African Integrated Resources Plan (IRP) forecast electricity sales price in 2020 (Department of Energy, 2010). The value for C_m here only includes the raw material cost of the rock, based on quotations from aggregate suppliers in South Africa.

As mentioned in section 4.4, Hänchen *et al.* (2011) and Zanganeh *et al.* (2012) show that the most significant changes in the temperature profile occur within the first 10 charge-discharge cycles, although there are still changes up to 20 (possibly 30) cycles. In this case, n = 15 cycles was found sufficient.

The flow rate from Eq. (144) and (145) was calculated for air properties at T_{avg}, giving an average value of $Re_p \approx 72$ ($Re \approx 80$). The void fraction of 0.4 is based on the experimental measurements for the crushed rock. For comparison, the void fraction for nominally single-sized "19 mm" stone is between 0.34 – 0.50, with an average of 0.46 (Grieve, 2001).

Air properties were calculated at the segment temperatures. The air density at the blower was calculated at the air temperature T_{flue} during discharging, and the bed outlet temperature (T_{co}) during charging. The pressure drop for calculating pumping power was obtained by means of Eq. (151).

A sample plot of the income, net income, and pumping and material cost for the case where D = 0.02 m is shown in Figure 90. For this particular case with D = 0.02 m, the maximum net income is obtained for a bed length around 6 – 7 m. The non-linearity in the pumping cost is caused by the temperature dependent variation of air properties through the bed and the blower.

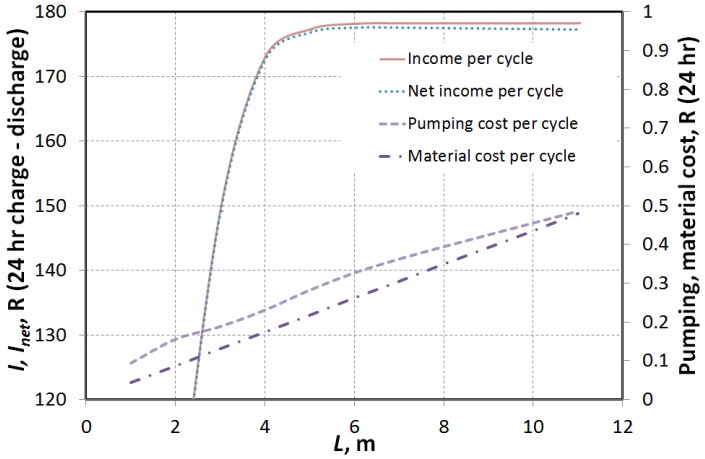

Figure 90: Income and cost for unit cross-sectional packed bed, D = 0.02 m

The income obtained for a range of values of D is shown in Figure 91 and in Figure 92 normalised by the thermal energy removed from the bed during a 12 hour discharge.

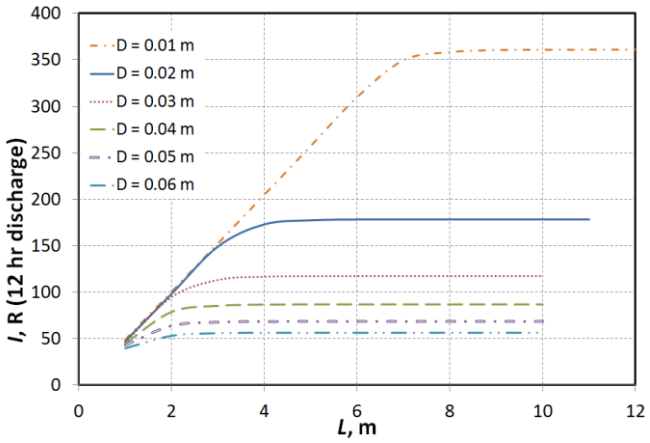

Figure 91: Income per 12 hr discharge for a range of *D*

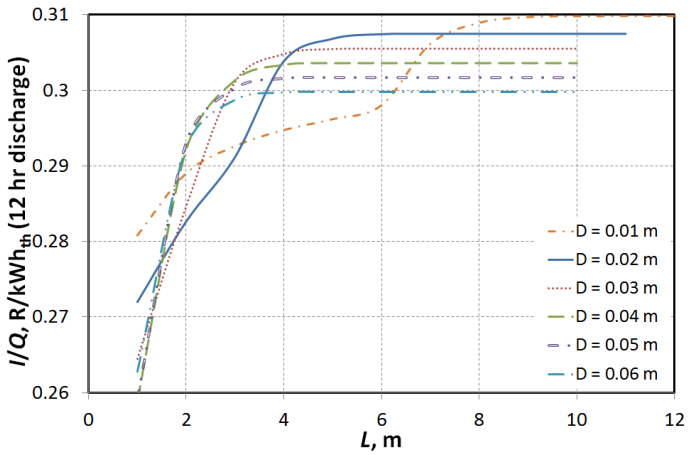

Figure 92: Income per discharge in normalised form for a range of *D*

The main reason for the inflection in the curve for D = 0.01 m is the thermocline and the bed discharge outlet air temperature profile, shown in Figure 93.

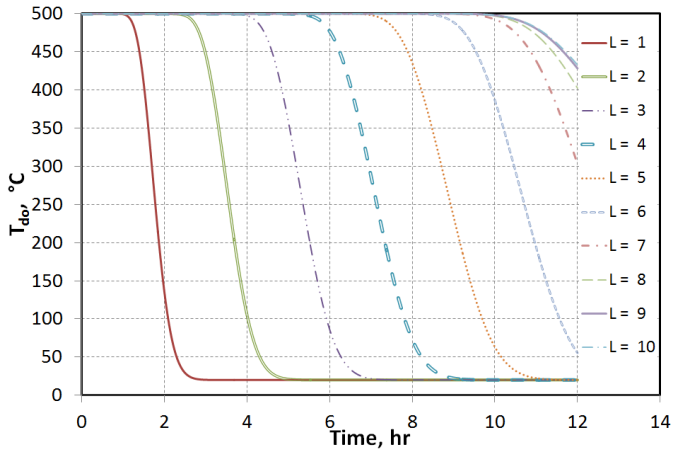

Figure 93: Discharge outlet temperature profile for *D* = 0.01 m

For $L \leq 6$ m the outlet temperature from the bed drops to about 50 °C or less before the end of the 12 hour discharge. However, for $L \geq 7$ m, the outlet temperature does not drop below 250 °C, and more power can be generated at a higher efficiency, as seen in Figure 94 and Figure 95.

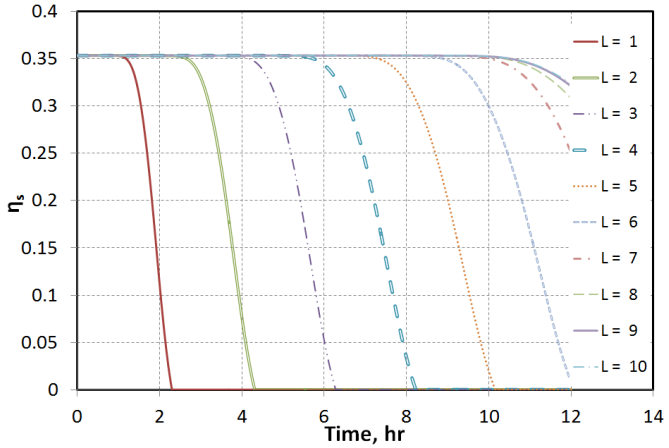

Figure 94: Variation of efficiency for D = 0.01 m

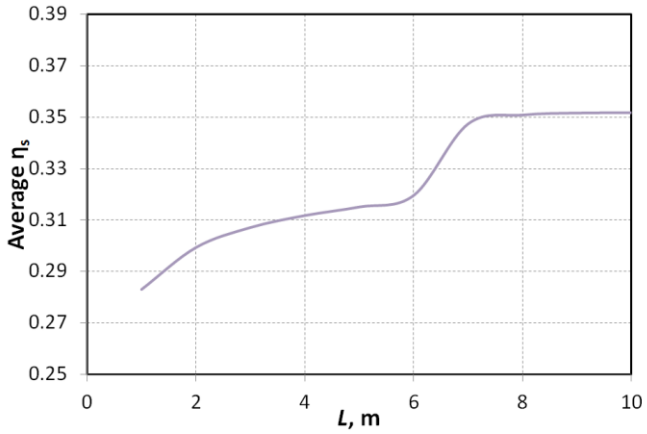

Figure 95: Average cycle efficiency during discharge for D = 0.01 m

The net income obtained during a 24 hr charge-discharge cycle is shown for particle sizes from 0.01 – 0.06 m in Figure 96 in normalised form. The optimum particle size and bed length combination which will give the maximum value of I_{net} for the shown cases is D = 0.02 m and L = 6 – 7 m. This is despite the fact that the smallest particle size allows the highest income (see Figure 92) and the most energy from the charging process to be stored (see Appendix J for additional information). For this particle size and L = 7 m, the ratio of the total pumping cost to the bed capital cost is 1.1. By comparison, the ratio for D = 0.01 m at the optimum length of 8 – 9 m is 20, while that for D = 0.06 m at L = 4 m is 0.01.

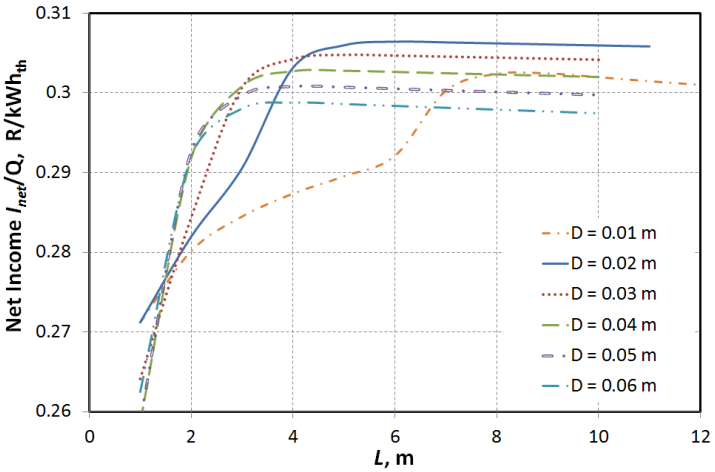

Figure 96: Normalised net income over a full charge-discharge cycle for a range of *D*

Thermal conduction and radiation heat transfer through the bed will cause the thermocline to spread out further, which would tend to increase the required value of *L*. Since there is little difference in the net income, *L* could easily be increased by 2 m (or more) to allow for this. As mentioned in section 7.3.1, an additional problem with packed beds is non-uniform resistance to flow caused by packing or particle size non-uniformity. To allow for this, a higher value of *L* than that calculated from the optimum would also be suitable. The optimum value of *L* would probably be at least 7 – 8 m in this case.

The results are summarized by plotting the maximum value of I_{net}/Q for each particle size as a function of *L* and *D*, as shown in Figure 97 and Figure 98.

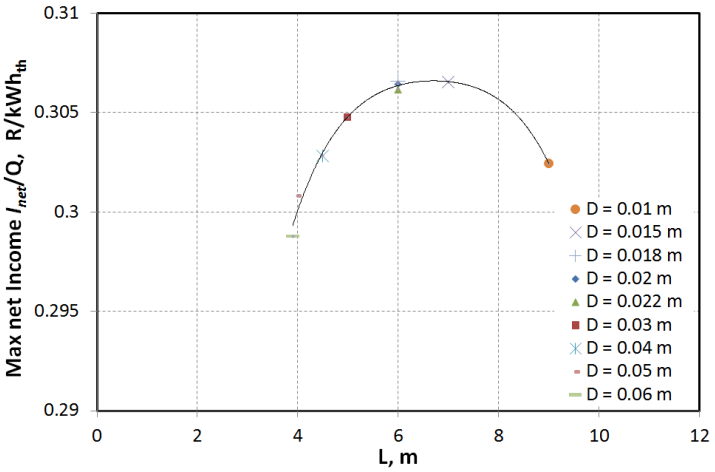

Figure 97: Maximum net income for different bed lengths

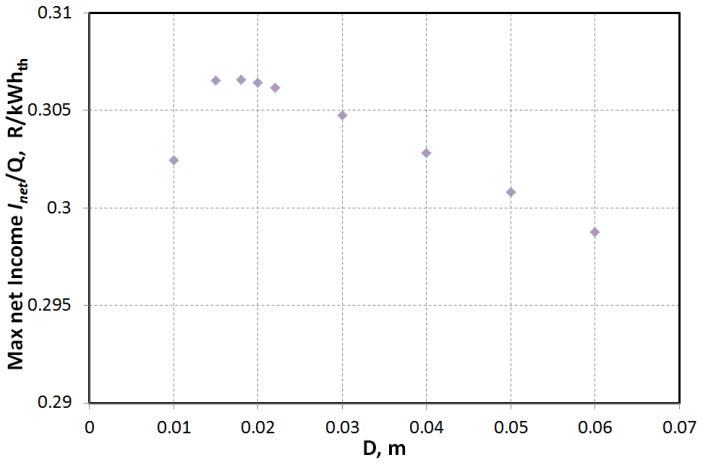

Figure 98: Maximum net income for different particle sizes

For a particle size of 0.02 m and a bed length of 7 m, a unit cross-sectional area is capable of storing 2 GJ (556 kWh_{th}) at G = 0.098 kg/m^2s, determined from the conditions specified in Table 19. If all the rock in the bed changed temperature by the maximum possible (480 °C), it would be capable of storing 4 GJ: only 50 % of the potential capacity of the bed is actually used.

At an average steam cycle efficiency of 0.33, average T_{do} = 492 °C and T_{flue} = 100 °C, 40 kW_{th} (480 kWh_{th}) would be available to be transferred to the steam cycle, enabling the generation of 13.2 kW_e. This is scaled for a range of steam cycle capacities in Table 20. Material capital costs are shown in Table 21. The cost of the rock bed storage system is estimated as a multiple of the material cost. For comparison, capital costs for a molten nitrate salt system are given for 12 hour operation, based on 22 \$/kWh_{th} (220 R/kWh_{th}) (Kolb *et al*. 2011).

Table 20: Bed sizes for D = 0.02 m and L = 7 m

Steam cycle rating, MW_e	Required A_{cs}, m^2	Bed volume, m^3	Rock volume, m^3	Rock mass, 10^3 kg
1 (3.03 MW_{th})	76 (8.7×8.7)	532	319	845
10	760 (28×28)	5320	3190	8450
50	3800 (62×62)	26 600	15 960	42 268
100	7600 (87×87)	53 200	31 900	84 535

Table 21: Rock cost and estimated bed cost for D = 0.02 m and L = 7 m

Steam cycle, MW_e	Rock cost, 10^6 R	Bed cost (2x), 10^6 R	Bed cost (3x), 10^6 R	Molten salt, 10^6 R
1 (3.03 MW_{th})	0.17	0.34	0.51	8.0
10	1.7	3.4	5.1	80
50	8.6	17	26	400
100	17	34	52	800

If the bed containment increases the capital cost by a factor of three from the rock cost (a factor which is feasible depending on the design; see Hardy *et al.*, 1977), the bed cost is an order of magnitude lower than molten salt. Even if the containment cost increases the rock cost by a factor of five, it is still an order of magnitude cheaper.

Future work using this method to obtain more precise estimates needs to address the simplifications that were made. The charging and discharging of the bed was continued for 12 hours, regardless of whether or not the bed was fully charged or discharged. In practice, pumping of air through the bed would be ceased before the discharge outlet temperature drops significantly, since the steam cycle limitations would prohibit the generation of electricity. The effect of thermal losses from the bed, which will depend on the volume-to-surface ratio of the bed layout, needs to be added.

The results were calculated for the smooth sphere pressure drop Eq. (79), which represents the lowest measured pressure drop through rock beds (13 mm crushed rock in cross-current packing). The particle type and packing direction will decide which correlation should be used. The blower efficiency must be taken into account.

The capital cost of the steam cycle should be included to take into account the cost of not producing electricity when the thermal storage is empty. Estimates of the packed bed construction and structural cost, as well as financial interest should also be included. This will enable a levelized cost of electricity (LCOE) to be calculated (see Appendix K), for comparison with existing LCOE. The effect of increasing the capital cost is illustrated in Figure 99, for an effective material cost (including construction and infrastructure) of 0.5 R/kg – 2.5 times higher than the raw material cost.

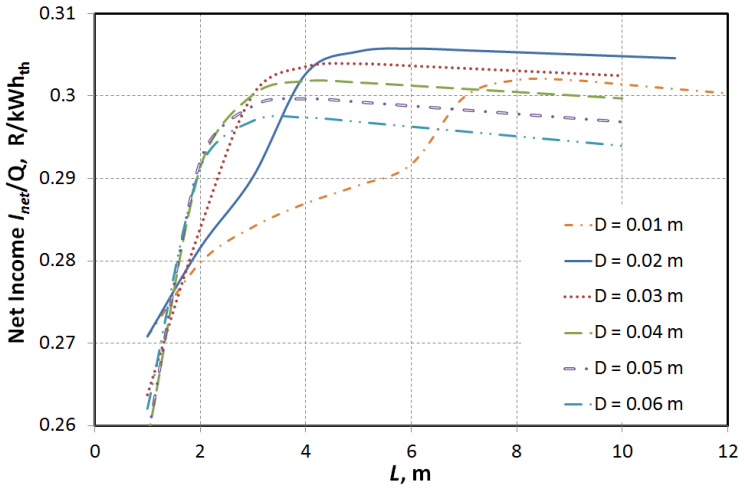

Figure 99: Effect of capital cost variation (effective material cost 0.5 R/kg)

This factor of increase is estimated from the costs given by Hardy *et al.* (1977) and Zunft *et al.* (2011). The net income decreases more rapidly from the optimum value with increasing length as the capital cost increases. However, the effect is relatively small.

7.6 Suitable rock bed design

The design of Kröger (2013a) is suggested as a suitable solution for rock bed thermal storage at temperatures of 500 – 600 °C. The basic concept is shown in Figure 100 and Figure 101. Rock is poured into the region between the retaining embankments and allowed to form a pile at the natural angle of repose of the rock. Depending on the type and the method of packing, this is about 35-40° (see Van Burkalow, 1945).

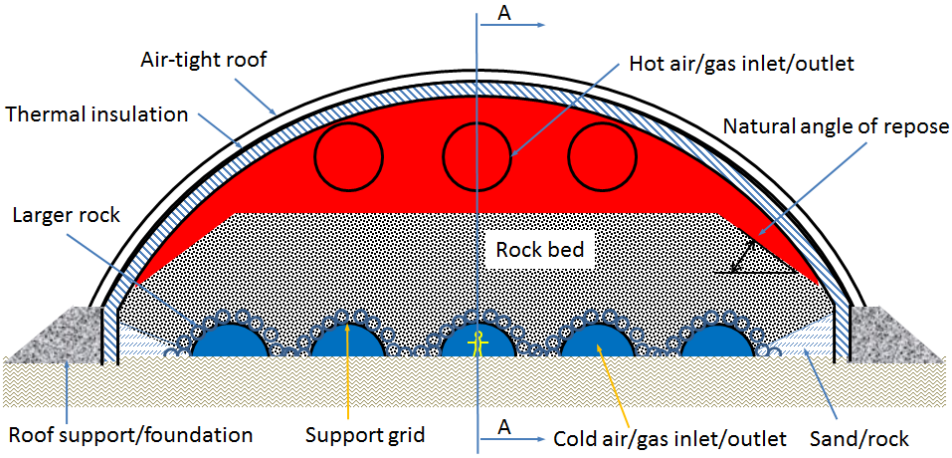

Figure 100: Cross-section of rock bed thermal storage unit (Kröger, 2013a)

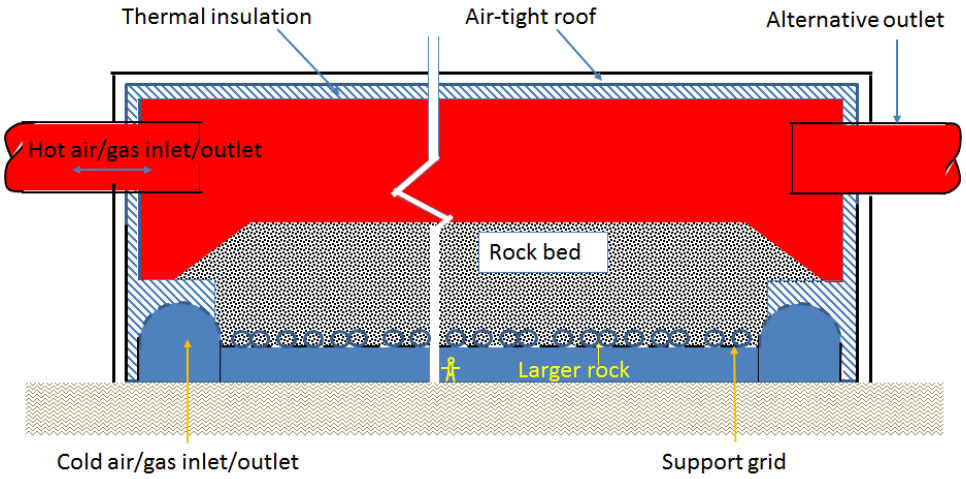

Figure 101: Rock bed, section on A-A (Kröger, 2013a)

The major advantages of the design are that the surface of the rock pile is free to expand, thereby eliminating ratcheting effects; and that the large plenum above the rock allows the high temperature air to be dispersed across the area at relatively low flow speeds. Due to the large surface area at high temperature, the containment dome will require insulation to prevent significant thermal losses.

Further development of the concept needs to address the design details of the air-tight containment structure, insulation, and the ducts to distribute the air under the rock bed, in addition to the method of packing the rock, which could significantly influence the pressure drop and flow distribution characteristics. This will enable a cost estimate for comparison with molten salt and other thermal storage concepts. The scalability of the design and the related influence on cost needs to be determined.

The design of Riaz *et al*/Hardy *et al.* is different from that shown in Figure 100 and Figure 101, and their containment structure is achieved by making use of ground and soil cover. However, their costs are used to provide a minimum estimate. Riaz *et al.* (1976) proposed a target cost of 0.18 \$/kWh$_{th}$ for a rock bed capable of storing tens of megawatt-years of heat at temperatures up to 500 °C for up to six months. This would be 0.7 \$/kWh$_{th}$ in 2013 when adjusted for inflation (United States Department of Labour, s.a.), which is similar to the concrete storage cost claimed by the University of Arkansas (2012), 0.78 US\$/kWh$_{th}$. Hardy *et al.* (1977), in a more detailed economic study on the same concept as Riaz *et al.*, estimated capital costs, including construction and interest expenses: 0.03 – 0.093 \$/kWh$_{th}$ (0.12 – 0.36 \$/kWh$_{th}$ in 2013). For comparison, the cost for a thermocline tank with molten salt and quartzite rock-sand fill was estimated in 2010 as 20 \$/kWh$_{th}$ (Williams and Stancich, 2010).

In 12 hours, the 1 MW$_e$ steam cycle requires 36 MWh$_{th}$, which, based on an assumed T_{flue} = 100 °C and T_{di} = 20 °C, implies a bed capacity of 43 MWh$_{th}$. At 0.36 \$/kWh$_{th}$ this would cost \$ 15 480 (R 154 800). At 0.7 \$/kWh$_{th}$ the cost would be \$ 30 100 (R 301 000). As shown in Table 21, the cost of a molten salt system would be about R 8 000 000.

Rock beds have the potential to significantly reduce thermal storage costs, even if the containment cost is several times greater than the rock cost.

8 Conclusion

Rock beds are a feasible alternative to existing thermal storage systems for concentrating solar power applications at temperatures in the region of 500 - 600 °C.

8.1 Contribution

The first two objectives of the study were to determine the suitability and availability of rock for thermal storage, with emphasis on the South African context. This work is presented in Chapter 2 (Allen *et al.,* 2013b). No previously published data is available on the thermal cycling resistance of South African rock, and very little is available elsewhere in the world in the proposed temperature range, especially for long-term thermal cycling. New thermal cycling tests at rates of 2 °C/min (more than 900 cycles) confirm that South African dolerite, granite, and some types of gneiss are resistant to thermal cycling. Based on heat capacity, density and thermal cycling failure resistance, igneous and metamorphic rock is more likely to be suited to use in rock beds than sedimentary rock. There is rock which is suitable for use in thermal storage applications at temperatures up to 500 – 600 °C. Maps of South Africa produced by eliminating potentially unsuitable rock show that there are significant quantities of dolerite and gneiss in regions suitable for solar power plants (section 2.5). Other rock types which may be suitable include hornfels and possibly some greywacke and even sandstone.

The third objective of the study was the development of correlations to predict the pressure drop (apparent friction factor) of rock beds. This is addressed in Chapters 3, 5 and 6 and Allen *et al.* (2013a). The assumption of duct flow was used to derive an apparent duct friction factor for packed beds, to allow consistent comparison of all measurements (see Appendix A). Friction factors for particles of differing shape, alignment and roughness show that there are no general correlations which predict the pressure drop with any degree of accuracy. The highest measured friction factors were more than 100 % above the lowest at the same Reynolds number, as shown in Chapter 3 and section 6.1.

Measurements with packed beds of five sets of rock (crushed and rounded) show that the friction factor of rock beds can vary significantly. No previous study has obtained measurements in co/counter- and cross-current flow from this number of rock sets. Empirical correlations are necessary for a particular set of rock in order to provide accurate pumping power estimates (an error less than 10 %), unless the Reynolds number is less than 100, where the friction factors appear to converge for a particular packing direction. Of particular importance is the finding that the friction factor for crushed rock is strongly dependent on the packing direction

(co/counter-current or cross-current) relative to the air flow. This is not found in previous work on rock beds. Presumably this is caused by the asymmetry of the particles, and the way they pack under the action of gravity. All experimental work must record the packing direction, as it can cause as much as a 70 % difference in friction factor.

Although it was shown with the duct flow analysis that the appropriate dimension for the packed bed is the duct hydraulic diameter, proportional to the ratio $\Sigma V_p/\Sigma A_p$, the measurement of rock particle surface areas is too time-consuming to be suitable for field use, and the equipment is relatively expensive. New correlations using the volume-equivalent sphere diameter D_v, which is easy to measure by volume displacement, are given for co- and cross-current packing (Equations (81) and (84) respectively) in section 6.2 for crushed rock ($\psi \approx 0.8$) under isothermal conditions. The crushed rock measurements for all co/counter-current packing are within 15 % of Eq.(81) for the specified range.

The friction factors for the high temperature tests on the crushed dolerite, with the exception of the first test (250 °C), are about 30 – 35 % higher than the isothermal prediction (Eq.(81)) corrected for buoyancy. Initially, under isothermal conditions before the thermal tests, the prediction was only 10 – 15 % below the measurement, so the packing characteristic changed during the thermal tests. Since the error occurs even in the case of the bed at steady state at 150 °C, where the air was not changing temperature, this is not caused by the non-isothermal nature of the tests. This is confirmed by the repeated isothermal test at ambient conditions after the thermal tests, which Eq. (81) under-predicts by 30 % on average. Despite the error, Eq.(81) is an improvement on the Ergun equation, which under-predicts the measured friction factor by 50-60 %.

The work on rock bed friction factors will enable techno-economic evaluation of rock beds using more accurate predictions of pumping power than was previously possible.

The fourth objective of the study was to find or develop heat transfer correlations suitable for rock beds, and compare predicted temperatures with measurements. This work is found in Chapters 4, 5 and 6. The low temperature (< 80 °C) thermal tests with different particle shapes and materials show that the temperature profile is insensitive to particle shape (spheres, cubes, crushed or rounded rock) or material (glass, steel, aluminium, rock) for the range of Reynolds numbers in which the tests were made ($100 < Re_p < 600$; $Bi < 0.2 – 0.3$). Unlike the friction factor, the temperature profile is insensitive to the packing direction of the rock. The Hughes E-NTU method and existing heat transfer coefficients were adequate to predict the temperature profiles without taking into account the effective thermal conductivity of the bed.

A simplified heat transfer correlation for air in terms of D_v was obtained from the low temperature measurements and existing correlations (Eq. (91)). This was done to allow field-estimates of the heat transfer coefficients without the need for measuring rock surface area. The simplified heat transfer correlation for air was combined with the Hughes E-NTU method to predict the temperature profile during the high temperature tests up to 530 °C. Provided the varying specific heat capacity of the rock with temperature is taken into account, the predicted outlet temperatures are within 10 °C of the measured value for all tests. For the highest temperature tests of 340 °C, 450 °C and 530 °C, the predicted outlet temperature is within 5 °C of the measured value.

The fifth objective was to develop a method for determining the optimum particle size, bed length and mass flux. The cost-optimum method presented in section 7.5 and Allen *et al.* (2013c) achieves this by fixing the Biot number (typically to 0.1). The mass flux is a function of the Biot number, and is determined from the Biot number. This is done to avoid internal particle resistance from influencing the heat transfer between the particle and surrounding air. The total cost of the bed is calculated from the capital cost (material, containment) and the pumping power requirements. The thermal energy stored in the bed is supplied to a boiler in a steam cycle, and the electricity generated from the steam cycle is used to calculate income. The net income from the combined bed and steam cycle is obtained by subtracting the cost from the income. The maximum net income leads to the optimum values of particle size and bed length.

A sample calculation with simplifying assumptions shows that, for typical HRSG parameters, optimum particle sizes are in the region of 20 mm, possibly up to 30 mm if an allowance is made for clogging of passages. Optimum bed lengths are 6-7 m for D = 20 mm, although allowance for conduction, radiation and non-uniformity in the bed will probably mean that a higher value is desirable.

The final objective was to give design recommendations and estimate the cost of a rock bed for use in a steam cycle having capacities between 1 – 100 MW_e. Design recommendations from literature and from current experience with rock beds are given in section 7.3. The cost estimate is given in section 7.5.2, based on the characteristics of the optimum bed (D = 0.02 m, L = 7 m). A 1 MW_e steam cycle would require a cross-sectional area of approximately 76 m^2 (8.7 × 8.7 m^2) and a rock mass of 845 × 10^3 kg. The rock material cost would be R 0.17 million. If the containment cost is assumed to increase the bed cost from the rock cost by a factor of five, the overall capital cost would be R 0.9 million. This is an order of magnitude less than a molten salt system, which would cost approximately R 8 million.

8.2 Future work

Further work is needed to explore the suitability of sedimentary rock and gneiss for thermal storage. A greater number of samples should be thermally cycled to determine resistance to disintegration. The GIS data that was used to produce the maps is on a scale of 1 : 1 000 000, so more detailed studies should be undertaken in regions of particular interest for solar power.

The friction factor increased by about 20 % as a consequence of thermal tests in the high temperature facility. Future work should determine whether this change in the friction factor with charging and discharging is from particle breakdown, settling and compaction of the particles, or some other cause.

Further work is needed to determine the importance of neglecting radiation and conduction heat transfer through the bed when it is repeatedly charged and discharged, or when there is no fluid flow (stagnant conditions).

The sample cost optimum calculation is based on a simplified model of the steam cycle, and future work should address the following: blower efficiency; a detailed thermodynamic model of the HRSG and steam cycle; the cost of the steam cycle; the effect of interest rate; and the construction and operating costs of the packed bed, including containment. The influence of the layout of the bed on thermal losses should be considered, as should radiation and conduction heat transfer through the bed over long time periods.

A techno-economic study of the design of Kröger (section 7.6) should be undertaken to provide a capital cost estimate for calculation of the optimum bed lengths and particle diameters. The optimum containment structure size and cost, taking into consideration structural limitations, thermal losses and insulation requirements, needs to be determined. The design and cost of the ducts under the rock on the cold side need to be determined.

The bulk packing methods of a large commercial-sized bed, and the influence that they may have on non-uniformity of the bed (void fraction variation, particle size distribution variation) need to be researched. This has the potential to alter the friction factor and cause non-uniform flow that reduces the effective thermal capacity, and needs to be better understood.

The development of air-cooled receivers needs further attention, since the intention is to use air as the heat transfer fluid in this type of system.

9 References

Abdel-Wahed, R.M., Emerson, P.F., Blackshear, P.L., Riaz, M., 1979. Effects on thermal storage efficiencies of modifying heat-transport properties of indigenous sandstones, *Energy* 4: 183 – 192

Achenbach, E., 1995. Heat and flow characteristics of packed beds, *Experimental Thermal and Fluid Science* 19:17 – 27

Adebiyi, G.A., Chenevert, D.J., 1996. An appraisal of one-dimensional analytical models for the packed bed thermal storage systems utilizing sensible heat storage materials, *ASME Journal of Energy Resources Technology* 118: 44 – 49

Adebiyi, G. A., Nsofor, E. C., Steele W. G., Jalalzadeh-Azar, A. A., 1998. Parametric study on the operating efficiencies of a packed bed for high temperature sensible heat storage, *ASME Journal of Solar Energy Engineering* 120: 2 – 13

Adinberg, R., 2011. Simulation analysis of thermal storage for concentrating solar power, *Applied Thermal Engineering* 31: 3588 – 3594

Afrisam, 2010. Cost quotation

Agarwal, P.K., O'Neill, B.K., 1988. Transport phenomena in multi-particle systems – I. Pressure drop and friction factors: Unifying the hydraulic-radius and submerged-object approaches, *Chemical Engineering Science* 43.9: 2487 – 2499

Ahamat, M.A., Tierney, M.J., 2011. Timewise temperature control with heat metering using a thermoelectric module, *Applied Thermal Engineering* 31.8-9: 1421 – 1426

Allen, K.G., 2010. Performance characteristics of packed bed thermal energy storage for solar thermal power plants, MScEng thesis, University of Stellenbosch

Allen, K.G., Kröger, D.G., Fluri, T.P., 2009. Thermal energy storage in a rock bed, *ISES 2009*, Johannesburg, South Africa

Allen, K.G., von Backström, T.W., Kröger, D.G., 2012. Packed beds of rock for thermal storage, *SASEC 2012*, Stellenbosch, South Africa

Allen, K.G., von Backström, T.W., Kröger, D.G., 2013a. Packed bed pressure drop dependence on particle shape, size distribution, packing arrangement and roughness, *Powder Technology* 246: 590 – 600

Allen, K.G., von Backström, T.W., Kröger, D.G., 2013b. Rock bed storage for solar thermal power plants: Rock characteristics, suitability, and availability, *Solar Energy Materials and Solar Cells* (**under review**)

Allen, K.G., von Backström, T.W., Kröger, D.G., 2013c. Packed rock bed thermal storage in power plants: design considerations, *SolarPACES* 2013, Las Vegas, United States (due for publication in Elsevier Energy Procedia – 2014)

Amelio, M., Morrone, P., 2007. Numerical evaluation of the energetic performances of structured and random packed beds in regenerative thermal oxidizers, *Applied Thermal Engineering* 27: 762 – 770

Ammar, A.S.A., El-Osairy, M.A., Ghoneim, A.A., 1992. Technical Note: Comparison of measured and predicted performance of heat storage unit packed with spheres of a local material, *Renewable Energy* 2.1: 73 – 76

Andersen, K.T., 2003. Theory for natural ventilation by thermal buoyancy in one zone with uniform temperature, *Building and Environment* 38:1281-1289

Arndt, J., Bartel, T., Scheuber, E., Schilling, F., 1997. Thermal and rheological properties of granodioritic rocks from the central Andes, North Chile, *Tectonophysics*, 271: 75-88

Australian Government department of resources, energy and tourism, 2011. *Update: Australia's electricity generation technology costs – reference case 2011*. Fossil fuel and renewable plant cost summary from http://www.ret.gov.au/energy/facts/Pages/EnergyFacts.aspx on 16th Jan 2013

Ávila-Marín, A.L., 2011. Volumetric receivers in solar thermal power plants with central receiver system technology: a review, *Solar Energy* 85: 891 – 910

Balakrishnan, A. R., Pei, D. C. T., 1979. Heat transfer in gas-solid packed bed systems: The conduction mode, *Industrial Engineering Chemistry Process Design and Development*, 18.1: 40 – 46

Barnea, E., Mednick, R.L., 1978. A generalized approach to the fluid dynamics of particulate systems Part III: General correlation for the pressure drop through fixed beds of spherical particles, *The Chemical Engineering Journal* 15: 215 – 227

Bauer, R., Schlünder, E.U., 1978a. Effective radial thermal conductivity of packings in gas flow. Part I. Convective transport coefficient, *International Chemical Engineering* 18.2: 181 – 188

Bauer, R., Schlünder, E.U., 1978b. Effective radial thermal conductivity of packings in gas flow. Part II. Thermal conductivity of the packing fraction without gas flow, *International Chemical Engineering* 18.2: 189 – 204

Becker, M., Fend, Th., Hoffschmidt, B., Pitz-Paal, R., Reutter, O., Stamatov, V., Steven, M., Trimis, D., 2006. Theoretical and numerical investigation of flow stability in porous materials applied as volumetric solar receivers, *Solar Energy* 80: 1241 – 1248.

Beasley and Clark, 1984. Transient response of a packed bed for thermal energy storage, Int Journal of Heat and Mass Transfer, 27.9: 1659 – 1669

Bennet, C.O., Myers, J.E., 1974. *Momentum, heat, and mass transfer*, 2nd edition, McGraw-Hill

Bejan, A., 1993. *Heat Transfer*, John Wiley and Sons, New York

Bejan, A., 1996. Method of entropy generation minimization, or modelling and optimization based on combined heat transfer and thermodynamics, *Revue Générale de Thermique* 35: 637 – 646

Beveridge, G.S.G., Haughey, D.P., 1971. Axial heat transfer in packed beds: Stagnant beds between 20 and 750 °C, *International Journal of Heat and Mass Transfer* 14: 1093 – 1113

Birch, F., Clark, H., 1940. The thermal conductivity of rocks and its dependence upon temperature and composition, *American Journal of Science*, 238.8: 529 – 558

Blackshear, P.L., Emerson, P., Baliga, B.R., Riaz, M., 1977. Gravel-filled trenches in earth for annual thermal energy storage, *Proceedings of the 1977 ISES Meeting in Orlando, Florida*, vol 1pp 16-16 to 16-19

Blake, F.C., 1922. The resistance of packing to fluid flow, *American institute of Chemical Engineers* 14: 415 – 421

Blum, H.J.R., Hald, J., 1997. Development of high-efficiency USC power plants in Denmark, *IMechE Conference Transactions: International conference on advanced steam plant*, C522/030/97

Brauer, H., 1971. Grundlagen der Einphasen –und Mehrphasenströmungen, Sauerländer AG, Aarau

Brown University, s.a.. Accessed 15th Oct 2013 http://www.engin.brown.edu/organizations/EWB/GISP/Callster%20-%20chapter_17.pdf

Burke, S.P., Plummer, W.B., 1928. Gas flow through packed columns, *Industrial and Engineering Chemistry* 20.11: 1196 – 1200

Cabeza, L.F., Solé, C., Castell, A., Oró, E., Gil, A., 2012. Review of solar thermal storage techniques and associated heat transfer technologies, *Proceedings of the IEEE* 100.2: 525 – 538

Calis, H.P.A., Nijenhuis, J., Paikert, B.C., Dautzenberg, F.M., Van den Bleek, C.M., 2001. CFD modelling and experimental validation of pressure drop and flow profile in a novel structured catalytic reactor packing, *Chemical Engineering Science* 56: 1713 – 1720

Carman, P.C., 1937. Fluid flow through granular beds, *Transactions of the Institute of Chemical Engineers (London)*, 15: 150 – 166

Carpinlioğlu, M.O., Őzahi, E., Gűndoğdu, M.Y., 2009. Determination of laminar and turbulent flow ranges through vertical packed beds in terms of particle friction factors, *Advanced Powder Technology* 20: 515 – 520

Çengel, Y.A., 2003. Heat Transfer: A Practical Approach, 2nd edition, McGraw-Hill, New York

Çengel, Y.A., Cimbala, J.M., 2006. *Fluid Mechanics: Fundamentals and Applications*, 1st SI edition, McGraw-Hill

Chaki, S., Takarli, M., Agbodjam, W.P., 2008. Influence of thermal damage on physical properties of a granite rock: porosity, permeability and ultrasonic wave evolutions, *Construction and Building Materials* 22: 1456 – 1461

Chandra, P., Willits, D. H., 1981. Pressure drop and heat transfer characteristics of air-rockbed thermal storage systems, *Solar Energy*, 27.6: 547 – 553

Chou, M-S., Cheng, W-H., Huang, B-J., 2000. Heat transfer model for regenerative beds, *Journal of Environmental Engineering* 126.10: 912 – 918

Choudhury, C., Chauhan, P.M., Garg, H.P., 1995. Economic design of a rock bed storage device for storing solar thermal energy, *Solar Energy* 55.1: 29 – 37

Clark, E., 2010. CSP thermal storage: Increasing the options, http://social.csptoday.com/technology/csp-thermal-storage-increasing-options accessed 17th March 2012.

Coutier, J.P., Farber, E.A., 1982. Two applications of a numerical approach of heat transfer process within rock beds, *Solar Energy* 29.6: 451 – 462

Crawford, C.W., Plumb, O.A., 1986. The influence of surface roughness on resistance to flow through packed beds, *ASME Journal of Fluids Engineering* 108: 343 – 347

Coulson, J.M., 1949. The flow of fluids through granular beds: Effect of particle shape and voids in streamline flow, *Transactions of the Institution of Chemical Engineers* 27: 237 – 257

Curto, P.A, Stern, G., 1980. Thermal storage using slag, *Alternative Energy Sources* 3, 1: 195 – 208 (from: *Miami International Conference on Alternative Energy Sources*, Miami Beach, Florida, 15th Dec 1980)

De Aar stonecrushers, 2012. Purchase invoice

De Nevers, N., 1991.*Fluid Mechanics for Chemical Engineers*, 2nd edition, McGraw Hill, inc., New York

Department of Energy, 2010. Executive Summary of the Draft Integrated Electricity
Resource Plan for South Africa - 2010 to 2030 (IRP 2010)

Di Felice, R., Gibilar, L.G., 2004. Wall effects for the pressure drop in fixed beds, *Chemical Engineering Science* 59: 3037 – 3040

Dincer, I., Dost, S. and Xianguo, L., 1997. Performance of sensible heat storage systems for thermal applications, *Int Journal of Energy Research*, 21:12 1157 – 1171

Dinter, F., 1992. Thermische Energiespeicher in Solarkraftwerken und ihre Bewertung. Aachen: Verlag Shaker

Dixon, A.G., Cresswell, D.L., 1979. Theoretical prediction of effective heat transfer parameters in packed beds, A*merican Institute of Chemical Engineering Journal* (AIChE) 25.4: 663 – 676

Domanski, R., Fellah, G., 1998. Thermoeconomic analysis of sensible heat, thermal energy storage systems, *Applied Thermal Engineering* 18.8: 693 – 704

Duffie, J.A., Beckmann, W.A., 1991. *Solar engineering of thermal processes*, Second edition, Wiley, New York

Dullien, F.A.L., 1979. *Porous Media: Fluid Transport and Pore Structure*, Academic Press, New York

Du Plessis, J.P., Woudberg, S., 2008. Pore-scale derivation of the Ergun equation to enhance its adaptability and generalisation, *Chemical Engineering Science*, 63: 2576-2586

Eisfeld, B., Schnitzlein, K., 2001. The influence of confining walls on the pressure drop in packed beds, *Chemical Engineering Science* 56: 4321 – 4329.

Eisfeld, B., Schnitzlein, K., 2005. A new pseudo-continuous model for the fluid flow in packed beds, *Chemical Engineering Science* 60 4105 – 4117

Elder, J.W., 1967. Steady free convection in a porous medium heated from below, *Journal of Fluid Mechanics* 27.1: 29 – 48

Encyclopaedia Britannica online, 2011. *Diabase*. Accessed 15th August 2011 http://www.britannica.com/EBchecked/topic/160909/diabase
Quartz, http://www.britannica.com/EBchecked/topic/486427/quartz
Igneous rock, http://www.britannica.com/EBchecked/topic/282318/igneous-rock/80229/Crystallization-from-magmas
Peridotite, http://www.britannica.com/EBchecked/topic/451736/peridotite

Encyclopaedia Britannica online, 2013. *Chrysotile*. Accessed 30th July 2013 http://global.britannica.com/EBchecked/topic/116497/chrysotile

Ergun, S., 1952. Fluid flow through packed columns, *Chemical Engineering Progress*, 48.2: 89-94

Ergun, S., Orning, A.A., 1949. Fluid flow through randomly packed columns and fluidized beds, *Industrial and Engineering Chemistry* 41.6: 1179 – 1184

Feldhoff, J.F., Schmitz, K., Eck, M., Schnatbaum-Laumann, L., Laing, D., Ortiz-Vives, F., Schulte-Fischedick, J., 2012. Comparative system analysis of direct steam generation and synthetic oil parabolic trough power plants with integrated thermal storage, *Solar Energy* 86: 520 – 530

Flueckiger, S., Yang, Z., Garimella, S.V., 2011. An integrated thermal and mechanical investigation of molten-salt thermocline energy storage, *Applied Energy*, 88: 2098 – 2105

Fluri, T.P., 2009. The potential of concentrating solar power in South Africa, *Energy Policy* 37: 5075 – 5080

Foster, R.J., 1985. *Geology*, 5th edition, Charles E. Merrill Publishing Company

Foumeny, E.A., Benyahia, F., Castro, J.A.A., Moallemi, H.A., Roshani, S., 1993. Correlations of pressure drop in packed beds taking into account the effect of confining wall, *International Journal of Heat and Mass Transfer* 36.2: 536 – 540

Freiwald, M.G., Paterson, W.R., 1992. Accuracy of model predictions and reliability of experimental data for heat transfer in packed beds, *Chemical Engineering Science* 47.7: 1545 – 1560

Freund, H., Zeiser, T., Huber, F., Klemm, E., Brenner, G., Durst, F., Emig, G. 2003. Numerical simulations of single phase reacting flows in randomly packed fixed-bed reactors and experimental validation, *Chemical Engineering Science* 58: 903 – 910

Fricker, H.W., 1991. High temperature heat storage using natural rock, *Solar Energy Materials* 24: 249 – 254

Fricker, H.W., 2004. Regenerative thermal storage in atmospheric air system solar power plants, *Energy*, 29: 871 – 881

Gauvin, W.H., Katta, S., 1973. Momentum transfer through packed beds of various particles in the turbulent flow regime, *American Institute of Chemical Engineers Journal* 19.4: 775 – 783

Geschäftsstelle des Kerntechnischen Ausschusses, 1981. KTA 3102.3: Reactor Core Design of High Temperature Gas-cooled Reactors. Part 3: Loss of Pressure through Friction in Pebble Bed Cores [publisher Kerntechnischer Ausschuss, KTA]

GEOL 615, 2010: Some useful numbers on the engineering properties of materials (geologic and otherwise). Stanford University. Accessed 15th Jan 2013 www.stanford.edu/~tyzhu/Documents/Some%20Useful%20Numbers.pdf

Glück, A., Tamme, R., Kalfa, H., Streuber, C., 1991. Investigation of high temperature storage materials in a technical scale test facility, *Solar Energy Materials* 24: 240 – 248

Gómez-Heras, M., Smith, B.J., Fort, R., 2006. Surface temperature differences between minerals in crystalline rocks: Implications for granular disaggregation of granites through thermal fatigue, *Geomorphology* 78: 236 – 249

Gonzalez, B., 2012. CSP Today Webinar examines the hurdles faced by developers in South Africa, *CSP Today* 10th Dec 2012, accessed on 15th Jan 2013 at http://social.csptoday.com/markets/csp-today-webinar-examines-hurdles-faced-developers-south-africa

Grasse, W., 1991. PHOEBUS international 30 MWe solar tower plant, *Solar Energy Materials* 24: 82 – 94

Grieve, G., 2001. Aggregates for concrete, in B Addis and G Owens (eds), *Fulton's Concrete Technology*, 8th edition, Cement and Concrete Institute, Midrand. p 25 - 59

Griggs, D.T., 1936. The factor of fatigue in rock exfoliation, *The Journal of Geology* 44.7: 783 – 796

Guardo, A., Coussirat, M., Recasens, F., Larrayoz, M.A., Escaler, X., 2006. CFD study on particle-to-fluid heat transfer in fixed bed reactors: Convective heat transfer at low and high pressure, *Chemical Engineering Science* 61: 4341 – 4353

Gunn, D.J., 1978. Transfer of heat or mass to particles in fixed and fluidised beds, *International Journal of Heat and Mass Transfer* 21: 467 – 476

Hall, K., 1999. The role of thermal stress fatigue in the breakdown of rock in cold regions, *Geomorphology* 31: 47 - 63

Hall, K., André, M-F., 2001. New insights into rock weathering from high-frequency rock temperature data: an Antarctic study of weathering by thermal stress, *Geomorphology* 41: 23 – 35

Hänchen, M., Brückner, S., Steinfeld, A., 2011. High temperature thermal storage using a packed bed of rocks – Heat transfer analysis and experimental validation, *Applied Thermal Engineering* 31: 1798–1806

Handley, D., Heggs, P.J., 1968. Momentum and heat transfer mechanisms in regular shaped packings, *Transactions of the Institution of Chemical Engineers* 46: T251 – T264

Hanley, E.J., Dewitt, D.P., Roy, R.F., 1978. The thermal diffusivity of eight well-characterized rocks for the temperature range 300 – 1000 K, *Engineering Geology*, 12: 31 – 47

Hardy, M.P., Albertson, V.D., Bligh, T.P., Riaz, M., Blackshear, P.L., 1977. Large-scale thermal storage in rock: construction, utilization, and economics, *12th Intersociety Energy Conversion Engineering Conference (IECEC)*, Vol 1 no. A 77 – 48701 pp 23 – 44

Hartnady, C.J.H., 2010. South Africa's diminishing coal reserves, *South African Journal of Science* 106 (9/10); article #369

Heller, P., Pfänder, M., Denk, T., Tellez, F., Valverde, A., Fernandez, J,. Ring, A., 2006. Test and evaluation of a solar powered gas turbine system, *Solar Energy* 80: 1225 – 1230

Heggs, P.J., Burns, D., 1988. Single-blow experimental prediction of heat transfer coefficients: A comparison of four commonly used techniques, *Experimental Thermal and Fluid Science* 1: 243 – 251

Hendricks, R.C., Athavale, M.M., Lattime, S.B., Braun, M.J., 1998. Virtual and experimental visualization of flows in packed beds of spheres simulating porous media flows, *NASA*, NASA / TM – 1998-207926

Hicks, R.E., 1970. Pressure drop in packed beds of spheres, *Industrial and Engineering Chemistry Fundamentals* 9.3: 500 – 502

Hicks, T.G., 2006. *Handbook of Mechanical Engineering Calculations: Part 1*, 2nd edition (electronic), McGraw-Hill

Hollands, K.G.T., Sullivan, H.F., Shewen, E.C., 1984. Flow uniformity in rock beds, *Solar Energy* 32.3: 343 – 348

Homand-Etienne, F., Houpert, R., 1989. Thermally induced microcracking in granites: Characterization and analysis, *International Journal of Rock Mechanics and Mining Science* 26.2: 125 – 134

Homand-Etienne, F., Troalen, J-P., 1984. Behaviour of granites and limestones subjected to slow and homogeneous temperature changes, *Engineering Geology* 20: 219 – 233

Hsu, C.T., Cheng, P., Wong, K.W., 1994. Modified Zehner-Schlunder models for stagnant thermal conductivity of porous media, *International Journal of Heat and Mass Transfer* 37.17: 2751 – 2759

Hughes, P.J., 1975. *The design and predicted performance of Arlington House.* MSc thesis, University of Wisconsin – Madison

Hughes, P.J., Klein, S.A., Close, D.J., 1976. Packed bed thermal storage models for solar air heating and cooling systems, *ASME Journal of Heat Transfer* 98: 336 - 338

Idelchik, I.E., 1989. *Flow Resistance: A Design Guide for Engineers*, Hemisphere Publishing Corporation, New York

Imperial Oil, s.a.. *The Importance of Energy*, accessed on 16th Jan 2013 at http://www.imperialoil.ca/Canada-English/about_what_upstream_energy.aspx

Inada, Y., Kinoshita, N., Ebisawa, A., Gomi, S., 1997. Strength and deformation characteristics of rocks after undergoing thermal hysteresis of high and low temperatures, *International Journal of Rock Mechanics and Mining Science* 34.3-4: paper no. 140

Incropera, F.P., DeWitt, D.P., Bergman, T.L., Lavine, A.S., 2007. *Introduction to Heat Transfer*, 5th edition, John Wiley and Sons, Hoboken

Ismail, K.A.R., Stuginsky, R., 1999. A parametric study on possible fixed bed models for pcm and sensible heat storage, *Applied Thermal Engineering* 19: 757 – 788

Jalalzadeh-Azar, A.A., Steele, W.G., Adebiyi, G.A., 1996. Heat transfer in a high temperature packed bed thermal energy storage system – roles of radiation and intraparticle conduction, *ASME Journal of Energy Resources Technology*, 118: 50 - 57

Jeffreson, C. P., 1972. Prediction of breakthrough curves in packed beds, *American Institute of Chemical Engineers Journal (AIChE)*, 18.2:409-420

Jõeleht, A., Kukkonen, I.T., 1998. Thermal properties of granulite facies rocks in the Precambrian basement of Finland and Estonia, *Tectonophysics*, 291: 195-203

Jones, B.W., Golshekan, M., 1989. Destratification and other properties of a packed bed heat store, *International Journal of Heat and Mass Transfer* 32.2: 351 – 359

Jones, D.E., Hill, J.E., 1979. *Testing of pebble-bed and phase change thermal energy storage devices according to ASHRAE standard 94-77*, National Engineering Lab. (NBS), Washington DC. Building Thermal and Service Systems Division.

Jones, D.P., Krier, H., 1983. Gas flow resistance measurements through packed beds at high Reynolds numbers, *ASME Journal of Fluids Engineering* 105: 168 – 173

Jones, M. Q. W., 2003. Thermal properties of stratified rocks from Witwatersrand gold-mining areas, *Journal of the South African Institute of Mining and Metallurgy*, April 2003:173-185

Jordi, R.G. Young, B.D., van Vliet, B.M., 1990. The effect of surface roughness on pressure drop in a packed bed, *Chemical Engineering Communications* 89: 137 – 146

Kays, W.M., London, A.L., 1984. *Compact Heat Exchangers*, 3rd edition. McGraw-Hill, New York

Kaviany, M., 1995. *Principles of Heat Transfer in Porous Media*, 2nd edition, Springer-Verlag, New York

Kearney & Associates - Flabeg Solar International - KJC Operating Co. - Nextant (Bechtel) – NREL – Sandia Natl. Lab – MWE, s.a. *Engineering evaluation of a molten salt HTF in a parabolic trough solar field, NREL Contract No. NAA-1-30441-04*, accessed 26th August 2013 at www.nrel.gov/csp/troughnet/pdfs/ulf_herrmann_salt.pdf

Kearney, D., Kelly, B., Cable, R., Potrovitza, N., Hermann, U., Nava, P., Mahoney, R., Pacheco, J., Blake, D., Price, H., 2003. Overview of use of a molten salt HTF in a trough solar field, presented at the *NREL Parabolic Trough Thermal Energy Storage Workshop*, Golden, CO, February 20-21, 2003

Kehlhofer, R.H., Warner, J., Nielsen, H., Bachmann, R., 1999. *Combined-cycle gas and steam turbine power plants*, 2nd edition, PennWell, Tulsa, Oklahoma

Keyser, M.J., Conradie, M., Coertzen, M., Van Dyk, J.C., 2006. Effect of coal particle size distribution on packed bed pressure drop and gas flow distribution, *Fuel* 85: 1439 – 1445

King, R., Burns, A.P., 1981. Sensible heat storage in packed beds, *International Conference on Energy Storage*, Brighton, 1981. Paper N1: 231 – 245

Kirkup, L., 1994. *Experimental Methods*, John Wiley and Sons Australia, Ltd., Sydney

Kisters, A., 2010. (Geology Dept., University of Stellenbosch) Personal communication, 4th October 2010

Klein, P., Roos, T.H., Shear, T.J., 2013. The effect of temperature dependent thermophysical properties on modelling high temperature regenerative thermal storage systems. Unpublished manuscript.

Kolb, G.J., Ho, C.K., Mancini, T.R., Gary, J.A., 2011. SANDIA report: *Power tower technology roadmap and cost reduction plan*, SAND2011-2419, Sandia National Laboratories, Albuquerque

Kotze, J.P., Von Backström, T.W., Erens, P.J., 2011. A combined latent thermal energy storage and steam generator concept using metallic phase change materials and metallic heat transfer fluids for concentrated solar power, *SolarPACES 2011*, Granada, Spain

Kotze, J.P., von Backström, T.W., Erens, P.J., 2013. High temperature thermal energy storage utilizing metallic phase change materials and metallic heat transfer fluids, *ASME Journal of Solar Energy Engineering*, 135: 035001-1

Kröger, D.G., 2004. *Air-Cooled Heat Exchangers and Cooling Towers*, Penwell Corporation, Tulsa, Oklahoma

Kröger, D.G., 2008. Personal communication

Kröger, D.G., 2013a. *Packed Rock Bed Thermal Storage,* South African provisional patent 2013/03068.

Kröger, D.G., 2013b. Presentation: *First Annual STERG Symposium*, Stellenbosch University

Krupiczka, R., 1967. Analysis of thermal conductivity in granular materials, *International Chemical Engineering* 7: 122 – 144 (not read)

Kunii, D., Smith, J.M., 1960. Heat transfer characteristics of porous rocks, A*merican Institute of Chemical Engineering Journal (AIChE)* 6.1: 71 – 78

Laing, D., Steinmann, W-D., Fiß, M., Tamme, R., Brand, T., Bahl, C., 2006. Solid media thermal storage development and analysis of modular storage operation concepts for parabolic trough power plants, *SolarPACES* 2006

Laing, D., Lehmann, D., 2008. Concrete storage for solar thermal power plants and industrial process heat, *3rd International Renewable Energy Storage Conference (IRES III 2008)*

Larraín, T., Escobar, R., 2012. Net energy analysis for concentrated solar power plants in northern Chile, *Renewable Energy* 41: 123 – 133

Li, P., Van Lew, J., Chan, C., Karaki, W., Stephens, J., O'Brien, J.E., 2012. Similarity and generalized analysis of efficiencies of thermal energy storage systems, *Renewable Energy* 39: 388 – 402

Macdonald, I.F., El-Sayed, M.S., Mow, K., Dullien, F.A.L., 1979. Flow through porous media – the Ergun equation revisited, *Industrial and Engineering Chemistry Fundamentals* 18.3: 199 – 208

Macleod, F., 2011. Reef Chernobyl 'will cost billions', Accessed 1st August 2011 http://mg.co.za/article/2011-03-04-reef-chernobyl-will-cost-billions/

Marewo, G.T., Henwood, D.J., 2006. A mathematical model for supplying air-cooling for a building using a packed bed, *Building Services Engineering Research and Technology* 27: 11 – 26

Margolis, S.B., 1979. An analytical solution for the multidimensional degradation of a packed bed thermocline, *Journal of the Franklin Institute* 307.1: 39 – 58

Martin, H., 2005. The Lévêque-analogy or How to predict heat and mass transfer from fluid friction, HEFAT2005 4th International Conference on Heat Transfer, Fluid Mechanics and Thermodynamics Cairo, Egypt Paper number: K2

Martin, J.J., McCabe, W.L., Monrad, C.C., 1951. Pressure drop through stacked spheres: Effect of orientation, *Chemical Engineering Progress* 47.2: 91 – 94

Mayerhofer, M., Govaerts, J., Parmentier, N., Jeanmart, H., Helsen, L., 2011. Experimental investigation of pressure drop in packed beds of irregular shaped wood particles, *Powder Technology* 205: 30 – 35

Medrano, M., Gil, A., Martorell, I., Potau, X., Cabeza, L.F., 2010. State of the art on high-temperature thermal energy storage for power generation. Part 2 – Case studies, *Renewable and Sustainable Energy Reviews* 14: 56 – 72

Meier, A. Winkler, C., Wuillemin, D., 1991. Experiment for modelling high temperature rock bed storage, *Solar Energy Materials*, 24: 255 – 264

Menendez, B., David, C., Darot, M., 1999. A study of the crack network in thermally and mechanically cracked granite samples using confocal scanning laser microscopy, *Physics and Chemistry of the Earth* 24.7: 627 – 632

Middleman, S. 1998. *An Introduction to Fluid Dynamics*, John Wiley and Sons

Mills, D.R., 2001. Solar thermal electricity, *The State of the Art ISES Position Papers*, ed. J Gordon, Cromwell Press, United Kingdom

Miyashita, K., 1997. Overview of advanced steam plant development in Japan, *ImechE Conference Transactions: International conference on advanced steam plant*, C522/029/97

Montillet, A., Le Coq, L., 2001. Characteristics of fixed beds packed with anisotropic particles – use of image analysis, *Powder Technology* 121: 138 – 148

Montillet, A., 2004. Flow through a finite packed bed of spheres: a note on the limit of applicability of the Forchheimer-type equation, *ASME Journal of Fluids Engineering* 126: 139 – 143

Montillet, A., Akkari, E., Comiti, J., 2007. About a correlating equation for predicting pressure drops through a packed bed of spheres in a large range of Reynolds numbers, *Chemical Engineering and Processing* 46: 329 – 333

Moores, J.E., Pelletier, J.D., Smith, P.H., 2008. Crack propagation y differential insolation on desert surface clasts, *Geomorphology* 102: 472 – 481

Moran, M.J., Shapiro, H.N., 1998. *Fundamentals of Engineering Thermodynamics: SI version*, 3rd edition, John Wiley and Sons Ltd, Chichester, England

Morcom, A.R., 1946. Fluid flow through granular materials, *Transactions of the Institution of Chemical Engineers* 24: 30 – 43

Morrone, P., Di Maio, F.P., Di Renzo, A.D., Amelio, M., 2006. Modeling process characteristics and performance of fixed and fluidized bed regenerative thermal oxidizer, *Industrial and Engineering Chemistry Research* 45: 4782 – 4790

Murrell, S.A.F., Chakravarty, S., 1973. Some new rheological experiments on igneous rocks at temperatures up to 1120 °C, *Geophysical Journal of the Royal Astronomical Society* 34.2: 211 – 250

Nel, R.G., 2013. Discrete Element Modelling of Packed Rock Beds for Thermal Storage Applications, Master's thesis, University of Stellenbosch

Nemec, D., Levec, J., 2005. Flow through packed bed reactors: 1. Single-phase flow, *Chemical Engineering Science* 60: 6947 – 6957

Niven, R.K., 2002. Physical insight into the Ergun and Wen & Yu equations for fluid flow in packed and fluidized beds, *Chemical Engineering Science* 57, 527-534

Nordell, B., Hellström, G., 2000. High temperature solar heated seasonal storage system for low temperature heating of buildings, *Solar Energy* 69.6: 511 – 523.

NREL, 2011. Concentrating solar power projects: Gemasolar thermosolar plant, Oct 24th, 2011. Accessed 15th Jan 2013. http://www.nrel.gov/csp/solarpaces/project_detail.cfm/projectID=40

Ordys, A.W., Pike, A.W., Johnson, M.A., Katebi, R.M., Grimble, M.J., 1994. *Modelling and Simulation of Power Generation Plants*, Springer-Verlag, London

Özkahraman, H.T., Selver, R., Isik, E.C., 2004. Determination of the thermal conductivity of rock from P-wave velocity, *International Journal of Rock Mechanics and Mining Sciences*, 41.4: 703-708

Powell, K.M., Edgar, T.F., 2012. Modeling and control of a solar thermal power plant with thermal energy storage, *Chemical Engineering Science* 711: 138 – 145

Punčochář, M., Drahoš, J., Limits of applicability of capillary model for pressure drop correlation, *Chemical Engineering Science* 55: 3951 – 3954

Py, X., Calvet, N., Olives, R., Echegut, P., Bessada, C., Jay, F., 2009. Low-cost recycled material for thermal storage applied to solar power plants, *SolarPACES* 2009

Rajpaul, V, 2012. *CSP in South Africa*, AfDB and World Bank Workshop – CSP scale up program for Middle East and North Africa region, Tunisia, June 2012.

Ramadan, M.R.I., El-Sebaii, A.A., Aboul-Enein, S., El-Bialy, E., 2007. Thermal performance of a packed bed double-pass solar air heater, *Energy* 32: 1524 – 1535

Ramana, Y.V., Sarma, L.P., 1980. Thermal expansion of a few Indian granitic rocks, *Physics of the Earth and Planetary Interiors* 22: 36 – 41

Reboussin, Y., Formigué, J.F., Marty, Ph., Citti, O., 2005. A numerical approach for the study of glass furnace regenerators, *Applied Thermal Engineering* 25: 2299 – 2320

Reddy, R.K., Joshi, J.B., 2010. CFD modelling of pressure drop and drag coefficient in fixed beds: wall effects, *Particuology* 8: 37 – 43

Riaz, M., Blackshear, P.L., Pfannkuch, H.O., 1976. High temperature energy storage in native rocks, *ISES Joint Conference: Sharing the Sun*, 8: 123 – 137

Riaz, M., 1977. Analytical solutions for single- and two-phase models of packed bed thermal storage systems, *ASME Journal of Heat Transfer* 99: 489 - 492

Riaz, M., 1978. Transient analysis of packed-bed thermal storage systems, *Solar Energy* 21: 123 – 128

Richter, D., Simmons, G., 1974. Thermal expansion behaviour of igneous rocks, *International Journal of Rock Mechanics and Mining Science & Geomechanics Abstracts* 11: 403 – 411

Roblee, L.H.S., Baird, R.M., Tierney, J.W., 1958. Radial porosity variations in packed beds, *American Institute of Chemical Engineering Journal*, 4.4: 460 – 464

Rohsenow, W.M., Hartnett, J.P., Cho, Y.I., 1998. *Handbook of Heat Transfer*, 3rd edition, McGraw Hill, New York (p 1.20)

Rosen, M.A., Hooper, F.C., Barbaris, L.N., 1988. Exergy analysis for the evaluation of the performance of closed thermal energy storage systems. *ASME J. Solar Energy Engineering* 110: 255 – 261

Rubio, E., Caselles, V., Coll, E., Valour, E., Sospedra, F., 2003. Thermal-infrared emissivities of natural surfaces: improvements on the experimental set-up and new measurements, *International Journal of Remote Sensing* 24.24: 5379 – 5390

Sagara, M., Schneider, P., Smith, J.M., 1970. The determination of heat transfer parameters for flow in packed beds using pulse testing and chromatography theory, *The Chemical Engineering Journal* 1: 47 - 56

Sanderson, T.M., Cunningham, G.T., 1995. Performance and design of packed bed thermal storage systems. Part 1, *Applied Energy* 50: 119 – 132

Sandia, 2012. *Renewable Energy: Solar Energy*, accessed on 16th Jan 2013 at http://energy.sandia.gov/?page_id=270

SASTELA, 2012. *CSP in South Africa*, http://www.sastela.org/csp-in-south-africa.html , accessed 27th November 2013

Schröder, E., Class, A., Krebs, L., 2006. Measurements of heat transfer between particles and gas in packed beds at low to medium Reynolds numbers, *Experimental Thermal and Fluid Science*, 30.6: 545 – 558

Schumann, T.E.W., 1929. Heat transfer: a liquid flowing through a porous prism, *Journal of the Franklin Institute* 208: 405 – 416

Shitzer, A., Levy, M., 1983. Transient Behaviour of a rock-bed thermal storage system subjected to variable inlet air temperature: analysis and experimentation, *ASME Journal of Solar Energy Engineering* 105: 200 – 206

Siemens AG, 2008. *Siemens Gas Turbines over 100 MW*, last accessed 31st October 2011
http://www.energy.siemens.com/us/pool/hq/power-generation/gas-turbines/downloads/SGT_over_100MW.pdf

Siemens AG, 2009. *SGT-800 Industrial Gas Turbine*, last accessed 17th Sept 2011
http://www.energy.siemens.com/hq/pool/hq/power-generation/gas-turbines/SGT-800/Brochure%20Gas%20Turbine%20SGT-800%20for%20Power%20Generation.pdf

Siemens AG, 2010. *Industrial Gas Turbines*, last accessed 31st October 2011

http://www.energy.siemens.com/hq/pool/hq/power-generation/gas-turbines/downloads/Industrial%20Gas%20Turbines/Industrial_Gas_Turbines_EN_new.pdf

Simmons, G., Cooper, H.W., 1978. Thermal cycling cracks in three igneous rocks, *International Journal of Mechanical and Mining Sciences & Geomechanics Abstracts* 15: 145 – 148

Singh, R., Saini, R. P., Saini, J. S., 2006. Nusselt number and friction factor correlations for packed bed solar energy storage system having large sized elements of different shapes, *Solar Energy*, 80.7: 760 – 771

Singh, H., Saini, R.P., Saini, J.S., 2010. A review on packed bed solar energy storage systems, *Renewable and Sustainable Energy Reviews* 14: 1059 – 1069

Somerton, W.H., Boozer, G.D., 1960. Thermal characteristics of porous rocks at elevated temperatures, *Journal of Petroleum Technology* 12.6: 77 – 81

Somerton, W.H., Mehta, M.M., Dean, G.W., 1965. Thermal alteration of sandstones, *Journal of Petroleum Technology* 17.5: 589 – 593

Sørensen, B., 2011. Renewable Energy: Physics, engineering, environmental impacts, economics and planning, 4th edition, Elsevier

Spiga, G., Spiga, M., 1981. A rigorous solution to a heat transfer two phase model in porous media and packed beds, *International Journal of Heat and Mass Transfer* 24: 355 – 364

Spiga, G., Spiga, M., 1982. Response of thermal storage units to periodic operating conditions. *International Journal of Heat and Fluid Flow*, 3.3: 143 – 146

Sragovich, D., 1989. Transient analysis for designing and predicting operational performance of a high temperature sensible thermal energy storage system, *Solar Energy*, 43.1: 7 – 16

Sullivan, H.F., Hollands, K.G.T., Shewen, E.C., 1984. Thermal destratification in rock beds, *Solar Energy* 33.2: 227 – 229

Summers, W.A., Shah, Y.T., Klinzing, G.E., 1989. Heat transfer parameters for an annular packed bed, *Industrial and Engineering Chemistry Research* 28: 611 – 618

Sundararagavan, S., Baker, E., 2012. Evaluating energy storage technologies for wind power integration, *Solar Energy* 86: 2707 - 2717

Tallmadge, J.A., 1970. Packed bed pressure drop – an extension to higher Reynolds' numbers, *American Institute of Chemical Engineering Journal (AIChE)* 16.6: 1092 – 1093

Tarbuck, E.J., Lutgens, F.K., 1984. *The Earth: An Introduction to Physical Geology*, Charles E. Merrill Publishing Company

Tarbuck, E.J., Lutgens, F.K., 2006. *Earth Science*, 11th edition, Pearson Prentice Hall

Thirumalai, K., Demou, S.G., 1970. Effect of reduced pressure on thermal-expansion behaviour of rocks and its significance to thermal fragmentation, *Journal of Applied Physics*, 41.13: 5147 – 5151

Thirumalai, K., Demou, S.G., 1974. Thermal expansion behaviour of intact and thermally fractured mine rocks, *International Symposium on Thermal Expansion of Solids (American Institute of Physics)*, Session II: 60 - 71

Tobiś, J., 2000. Influence of bed geometry on its frictional resistance under flow conditions, *Chemical Engineering Science* 55: 5359 – 5366

Tobiś, J., 2001. Turbulent resistance of complex bed structures, *Chemical Engineering Communications* 184: 71 – 88

Torab, H., Beasley, D.E., 1987. Optimization of a packed bed thermal energy storage unit, *ASME J. Solar Energy Engineering* 109: 170 – 175

Tsotas, E., Martin, H., 1987. Thermal conductivity of packed beds: a review, *Chemical Engineering Processes* 22: 19 – 37

United States Department of Labour, s.a. Bureau of Labour Statistics, CPI inflation calculator, http://www.bls.gov/data/inflation_calculator.htm accessed 15th Nov 2013.

University of Arkansas, 2012. Researchers develop effective thermal energy storage system, University of Arkansas Newswire, 9th Nov 2012, accessed 8th Feb 2013 http://newswire.uark.edu/article.aspx?id=19653

Van Antwerpen, W., Du Toit, C.G., Rousseau, P.G., 2010. A review of correlations to model the packing structure and effective thermal conductivity in packed beds of mono-sized spherical particles, *Nuclear Engineering and Design* 240: 1803 – 1818

Van Burkalow, A., 1945. Angle of repose and angle of sliding friction: An experimental study, Geological Society of America Bulletin 56.6: 669 – 707

Van der Merwe, D.F., Gauvin, W.H., 1971. Pressure drag measurements for turbulent air flow through a packed bed, *American Institute of Chemical Engineering Journal (AIChE)* 17.2: 402 – 409

Van der Merwe, C., 2009. Accessed 5th November 2009 http://www.polity.org.za/article/sas-emission-reduction-plan-lacks-action-wwf-2009-07-01-1 , SA's emission reduction plan lacks action – WWF.

Verlotski, V., Schaus, M., Pohl, M., 1997. A solar thermal MgO-powder receiver with working temperatures of more than 1600 °C: Model investigation by using a laser as an irradiation source, *Solar Energy Materials and Solar Cells* 45: 227 – 239

Vortmeyer, D., Schaefer, R.J., 1974. Equivalence of one- and two-phase models for heat transfer processes in packed beds: one dimensional theory, *Chemical Engineering Science* 29: 485 – 491

Vosteen, H.D., Schellschmidt, R., 2003. Influence of temperature on thermal conductivity, thermal capacity and thermal diffusivity for different types of rock, *Physics and Chemistry of the Earth*, 28: 499–509

Wakao, N., Funazkri, T., 1978. Effect of fluid dispersion coefficients on particle-to-fluid mass transfer coefficients in packed beds: Correlation of Sherwood numbers, *Chemical Engineering Science* 33: 1375 – 1384

Wakao, N., Kaguei, S., Funazkri, T., 1979. Effect of fluid dispersion coefficients on particle-to-fluid heat transfer coefficients in packed beds: Correlation of Nusselt numbers, *Chemical Engineering Science* 34: 325 – 336

Waked, A.M., 1986. Solar energy storage in rocks, *Solar and Wind Technology* 3.1: 27 – 31

Wang, U., 2011. The rise of concentrating solar thermal power, *Renewable Energy World*, 6th June 2011. Accessed 15th Jan 2013, http://www.renewableenergyworld.com/rea/news/article/2011/06/the-rise-of-concentrating-solar-thermal-power

Waples, D.W., Waples, J.S., 2004. A review and evaluation of specific heat capacities of rocks, minerals, and subsurface fluids. Part 1: Minerals and nonporous rocks, *Natural Resources Research*, 13.2: 97 - 122

Warerkar, S., Schmitz, S., Göttsche, J., Hoffschmidt, B., Tamme, R., 2008. Performance analysis of an air-sand heat exchanger prototype for high-temperature storage, *EUROSUN 2008* (paper 210)

Weinert, H.H., 1980. *The Natural Road Construction Materials of Southern Africa*, 1st Ed., H & R Academica, Cape Town

Wentz, C.A., Thodos, G., 1963a. Pressure drops in the flow of gases through packed and distended beds of spherical particles, *American Institute of Chemical Engineering Journal (AIChE)*, 9.1: 81 – 84

Wentz, C.A., Thodos, G., 1963b Total and form drag friction factors for the turbulent flow of air through packed and distended beds of spheres, *American Institute of Chemical Engineering Journal (AIChE)*, 9.3: 358 – 361

Williams, A., Stancich, R., 2010. *Thermal Storage: How the Options Stack Up*, Accessed 14th December 2010. http://social.csptoday.com/technology/thermal-storage-how-options-stack

Willits, D.H., Chandra, P., Peet, M.M., 1985. Modelling solar energy storage systems for greenhouses, *Journal of Agricultural Engineering Research* 32: 73 – 93

Willmott, A.J., 1964. Digital computer simulation of a thermal regenerator, *International Journal of Heat and Mass Transfer* 7: 1291 – 1302

Winterberg, M., Tsotsas, E., 2000. Correlations for effective heat transport coefficients in beds packed with cylindrical particles, *Chemical Engineering Science* 55: 5937 – 5943;

Wong ,T.F., 1982. Effects of temperature and pressure on failure and post-failure behaviour of Westerley granite, *Mechanics of Materials*, 1: 3 – 17

Woudstra, N., Woudstra, T., Pirone, A., van der Stelt, T., 2010. Thermodynamic evaluation of combined cycle plants, *Energy Conversion and Management* 51: 1099 – 1110

Wu, D., Song, L., Zhang, B., Li, Y., 2003. Effect of the mechanical failure of catalyst pellets on the pressure drop of a reactor, *Chemical Engineering Science* 58: 3995 – 4004

Yagi, S., Kunii, D., 1957. Studies on effective thermal conductivities in packed beds, *American Institute of Chemical Engineering Journal (AIChE)* 3.3: 373 – 381

Yagi, S., Kunii, D., Wakao, N., 1960. Studies on axial effective thermal conductivities in packed beds, *American Institute of Chemical Engineering Journal (AIChE)* 6.4: 543 – 546

Yang, J., Wang, Q,. Zeng, M., Nakayama, A., 2010. Computational study of forced convective heat transfer in structured packed beds with spherical or ellipsoidal particles, *Chemical Engineering Science* 65: 726 – 738

Zanganeh, G., Pedretti, A., Zavattoni, S., Barbato, M., Steinfeld, A., 2012. Packed bed thermal storage for concentrated solar power – Pilot-scale demonstration and industrial-scale design, *Solar Energy* 86: 3084 – 3098

Zavattoni, S.A., Barbato, M.C., Pedretti, A., Zanganeh, G., 2011. CFD simulations of a pebble bed thermal energy storage system accounting for porosity variations effects, *SolarPACES 2011*, Granada

Zhou, Z., Hou, Q., Yu, A., 2011. Particle scale simulation of heat transfer in fluid bed reactors; in: *Heat Transfer – Mathematical Modelling, numerical methods and information technology*, ed. A Belmiloudi, InTech, http://www.intechopen.com/books/heat-transfer-mathematical-modelling-numerical-methods-and-information-technology

Zunft, S., Hänel, M., Krüger, M., Dreissigacker, V., 2009. High-temperature heat storage for air-cooled solar central receiver plants: a design study, *SolarPACES 2009*

Zunft, S., Hänel, M., Krüger, M., Dreissigacker, V., Göhring, F., Wahl, E., 2011. Jülich solar power tower – experimental evaluation of the storage subsystem and performance calculation, *ASME Journal of Solar Energy Engineering* 133: 031019-1

Appendix A: Analysis of packed bed pressure drop assuming duct flow[6]

The assumption underlying the Ergun (1952) equation is that of duct flow (for example, see Middleman, 1998). This assumption is applied to a number of different packing arrangements in this appendix, and used to obtain an apparent friction factor for presentation of the experimental results.

The pressure drop in a duct is calculated from (Çengel and Cimbala, 2006)

$$\Delta p = f_{da} L(\rho v_d^2/2)/D_h \qquad \textbf{(A-1)}$$

or, in dimensionless form, the apparent duct friction factor

$$f_{da} = \frac{\Delta p}{L(\rho v_d^2/2)} D_h \qquad \textbf{(A-2)}$$

where f_{da} is the apparent friction factor of the duct. L is the duct length, v_d is the flow speed in the duct, and D_h is the hydraulic diameter of the duct.

To illustrate how this is applied to a packed bed of particles, consider a structured packing, divided into repeatable control volumes, pitched at P_l in the flow direction and P_{t1} and P_{t2} in the transverse direction, with fluid flowing upstream from the packing at a speed v_s (the superficial speed) in the direction shown in Figure A-1:

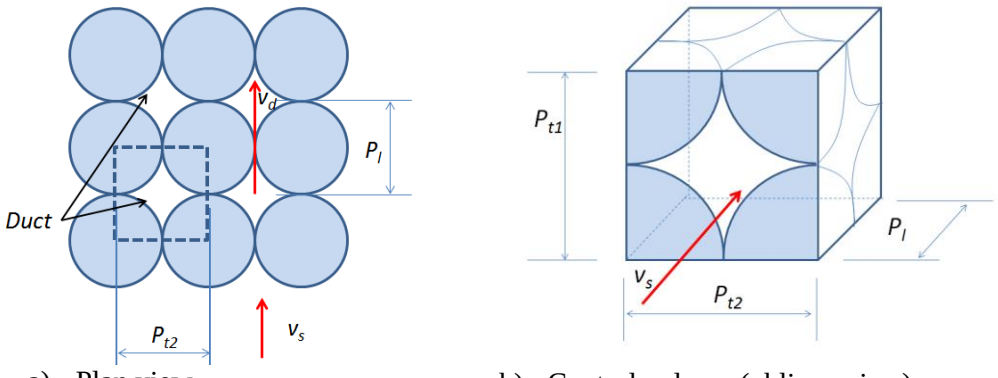

a) Plan view b) Control volume (oblique view)

Figure A-1: Repeatable control volume of structured packing indicating pitch

The average area available for the fluid flow through a control volume such as the one shown in Figure A-1 is given by

[6] A condensed version of this appendix was published in Allen *et al.* (2013a).

$$A_{flow} = V_v/P_l \quad \textbf{(A-3)}$$

where V_v is the void volume in the control volume, calculated from the total control volume V_t and the particle volume V_p:

$$V_v = V_t - V_p = P_l P_{t1} P_{t2} - V_p \quad \textbf{(A-4)}$$

The mass conservation equation for the control volume may be expressed in terms of the average duct speed v_d in the packed bed, and the upstream superficial speed v_s through the total cross-sectional area $A_{cs} = P_{t1}P_{t2}$:

$$\rho A_{flow} v_d = \rho A_{cs} v_s \quad \textbf{(A-5)}$$

where ρ is the fluid density, which is assumed to remain constant. When Eq (A-3) is substituted into Eq (A-5), an expression for v_d is obtained:

$$v_d = A_{cs} v_s / A_{flow} = P_l P_{t1} P_{t2} v_s / V_v = v_s V_t / V_v \quad \textbf{(A-6)}$$

The volumetric void fraction of the control volume is defined as

$$\varepsilon = V_v/V_t = (V_t - V_p)/V_t \quad \textbf{(A-7)}$$

From Eq (A-6) and (A-7) it is possible to write v_d in terms of the void fraction and v_s,

$$v_d = v_s/\varepsilon \quad \textbf{(A-8)}$$

which is a frequently used relation for packed beds. The hydraulic diameter of the duct is defined as

$$D_h = 4A_{flow}/P_{wet} \quad \textbf{(A-9)}$$

where P_{wet} is the average wetted perimeter of the duct, $P_{wet} = A_p/P_l$. A_p is the particle surface area in the control volume. The hydraulic diameter is therefore

$$D_h = 4A_{flow} P_l / A_p = 4V_v/A_p \quad \textbf{(A-10)}$$

For spherical particles, this reduces to the relationship $2\varepsilon D/[3(1-\varepsilon)]$. The friction factor f_{da} is a function of surface roughness and Reynolds number. The latter is defined as

$$Re = \rho v_d D_h/\mu \quad \textbf{(A-11)}$$

Substitute Eq (A-7), (A-8) and (A-10) into Eq (A-11) to obtain

$$Re = \frac{\rho v_s}{\mu\varepsilon}\frac{4V_v}{A_p} = 4\frac{\rho v_s}{\mu}\frac{V_t}{A_p} = 4\frac{\rho v_s}{\mu(1-\varepsilon)}\frac{V_p}{A_p} \quad \textbf{(A-12)}$$

Substitute Eq (A-7), (A-8), and (A-10) into Eq (A-2) and find

$$f_{da} = \frac{\Delta p}{P_l(\rho v_s^2/2)}\frac{\varepsilon^3}{(1-\varepsilon)}\frac{4V_p}{A_p} = f(Re) \quad \textbf{(A-13)}$$

The packed bed friction factor f_{da} may depend on the particle shape, surface roughness and packing arrangement or void fraction; consequently, each packing arrangement should have a particular friction factor associated with it.

For a void fraction of 0.4, Eq. (A-8) gives duct flow speeds that are 2.5 times higher than the superficial flow speed v_s. However, the maximum duct speed can be significantly more than this; for example, Freund *et al.* (2003) calculated duct speeds as much as 8 times higher than the superficial speed.

Simple cubic packing

The above equations are now applied to specific packing arrangements, the first of which is simple cubic (SC) packing of smooth spheres.

The representative control volume shown in Figure A-1 for simple packing contains a total of one sphere. The control volume is symmetrical, so $P_{t1} = P_{t2} = P_l = D$, the sphere diameter. The total volume is thus $V_t = D^3$; the particle volume is the volume of a sphere, $V_p = \pi D^3/6$, and the particle surface area $A_p = \pi D^2$. The flow area from Eq (A-3) $A_{flow} = (D^3 - \pi D^3/6)/D$, and the void fraction

$$\varepsilon_{SC} = V_v/V_t = 1 - \pi/6 = 0.476 \quad \textbf{(A-14)}$$

The hydraulic diameter, from Eq (A-10) and (A-4), is

$$D_h = \frac{4V_v}{A_p} = \frac{4(D^3 - \pi D^3/6)}{\pi D^2} = \frac{4D}{\pi}\left(1 - \frac{\pi}{6}\right) \quad \textbf{(A-15)}$$

According to Eq (A-13),

$$f_{SC} = \frac{\Delta p}{P_l(\rho v_s^2/2)}\frac{\varepsilon_{SC}^3}{(1-\varepsilon_{SC})}\frac{4V_p}{A_p} = \frac{\Delta p}{D(\rho v_s^2/2)}\frac{\varepsilon_{SC}^3}{(1-\varepsilon_{SC})}\frac{4D}{6} = f(Re_{SC}) \quad \textbf{(A-16)}$$

where f_{SC} is the friction factor for simple cubic packing. The Reynolds number defined in Eq (A-12) reduces to

$$Re_{SC} = 4\frac{\rho v_s}{\mu(1-\varepsilon_{SC})}\frac{V_p}{A_p} = \frac{2}{3}\frac{\rho v_s D}{\mu(1-\varepsilon_{SC})} \quad \textbf{(A-17)}$$

Offset simple cubic layers

Equations (A-1) to (A-13) are now applied for offset simple cubic (OSC) layers of smooth spheres, with the layers offset as shown in Figure A-2:

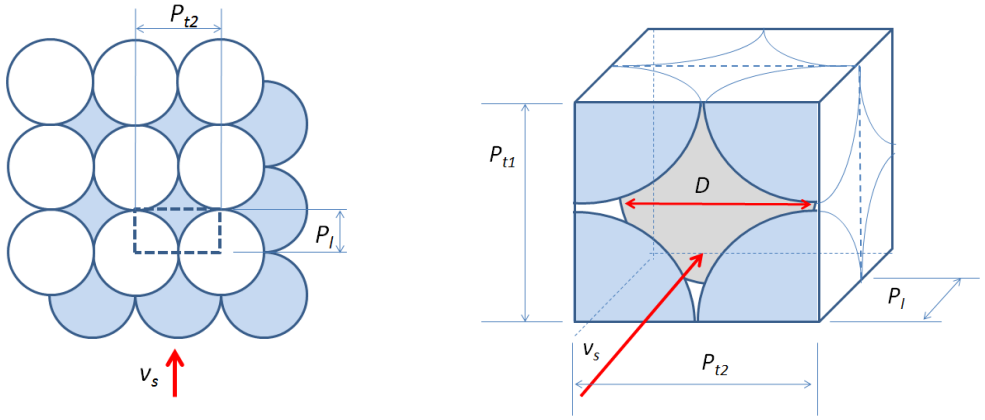

a) Plan view b) Representative vol. (oblique view)

Figure A-2: Offset simple cubic packing arrangement

The total particle volume $V_p = (1/2 + 4 \times 1/8)\pi D^3/6 = \pi D^3/6$. $P_{t2} = D$, $P_l = D/2$, and $P_{t1} = \sqrt{2}D$. The flow area from Eq (A-3) is

$$A_{flow} = V_v/P_l = \left(D^3/\sqrt{2} - \pi D^3/6\right)/(D/2) = D^2(\sqrt{2} - \frac{\pi}{3}) \quad \textbf{(A-18)}$$

The void fraction is

$$\varepsilon_{OSC} = V_v/V_t = 1 - \sqrt{2}\,\pi D^3/6D^3 = 0.2595 \quad \textbf{(A-19)}$$

The hydraulic diameter, from Eq (A-10) and (A-4), is

$$D_h = \frac{4V_v}{A_p} = \frac{4\left(D^3/\sqrt{2} - \pi D^3/6\right)}{\pi D^2} = \frac{2D}{\pi}(\sqrt{2} - \frac{\pi}{3}) \quad \textbf{(A-20)}$$

Eq (A-13) reduces to a friction factor f_{OSC}, for this offset simple cubic packing arrangement:

$$f_{OSC} = \frac{\Delta p}{P_l(\rho v_s^2/2)}\frac{\varepsilon_{OSC}^3}{(1-\varepsilon_{OSC})}\frac{4V_p}{A_p} = \frac{\Delta p}{(D/2)(\rho v_s^2/2)}\frac{\varepsilon_{OSC}^3}{(1-\varepsilon_{OSC})}\frac{4D}{6} = f(Re_{OSC}) \quad \textbf{(A-21)}$$

The Reynolds' number defined in Eq (A-12) reduces to

$$Re_{OSC} = 4\frac{\rho v_s}{\mu(1-\varepsilon_{OSC})}\frac{V_p}{A_p} = \frac{2}{3}\frac{\rho v_s D}{\mu(1-\varepsilon_{OSC})} \quad \textbf{(A-22)}$$

Close packed spheres stacked in identical layers

A packing arrangement of layers of close packed spheres (CPL) is shown in Figure A-3:

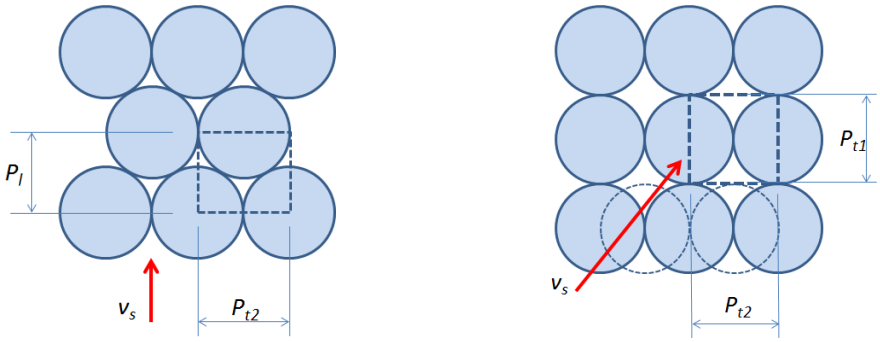

a) Plan view of close-packed layer b) Front view of three layers

Figure A-3: Close-packed spheres in repeated identical layers

The particle volume $V_p = (1/2+2 \times 1/4)\pi D^3/6 = \pi D^3/6$. $P_{t1} = P_{t2} = D$, and $P_l = \sqrt{3}D/2$. The flow area from Eq (A-3) is

$$A_{flow} = V_v/P_l = (\sqrt{3}D^3/2 - \pi D^3/6)2/(\sqrt{3}D) = D^2(1-\pi/(3\sqrt{3})) \quad \textbf{(A-23)}$$

The void fraction

$$\varepsilon_{CPL} = V_v/V_t = (P_{t1}P_{t2}P_l - \pi D^3/6)/P_{t1}P_{t2}P_l = 1 - \pi/(3\sqrt{3}) = 0.395 \quad \textbf{(A-24)}$$

The hydraulic diameter, from Eq (A-10) and (A-4), is

$$D_h = \frac{4V_v}{A_p} = \frac{4\left(\sqrt{3}D^3/2 - \pi D^3/6\right)}{\pi D^2} = \frac{2D}{\pi}(\sqrt{3} - \pi/3) \quad \textbf{(A-25)}$$

Eq (A-13) reduces to a friction factor f_{CPL} for this arrangement of repeated close packed spheres in simple layers:

$$f_{CPL} = \frac{\Delta p}{P_l(\rho v_s^2/2)} \frac{\varepsilon_{CPL}^3}{(1-\varepsilon_{CPL})} \frac{4V_p}{A_p} = \frac{\Delta p}{(\sqrt{3}D/2)(\rho v_s^2/2)} \frac{\varepsilon_{CPL}^3}{(1-\varepsilon_{CPL})} \frac{4D}{6} = f(Re_{CPL}) \quad \textbf{(A-26)}$$

The Reynolds' number defined in Eq (A-12) is

$$Re_{CPL} = 4\frac{\rho v_s}{\mu(1-\varepsilon_{CPL})}\frac{V_p}{A_p} = \frac{2}{3}\frac{\rho v_s D}{\mu(1-\varepsilon_{CPL})} \quad \textbf{(A-27)}$$

A mixture of two differently sized spheres

Equations (A-1) to (A-13) are now applied to a representative volume which contains smooth spheres of two different sizes, arranged as shown in Figure A-4. There is a total of 4 × 1/8 = 1/2 sphere of diameter D_1 and 4 × 1/8= 1/2 sphere of diameter D_2 in the control volume, so the total particle volume is

$$\Sigma V_p = \sum_i n_i V_{pi} = \pi(D_1^3 + D_2^3)/12 \quad \textbf{(A-28)}$$

where n_i is the number of spheres of diameter i and V_{pi} is the volume each individual sphere.

The transverse pitch $P_{t2} = (D_1 + D_2)/2$ and $P_{t1} = P_l = \frac{1}{2}\sqrt{3D_1^2 - 2D_1D_2 - D_2^2}$.

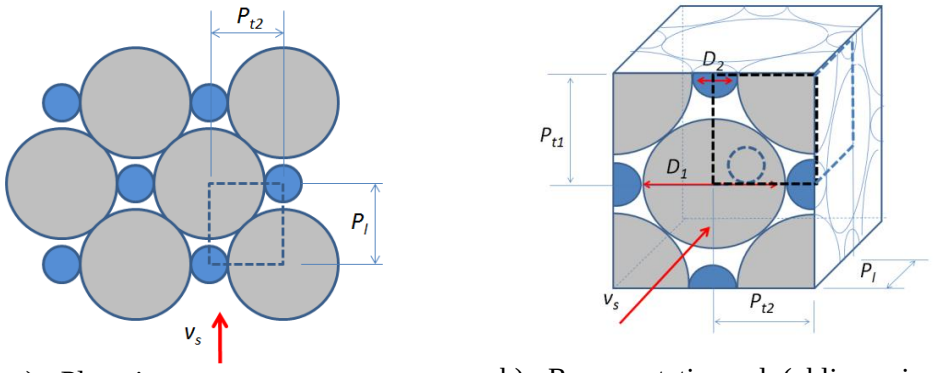

a) Plan view b) Representative vol. (oblique view)

Figure A-4: Two different sphere sizes alternated in packing position

The void fraction for this arrangement of mixed spheres (MS), from Eq (A-7), is

$$\varepsilon_{MS} = \frac{V_v}{V_t} = 1 - \frac{\Sigma V_p}{V_t} = 1 - \frac{4\pi(D_1^3 + D_2^3)}{6(3D_1^2 - 2D_1D_2 - D_2^2)(D_1 + D_2)} \quad \textbf{(A-29)}$$

The total surface area of particles in the control volume is

$$\Sigma A_P = \sum_i n_i A_{pi} = \pi(D_1^2 + D_2^2)/2 \quad \textbf{(A-30)}$$

The hydraulic diameter from Eq (A-4) and (A-10) is

$$D_h = \frac{4V_v}{\Sigma A_p} = \frac{4\big((D_1 + D_2)(3D_1^2 - 2D_1D_2 - D_2^2)/8 - \pi(D_1^3 + D_2^3)/12\big)}{\pi(D_1^2 + D_2^2)/2} \quad \textbf{(A-31)}$$

Eq (A-13) reduces to a friction factor f_{MS} for this arrangement:

$$f_{MS} = \frac{\Delta p}{P_l(\rho v_s^2/2)} \frac{\varepsilon_{MS}^3}{(1-\varepsilon_{MS})} \frac{4\Sigma V_p}{\Sigma A_p} = \frac{\Delta p}{P_l(\rho v_s^2/2)} \frac{\varepsilon_{MS}^3}{(1-\varepsilon_{MS})} \frac{4(D_1^3 + D_2^3)}{6(D_1^2 + D_2^2)} = f(Re_{MS}) \quad \textbf{(A-32)}$$

The Reynolds' number defined in Eq (A-12) is

$$Re_{MS} = 4\frac{\rho v_s}{\mu(1-\varepsilon_{MS})}\frac{\Sigma V_p}{\Sigma A_p} = \frac{2}{3}\frac{\rho v_s}{\mu(1-\varepsilon_{MS})}\frac{D_1^3 + D_2^3}{(D_1^2 + D_2^2)} \quad \textbf{(A-33)}$$

For the limiting case where the diameters of the two spheres are the same, $D_1 = D_2$, Eq (A-32) reduces to the same form of expression that was obtained for single sized spheres in Eq (A-16), (A-21) and (A-26):

$$f_{da} = \frac{\Delta p}{P_l(\rho v_s^2/2)} \frac{\varepsilon^3}{1-\varepsilon} \frac{4D}{6} \quad \textbf{(A-34)}$$

Eq (A-32) and (A-33) can be written in general, for a mixture of particle sizes, as

$$f_{da} = \frac{\Delta p}{P_l(\rho v_s^2/2)} \frac{\varepsilon^3}{(1-\varepsilon)} \frac{4\sum_i n_i V_{pi}}{\sum_i n_i A_{pi}} = f(Re) \quad \textbf{(A-35)}$$

$$Re = 4\frac{\rho v_s}{\mu(1-\varepsilon_{MS})}\frac{\sum_i n_i V_{pi}}{\sum_i n_i A_{pi}} \quad \textbf{(A-36)}$$

Generalized equations for f_{da} and Re

In general, for different particle sizes and shapes, the duct apparent friction factor can be written in terms of the sum of the particle volumes ΣV_p and surface areas ΣA_p as

$$f_{da} = \frac{\Delta p}{P_l(\rho v_s^2/2)} \frac{\varepsilon^3}{(1-\varepsilon)} \frac{4\Sigma V_p}{\Sigma A_p} = f(Re) \quad \textbf{(A-37)}$$

where

$$Re = 4\frac{\rho v_s}{\mu(1-\varepsilon)}\frac{\Sigma V_p}{\Sigma A_p} \quad \textbf{(A-38)}$$

This applies to spherical or non-spherical particles. For the assumption of duct flow, the ratio of the total particle volume to surface area $\Sigma V_p/\Sigma A_p$,– used as early as Blake (1922), Burke and Plummer (1928), Carman (1937) or Coulson (1949) – should be understood to refer to the duct size rather than an equivalent particle size $6\Sigma V_p/\Sigma A_p$, as used by Ergun (1952).

The apparent friction factor f_{da} may depend on the particle shape, surface roughness, packing arrangement and void fraction; consequently, every packing arrangement should have a particular apparent friction factor associated with it.

Gauvin and Katta (1973) state that duct pressure drop models for packed beds are applicable only for high particle sphericities ($\psi > 0.6$). According to Punčochář and Drahoš (2000), the duct flow approximation should be valid for void fractions less than 0.6 for $0.01 < Re_p < 100$, and presumably for $Re_p > 100$ although they do not specifically state this. Carman (1937) notes that a size-ratio of 4:1 or more between maximum and minimum sphere sizes can cause the duct flow approximation to break down, as a consequence of unevenness in the pore size. The assumption of approximately equal flow area throughout the length of the bed seems to be valid (Coulson, 1949).

There are other approaches to packed bed pressure drop calculation – for example Barnea and Mednick (1978), who used a single particle drag model for spheres and adjusted the drag coefficient and Reynolds number for packed beds so that the relation was valid for void fractions up to 1 (a single particle in a large volume). However, the method does not appear to provide more accurate predictions than hydraulic radius models for void fractions between 0.3 - 0.5. See also Agarwal and O'Neill (1988).

Note the comment of Bauer and Schlünder (1978a) that the pressure drop is proportional to the fifth power of the channel diameter. For more on duct flow, see Eisfeld and Schnitzlein (2001), or fluid dynamics books like Bennett and Myers (1974); Dullien (1979); or Kaviany (1995).

Appendix B: Biot number

The dimensionless temperature θ_B of the surface and centre of a sphere is plotted as a function of the Fourier number *Fo* in Figure B-1. T_i is the initial uniform temperature of the sphere before exposure to a fluid at T_∞.

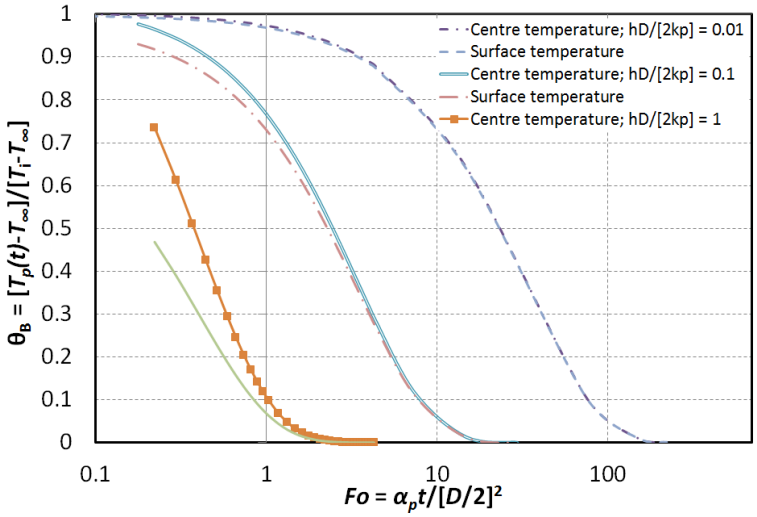

Figure B-1: Influence of Biot number on the difference between surface and centre temperature of a sphere

The maximum difference between the surface (T_{r*}) and centre (T_{o*}) temperature is plotted as a function of *Bi* in Figure B-2. For *Bi* = 0.1, the maximum difference between the dimensionless temperature at the centre and surface of the sphere will be 0.05. In the case of a sphere initially at 0 °C suddenly exposed to a fluid at 100 °C (*Fo* > 0.2), there will be a maximum temperature difference between the surface and centre of the sphere of 5 °C. For *Bi* = 0.3, this will increase to almost 13 °C.

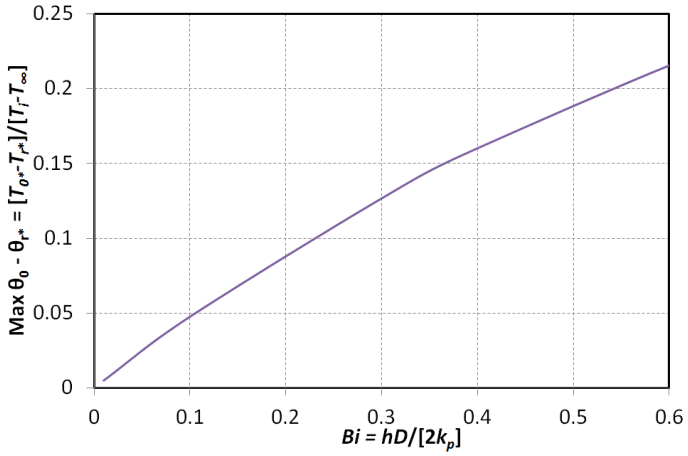

Figure B-2: Difference between surface and centre temperature of a sphere (*Fo* > 0.2)

The Biot number of a particle may also be defined (Çengel, 2003) as

$$Bi = \frac{h}{k_p}\frac{V_p}{A_p} \quad \textbf{(B-1)}$$

For a sphere, Eq. (B-1) becomes

$$Bi = \frac{hD}{6k_p} \quad \textbf{(B-2)}$$

However, Eq. (35), which is a factor of three bigger, is recommended by Incropera *et al.* (2007) as being more appropriate.

Zanganeh *et al.* (2012) defined the Biot number as hD_v/k_p; they found a value of 0.18 to be suitably low to avoid intraparticle conduction effects.

Appendix C: Heat capacity measurement

A container with a volume of approximately 4 L was insulated with 50-100 mm thick polystyrene on all sides. A known mass of the particles m at a measured initial temperature was placed in the container. Hot water of a known initial temperature and mass m_w was poured into the container, and the temperature was measured to steady-state. If there are no losses, the energy lost from the water should equal the energy absorbed by the particles:

$$m_w c_w \Delta T_w = mc\Delta T_p \quad \textbf{(C-1)}$$

Since the mass of the particles and water is known, as is the specific heat capacity of water and the temperature change of the water and particles, it is possible to calculate the specific heat capacity of the particles c. It is not possible to use this method for measuring the heat capacity at temperatures above 100 °C, since the water would boil. An alternative fluid (like oil) or a different measuring technique such as differential scanning calorimetry (DSC) is required.

A stirrer was used to ensure that the contents were at a uniform temperature throughout. Despite the insulation, there were thermal losses from the container, and the container and stirring mechanism absorbed some energy. The stirring process itself introduced energy into the system. To take this into account, several calibration tests were conducted without particles to determine the thermal loss characteristics of the system. A time-dependent average universal heat transfer coefficient was calculated as a function of the temperature difference between the container and ambient temperature, and used to correct all the heat capacity tests.

Samples of the measured temperature and calculated specific heat capacity are shown for the "13 mm" crushed rock in Figure C-1 and Figure C-2 respectively.

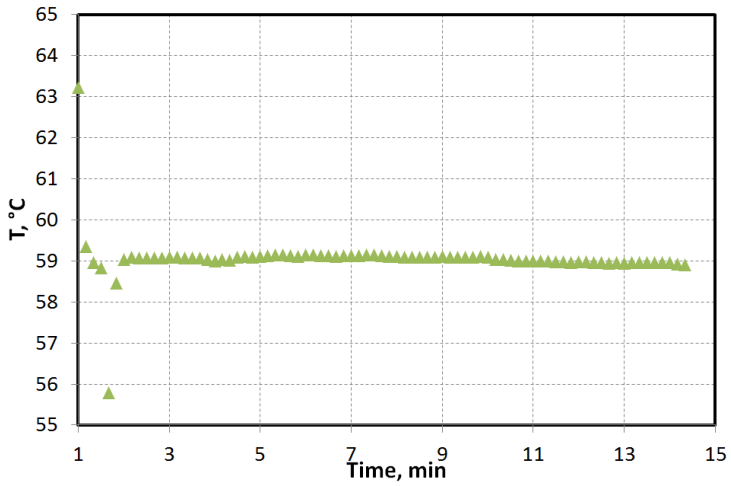

Figure C-1: Avg. temperature measured in container during test ("13 mm" rock)

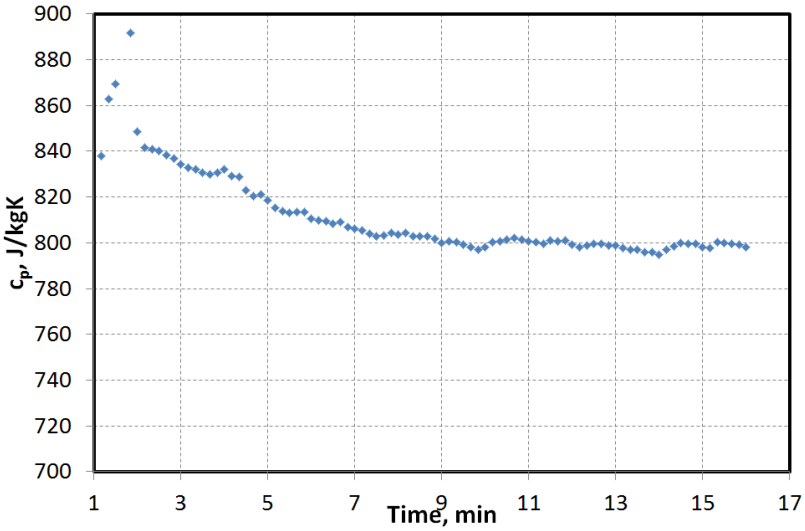

Figure C-2: Average calculated specific heat capacity of rock as a function of time (corrected for container absorption and losses)

A minimum of four measurements were made for each particle type.

Appendix D: High temperature test facility

A photograph of the high temperature test facility is shown in Figure D-1.

Figure D-1: High temperature test facility showing test section with top plenum chamber removed

Appendix E: Friction factor uncertainty

The cumulative uncertainty of the friction factor due to error propagation is shown for sample measurements with the 16 mm aluminium cubes in Figure E-1 and Figure E-2. It was calculated by means of the method in Kirkup (1994), and takes into account the uncertainty of the pressure measurements at the test section and flow measurement nozzle, in addition to the flow nozzle dimensions, particle size and density, test section cross-sectional area, volume, and void fraction.

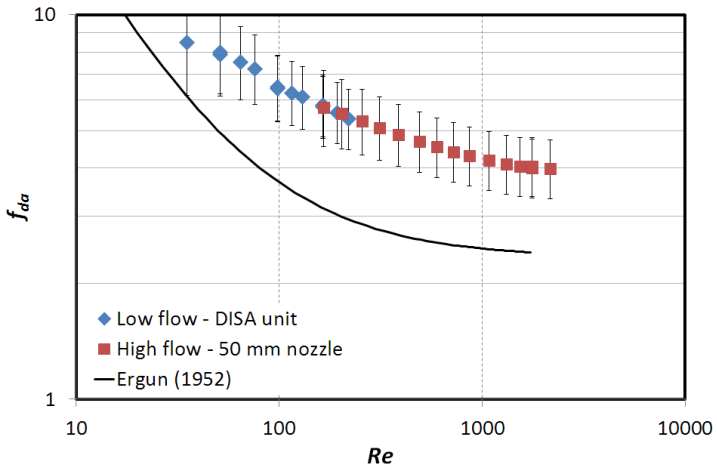

Figure E-1: Al cubes, friction factor uncertainty (showing what it would be if a wall liner had been used)

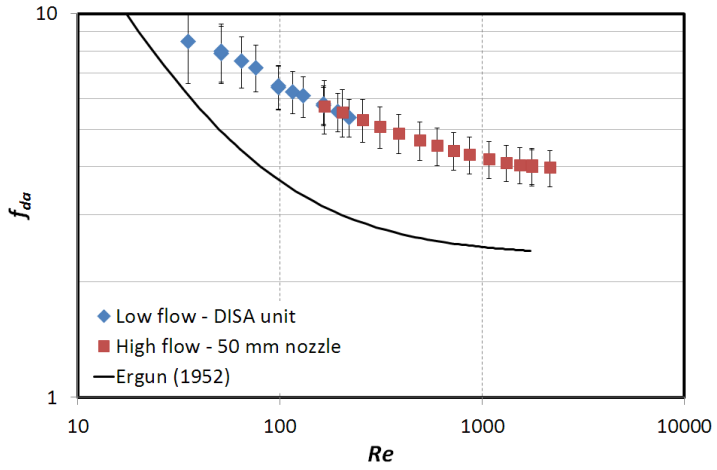

Figure E-2: Al cubes, friction factor uncertainty (without liner)

The uncertainty estimate in Figure E-1 is based on a void fraction uncertainty if a flexible lining is used, while the estimate in Figure E-2 is for a void fraction uncertainty without the use of a lining. The void fraction can be the dominant cause of uncertainty, especially for the high flow tests, and it is desirable to avoid the use of a liner if possible. Without the liner, the uncertainty is 10 – 15 %/

The uncertainty for a selection of the other test results is given in Figure E-3 - Figure E-6. A set of smooth sphere measurements is shown in Figure E-3. For most of the range, the uncertainty falls between 10 – 15 %. It is only near the minimum flow rate measurements that it rises to 15 – 20 %.

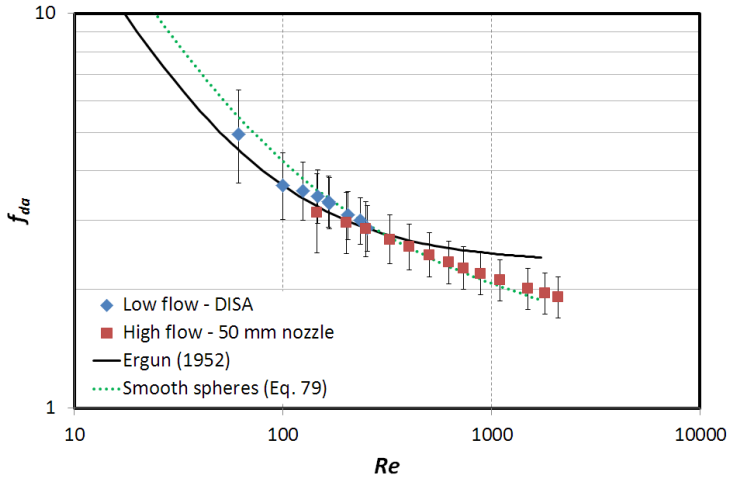

Figure E-3: Randomly packed smooth spheres, friction factor uncertainty (without liner)

The smooth sphere tests were benchmarked against the data of Kays and London (1984) and the correlations of Brauer (1971) and Carman (1937) (see Figure 29 and Figure 30). The favourable comparison with reliable data and recognised correlations for smooth spheres, combined with the repeatability of the tests, gives confidence in the measurements for other particle types.

The calculated uncertainty for the acorns (Figure E-4) in parallel packing is the worst (20 – 30 %, exceeding 40 % near the limits of the measurement equipment).

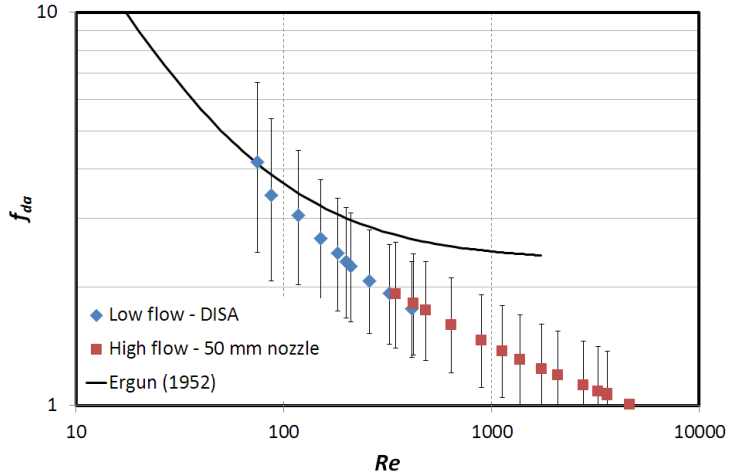

Figure E-4: Acorns aligned parallel to flow, friction factor uncertainty (with liner)

This is primarily because of the void fraction uncertainty caused by the use of a liner. Comparison with the other dataset that was obtained to check repeatability (Figure 33) suggests that this probably over-estimates the uncertainty.

The uncertainty of the crushed rock in co/counter-current packing is shown in Figure E-5 and Figure E-6. For the '13 mm' rock the uncertainty is between 15 – 20 %, while that for the '26 mm' Durbanville is 10 – 20 %, with the exception of the measurements at the lowest flow rates.

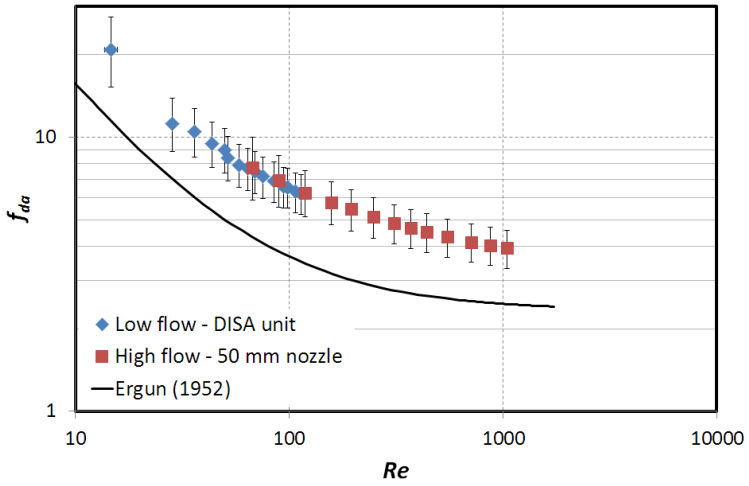

Figure E-5: Randomly packed crushed '13 mm' rock (co/cross-current), friction factor uncertainty (without liner)

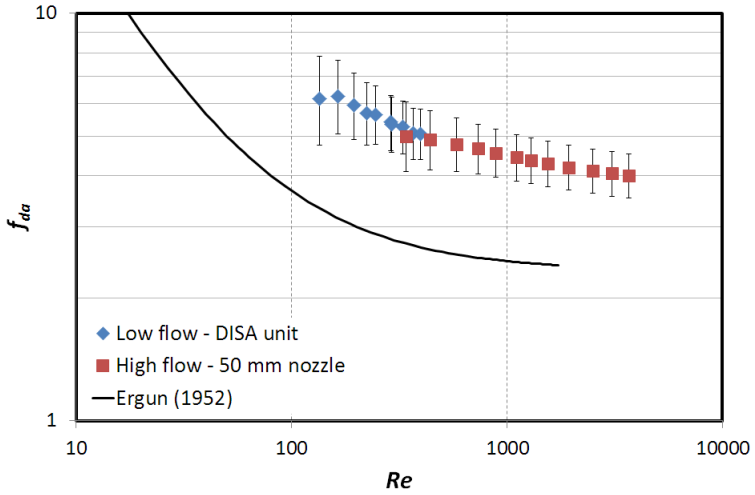

Figure E-6: Randomly packed crushed '26 mm' rock (Durbanville; co/cross-current), friction factor uncertainty (without liner)

Appendix F: Rock pressure drop measurements

It was proposed that the pressure drop could be expressed by means of an equation of the form

$$\frac{\Delta p}{L}\frac{\varepsilon^3}{1-\varepsilon} = a_4 G^{a_5} D^{a_6} \qquad \textbf{(F-1)}$$

where a_4, a_5, and a_6 are constants. However, no single values for a_5 and a_6 could be determined. Figure F-1 shows the measurements and curve fits from the four rock sets tested in co-current packing, plotted as a function of mass flux G.

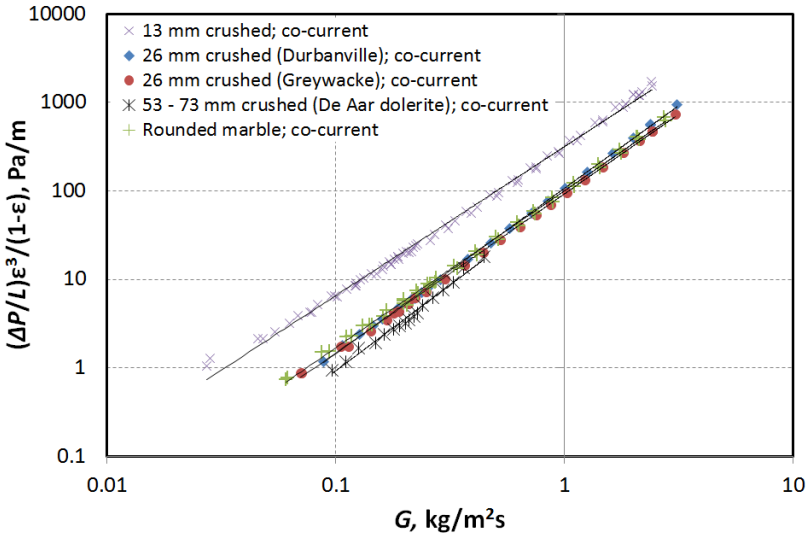

Figure F-1: Pressure drop dependence on mass flux; co/counter-current

From the results plotted in Figure 36 and Figure 37 (section 6.1), it seems that the power of the Reynolds term may vary with particle size. Figure F-1 also suggests that the power of the mass flux term (a_5) may be dependent on D, since it progressively increases with D (1.68 for "13 mm" to 1.94 for "53-73 mm" particles; average of 1.814). The values are summaries in Table F-1.

Table F-1: Values of a_5 for co/counter-current packing

Rock set	a_5
"13 mm" (Durbanville)	1.68
"26 mm" (Durbanville)	1.87
"26 mm" (Greywacke)	1.80
"53-73 mm" De Aar dolerite	1.94
Rounded marble	1.78

The dependence of pressure drop on particle size is shown for a range of mass fluxes in Figure F-2. The pressure drop at each mass flux was calculated by means

of curve fits to the data shown in Table F-1. The varying values of a_6 (average of -1.13) suggest a dependence on the mass flux, as shown in Table F-2:

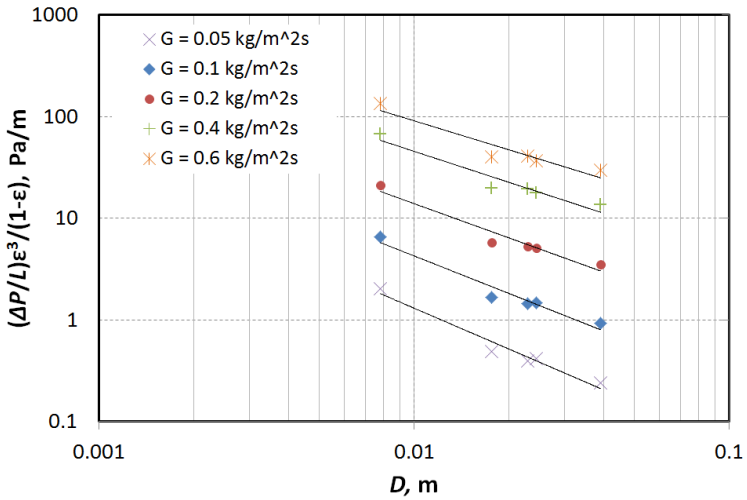

Figure F-2: Pressure drop dependence on particle size; co-current

Table F-2: Values of a_6 for co/counter-current packing

Mass flux, kg/m^{2}s	a_6
0.05	-1.34
0.1	-1.23
0.2	-1.12
0.4	-1.01
0.6	-0.95

Appendix G: Diesel fuel combustion

The stoichiometric equation for the (ideal) combustion of diesel fuel is:

$2C_{12}H_{26} + 37(O_2 + 3.76N_2) \rightarrow 24CO_2 + 26H_2O + 139.12N_2$

where $O_2 + 3.76N_2$ is the approximation for air and $C_{12}H_{26}$ the approximation for diesel fuel (Moran and Shapiro, 1998).

The atomic mass of the elements is: C: 12; H: 1; O: 16; N: 14
The atomic mass of the individual molecules is:
Diesel: 12(12) + 26(1) = 170; O_2: 32; N_2: 28; CO_2: 44; H_2O: 18; air: 32 + 3.76(28) = 137.28

$2(170) + 37(137.28) \rightarrow 24(44) + 26(18) + 139.12(28)$

The air : fuel mass ratio is 5080/340 = 14.9. This means that 14.9 kg of air are required for every 1 kg of diesel.

The 530 °C test used on average 0.0025 kg/s diesel, requiring 0.0373 kg of air for stoichiometric combustion, and producing a total of 0.0373(1056+468+3895)/5080 = 0.0398 kg/s of combustion gases. The total average air flow through the system was 0.178 kg/s, so the air used in combustion would be around 21 % of the total air flowing through the system, while the combustion product would amount to 22 %.

The unchanged N_2 constitutes 3895/(1056+468+3895) = 72 % of the combustion product. The CO_2 and H_2O make up 28 %. The total system mass flow for the 530 °C test contains only 0.0398(0.28) = 0.0111 kg/s of CO_2 and H_2O – 6 % of the total mass flow.

The specific heat capacity of an ideal gas mixture is the sum of the individual specific heat capacities multiplied by the mole fraction (Moran and Shapiro, 1998). The combustion products should increase the overall heat capacity of the air flowing through the test section for this test by 3 %. Lower temperature tests made less use of the diesel burner, so the proportion of CO_2 and H_2O was smaller.

The density variation is negligible (< 0.5 %).

Appendix H: HRSG flue gas outlet temperature estimate

For this work, the HRSG was assumed to be unfired, supplied purely by thermal energy from the gas turbine (directly or via the packed bed). In order to estimate the steam conditions and flue gas outlet temperature based on the gas turbine exhaust energy, the analysis of Hicks (2006) was applied to a simple steam cycle with no reheat, at steam superheat (SH) temperatures of 400 °C and 450 °C, and steam pressures between 1 – 10 MPa. These values are similar to the solar-powered steam cycle proposed by Larraín and Escobar (2012): 6.5 MPa, 400 °C at 142 kg/s for a 100 MW_e gross output.

Two characteristic parameters of the HRSG that limit the efficiency are the approach temperature and the pinch point (Kehlhofer *et al.*, 1999), shown in Figure H-2. The pinch point is the difference between the gas temperature at the outlet of the evaporator and the evaporator water temperature, and is a function of the evaporator surface area (indirectly, cost). The approach point is the difference between the temperature of the feedwater entering the evaporator (approximately the same as the water exiting the economizer) and the evaporator water saturation temperature. The feedwater is generally a few degrees cooler than the boiling temperature to prevent it from boiling before it reaches the evaporator.

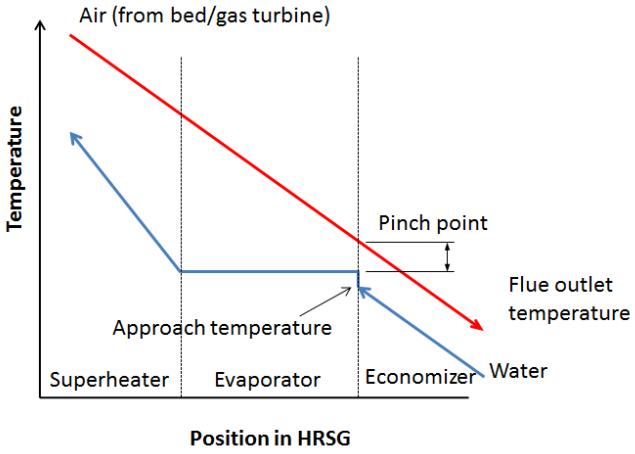

Figure H-1: HRSG water and air flow schematic (based on Kehlhofer *et al.*, 1999)

Typical values for the pinch point lie between 8 – 15 °C and the approach temperature differences are between 5 – 12 °C (Kehlhofer *et al*). According to Hicks (2006), typical approach and pinch point temperatures are between about 5 – 17 °C. Siemens specify an approach point of 5 °C and a pinch point of 8 °C for their combined cycle HRSG and SGT-800 gas turbine (Siemens AG, 2009).

In order to estimate the HRSG flue gas outlet temperature characteristics, it was assumed that a turbine similar to the Siemens SGT 800 (Siemens AG, 2009) would be used. This turbine is rated at 47 MW_e, a mass flow rate of 131.5 kg/s

and exhaust gas temperature of 544 °C. The air inlet temperature to the HRSG was rounded to 540 °C, to make an allowance for an air temperature drop in the ducts between the gas turbine and HRSG – a loss of the order of 1 %. HRSG heat losses of 1 % of the incoming heat and blowdown losses of 2 %, were assumed, based on Hicks (2006).

The feedwater temperature at the economizer inlet was assumed to be 60 °C, a value used by Kehlhofer *et al.* (1999). This matches the condensate temperature from air-cooled condensers in Kröger (2004). Lower temperatures can be obtained with wet cooling; for example, 27 – 33 °C (Ordys *et al.*, 1994).

The variation of the flue gas temperatures as a function of the design parameters is shown in Figure H-2. Gas turbine exhaust temperature supplied to the HRSG is abbreviated as GT, the pinch point as PP, and the superheat temperature as SH. A curve has also been plotted to show the effect on the flue gas temperature of increasing the gas turbine exhaust temperature to 560 °C. An approach point of 5 °C and a pinch point of 5°C and 10 °C were used. For a steam cycle operating at 5 – 10 MPa, the flue gas temperature would be about 150 °C or more for the chosen HRSG parameters and gas turbine exhaust temperature.

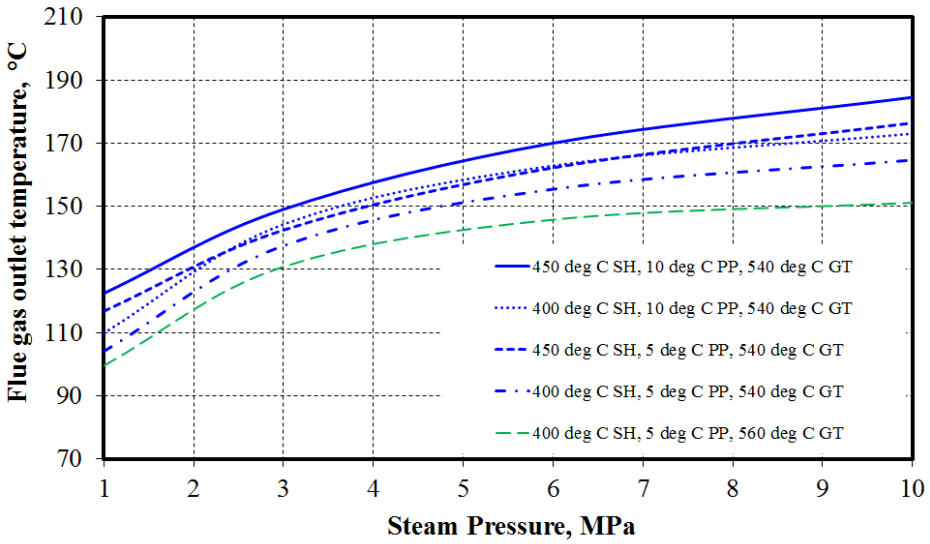

Figure H-2: HRSG flue gas temperature as a function of steam side pressure and heat exchanger parameters for a simple, single pressure steam cycle without reheat

In combined cycles, the steam superheat temperature is usually below the gas turbine exhaust temperature by 30 – 80 °C, depending on the plant design (see Woudstra *et al.*, 2010; Kehlhofer *et al.*, 1999). The 1300 MW_e combined cycle plant at Lumut (Malaysia), which has an unfired HRSG, has the following operating parameters (Kehlhofer *et al.*, 1999):
Gas turbine exhaust temperature: 544 °C; Flue gas outlet temperature: < 100 °C; Superheated steam temperature: 508 °C (at 6.7 MPa).

Appendix I: Crushed rock sales prices in South Africa

The sales prices shown in Figure I-1 are for a number of suppliers throughout South Africa. The smaller crushed rock tends to be higher in cost, presumably because of demand or higher crushing costs or a combination of the two effects.

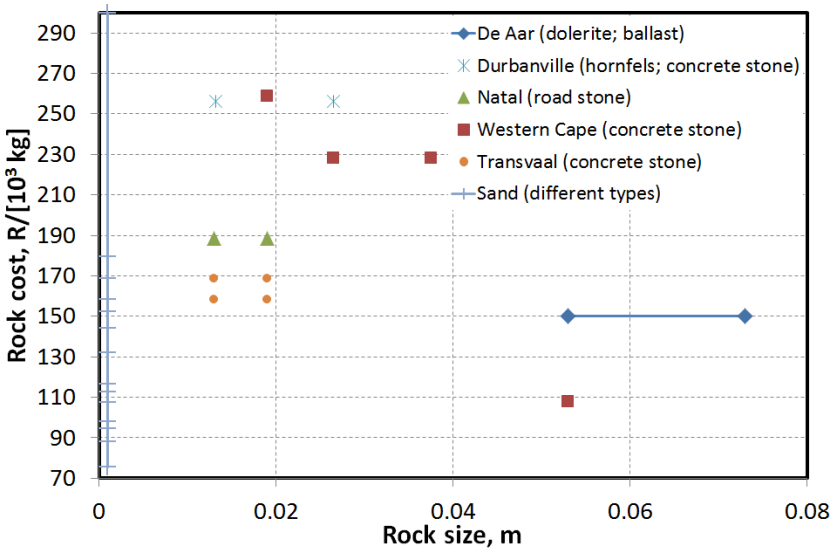

Figure I-1: Sample sales prices of crushed rock of different sizes from different locations in South Africa

Appendix J: Additional cost optimum information

The thermal energy recovered from the bed during discharging is shown in Figure J-1 as a percentage of the energy available in the air stream during charging. The smallest particle size allows the highest proportion of the charging energy to be captured and recovered per discharge. For D = 0.01 m, 99 % of the charging air stream energy can be stored and withdrawn from the bed during discharging, while for D = 0.06 m, only 95 % can be withdrawn. The remainder of the energy is lost at the bed outlet during charging.

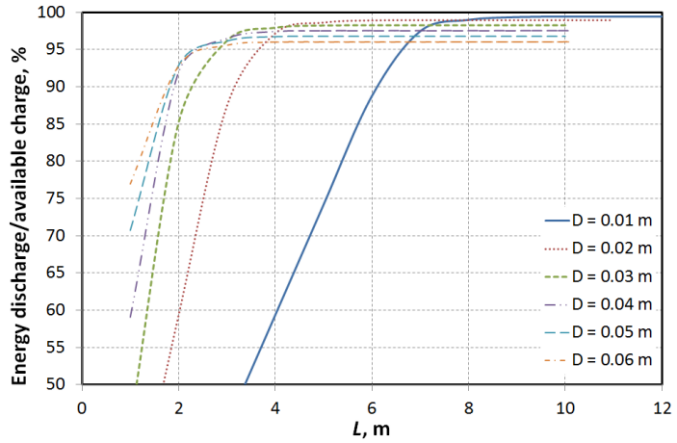

Figure J-1: Discharge thermal energy as a percentage of the total energy contained in the charging air stream (at steady state)

The normalised net income was also calculated for variable rock heat capacity, and is shown in Figure J-2.

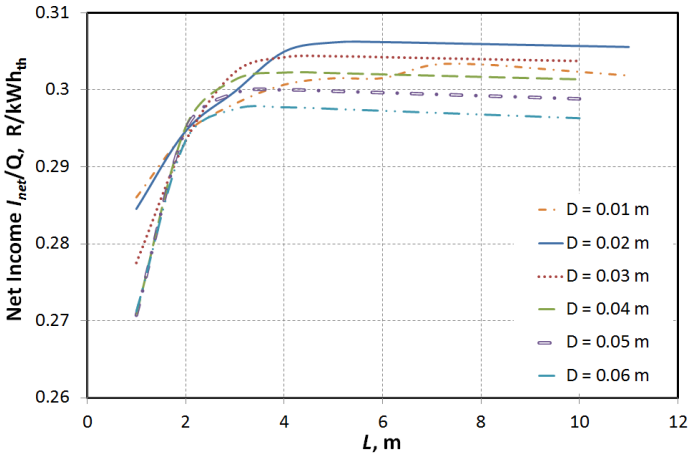

Figure J-2: Net income (normalised) based on variable specific heat capacity

There is little difference from Figure 96, which was obtained for a constant heat capacity of 820 J/kgK. The optimum is still for D = 0.02 m at a slightly shorter length L = 5 – 6 m. The greatest change is for D = 0.01 m, which has a higher net

income for $L < 7$. This is because the thermocline is less dispersed with the smaller particles, and the particles undergo a greater change in temperature, which means that their thermal capacity can be used to a greater extent.

Appendix K: Levelized cost of electricity

Feldhoff *et al.* (2012) use the following method to calculated the LCOE for a solar power plant which includes thermal storage:

$$LCOE = \frac{C_a}{W_{e,net}} = \frac{FCR \times I_c \ + \ C_{O\&M} \times A_c}{W_{e,net}} \quad \textbf{(K-1)}$$

C_a is the total annual plant cost and $W_{e,net}$ is the annual net electricity production. $C_{O\&M}$ is the operating and maintenance cost per unit collector area, where A_c is the total net collector area. I_c is the total initial investment, and FCR is the fixed charge rate, defined as

$$FCR = \ f_{ins} + a_f \quad \textbf{(K-2)}$$

f_{ins} is the administration and insurance cost, and a_f is the annuity factor (or capital recovery factor – Choudhury *et al.*, 1995) for the initial investment, defined by

$$a_f = \frac{(1 + i_r)^n \times i_r}{(1 + i_r)^n - 1} \quad \textbf{(K-3)}$$

i_r is the interest rate and n is the time period, taken as the depreciation period. It is assumed that the entire cost is financed by debt and that the interest rate applies to the total investment amount. Feldhoff *et al.* used the following values: i_r = 8 %/year; n = 20 years; f_{ins} = 1 %/year (based on total investment amount).